Mineral resources: Introduction to ore formation in a global context

Bernd Lehmann
Techn U Clausthal

Solar nebula condensation

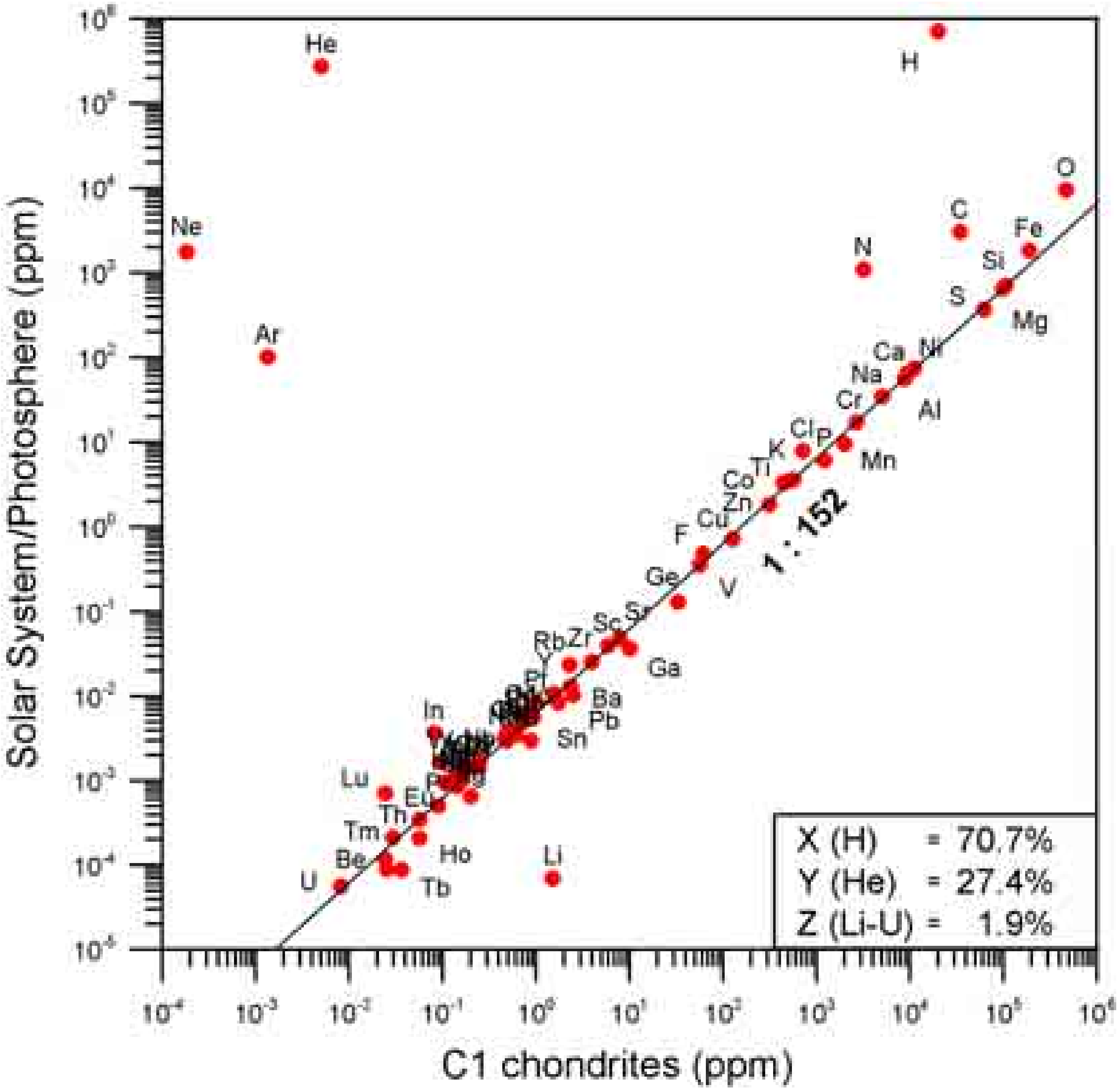

Marlow, L5 chondrite, Oklahoma, USA: Olivine

Fluid inclusions in halite of Monahans H5 chondrite
(Fall of 22 Mar 1998, Monahans, Texas, USA)

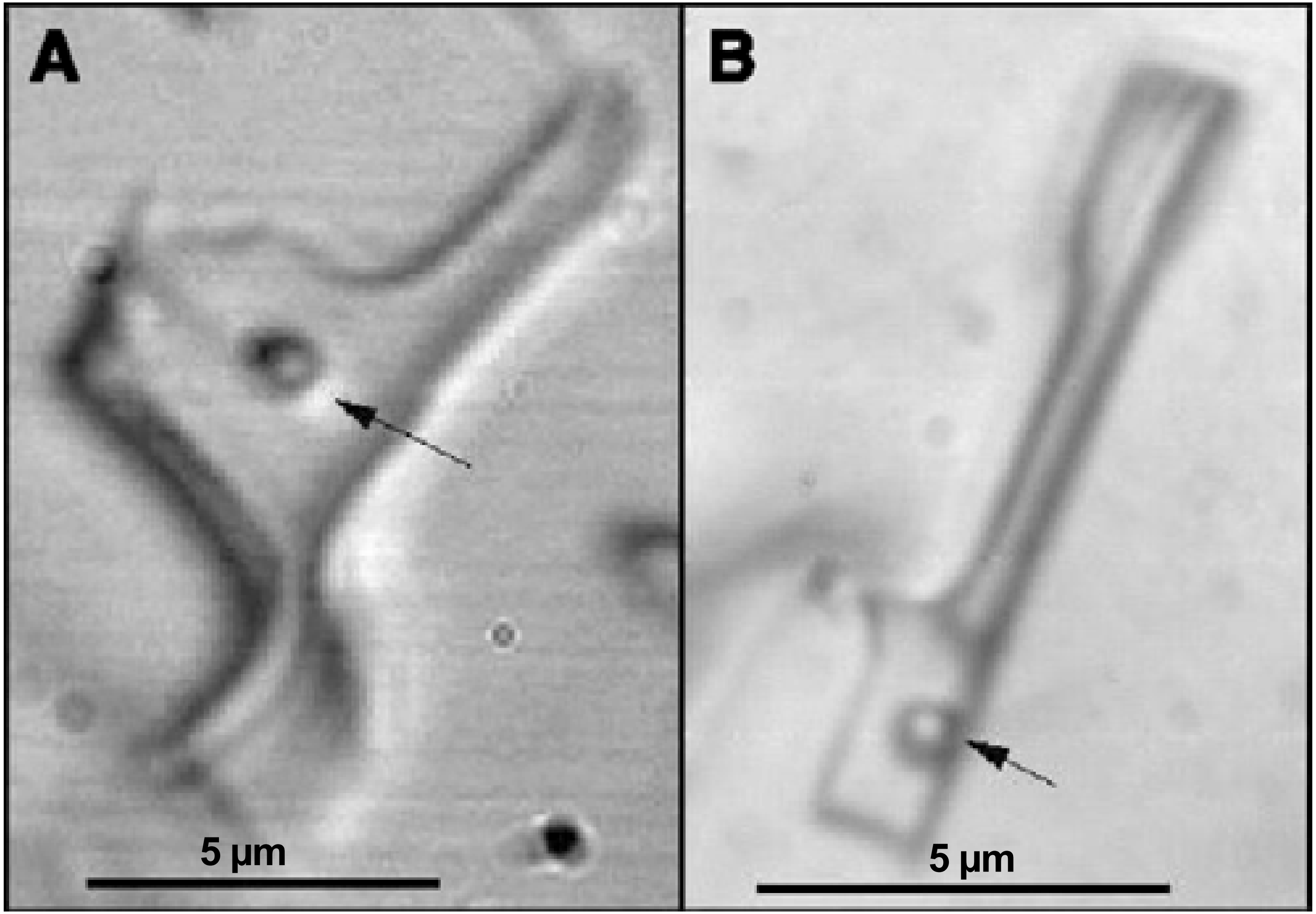

Zolensky et al., Science 285, 1377 -1379 (1999)

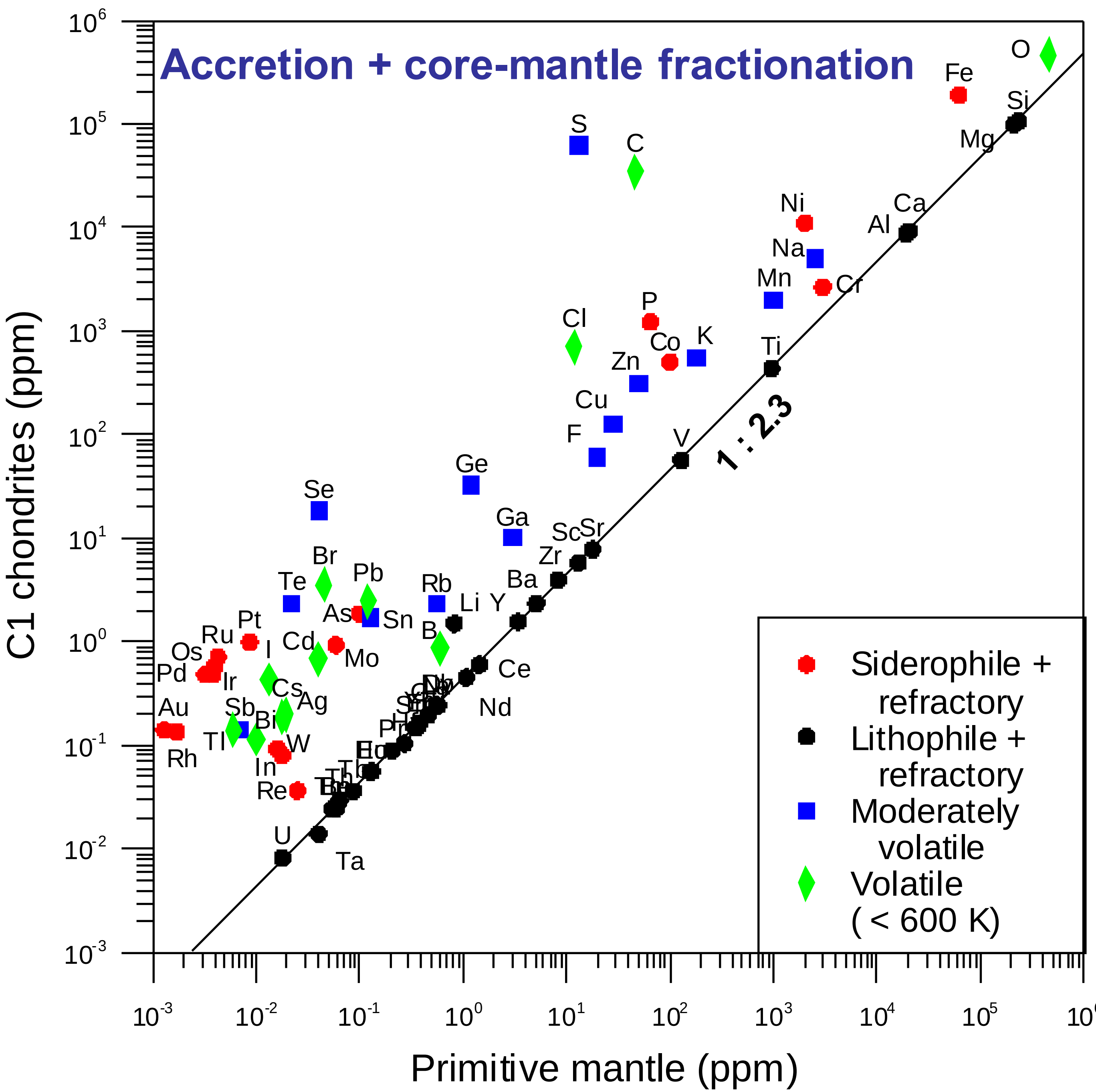

Accretion + core-mantle fractionation
C1 chondrites (ppm)
Primitive mantle (ppm)
1 : 2.3
Siderophile + refractory
Lithophile + refractory
Moderately volatile
Volatile
(< 600 K)
O
Fe
Si
Mg
S
C
Ni
Ca
Al
Na
Mn
Cr
Cl
P
Co
K
Zn
Ti
Cu
F
V
Ge
Se
Ga
Sc
Sr
Zr
Ba
Br
Te
Pb
Rb
Li
Y
As
Sn
B
Pt
Ru
Os
Pd
Ir
I
Cd
Mo
Ce
Cs
Ag
Nd
Au
Sb
Bi
Tl
W
Rh
In
Re
U
Ta

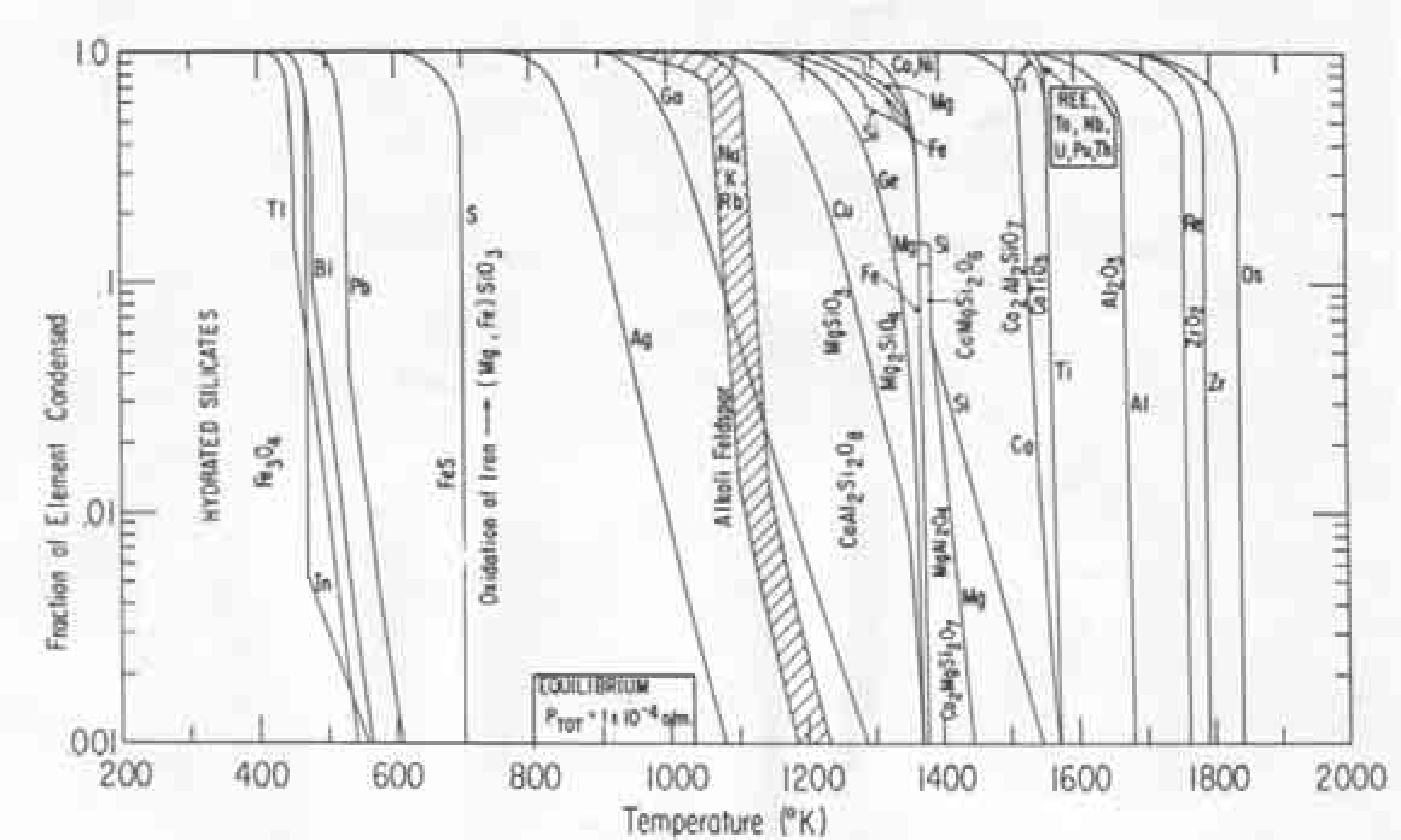

Condensation of the elements from a gas phase of solar composition at 10^{-4} atm
Grossman and Larimer (1974)

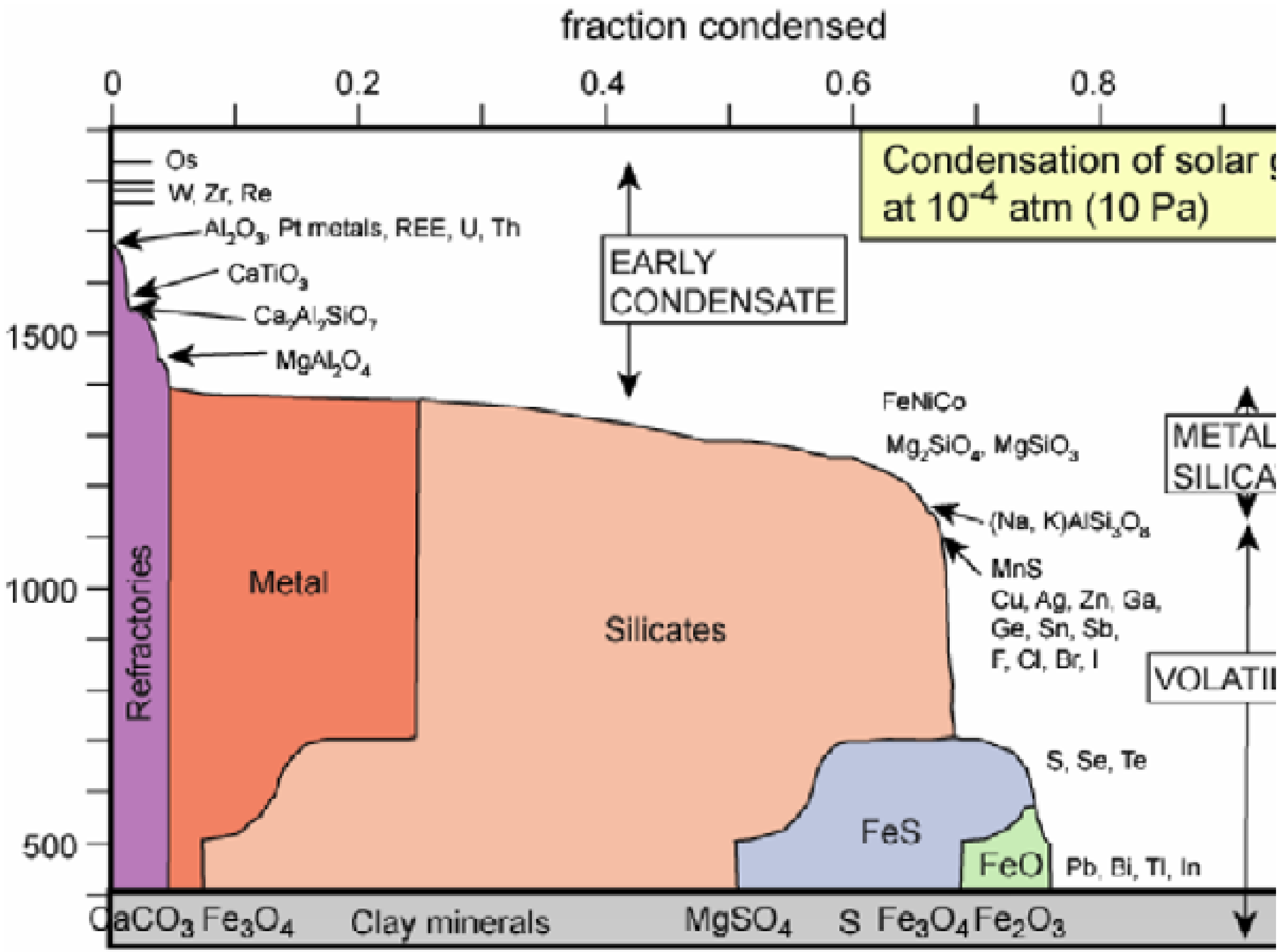
fraction condensed
0
0.2
0.4
0.6
0.8
Condensation of solar g
at 10-4 atm (10 Pa)
Os
W, Zr, Re
Al2O3, Pt metals, REE, U, Th
CaTiO3
Ca2Al2SiO7
MgAl2O4
EARLY CONDENSATE
FeNiCo
Mg2SiO4, MgSiO3
METAL
SILICA
(Na, K)AlSi3O8
MnS
Cu, Ag, Zn, Ga,
Ge, Sn, Sb,
F, Cl, Br, I
VOLATI
S, Se, Te
Pb, Bi, Tl, In
1500
1000
500
Refractories
Metal
Silicates
FeS
FeO
CaCO3 Fe3O4 Clay minerals MgSO4 S Fe3O4 Fe2O3

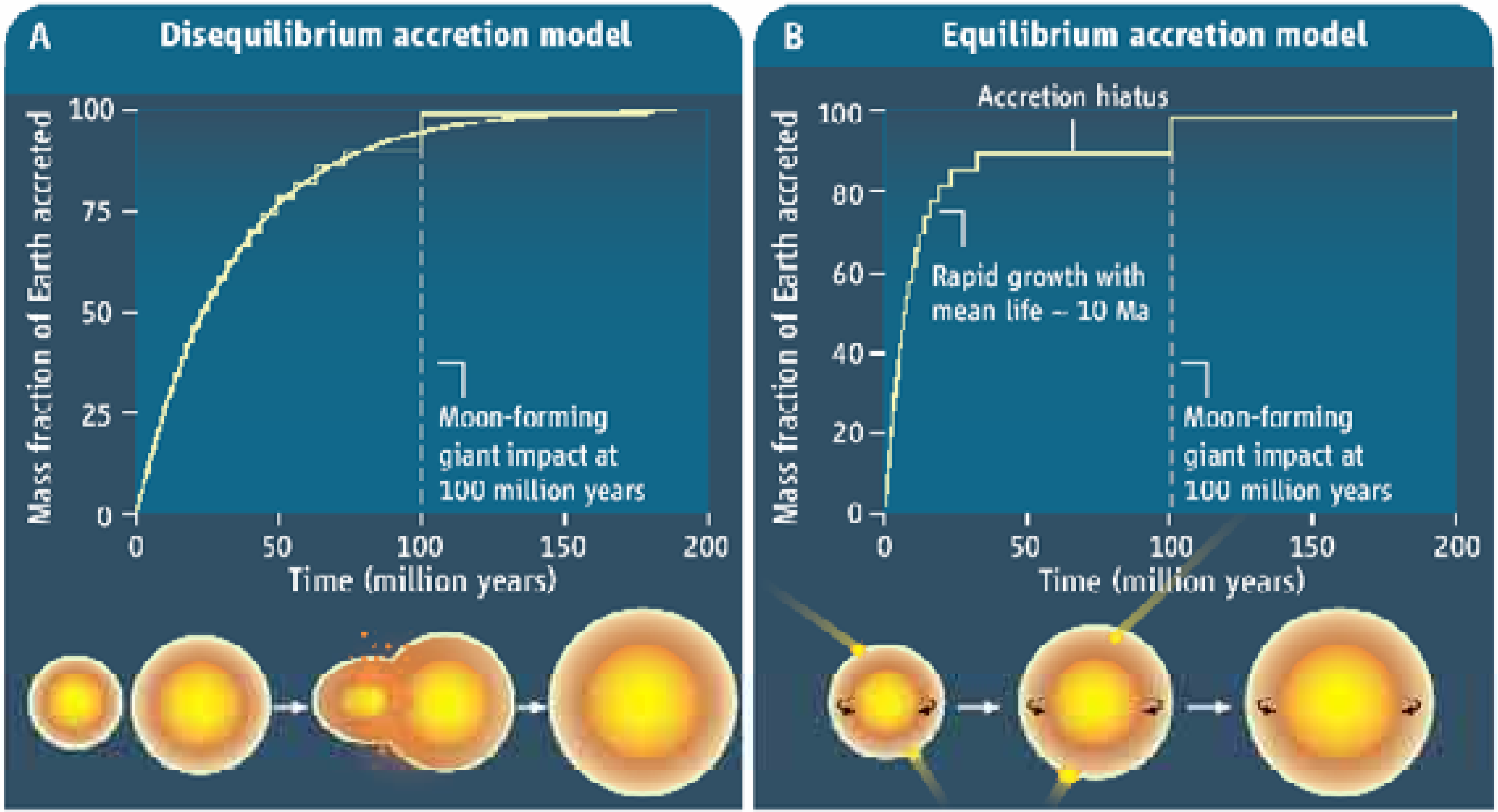

Earth's first 100 million years. Earth grew mainly from a series of accretion events (*15*) broadly comparable in scale to the giant impact, which formed the Moon ~100 million years after the start of the solar system (*8, 10*). In disequilibrium accretion (**A**), the giant impact added metal directly to the core. In equilibrium accretion (**B**), metal segregated from silicate in a magma ocean. The concentrations of metal-loving elements left in the silicate Earth after core formation are better explained by scenario (B) (*12*). However, W isotope data then imply that accretion and core formation were mainly rapid, possibly with a substantial hiatus before the giant impact.

Halliday and Wood (2009) Science 325: 44

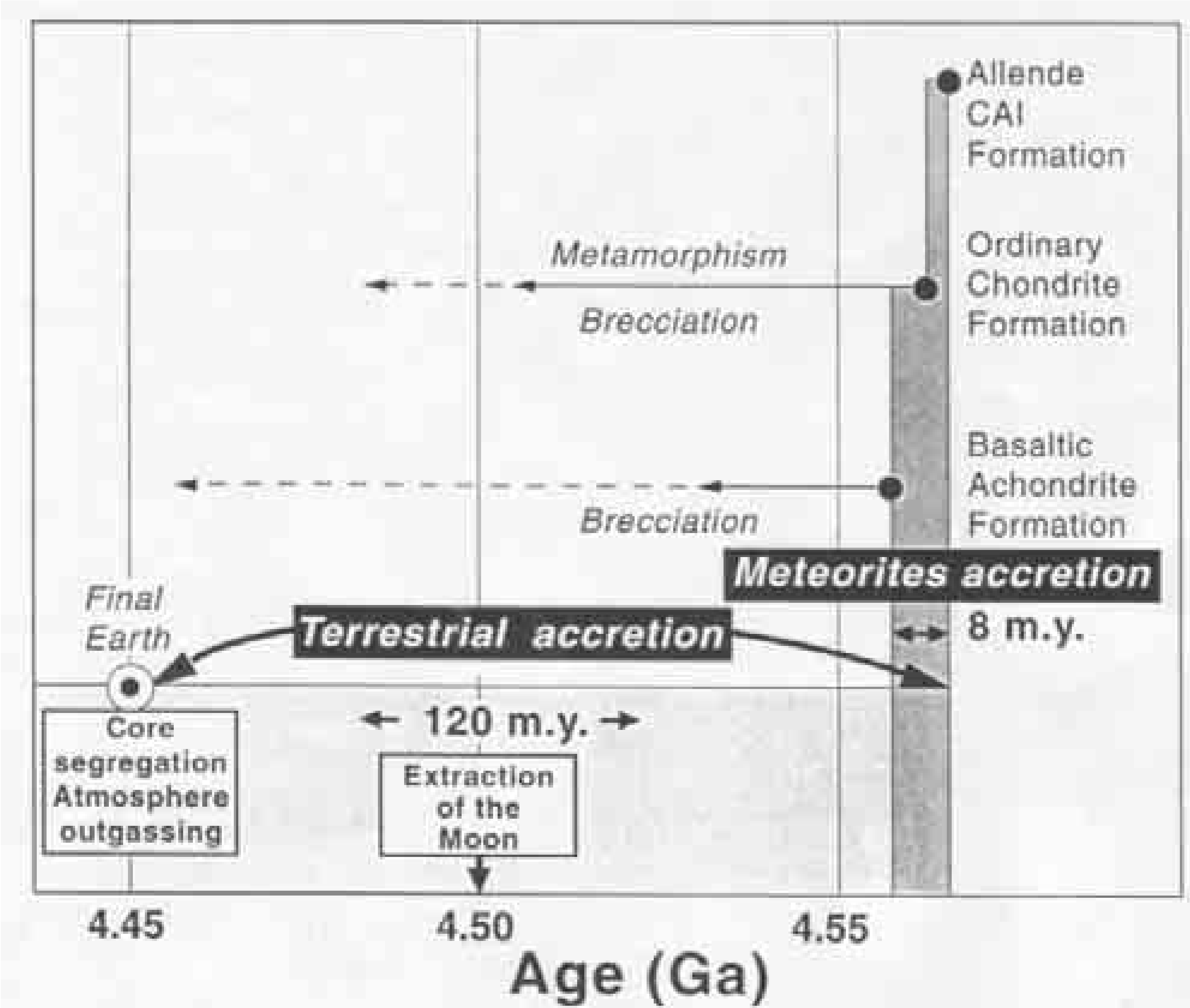

Allègre et al, GCA 59:1445-1456 (1995)

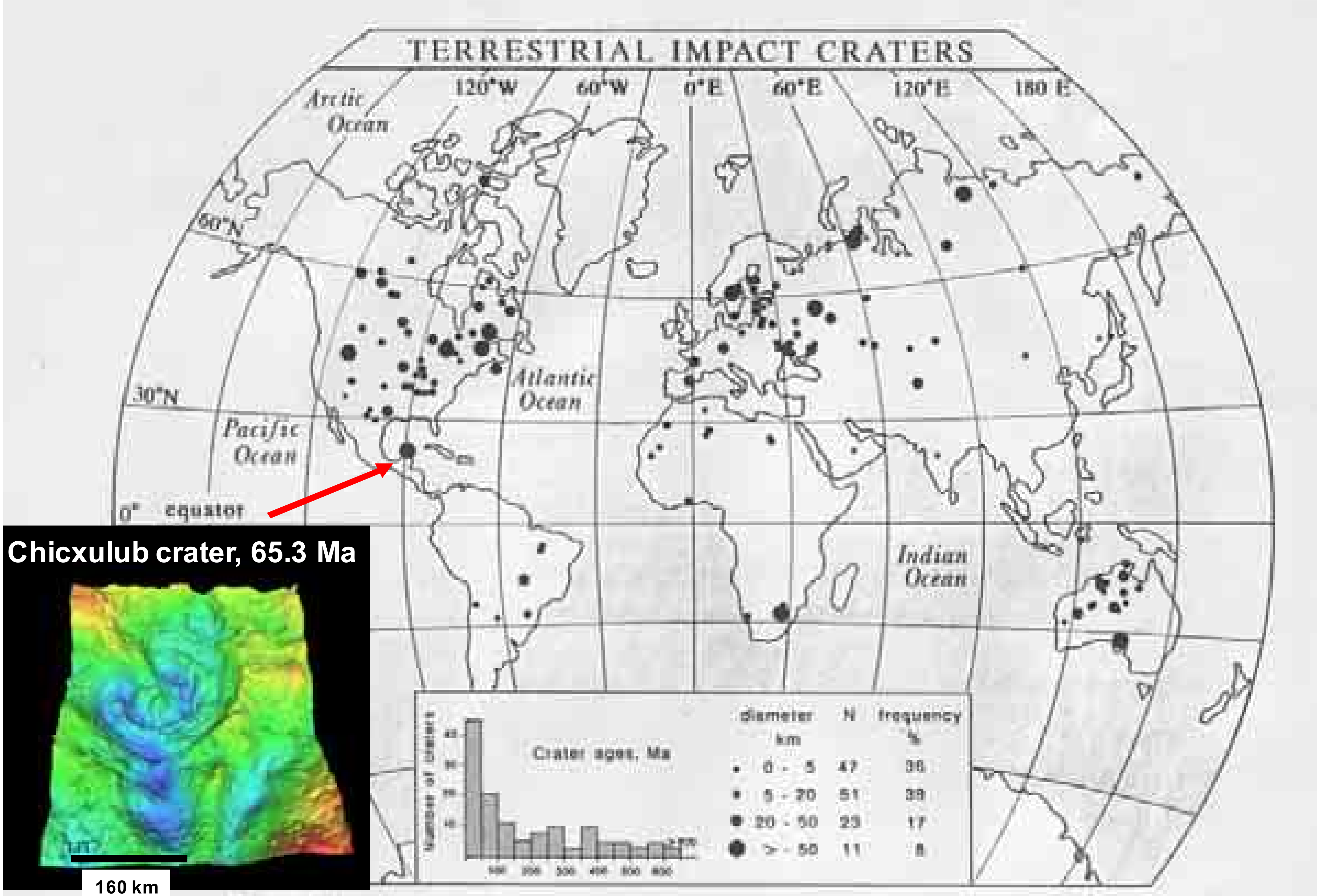

Fig. 7. Location of presently known terrestrial impact craters. Note concentrations on cratons in North America, Europe (including the area of the former U.S.S.R.) and Australia, because of their geologic stability and active search programs. Inset: histogram of known crater ages (N = 131). Note bias towards younger ages, reflecting the effects of terrestrial erosion.

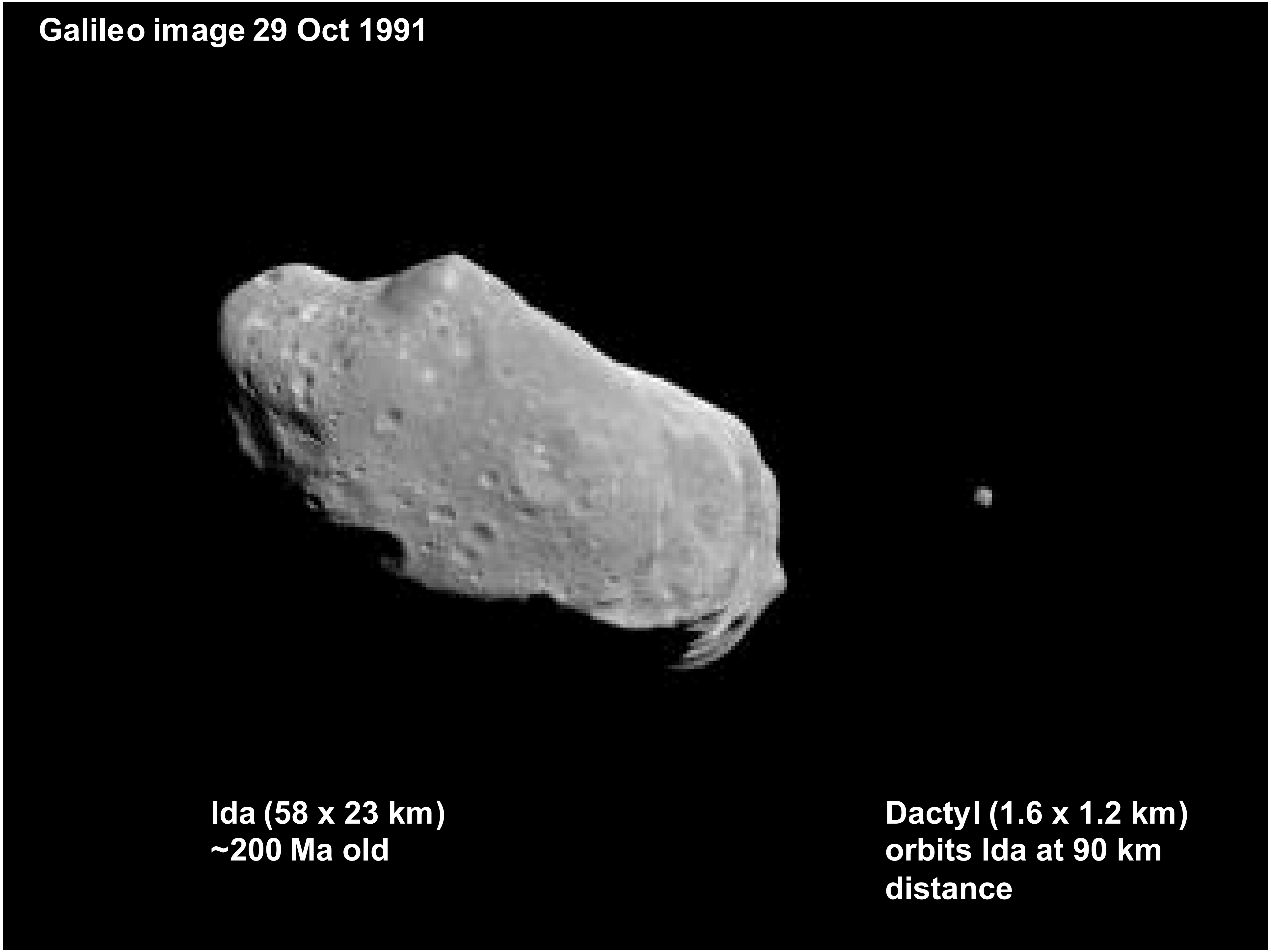
Galileo image 29 Oct 1991
Ida (58 x 23 km)
~200 Ma old
Dactyl (1.6 x 1.2 km)
orbits Ida at 90 km
distance

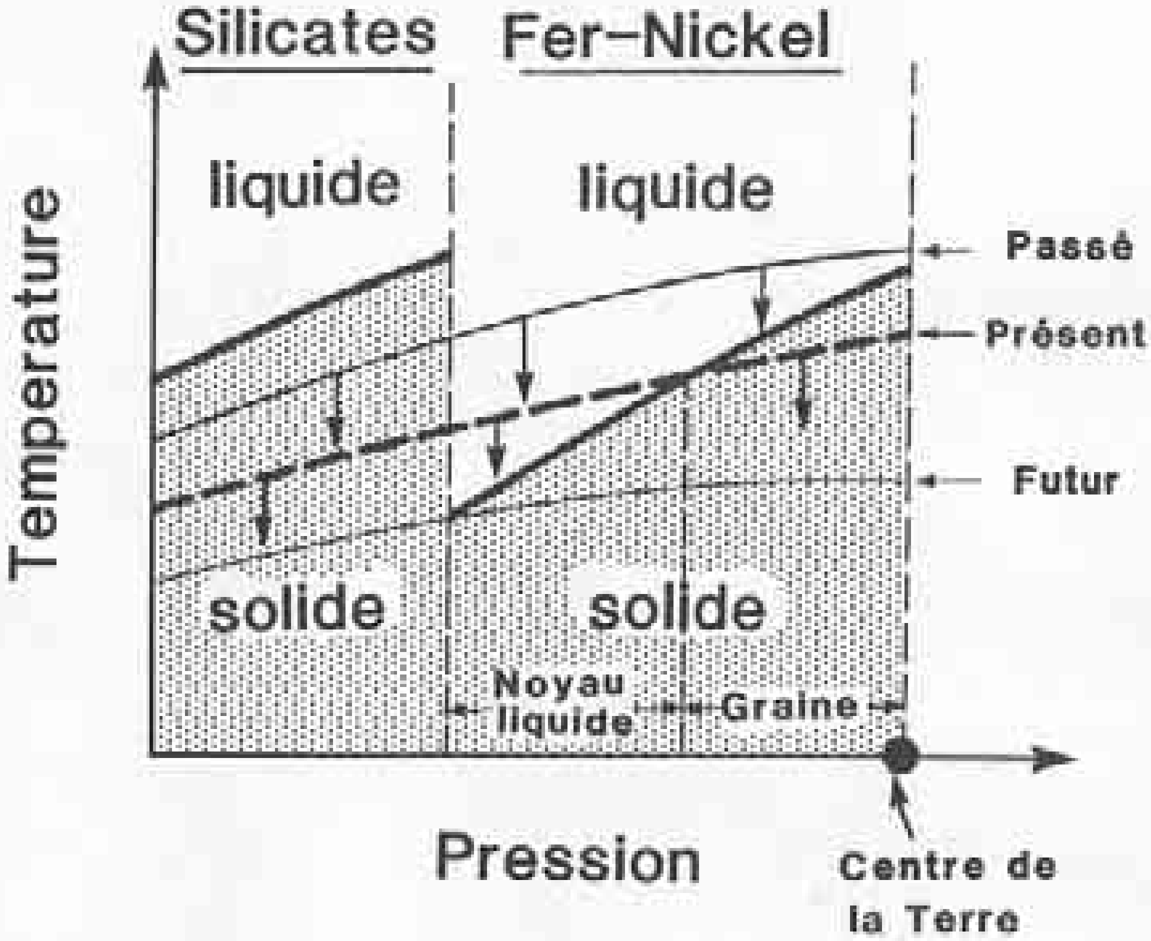

FIG. 51. — Explication de l'existence d'un noyau externe liquide. Les courbes de fusion des silicates et de l'alliage fer-nickel sont indiquées en traits pleins. On note que le point de fusion augmente avec la pression, donc avec la profondeur. La courbe d'augmentation de température avec la profondeur (en pointillés) est située sous la courbe de fusion des silicates, donc dans le domaine solide des silicates. Par contre, elle coupe la courbe de fusion du fer, séparant donc le noyau en deux domaines : un domaine liquide et un domaine solide.

Au fur et à mesure que la Terre se refroidit, la courbe de température terrestre « descend », donc la partie solide du noyau augmente de volume. On peut imaginer l'époque ancienne où le noyau était entièrement liquide (ligne mince), et l'époque future où il sera totalement solidifié (ligne double).

Allègre (1985) De la pierre à l'étoile, p. 238

EARTH

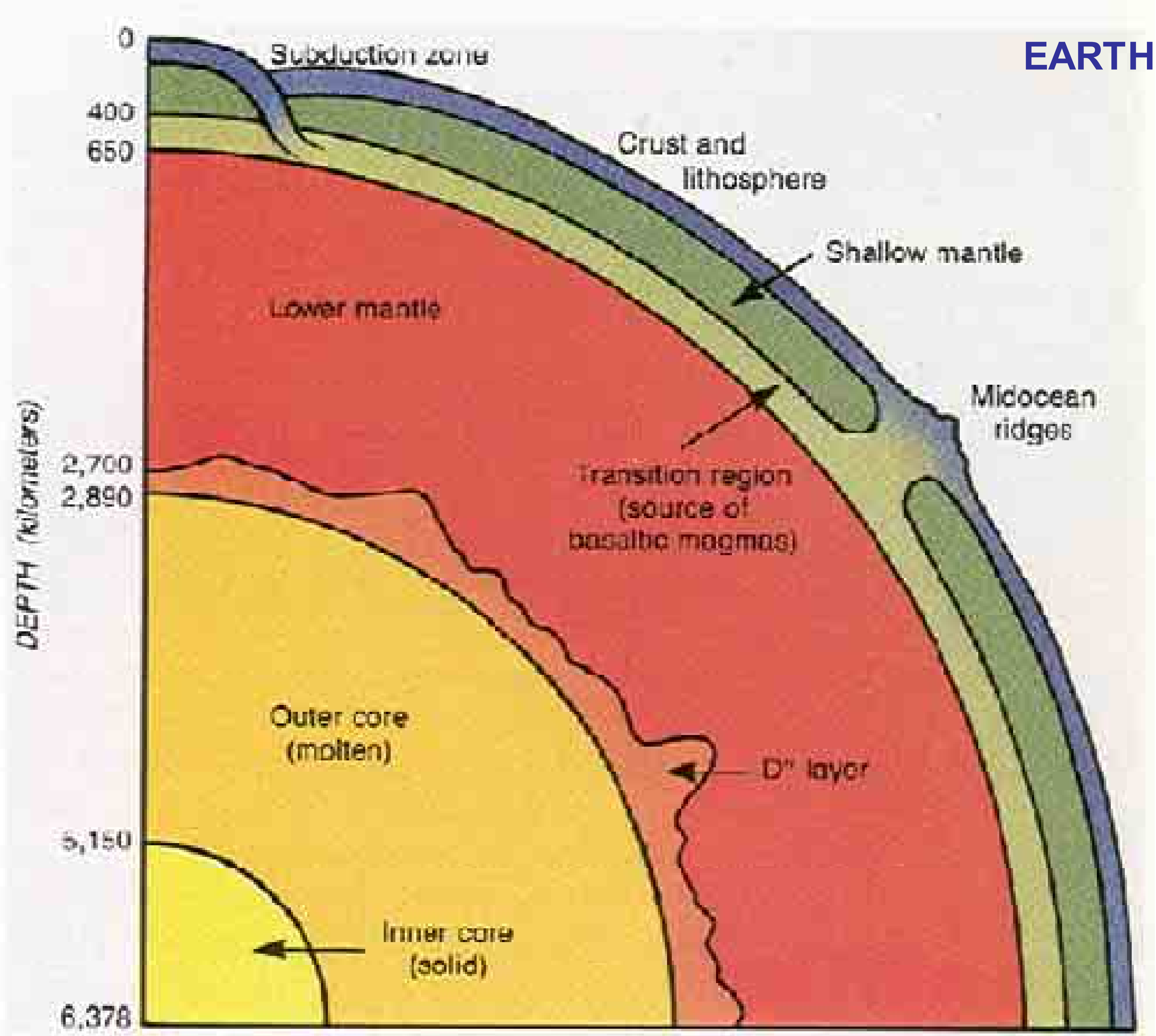
0
400
650
2,700
2,890
5,150
6,378
DEPTH (kilometers)
Subduction zone
Crust and lithosphere
Shallow mantle
Midocean ridges
Lower mantle
Transition region (source of basaltic magmas)
D" layer
Outer core (molten)
Inner core (solid)

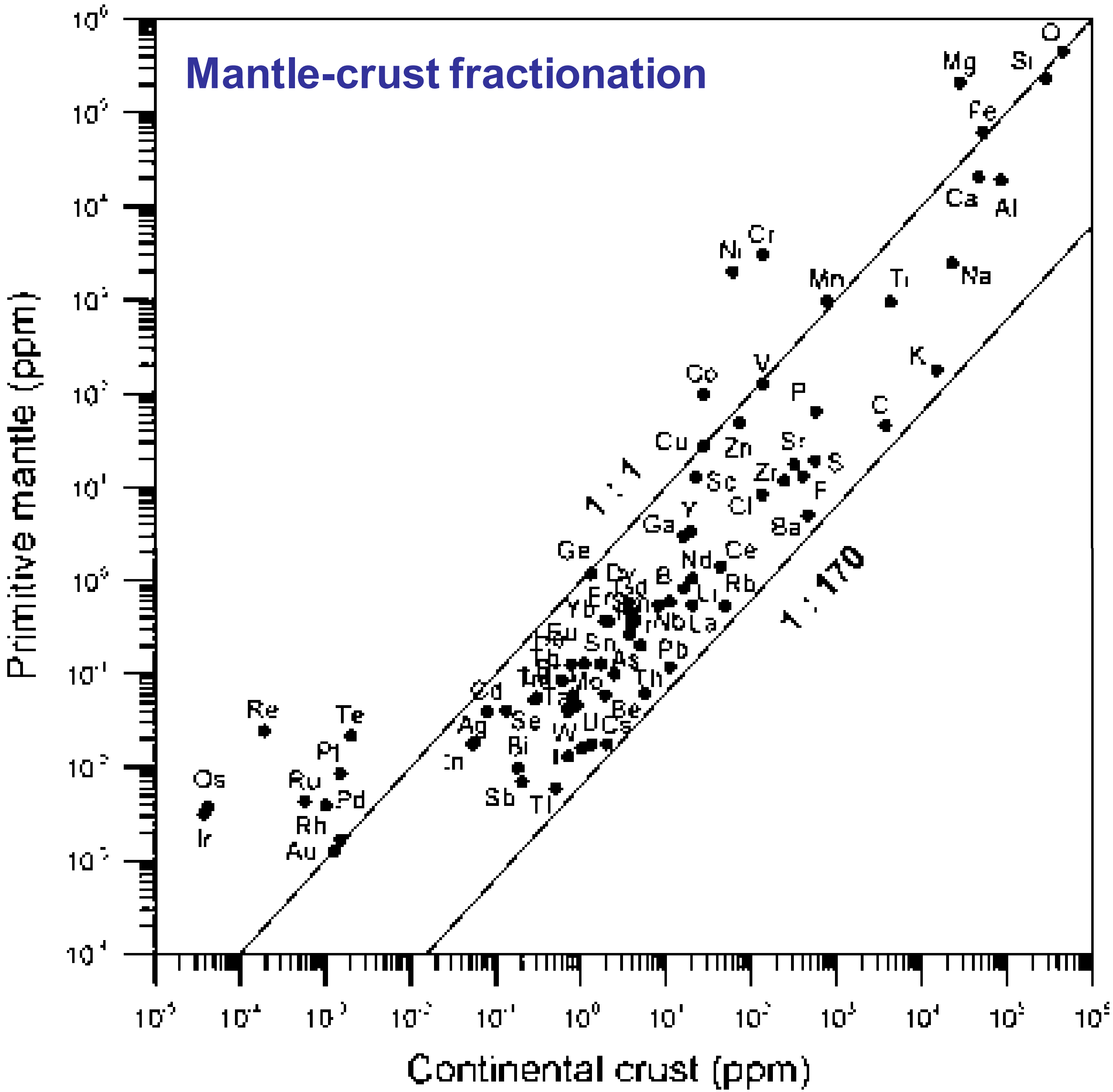
Mantle-crust fractionation
Primitive mantle (ppm)
Continental crust (ppm)
1 : 1
1 : 170
O
Mg
Si
Fe
Ca
Al
Ni
Cr
Mn
Ti
Na
Co
V
K
P
C
Cu
Zn
Sr
S
Sc
Zr
F
Cl
Ga
Y
Ba
Ge
Ce
Nd
Rb
B
Li
Nb
La
Sn
Pb
As
Mo
Th
Cd
Ag
Se
Be
W
U
Cs
Bi
In
Sb
Tl
Re
Te
Pt
Os
Ru
Pd
Ir
Rh
Au

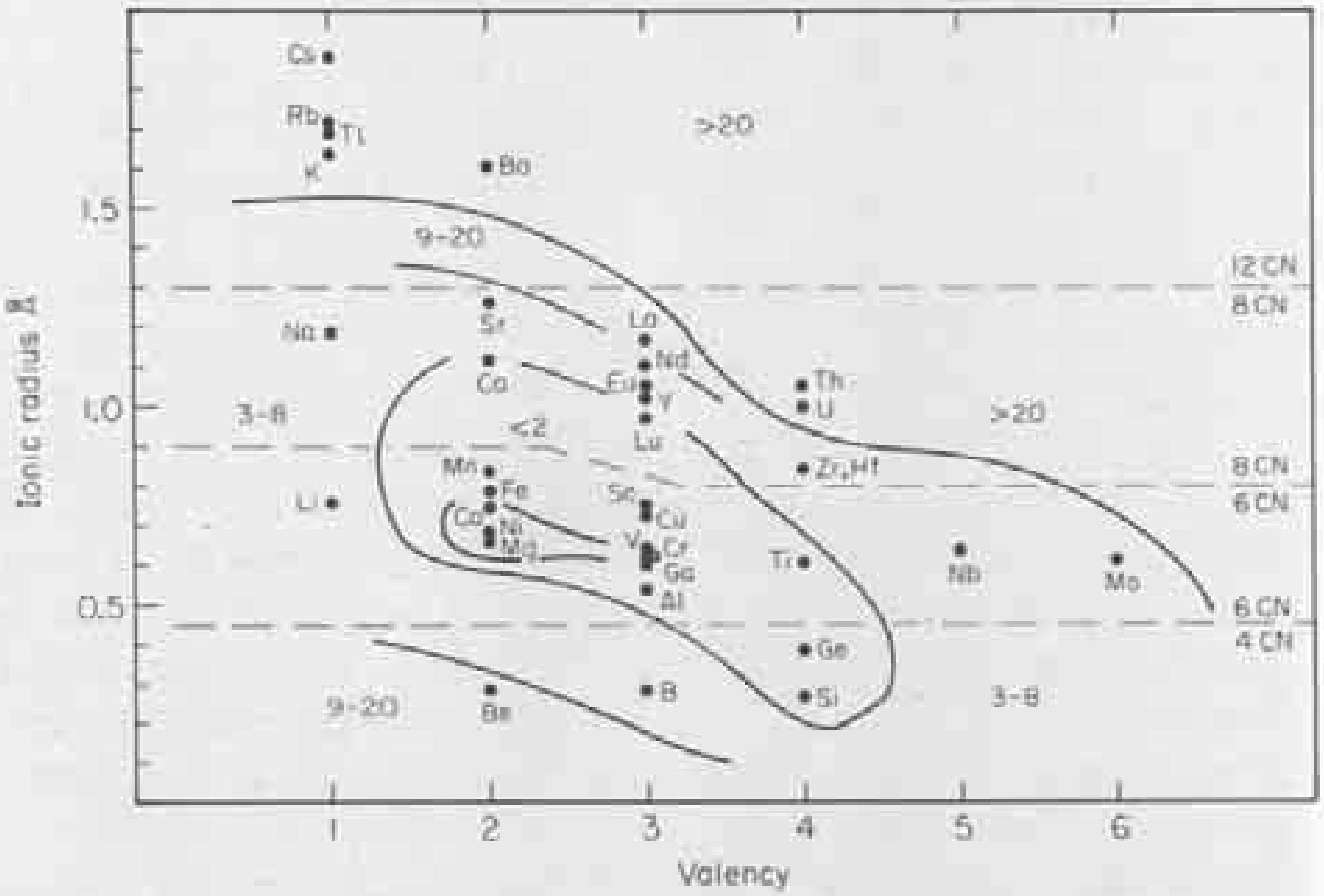

Fig. 11.6. The enrichment of lithophile elements in the continental crust relative to abundances in the primitive mantle (data from Tables 3.5 and 11.3), plotted against ionic radius and valency. Ionic radii data from Shannon [25] are plotted for 4-, 6-, 8- and 12-fold co-ordination with oxygen, as indicated. Elements are enriched in the crust to the degree that their radius or valency differs from that of the principal mantle cations (Mg, Fe) in 6-fold co-ordination. This enrichment is a consequence of crystal–liquid fractionation.

Taylor and McLennan (1985: 266)

	Ni (ppm)	Pt (ppb)	Pd (ppb)	Au (ppb)
Bulk Earth	18,200	1,670	890	257
Primitive mantle	1,960	9	4	1
Bulk continental crust	59	1.5	1	1
Upper continental crust	47	0.5	0.5	1

Magmatic sulfide ore deposits:

Bushveld/Merensky Reef	1,800	4,900	2,100	270
Sudbury, Canada	12,000	~500	~500	~100
Norilsk, Russia	18,000	3,000	1,000	380
Stillwater, USA	250	4,300	14,900	540

Sulfur solubility in mid-ocean ridge basalt

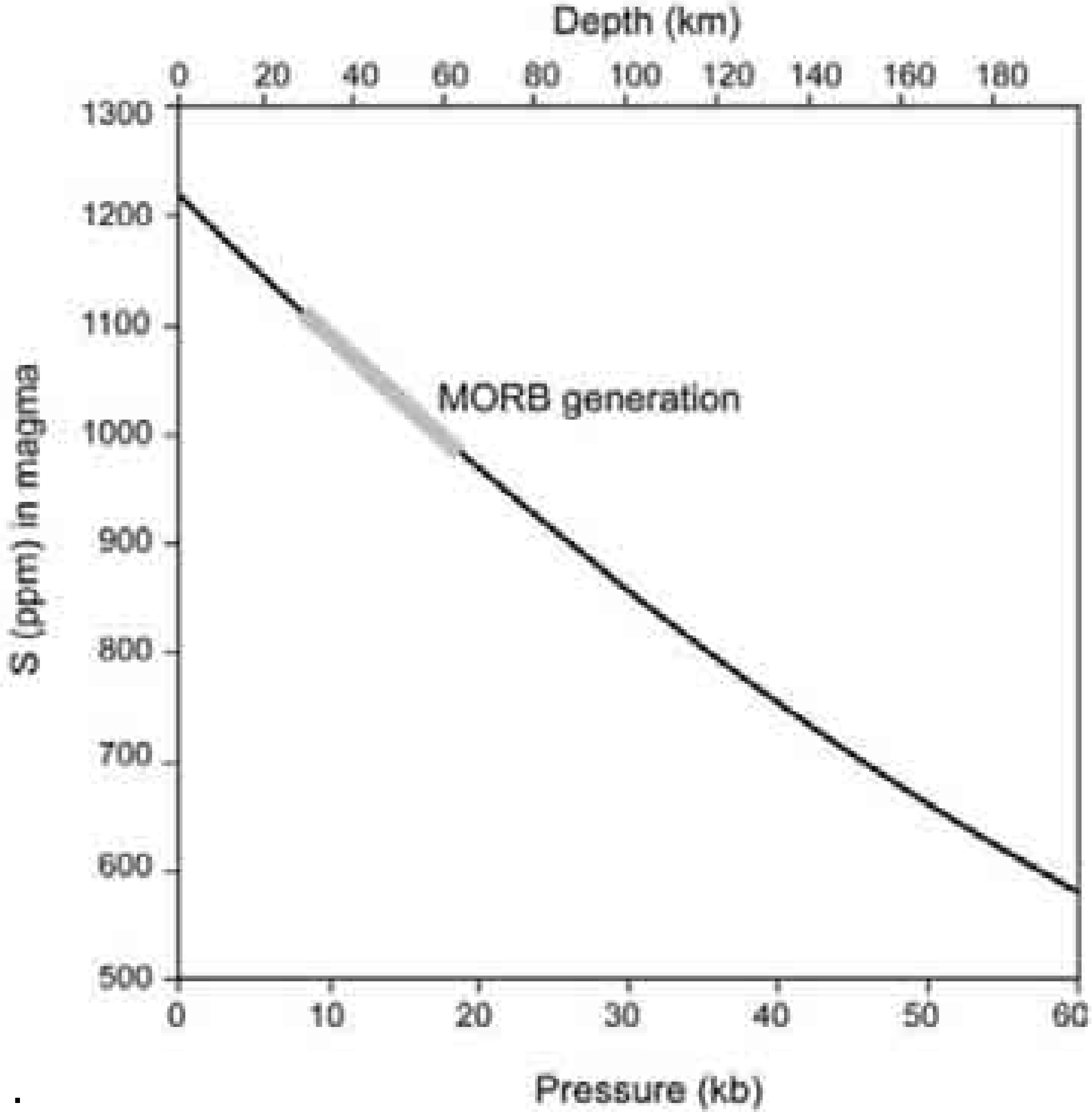

$O^{2-} \leftrightarrow S^{2-}$

$\frac{1}{2} S_2$ + FeO (melt) =
$\frac{1}{2} O_2$ + FeS (melt)

S in melt ≈ $f{S_2}^{1/2} / f{O_2}^{1/2}$
increase with T
decrease with p

.
T is 1200°C at the surface, and increases with an adiabatic gradient of 3°C/kbar.
logfO_2: QFM-2. Li and Ripley (2002) MD 40:224

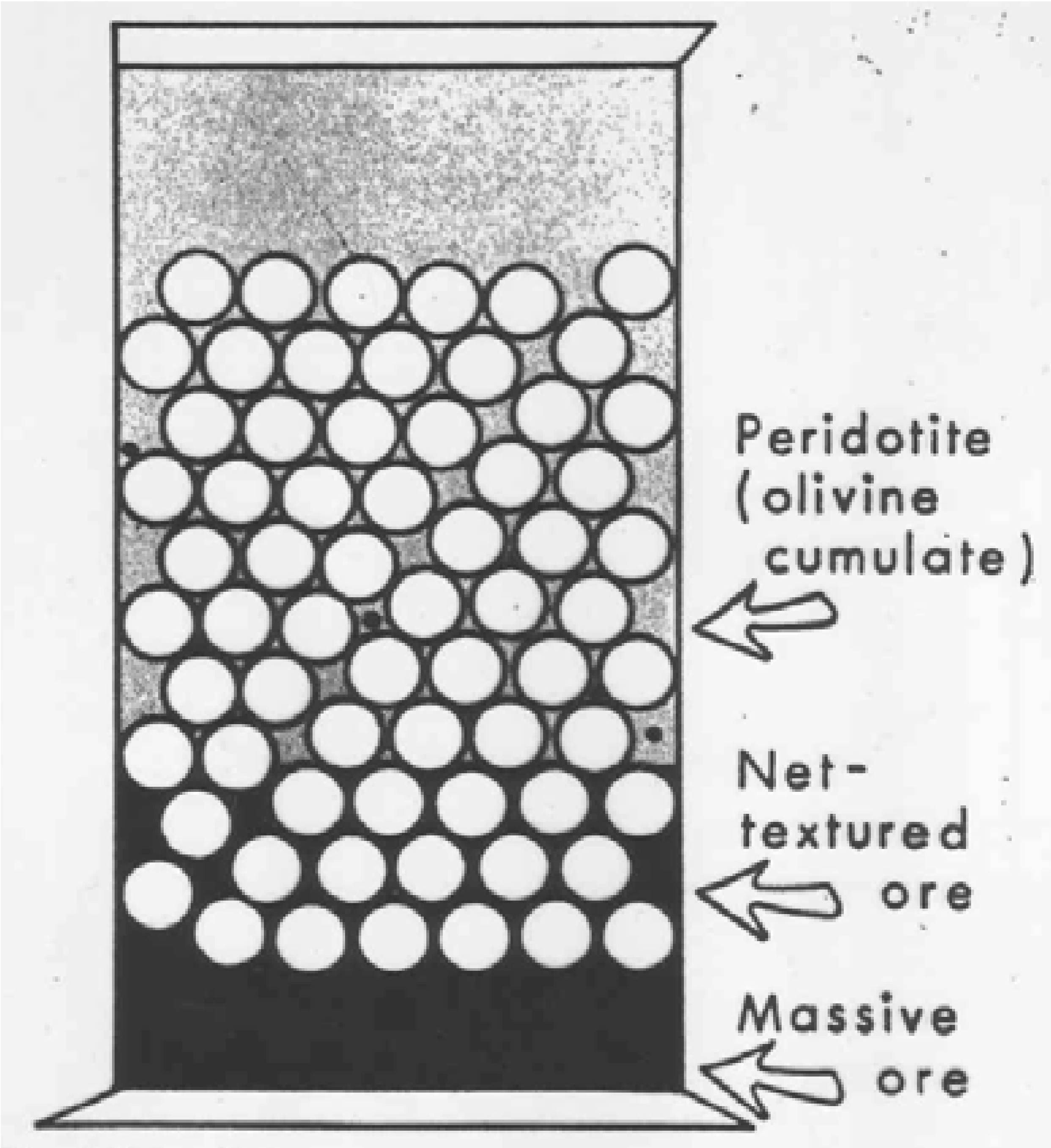

Billard Ball Model (Naldrett 1973)

Density stratification:
Olv cumulate xtls ($\sim$3.5 g/cm^3) float in FeS melt ($\sim$4,2 g/cm^3) and silicate melt ($\sim$2.7 g/cm^3)

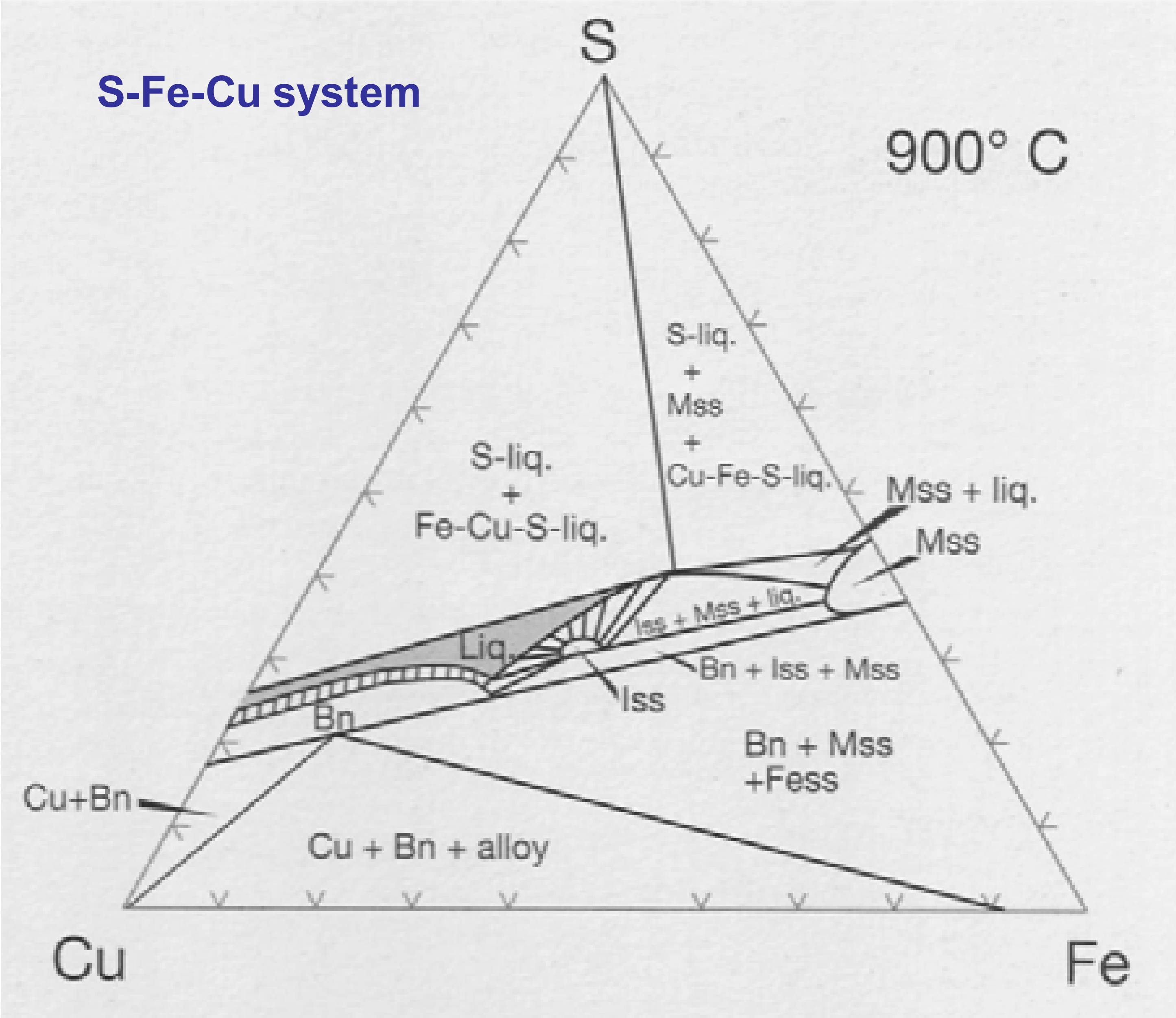

First crystallization of Fe-rich monosulfide solution (with Fe, Os, Ir, Ru, Rh) with the remaining sulfide liquid Ni- and Cu-rich (with Pd, Pt, Au)

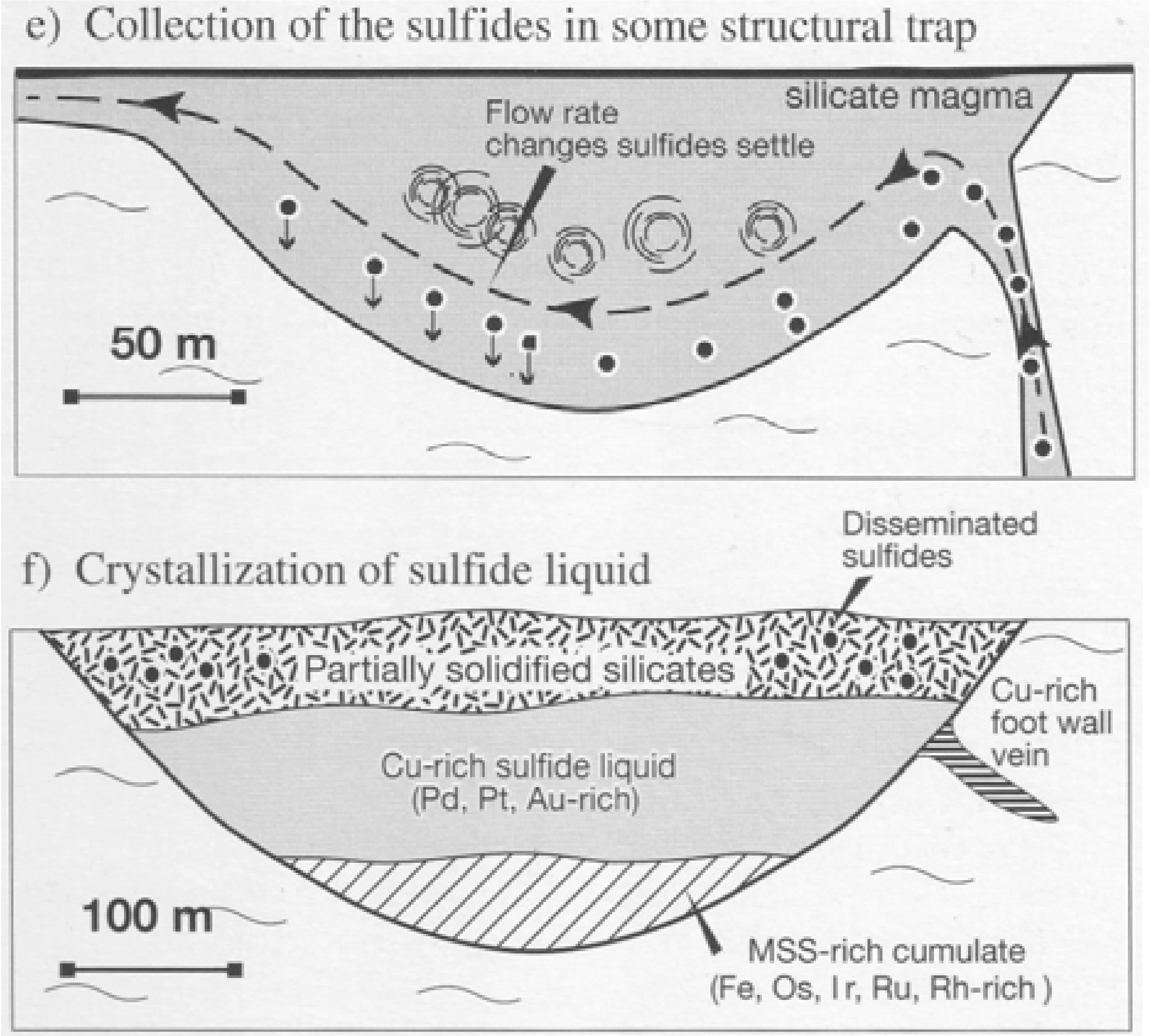

Magmatic sulfide deposits Barnes and Lightfoot (2005) EG Ann Vol 202

Metal content in sulfide melt vs ratio of silicate/sulfide melt: Extreme PGE enrichment in high-R systems such as in the Bushveld and Stillwater intrusions

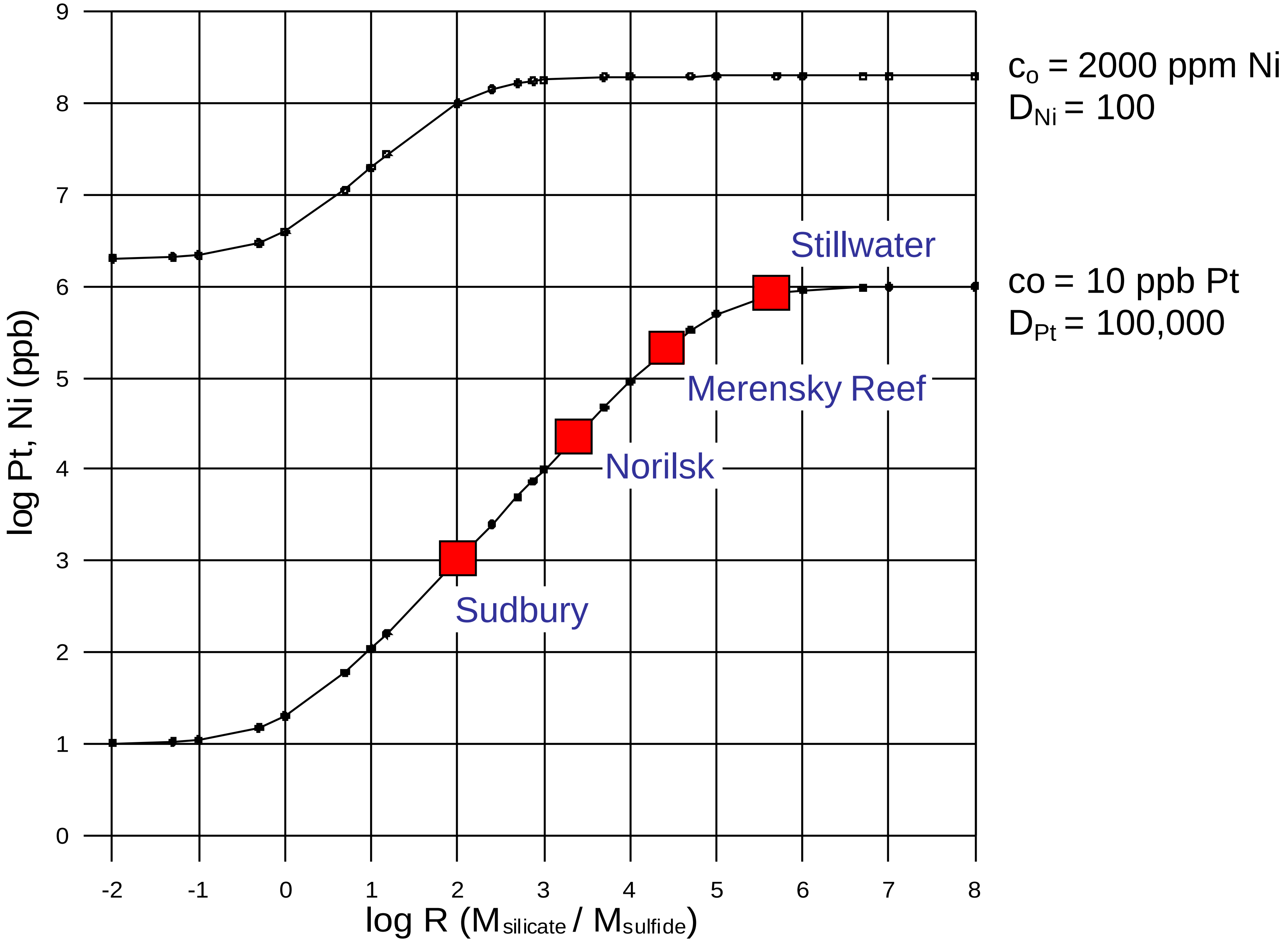

PLATINUM WORLD MINE PRODUCTION 2007 (230 t)

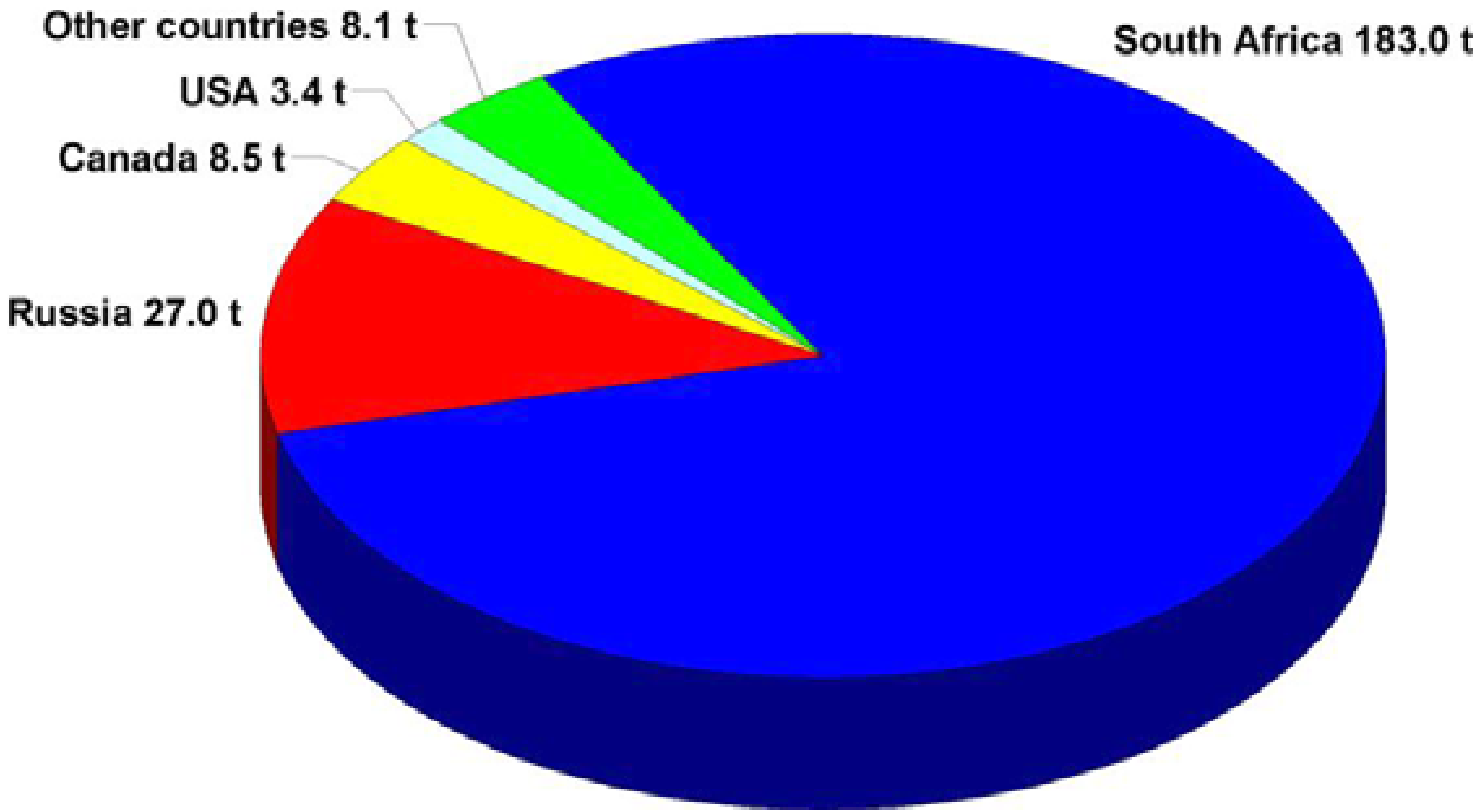

PALLADIUM WORLD MINE PRODUCTION 2007 (232 t)

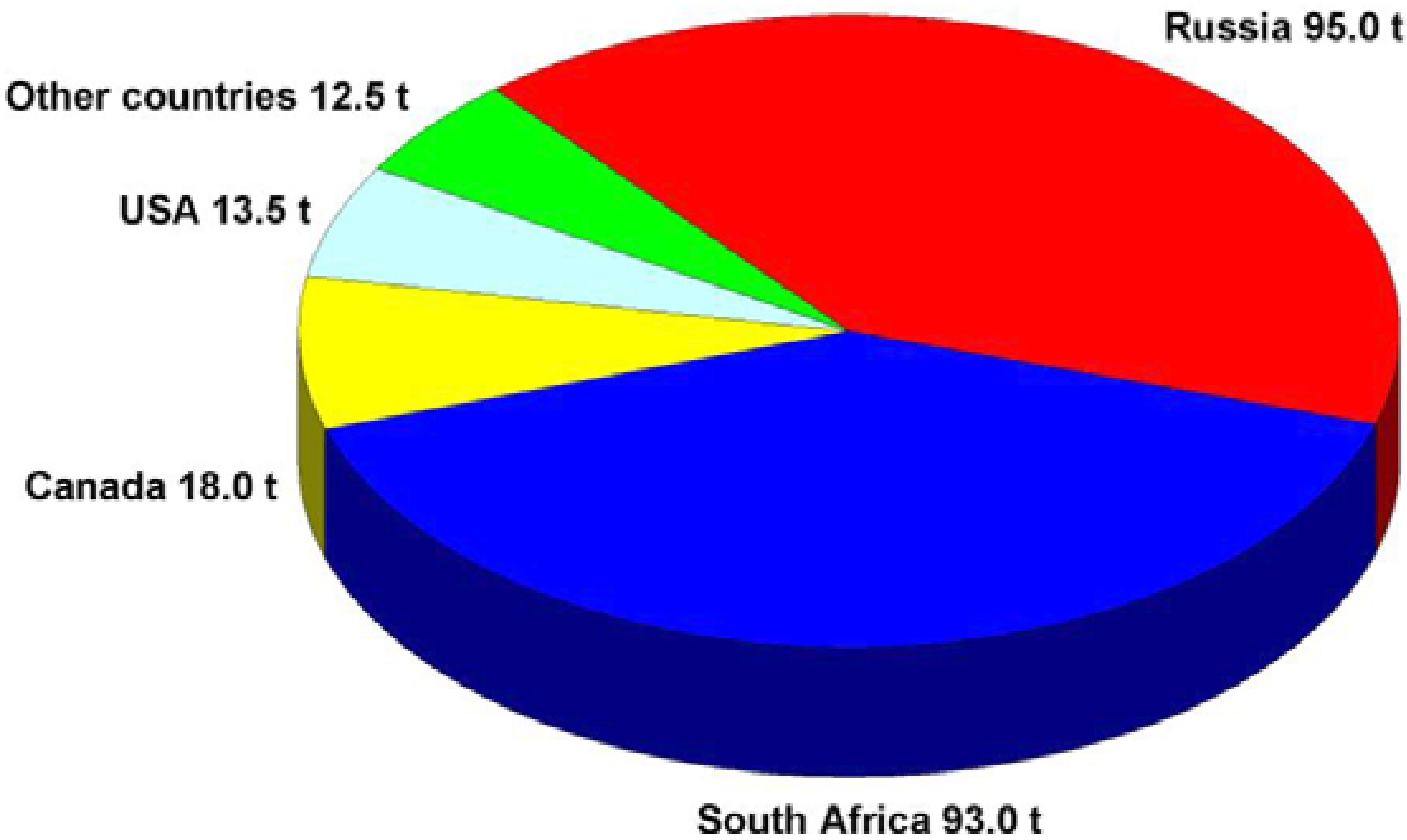

Norilsk annual production:
250.000 t Ni
450.000 t Cu
26 t Pt, 85 t Pd
from ~13 Mt ore/year
(~10 b USD)

251 ± 0.5 Ma
Resources:
1.3 Gt @ 1.8% Ni, 3.6% Cu,
4.7 g/t PGE

NORILSK NICKEL

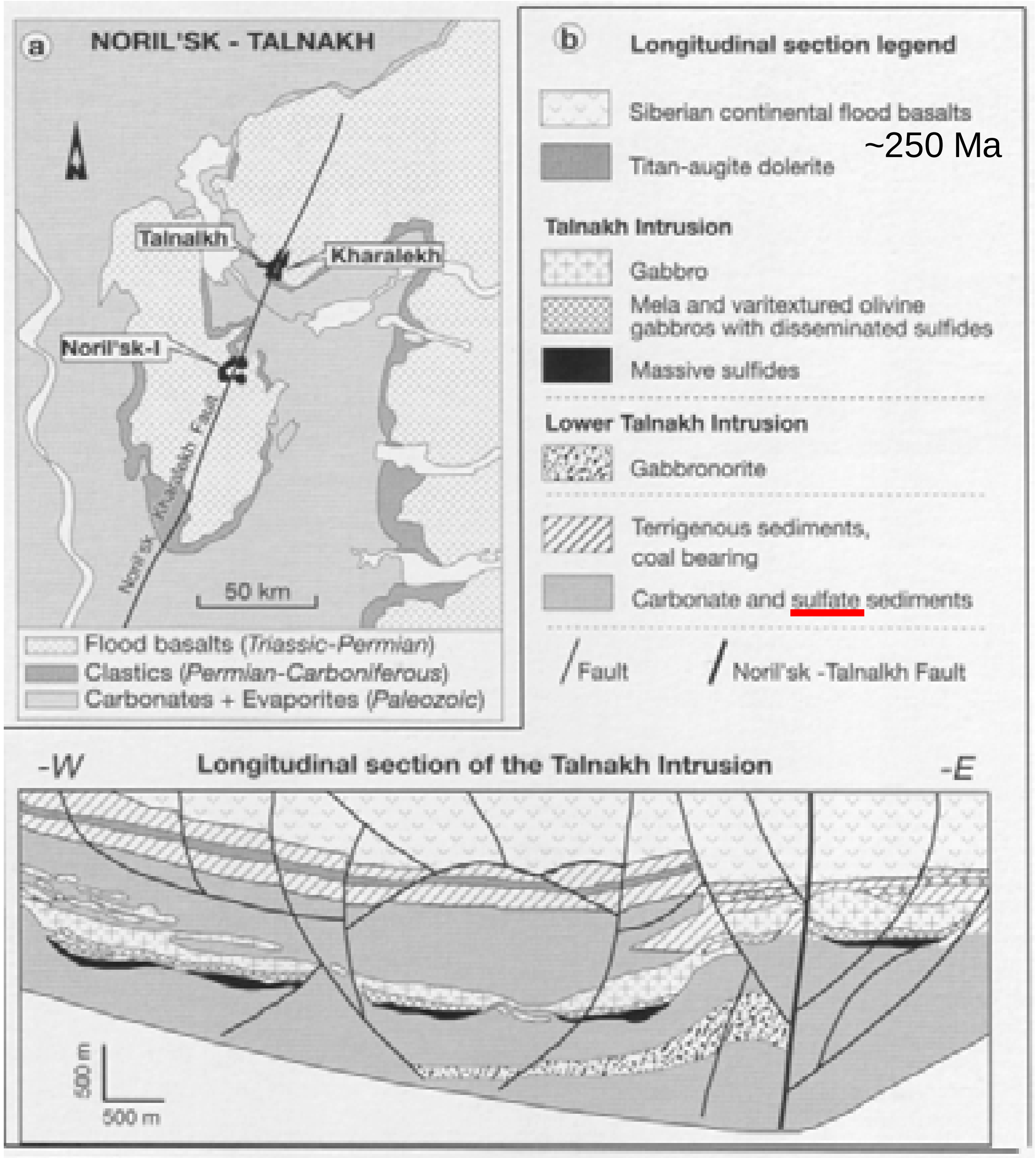

Norilsk, Russia

1.3 Gt @ 1.8 % Ni
3.6 % Cu
4.7 g/t PGE

Barnes and Lightfoot (2005) EG Ann Vol 186

Geological map of the Bushveld Complex, South Africa

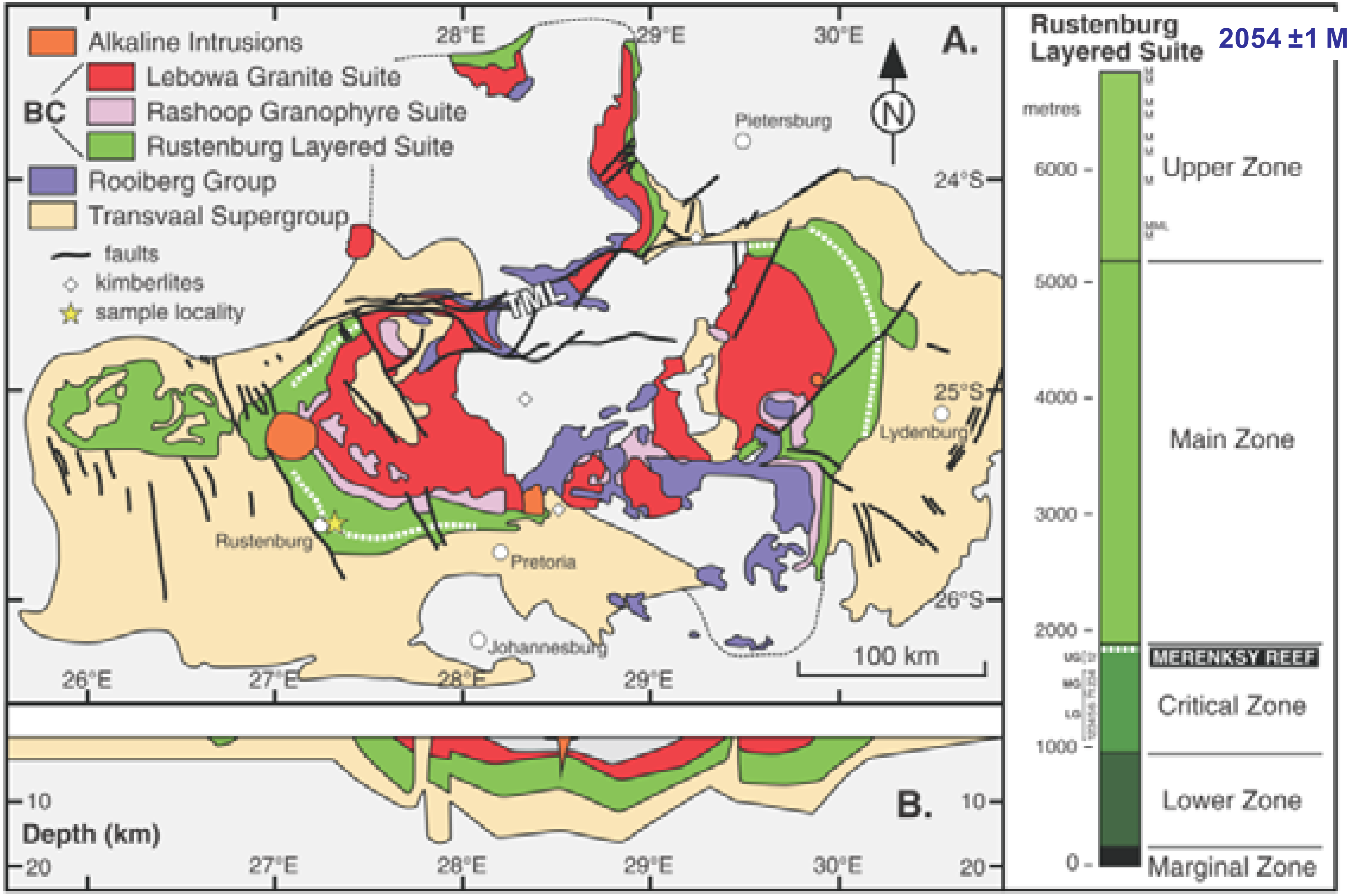

LG-UG: major chromite reefs
M, MML: major magnetite reefs

Scoates and Friedman (2006) EG 103: 466

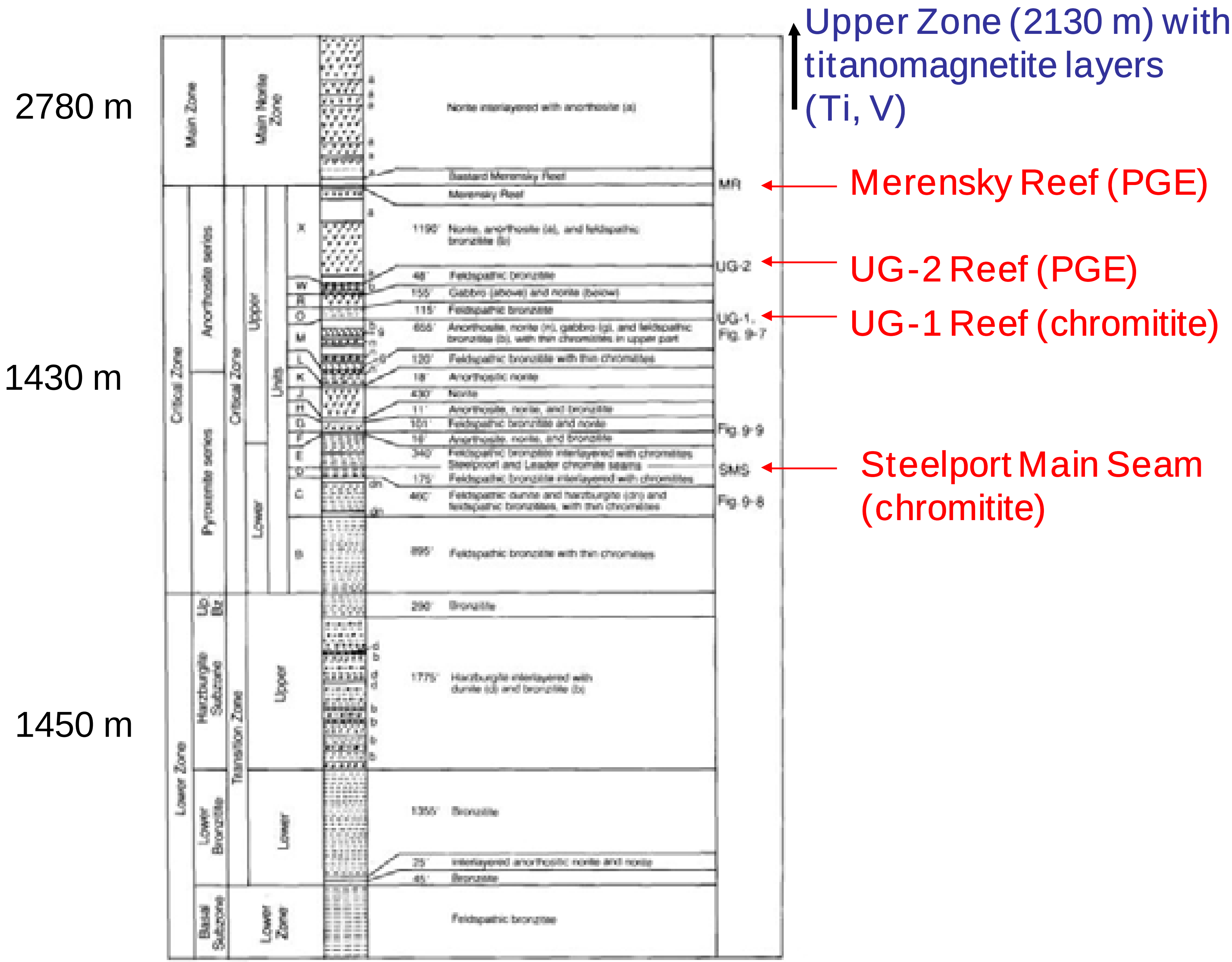
Upper Zone (2130 m) with titanomagnetite layers (Ti, V)
2780 m
1430 m
1450 m
Merensky Reef (PGE)
UG-2 Reef (PGE)
UG-1 Reef (chromitite)
Steelport Main Seam (chromitite)
MR
UG-2
UG-1, Fig. 9-7
Fig. 9-9
SMS
Fig. 9-8
Merensky Reef
Feldspathic bronzite
Anorthositic norite
Norite
Bronzite
Steelpoort and Leader chromite seams

Bushveld Complex (low-lying topography)

Bushveld Complex: View from the surrounding quartz-rich country rocks

Bushveld Layered Mafic Intrusion (see dip to the left)

Merensky Reef, Atok Mine

UG-2, Karee Mine

Merensky Reef at Impala mine (Implats)
right: footwall anorthosite; middle: chromitite, left: pegmatitic pyroxenite with pentlandite-pyrrhotite-chalcopyrite. Length of photograph is about 15 cm.


UG-2, Maandagshoek

Platreef: Sandsloot Pit near Mokopane (Potgietersrus)

PPL Mine, Reserves and resources: 1 Gt @ 2.7 g/t PGE

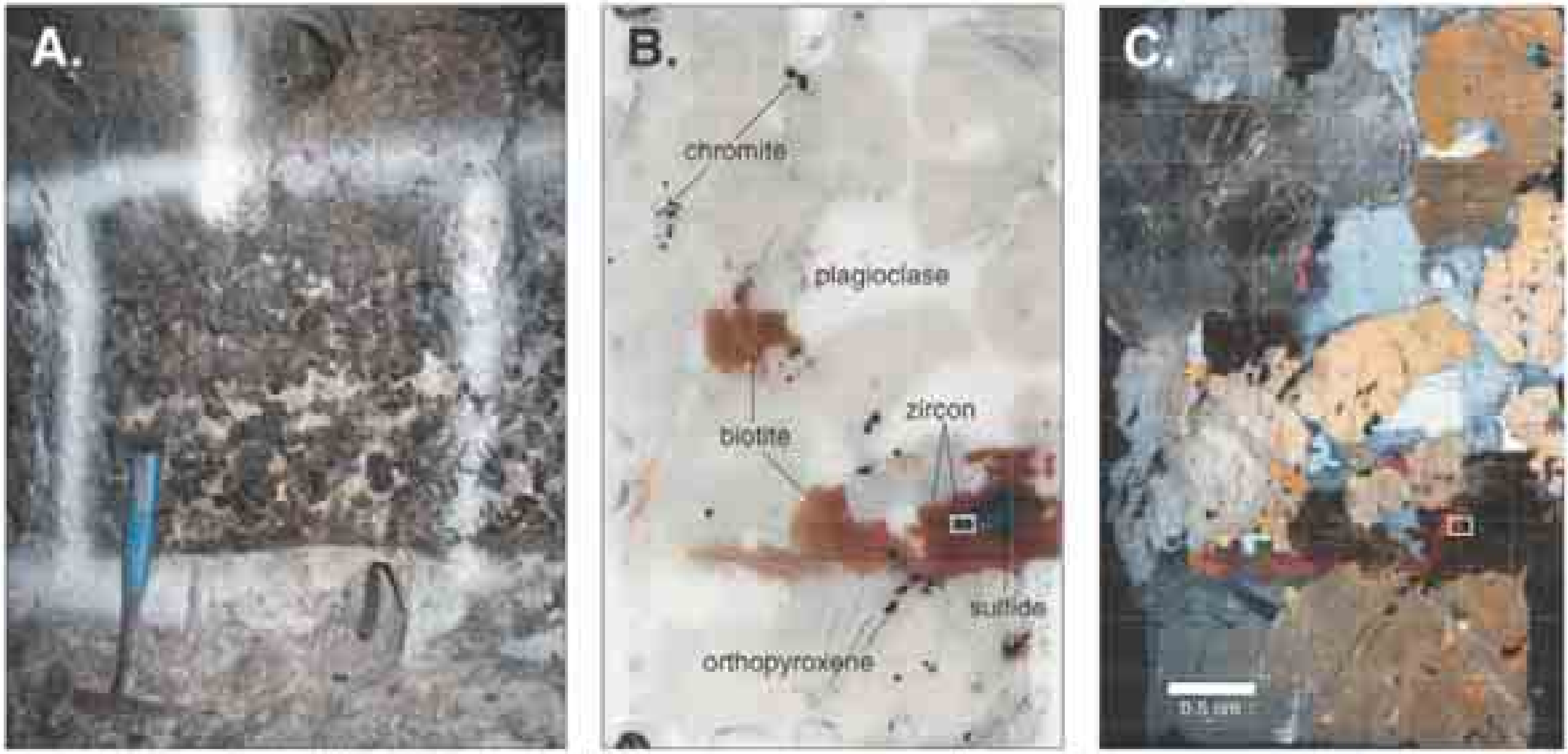

FIG. 2. A. Photograph of the mining face of the Merensky reef in the West mine (Townlands shaft, level 22, ~830 m below surface), Rustenburg mining section, showing the coarse grain size and heterogeneous texture of the pegmatitic feldspathic orthopyroxenite. Photograph courtesy of Pat Hayman. B and C. Photomicrographs of an entire petrographic thin section (SA04-11B) from the pegmatitic feldspathic orthopyroxenite, showing the relative sizes and distribution of the main minerals (orthopyroxene, plagioclase, biotite, chromite) and the location of the zircon rim around sulfide shown in Figure 3A (outlined with a white box). B, ordinary light; C, cross-polarized light. The stratigraphic up-direction is toward the top of the photomicrographs.

Scoates and Friedman (2006) EG 103: 467

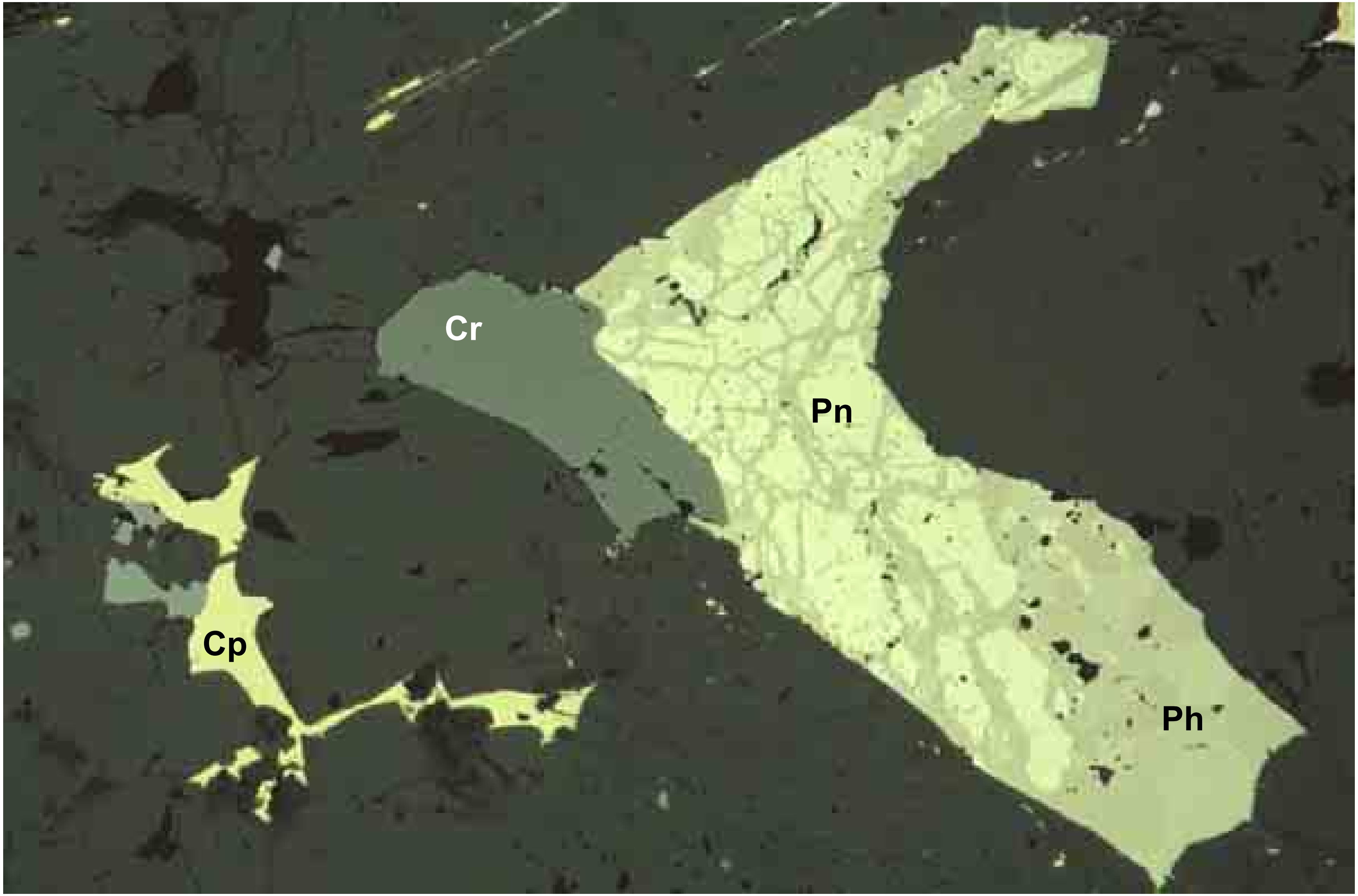

Merensky Reef: pentlandite [(Ni,Fe)S] (Pn), pyrrhotite [FeS] (Ph), chalcopyrite [$CuFeS_2$] (Cp), and chromite (Cr) in plagioclase-pyroxene matrix (dark), 5x obj.

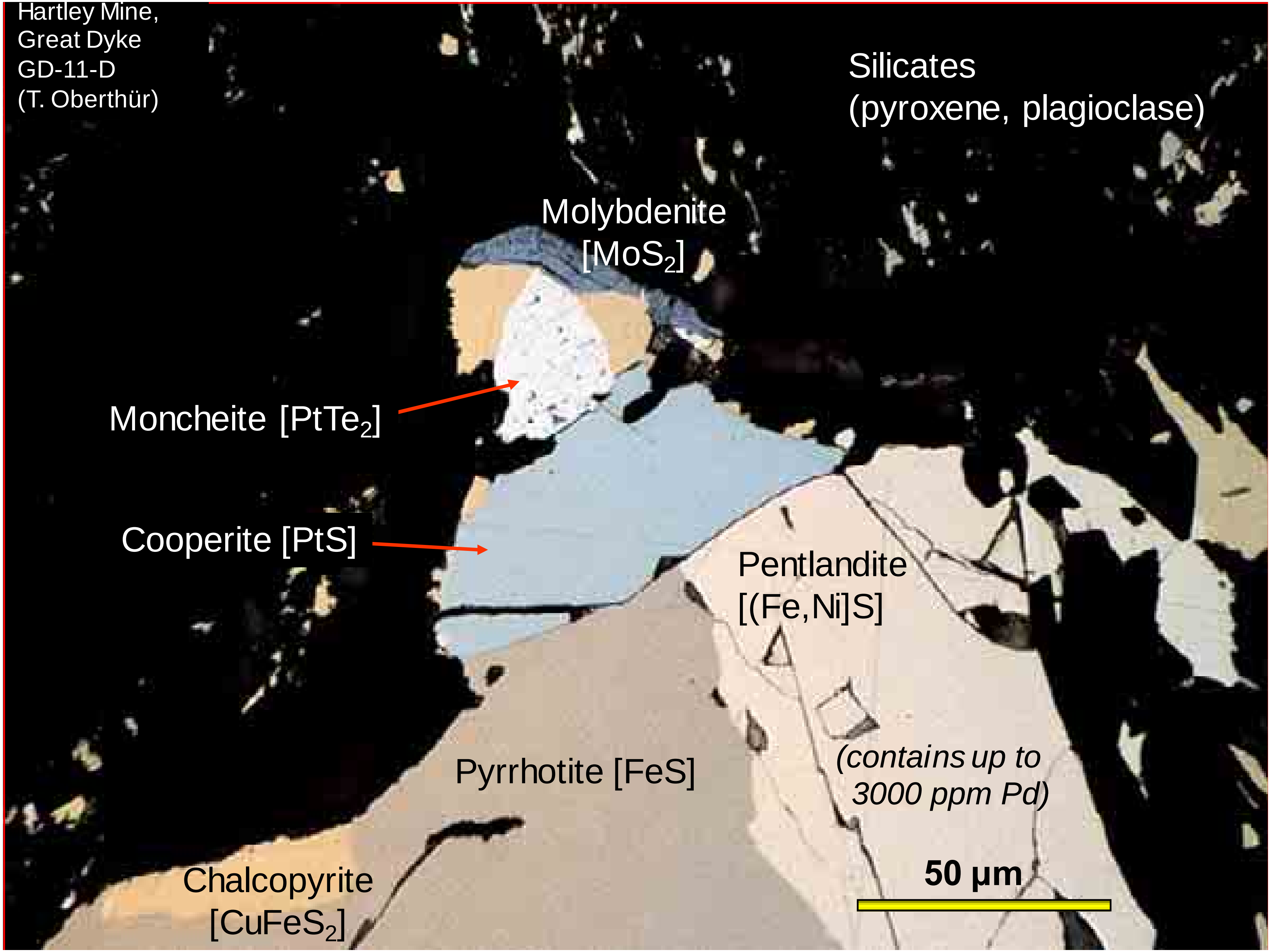
Hartley Mine,
Great Dyke
GD-11-D
(T. Oberthür)
Silicates
(pyroxene, plagioclase)
Molybdenite
[MoS_2]
Moncheite [$PtTe_2$]
Cooperite [PtS]
Pentlandite
[(Fe,Ni]S]
(contains up to
3000 ppm Pd)
Pyrrhotite [FeS]
Chalcopyrite
[$CuFeS_2$]
50 µm

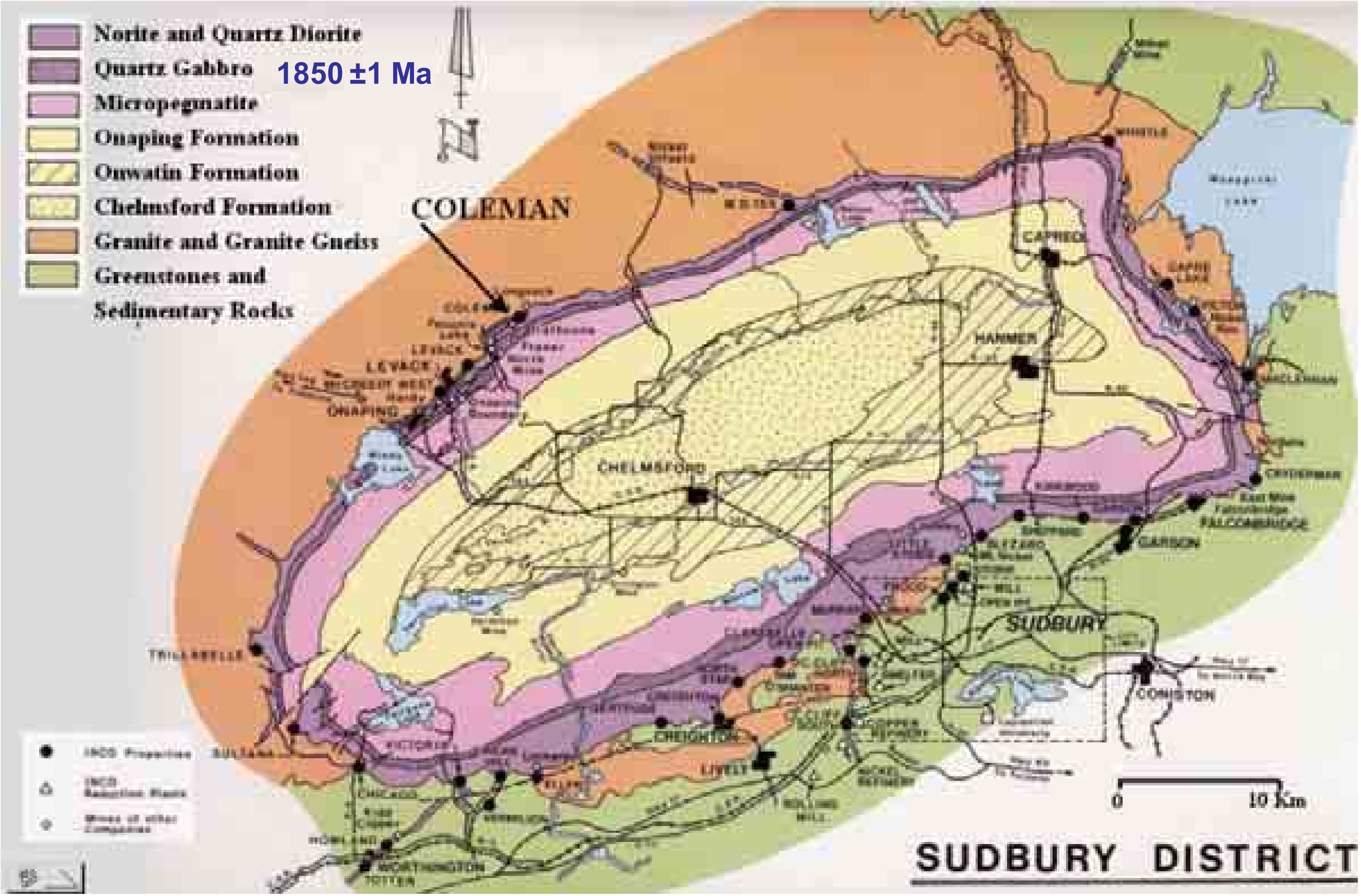

1.6 Gt @ 1.2% Ni, 1.0 % Cu, 0.8 g/t PGE

Sudbury district: Shatter cones in Early Proterozoic Mississagi Formation

Frood-Stobie Mine

O’Donnell Roast Beds

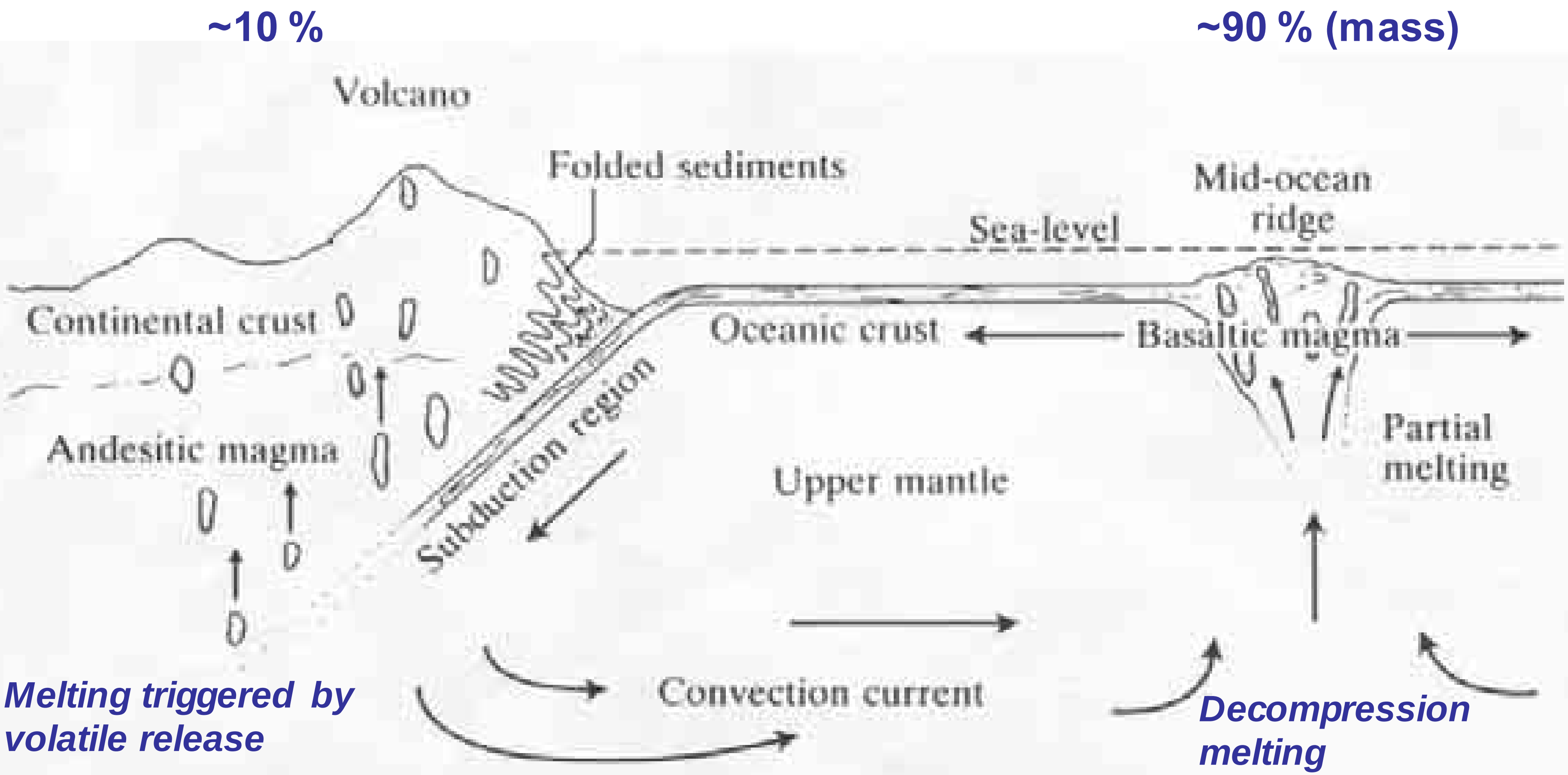

Fig. 5.4. Simplified illustration of the tectonic processes, driven by mantle convection, that form the oceanic and continental crust.

Cox (1989)

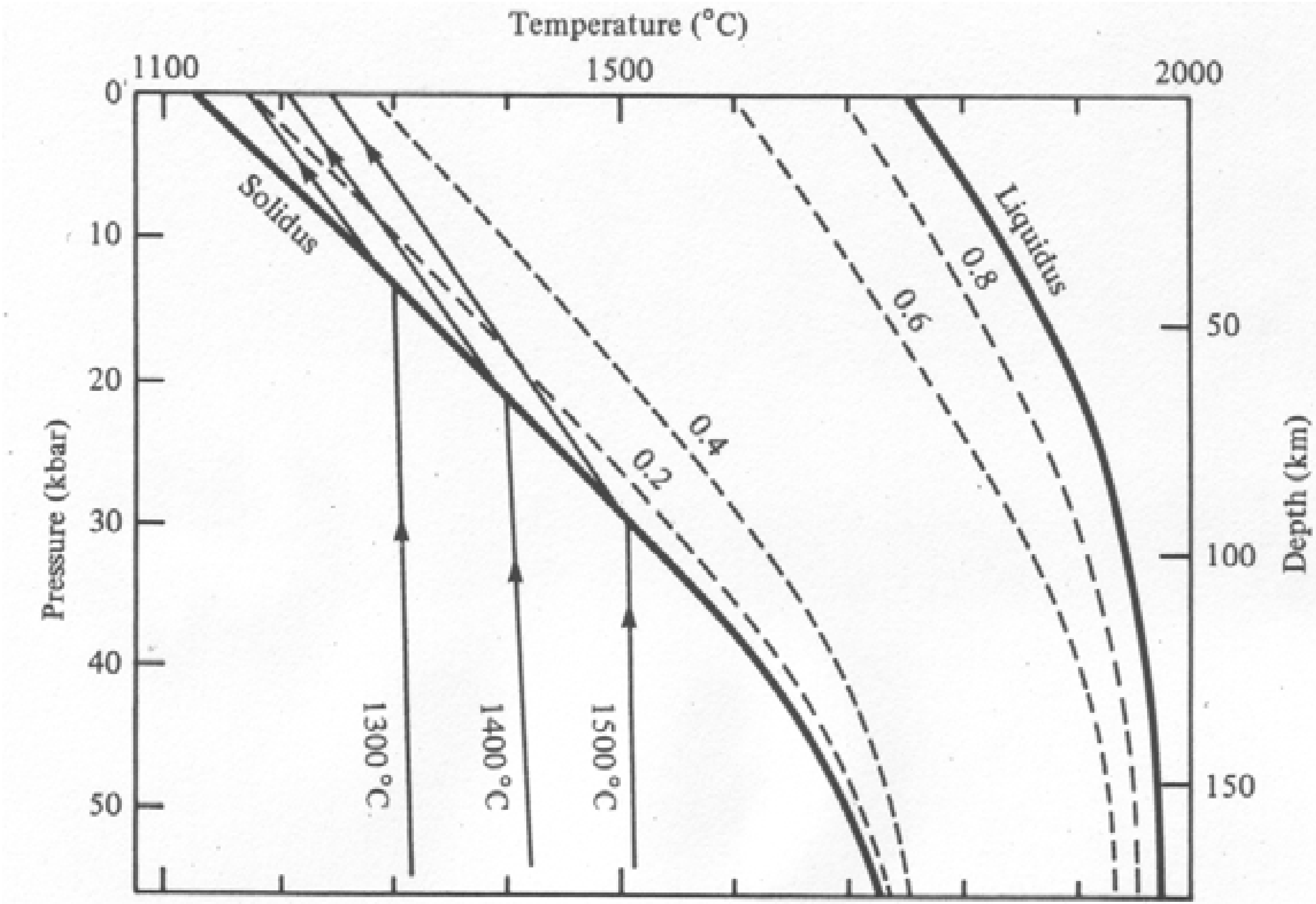

Decompression melting of the mantle (peridotite)
Dashed curves: Fraction of partial melt

Heat Flow

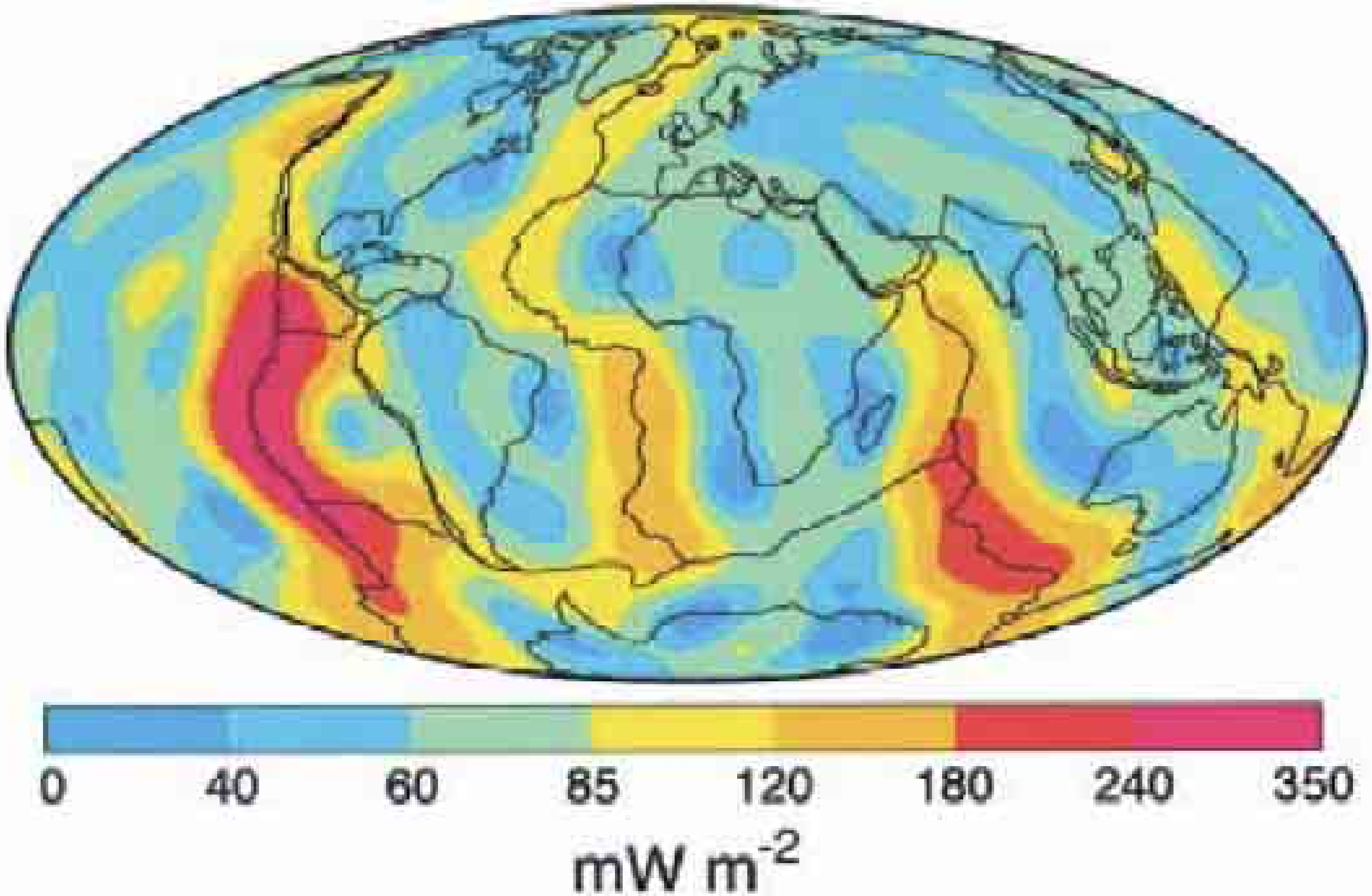

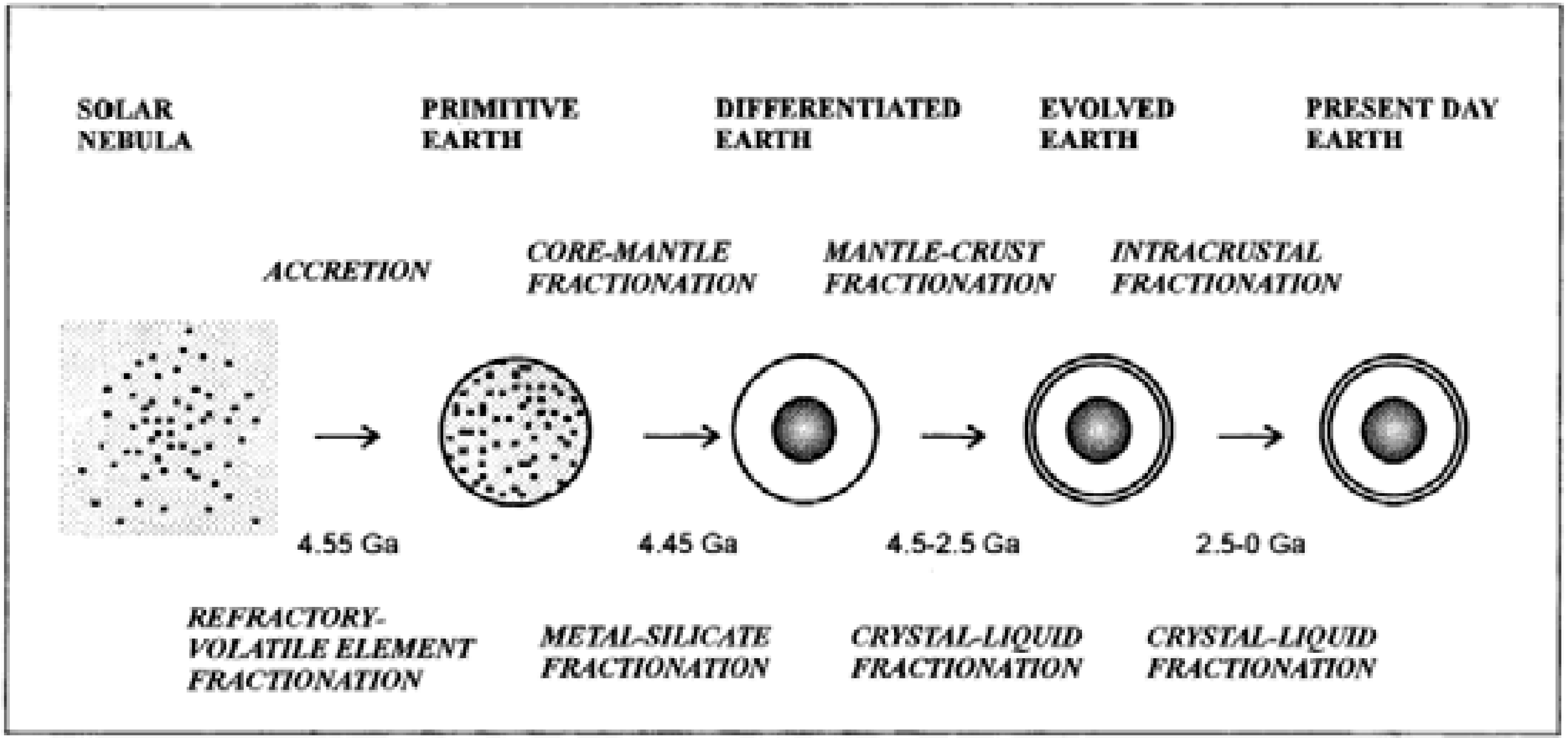

	C1 CHONDRITES	BULK EARTH	PRIMITIVE MANTLE	BULK CRUST	LOWER CRUST	UPPER CRUST
24 Cr	2660 ppm	4120 ppm	2625 ppm	120 ppm	215 ppm	35 ppm
29 Cu	126 ppm	31 ppm	30 ppm	26 ppm	26 ppm	25 ppm
42 Mo	0.928 ppm	2.35 ppm	0.05 ppm	0.65 ppm	0.45 ppm	1.5 ppm
50 Sn	1.72 ppm	0.39 ppm	0.13 ppm	1.5 ppm	1.1 ppm	2.5 ppm
73 Ta	0.014 ppm	0.023 ppm	0.037 ppm	0.7 ppm	0.6 ppm	0.96 ppm
74 W	0.093 ppm	0.18 ppm	0.029 ppm	0.69 ppm	0.5 ppm	2.0 ppm
78 Pt	0.99 ppm	1.67 ppm	0.007 ppm	0.0018 ppm	0.0019 ppm	0.0015 ppm
79 Au	0.140 ppm	0.26 ppm	0.001 ppm	0.003 ppm	0.0014 ppm	0.0018 ppm
82 Pb	2.5 ppm	0.115 ppm	0.15 ppm	12.5 ppm	4.3 ppm	20 ppm
92 U	0.008 ppm	0.014 ppm	0.02 ppm	1.4 ppm	0.28 ppm	2.8 ppm
Rb/Sr	0.295	0.032	0.028	0.17	0.03	0.32

Simkin et al. (1989)

Seafloor spreading in the Pacific

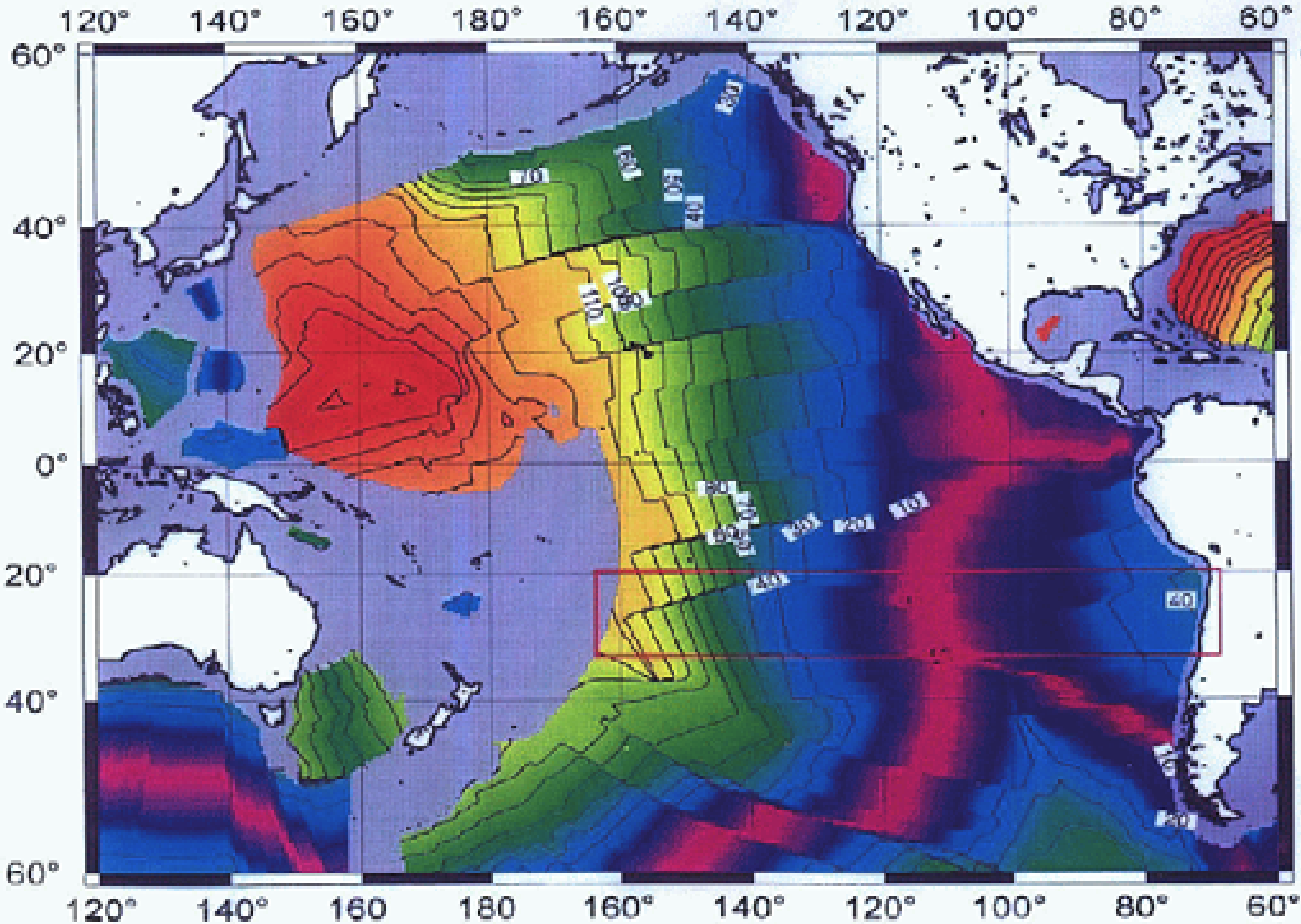

Mueller et al 1997

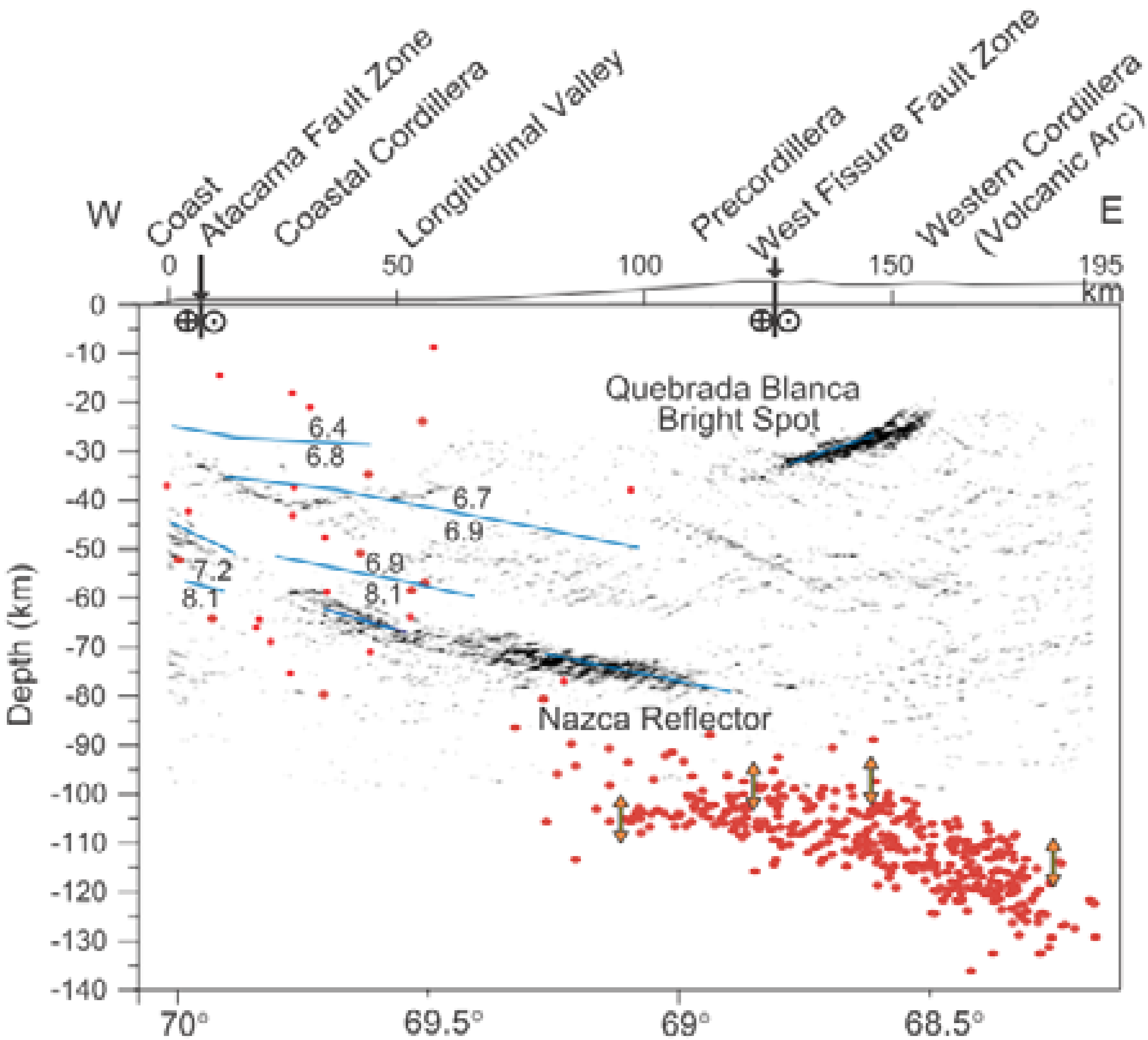

Seismic cross section at 21°S (Ancorp Working Group 1999, Nature 397: 343)

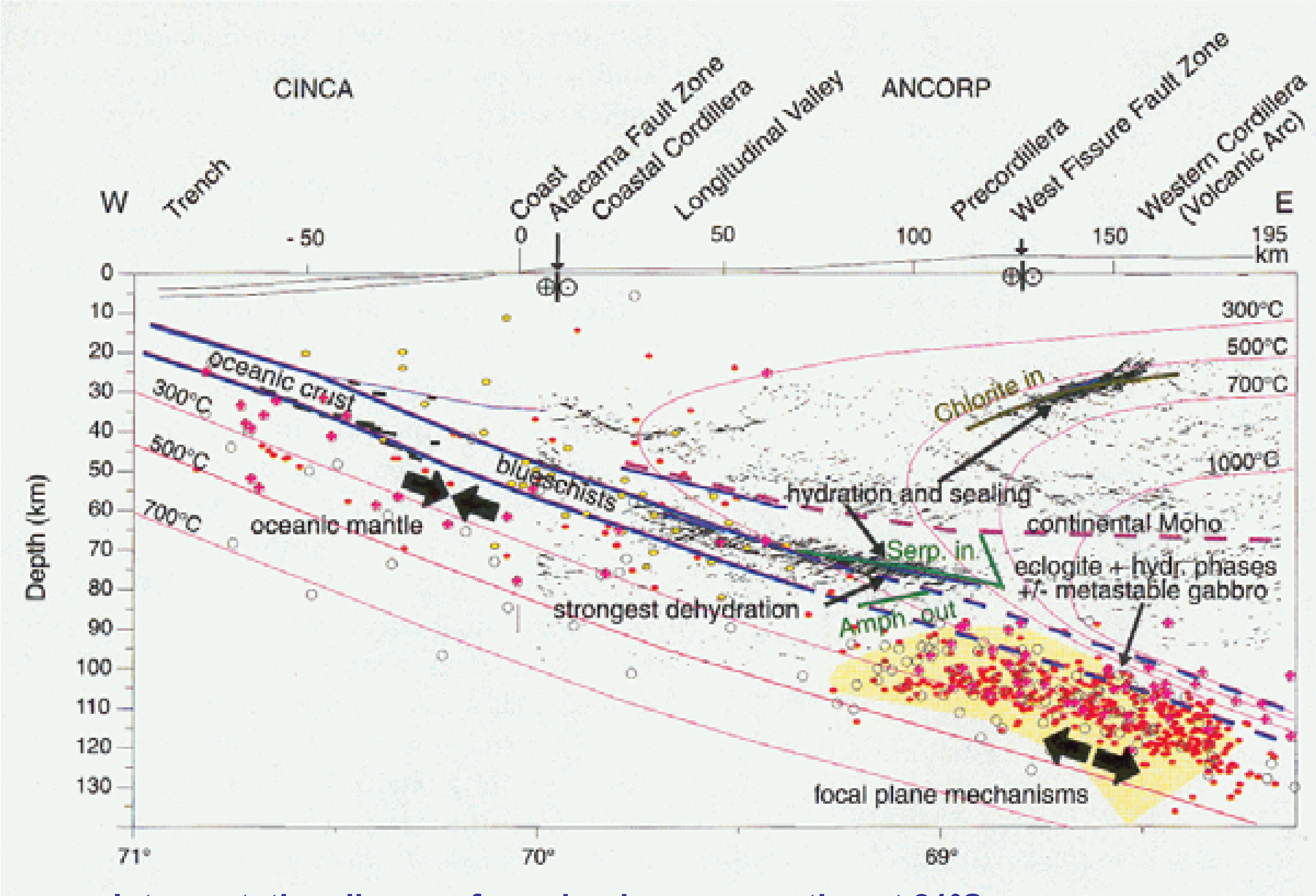

Interpretation diagram for seismic cross section at 21°S
(Ancorp Working Group 1999, Nature 397: 343)

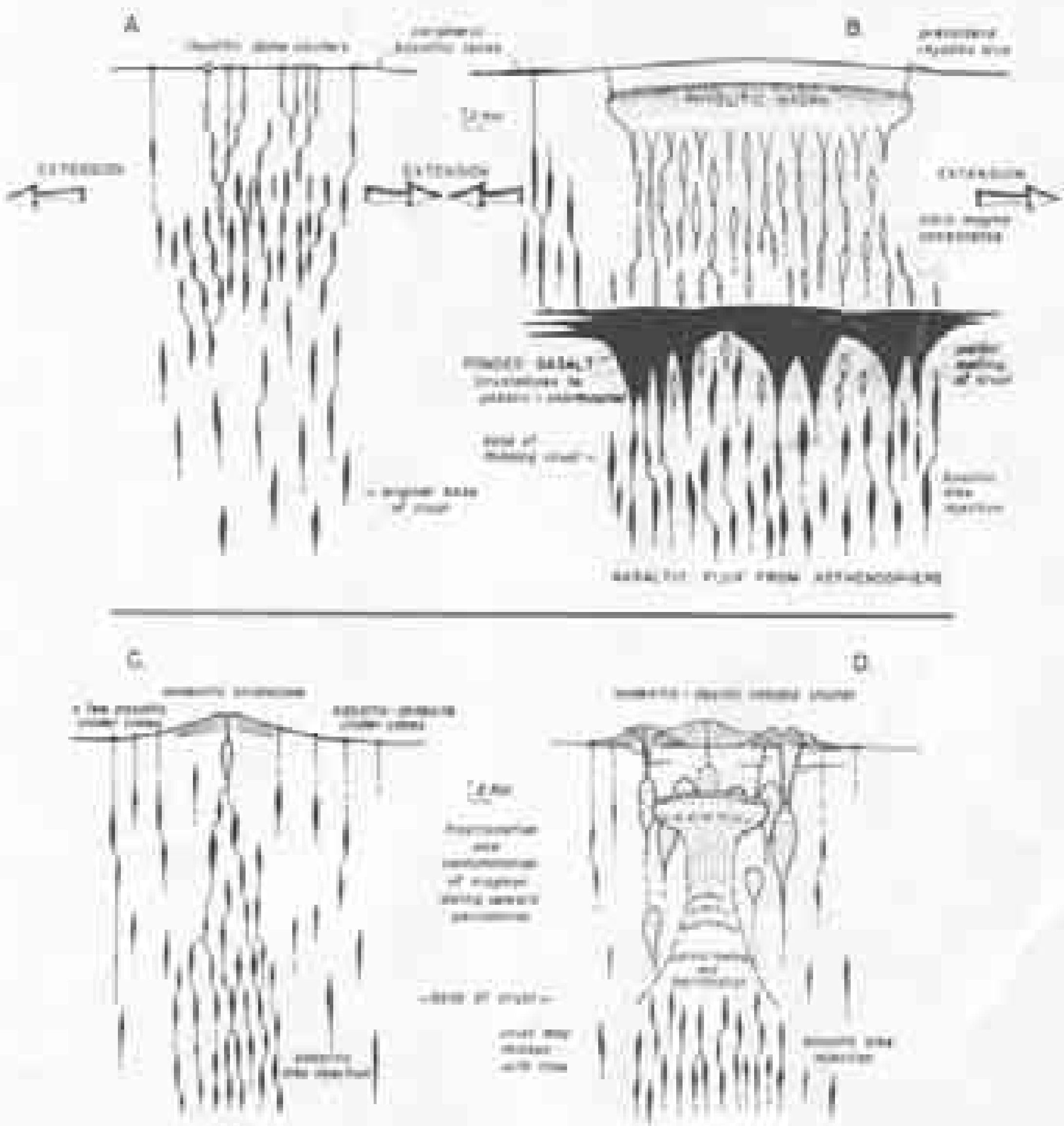

Fig. 13. Some contrasting styles of lithospheric magmatism. Top pair of cartoons depicts rhyolite-basaltic magmatism under stress conditions favoring marked crustal extension: (A) modest power input; (B) large power input, advanced stage. Shaded regions indicate partial melting of crustal rocks sufficient to permit separation of rhyolitic magmas as path veins and dikes. Lower pair of cartoons depicts two possible stages in development of volcanic systems where tectonic extension, if any, is subordinate and shallow: (C) early stage; (D) intermediate stage; for advanced stage see Figure 12. This model applies to island arc, continental margin arc, and continental interior systems that produce abundant intermediate magmas. All four sketches are idealized and refer to no particular systems. The models are independent of the mode or site of generation of basaltic magma, but basalt is thought to provide the power supply for virtually all other magmatism. The power spectrum, the penetration rate of magmas, and the volatile flux from the mantle, all in concert with the stress state, thermal history, and compositional structure of the lithosphere, must control the chemistry of the magmas ultimately containing in shallow reservoirs.

Hildreth (1981) Gradients in silicic magma chambers. J Geophys Res 86: 10179

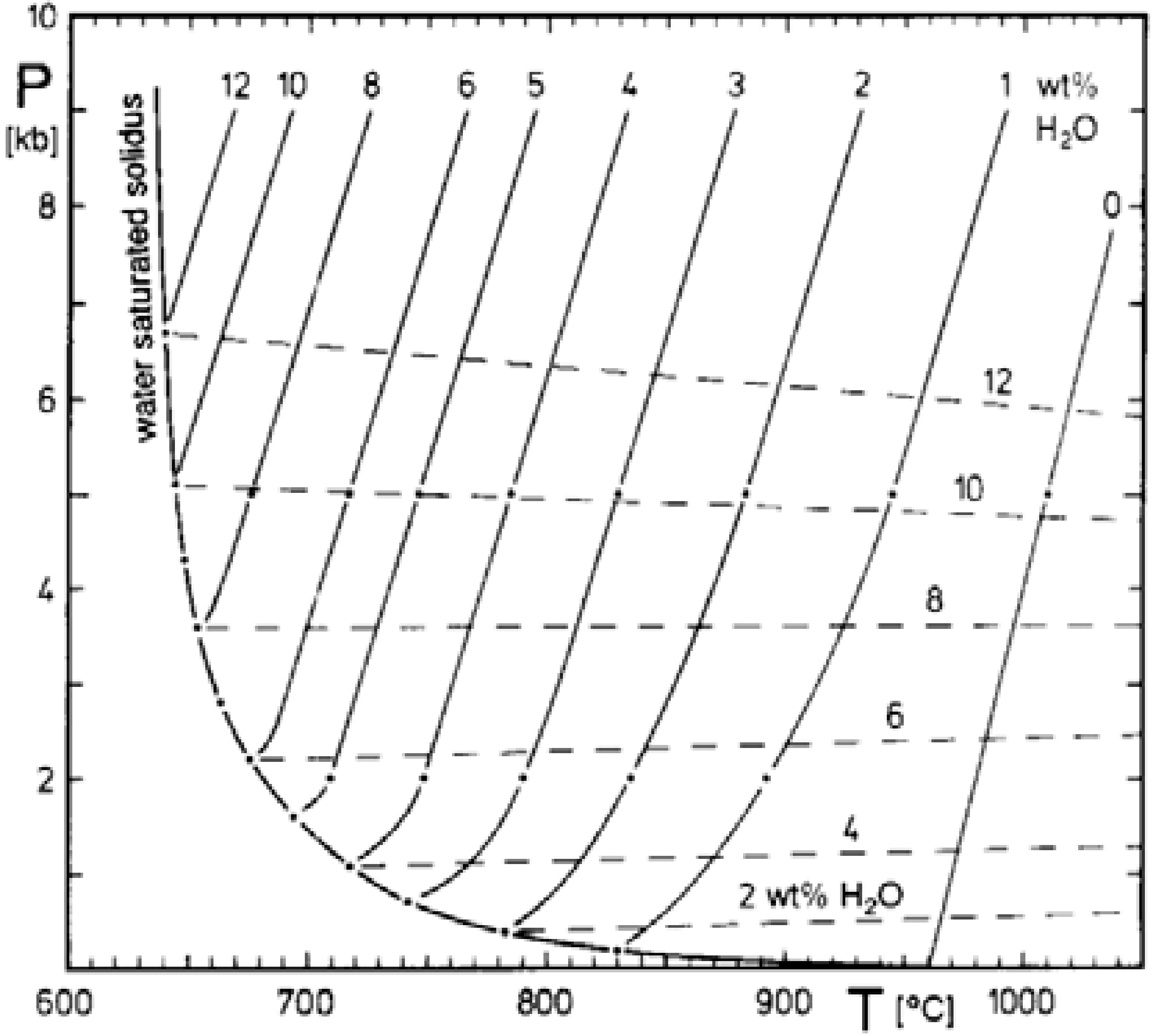

The system Qz-Ab-Or-H_2O: Liquidus curves for given amount of H_2O (solid lines) and H_2O solubility curves (dashed lines) for minimum eutectic compositions.
Holtz and Johannes (1994) Lithos 32: 149-159

Main-phase granite, Rayong Pluton, Thailand
(K-feldspar megacrystic medium- to coarse-grained biotite granite)

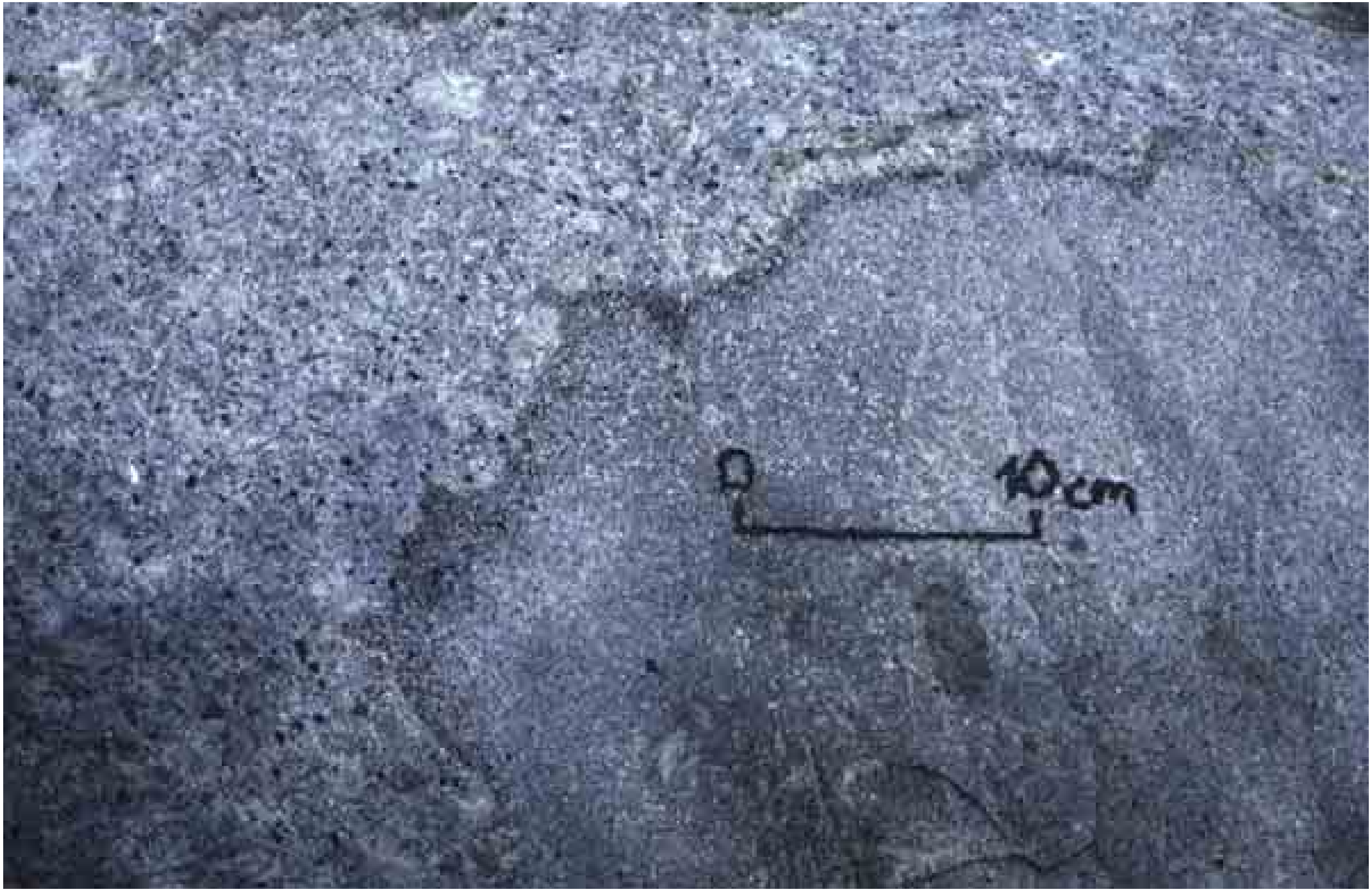

Microgranite intrudes two-phase granite, Belitung Island, Indonesia

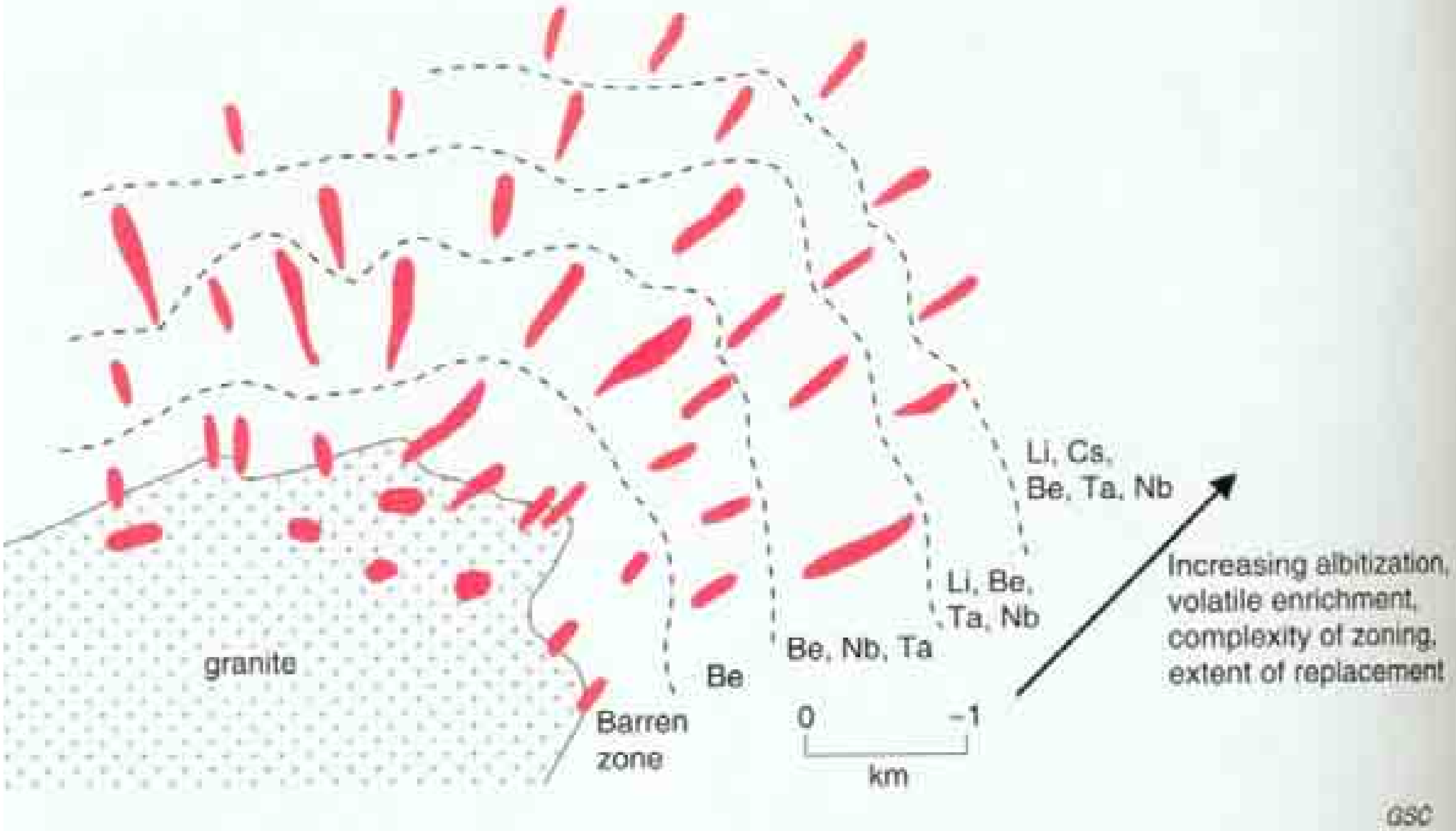

Figure 21-4. Schematic representation of the regional zonation of pegmatites (red) around a granite intrusion (modified from Trueman and Černý, 1982).

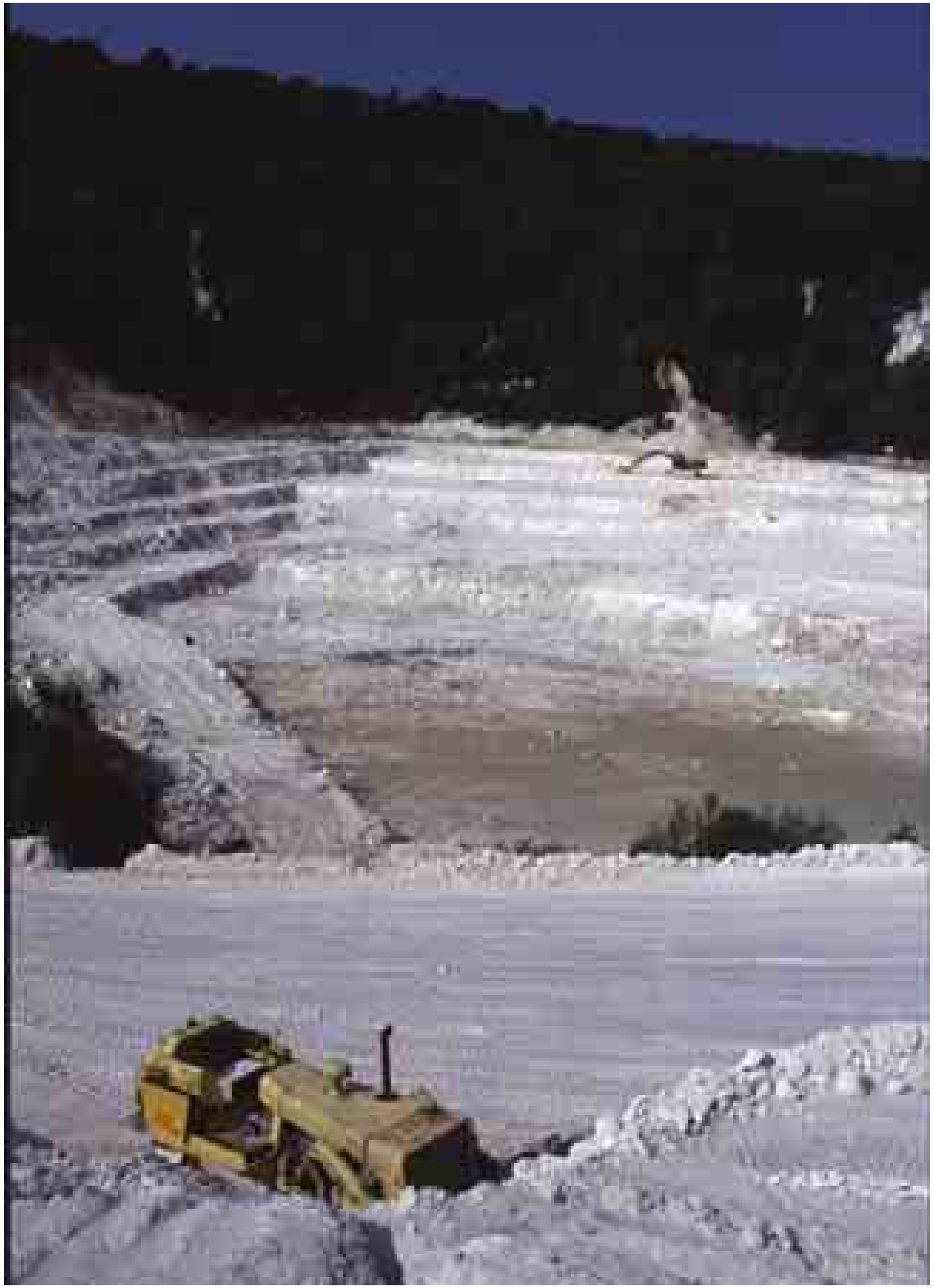

Beauvoir,
Massif Central,
France

Albite granite,
argillic alteration

China clay mine
with
800 g/t Sn
190 g/t Ta
120 g/t Nb
0.31 % Li


Transbaikalia, Russia

Orlovka rare-metal granite, Siberia, Russia

Orlovka rare-metal granite, Russia: pegmatite-aplite layering with unidirectional solidification texture of amazonite (green microcline) megacrysts

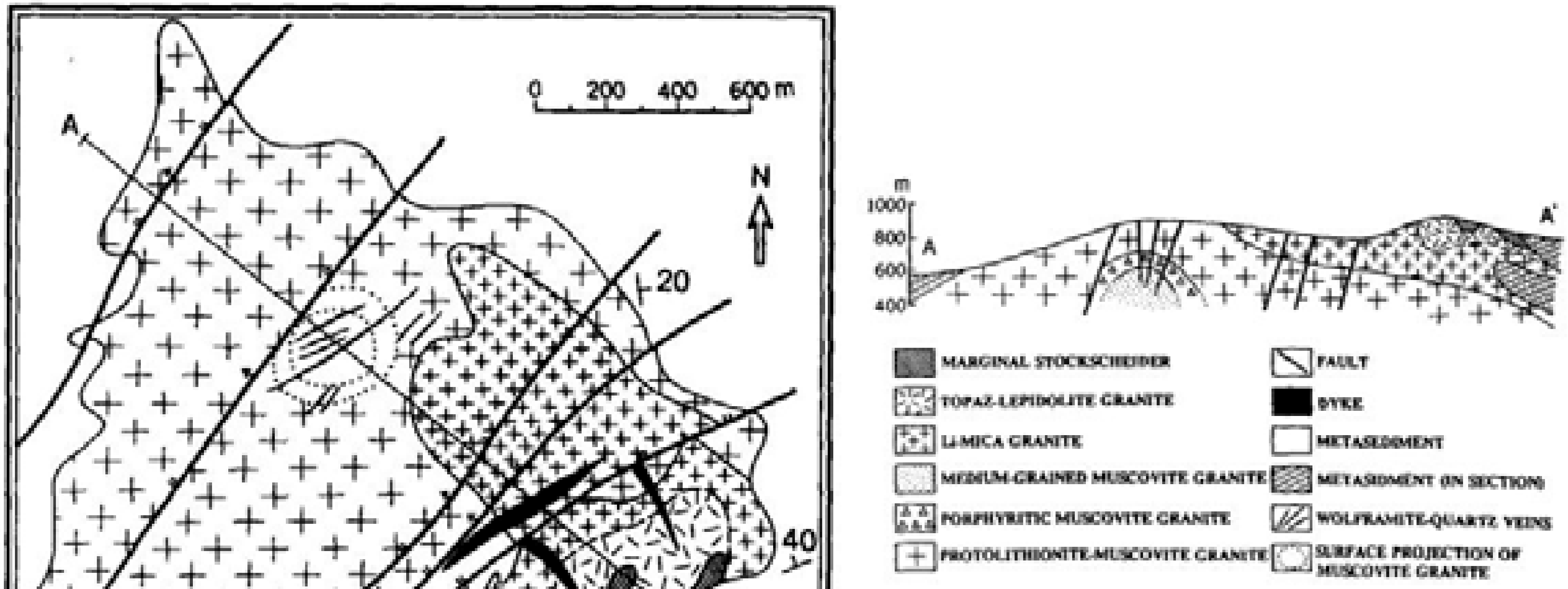

FIG. 1. Simplified geologic map and cross section of the Yashan batholith.

Multiple intrusion sequence
(Yin et al. 1995: 578)

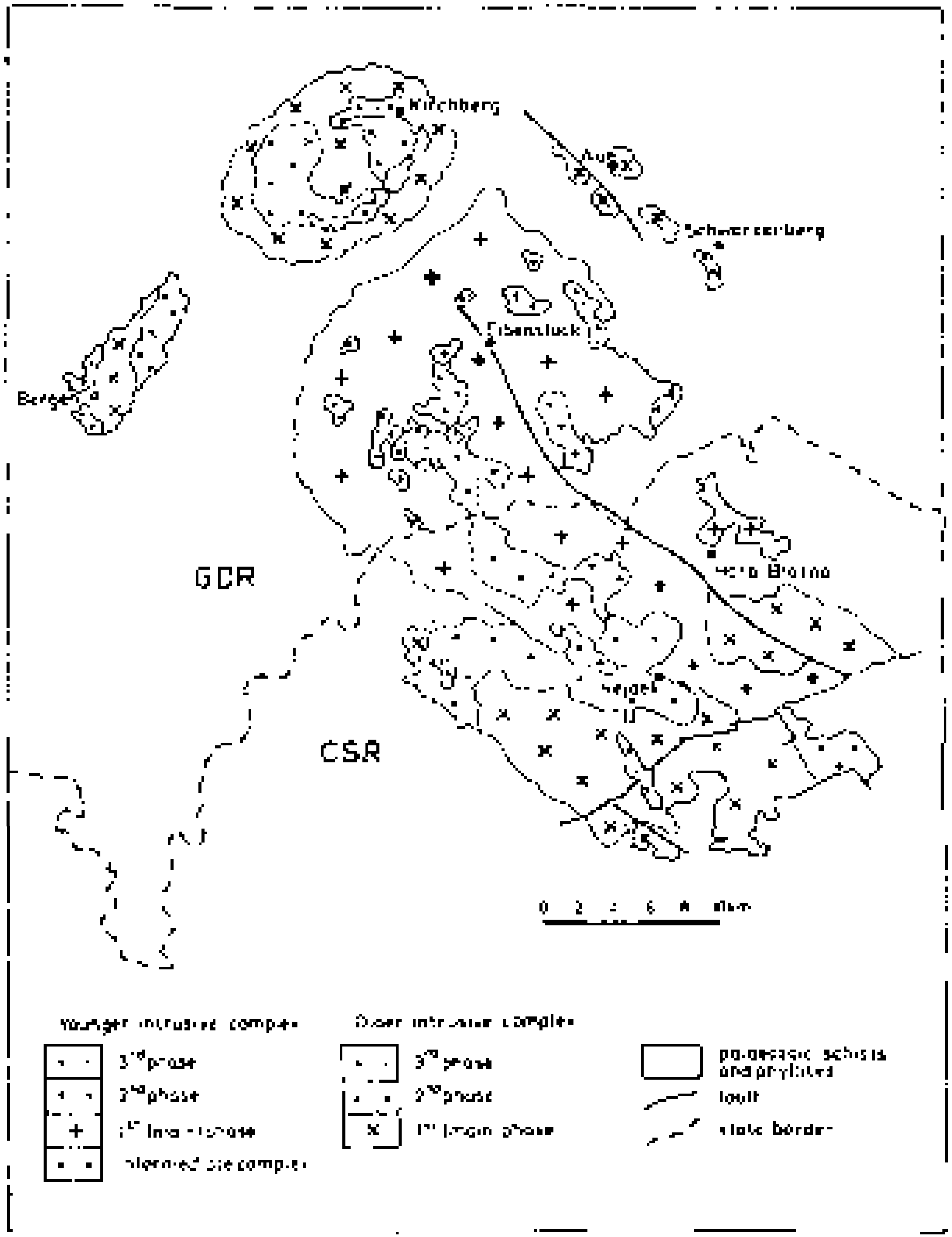

Western Erzgebirge/
Krusne Hory Mts
Variscan granite
sequence (300 Ma)

Tischendorf (1989)

Pilok Sn-W-Ta mine, Thailand: Apical portion (little exposed) of a larger granite system

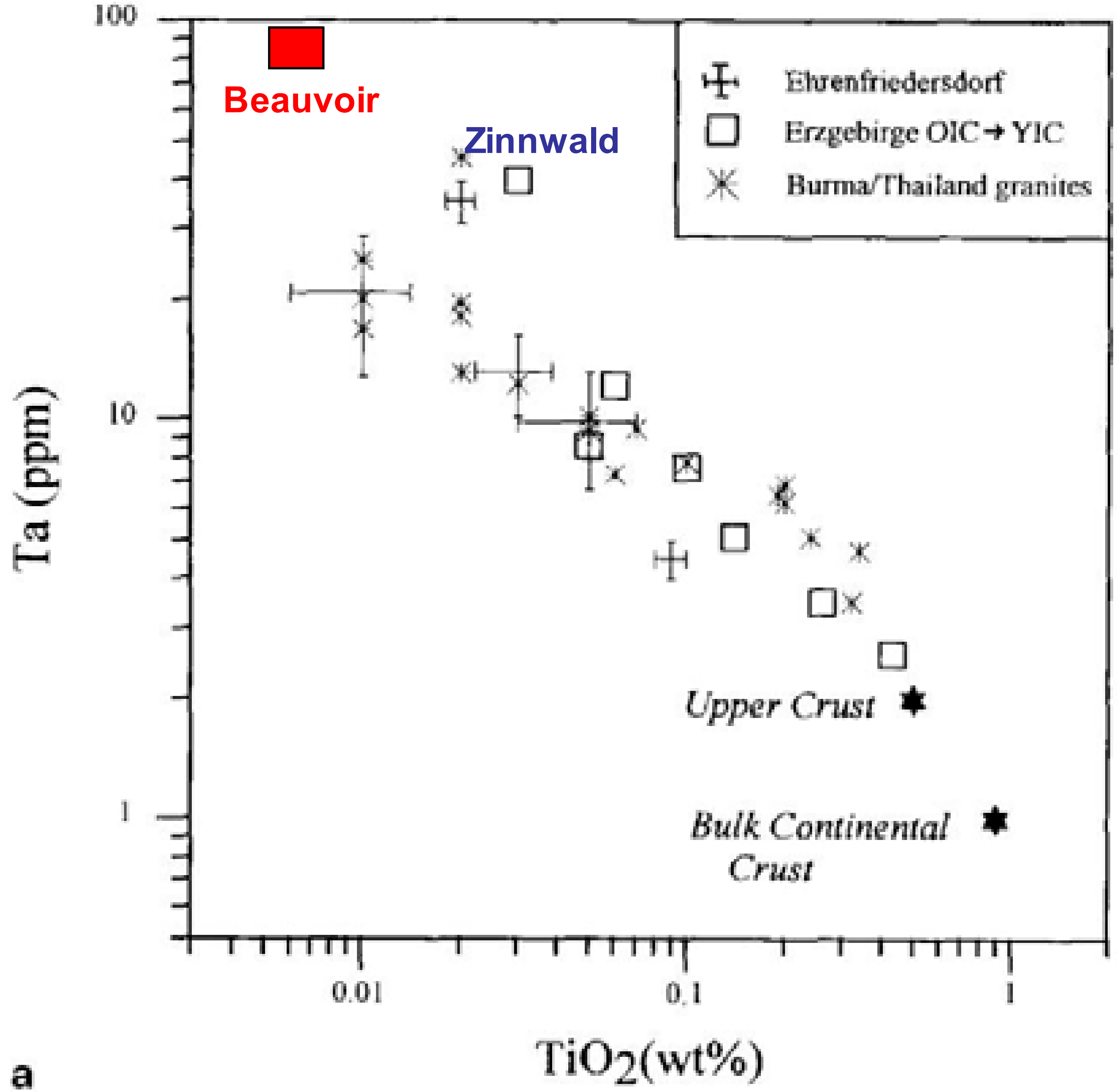

Beauvoir
Zinnwald
Ehrenfriedersdorf
Erzgebirge OIC → YIC
Burma/Thailand granites
Upper Crust
Bulk Continental Crust
100
10
1
0.01
0.1
1
Ta (ppm)
TiO2(wt%)

a

Central Africa: Rwanda/Burundi

Kabarore rare-metal pegmatite, Burundi

Kabarore rare-metal pegmatite, Burundi: ground sluicing

Artisanal mining for tantalum and tin, Burundi

Kabarore rare-metal pegmatite, Burundi: ground sluicing

Kabarore rare-metal pegmatite, Burundi

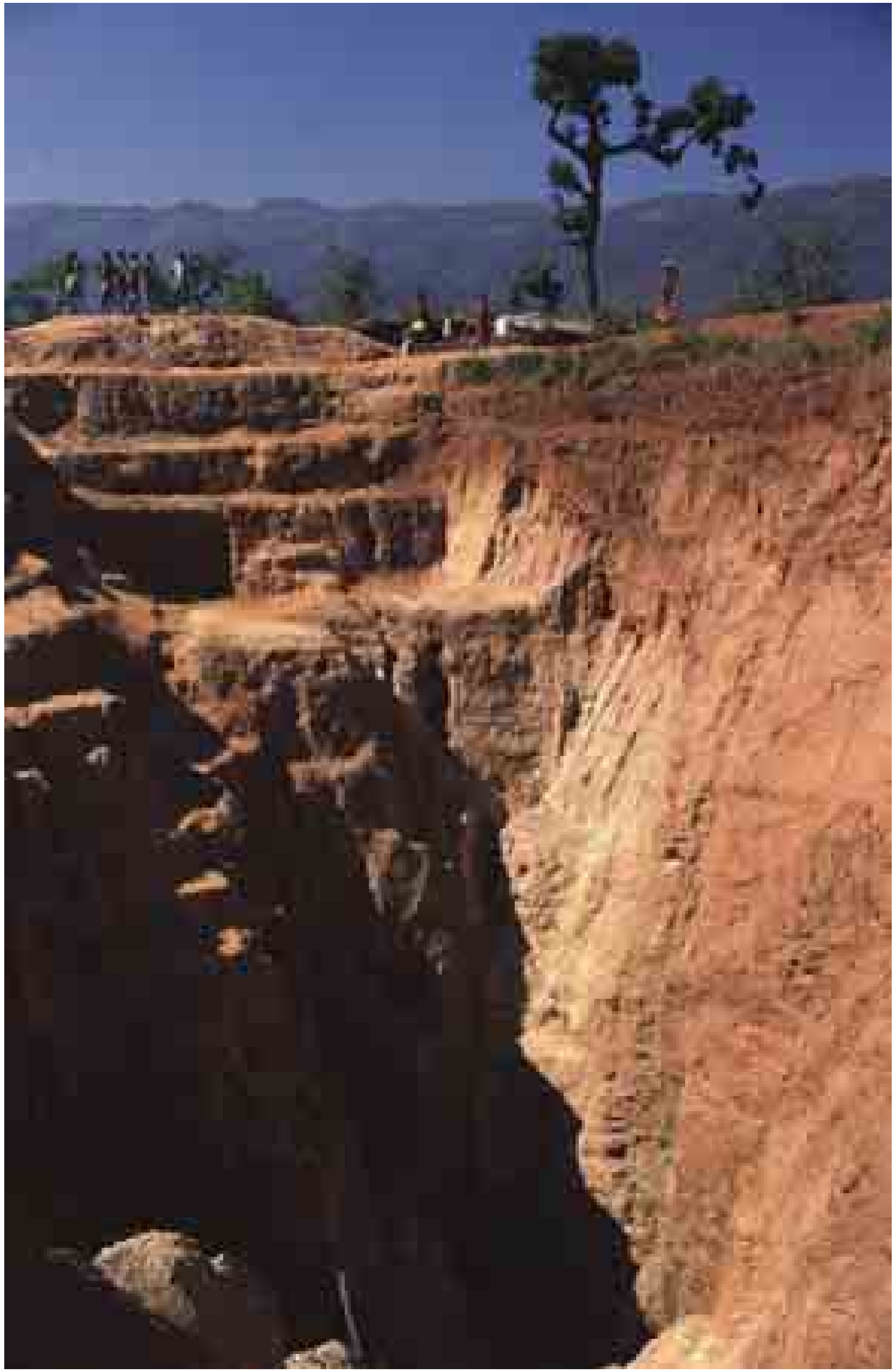

Rare-metal pegmatite in Madhya Pradesh, India (under lateritic cover)

Madhya Pradesh, India: Washing weathered pegmatite

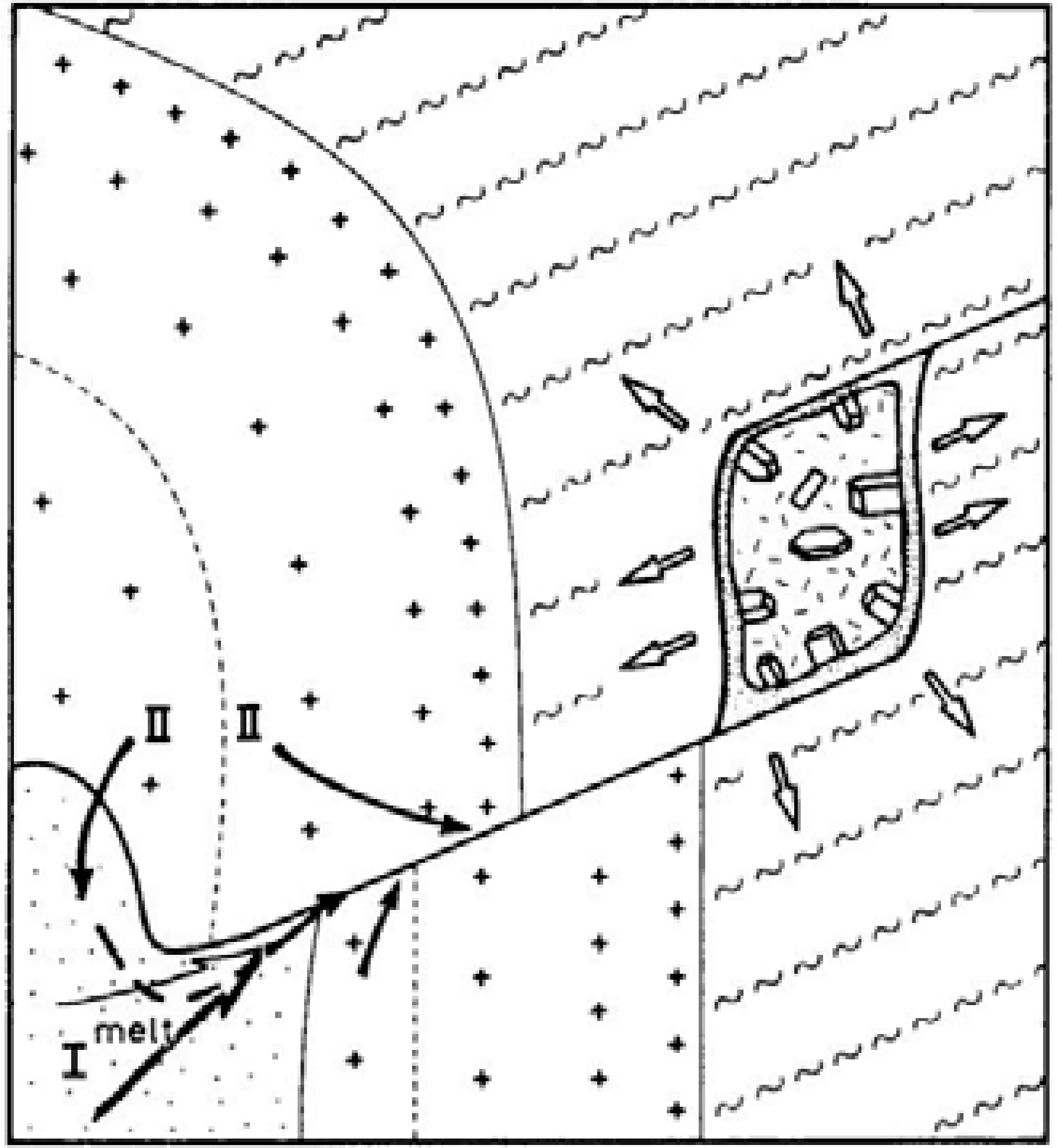

Fig. 11. A simplified model showing the discussed relationship of pegmatites to their parental granites and the different sources of fluids. *Fluid I* is a late residual hydrous granitic melt, *fluid II* represents the intergranular liquid which mixes continuously with the former. The pegmatite is considered as an open system at least for all non-hydrolyzing ions

Möller (1989: 120)

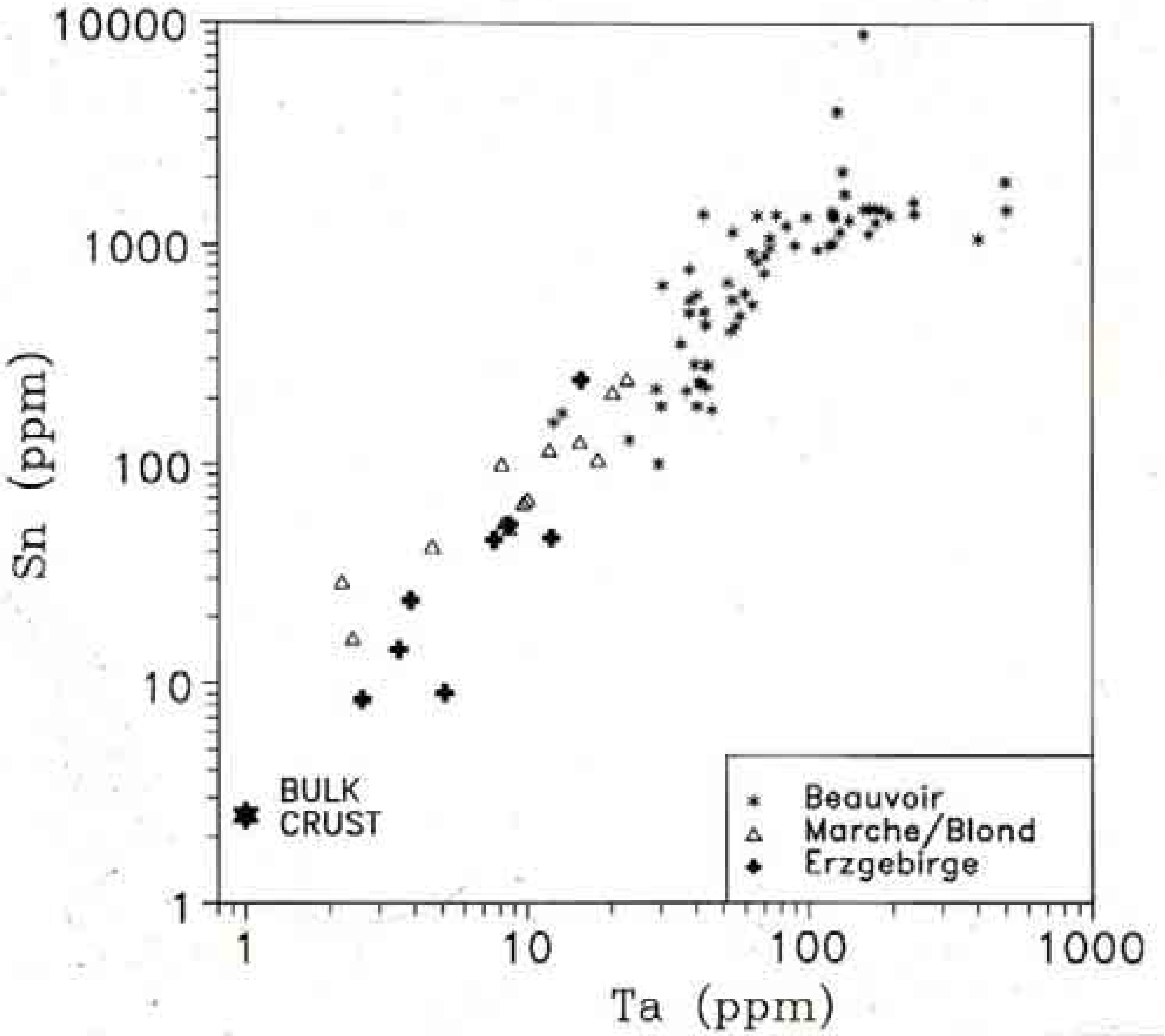

10000
1000
100
10
1
Sn (ppm)
1
10
100
1000
Ta (ppm)
BULK
CRUST
Beauvoir
Marche/Blond
Erzgebirge

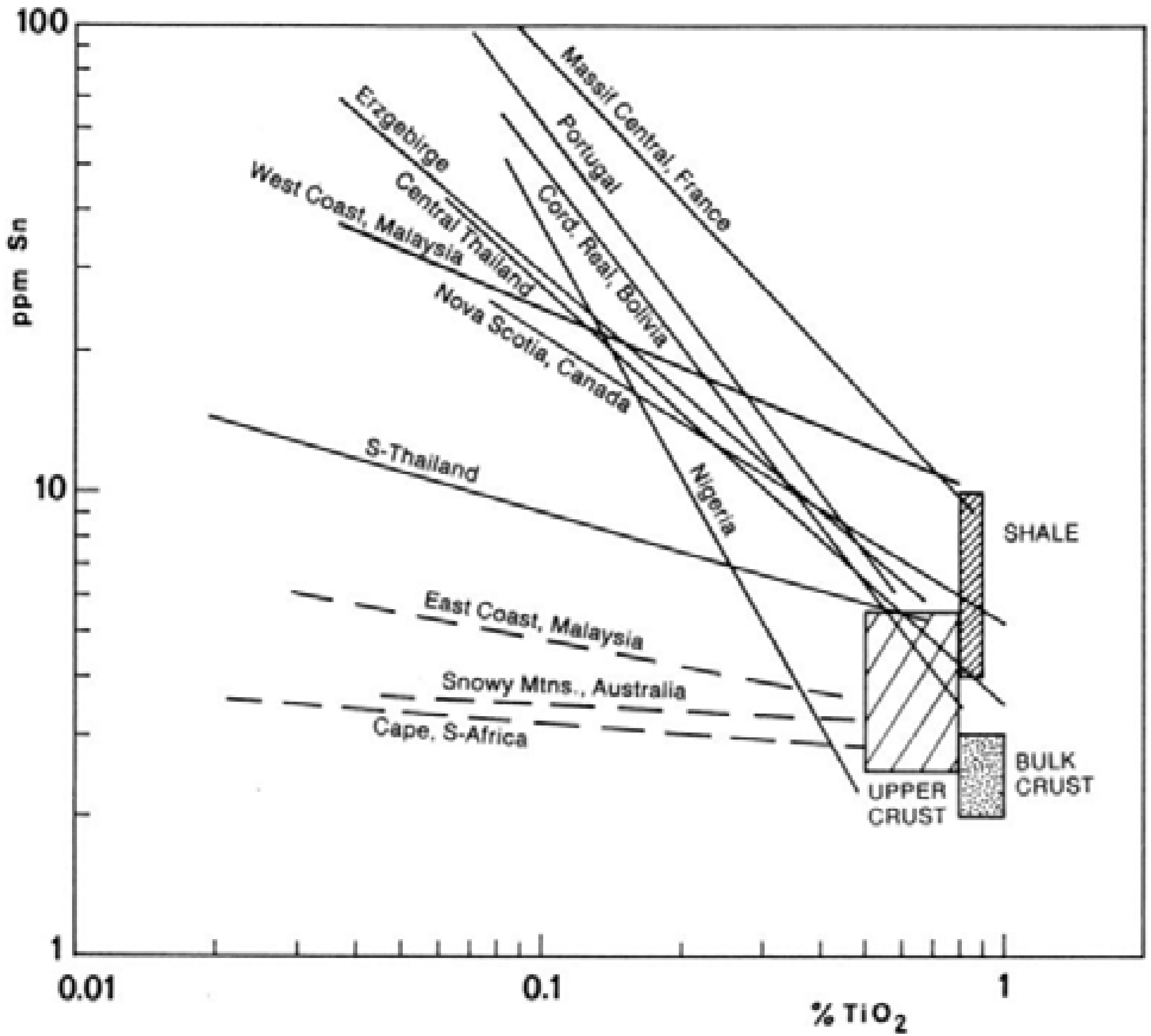

100
10
1
0.01
0.1
1
ppm Sn
% TiO_2
Massif Central, France
Portugal
Erzgebirge
Cord. Real, Bolivia
Central Thailand
West Coast, Malaysia
Nova Scotia, Canada
Nigeria
S-Thailand
East Coast, Malaysia
Snowy Mtns., Australia
Cape, S-Africa
SHALE
UPPER CRUST
BULK CRUST

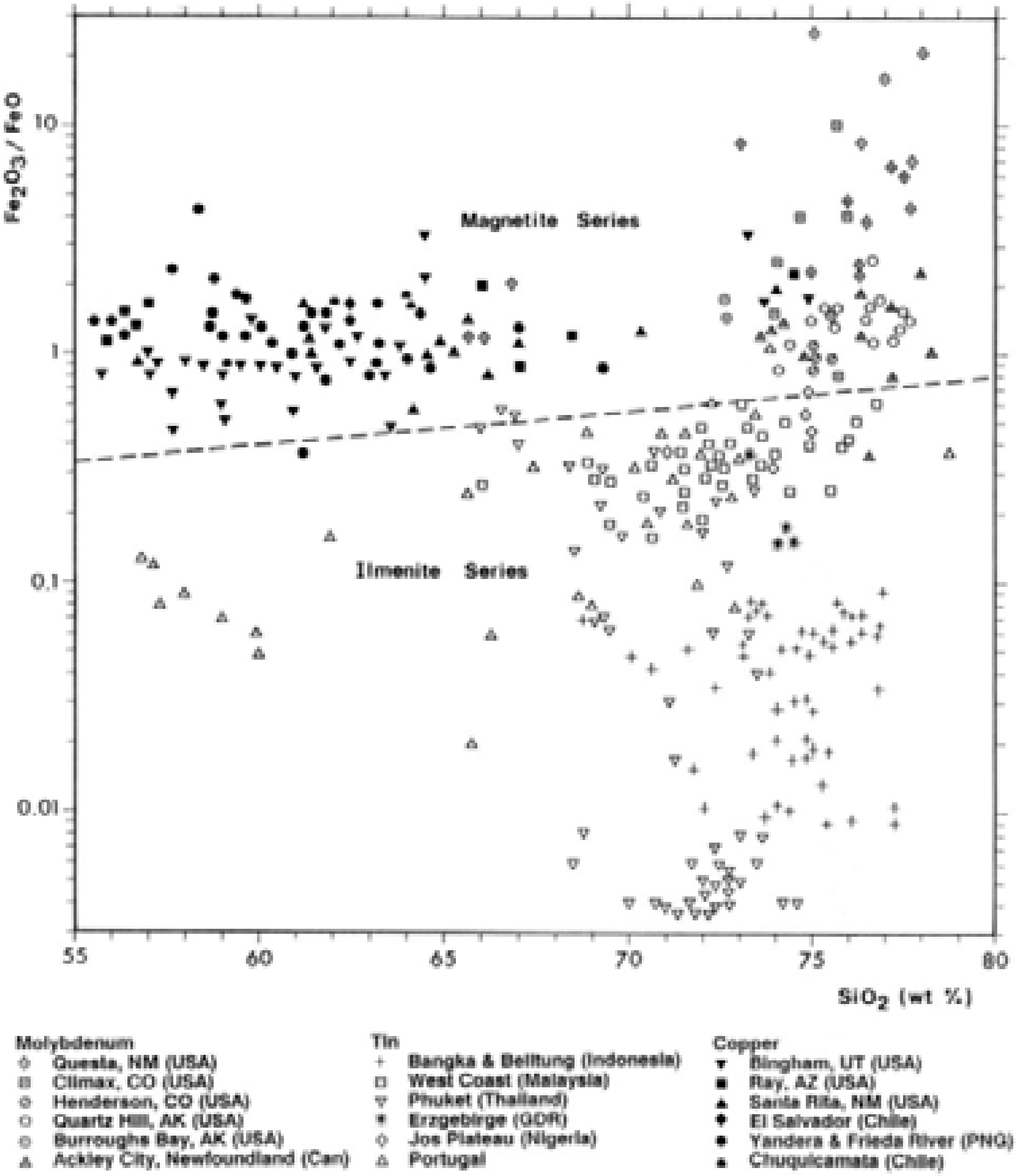

$O^{2-} + Sn^{4+} = Sn^{2+} + ½O_2$

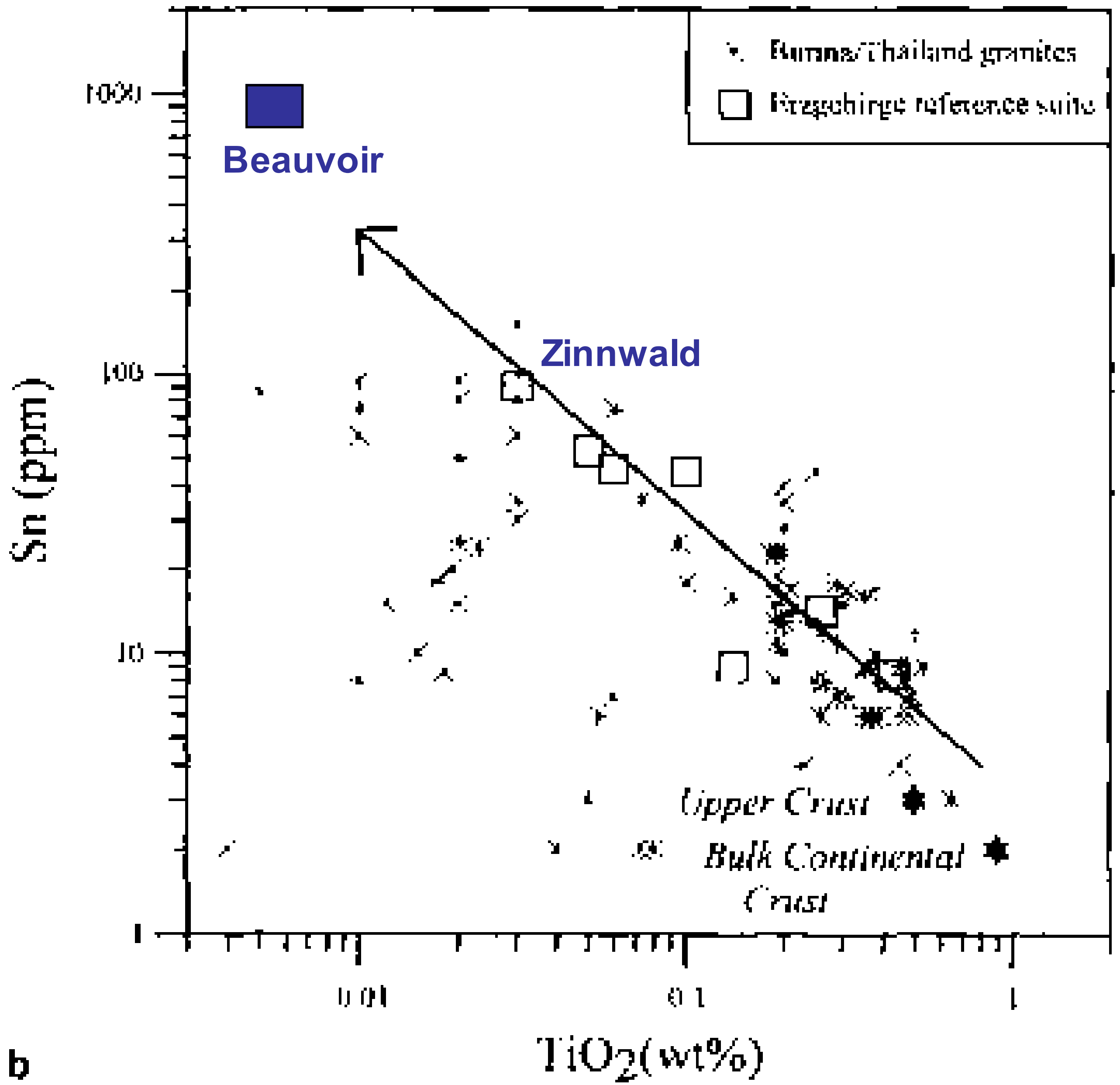

Burma/Thailand granites
Erzgebirge reference suite
1000
100
10
1
Beauvoir
Zinnwald
Upper Crust
Bulk Continental Crust
Sn (ppm)
0.01
0.1
1
TiO_2 (wt%)

b

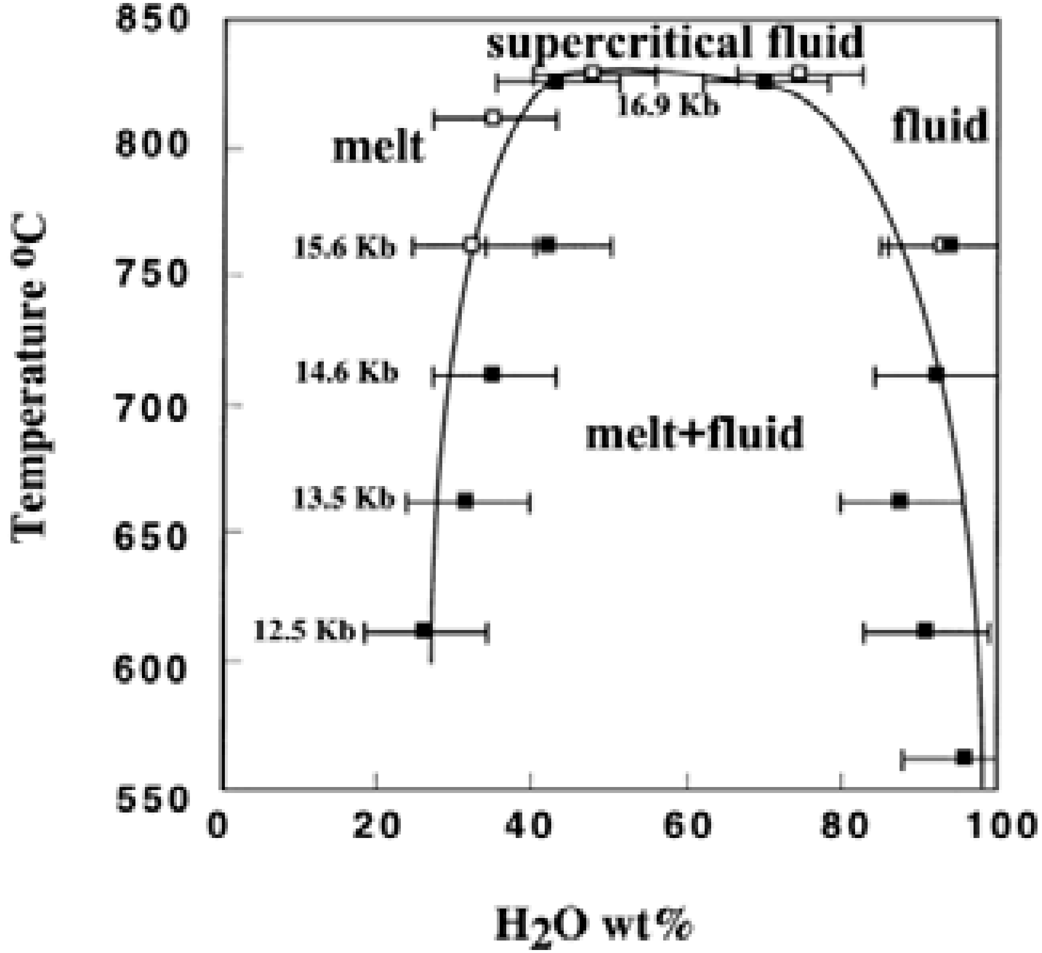

Fig. 4. Phase diagram of the system haplogranite–H_2O under isochoric conditions for a bulk density of water of 1.016 g cm^{-3}. The compositions of the coexisting phases were derived from in-situ FTIR spectra. Open and closed symbols refer to two different sets of measurements.

Boudreau and Keppler (1999) EPSL 165: 193

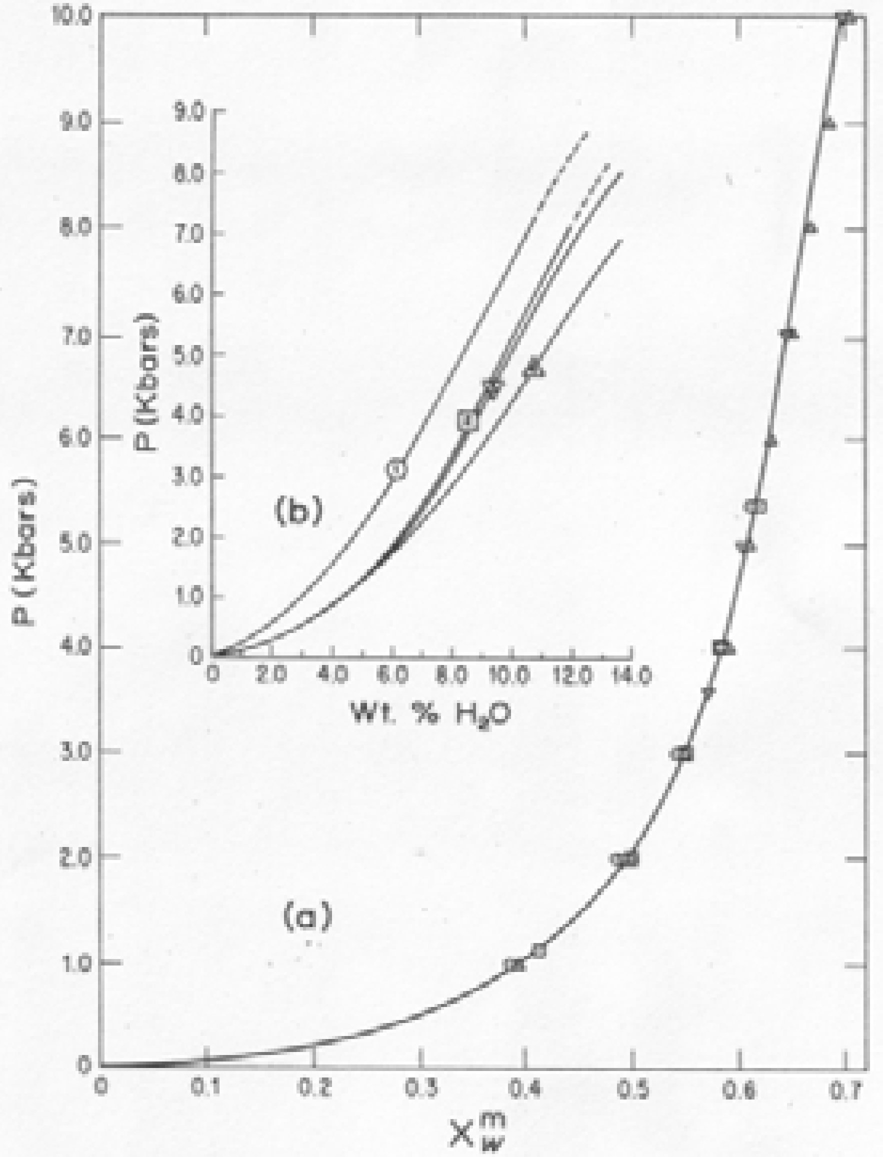

Figure 16-4. Solubility of H_2O in aluminosilicate melts. Circles (1), Columbia River basalt; squares (2), Mt. Hood andesite; inverted triangles (3), albite; and upright triangles (4), Harding pegmatite. (a) Equimolal solubilities at 1373K (1100°C) calculated from experimental weight-percent solubilities in (b), using text Eqs. 16-3, 16-4, 16-5, 16-6, and values of M_s and M'_s from Table 16-1. (b) Experimental weight-percent solubilities at various temperatures, from Burnham and Jahns (1962) and Hamilton *et al.* (1964).

$X_w = Moles\ H_2O\ /$
$(Moles\ H_2O + Moles\ Silicate)$

Burnham (1979)

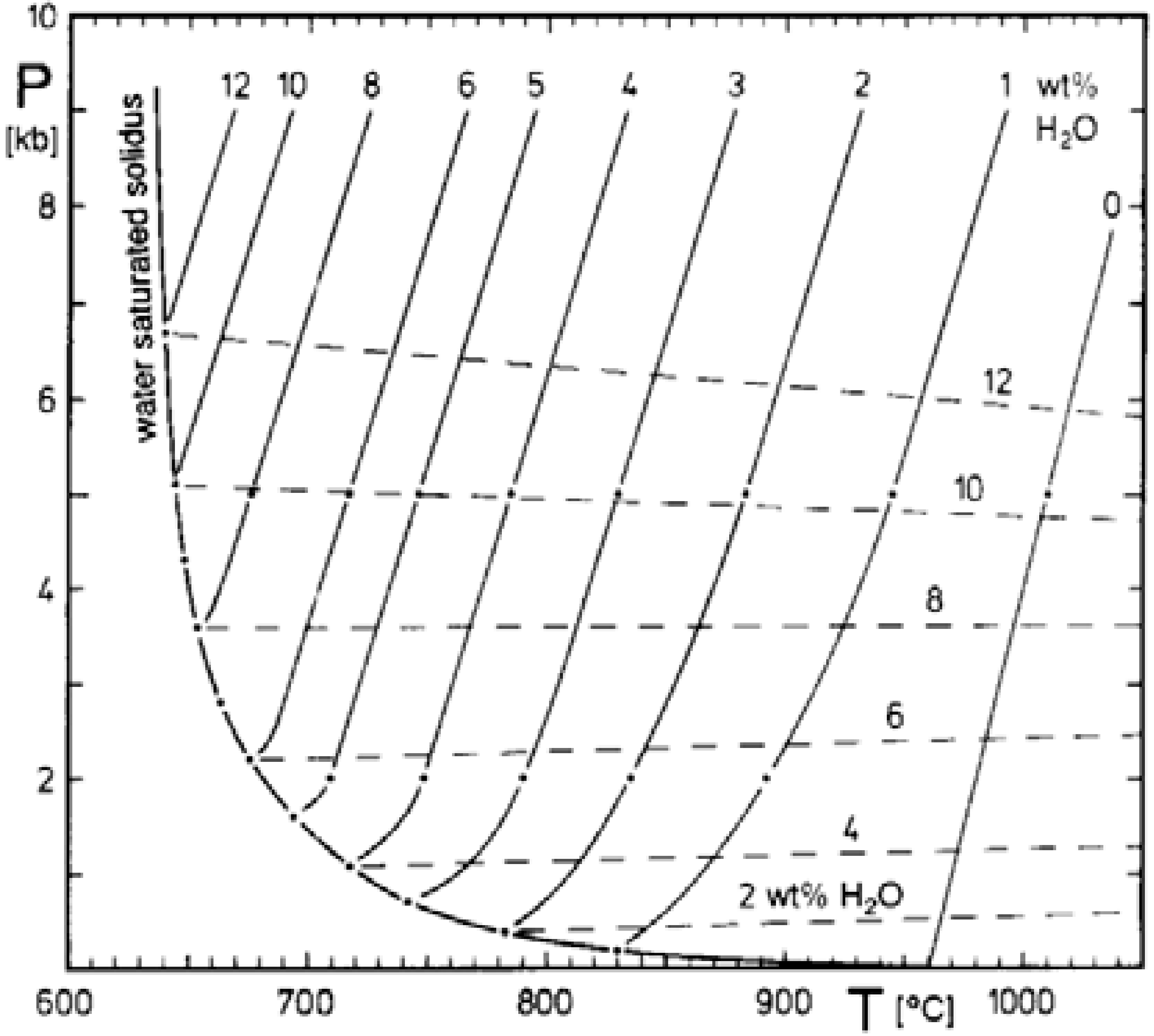

The system Qz-Ab-Or-H_2O: Liquidus curves for given amount of H_2O (solid lines) and H_2O solubility curves (dashed lines) for minimum eutectic compositions.

Holtz and Johannes (1994) Lithos 32: 149-159

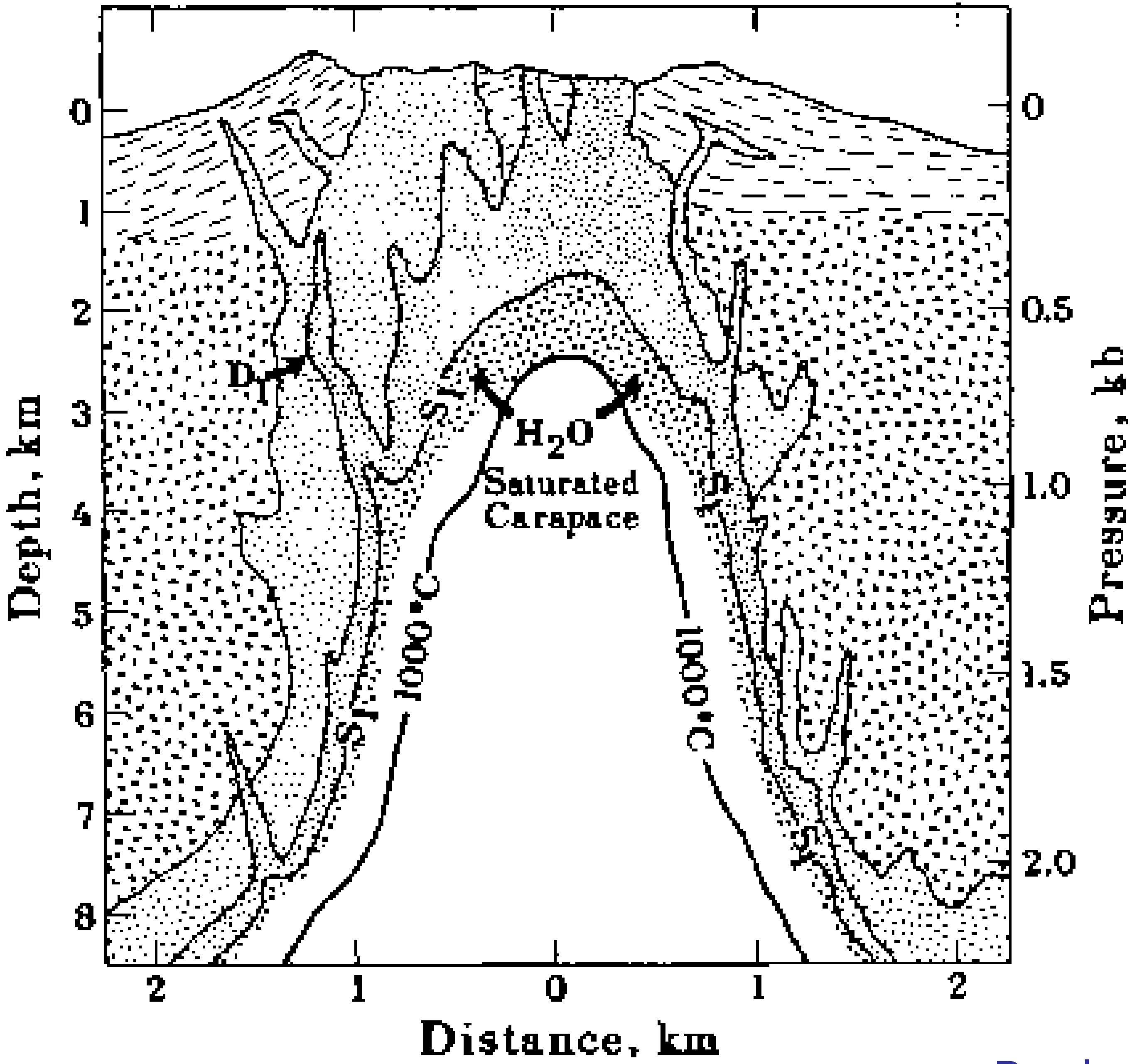

Burnham (1979)

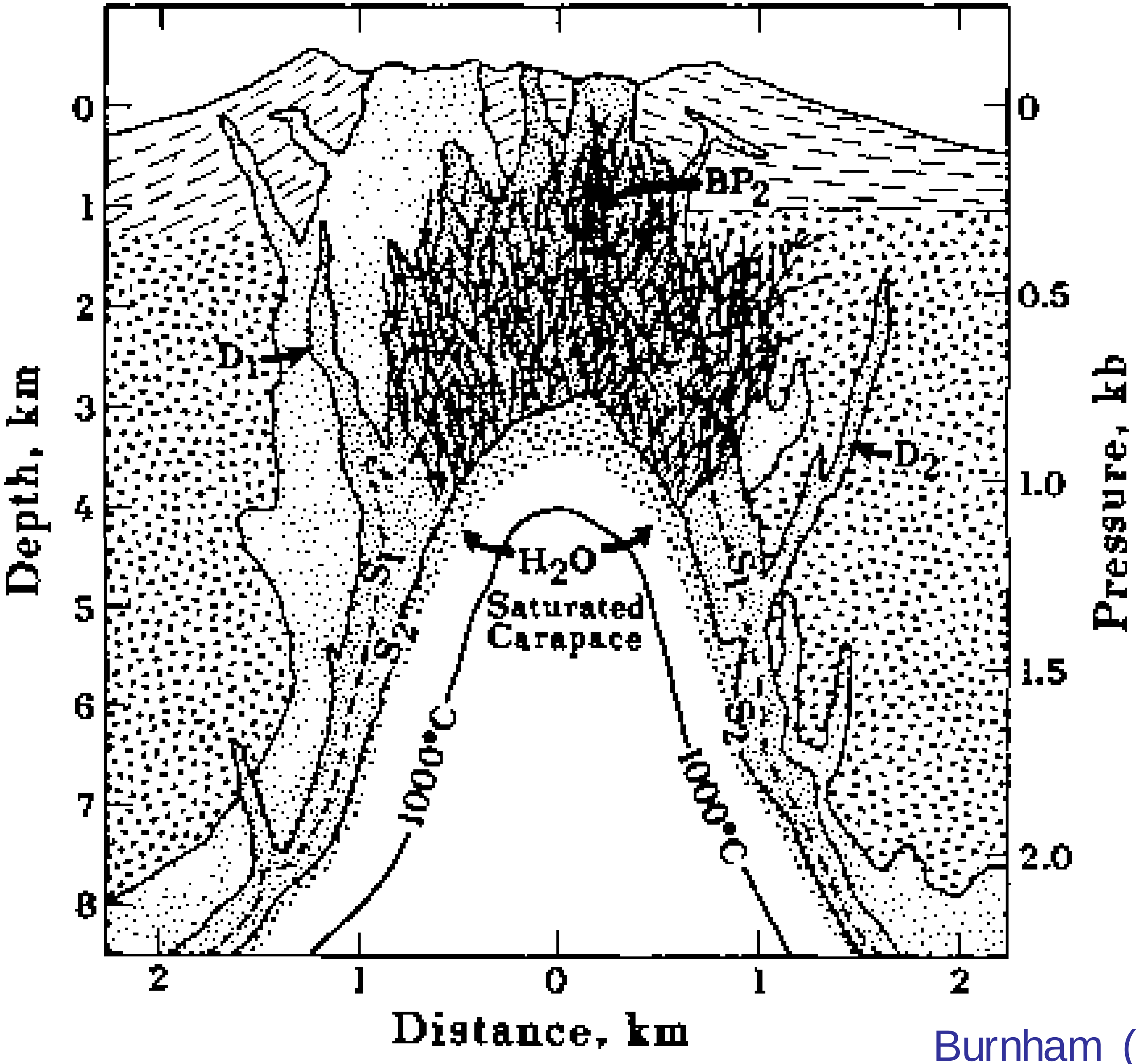

Burnham (1979)

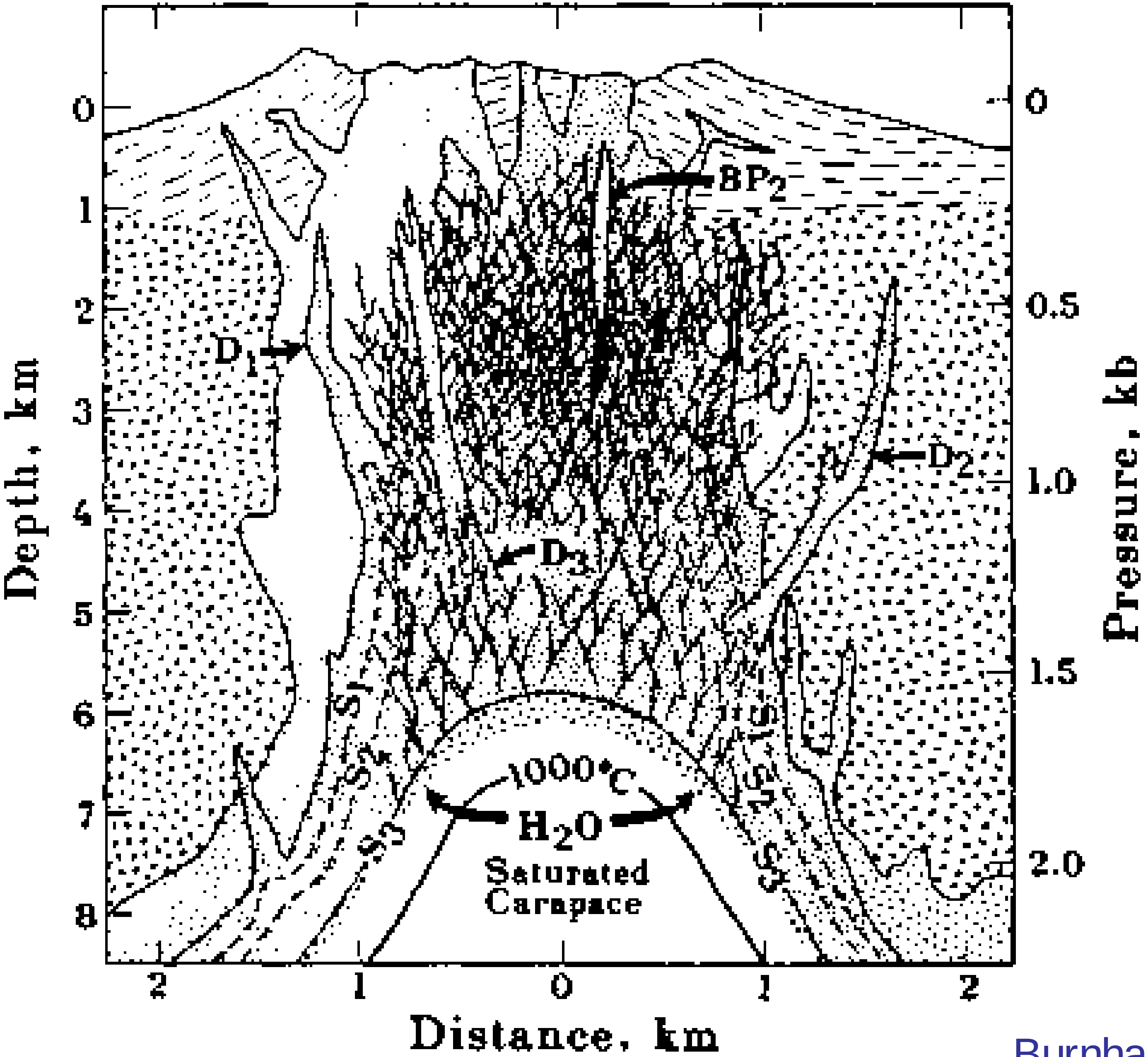

Burnham (1979)

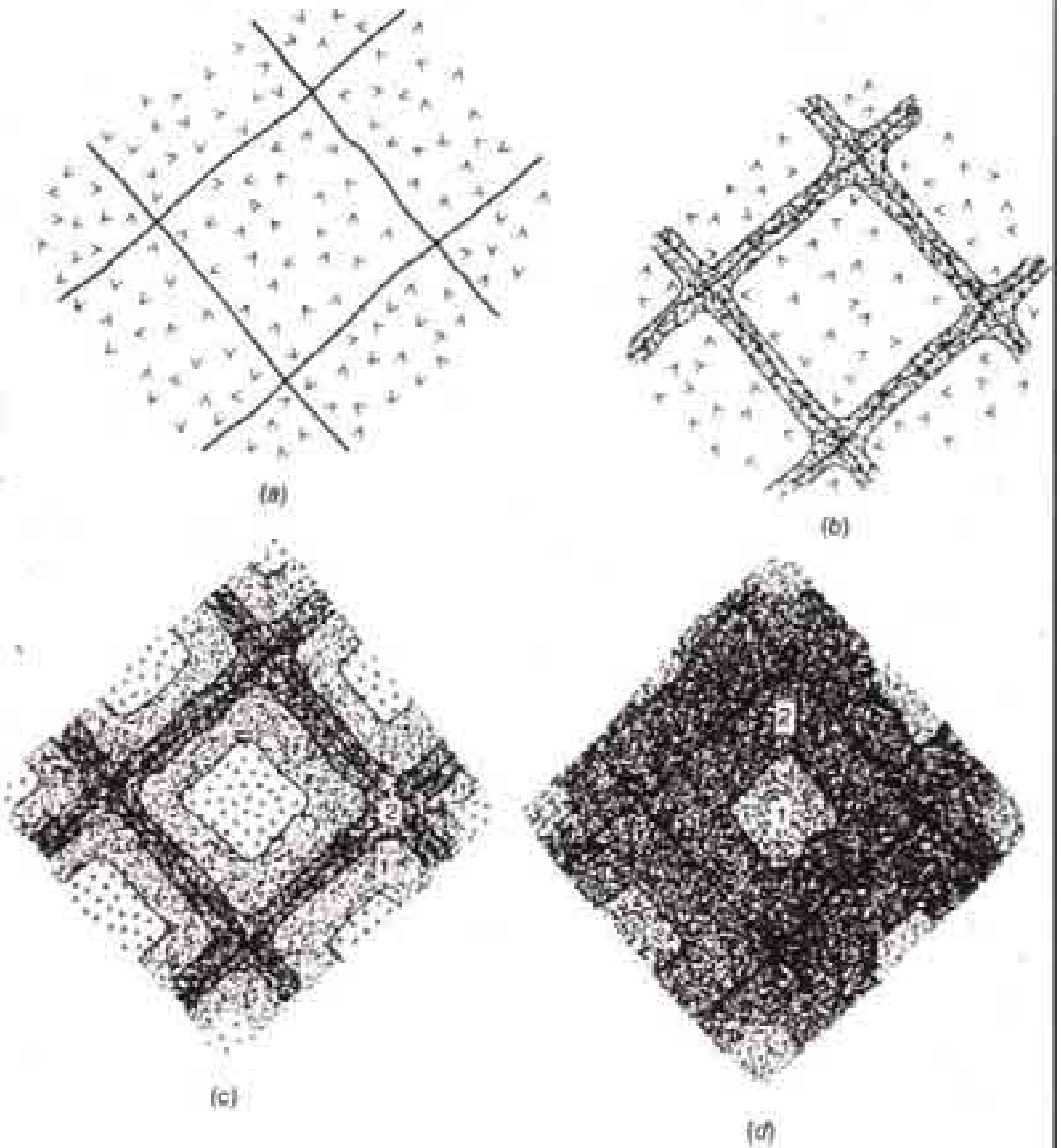

Entwicklungsmuster
Hydroth. Überprägung

Guilbert and Park
(1986), Fig. 5-8

Hydrothermal alteration

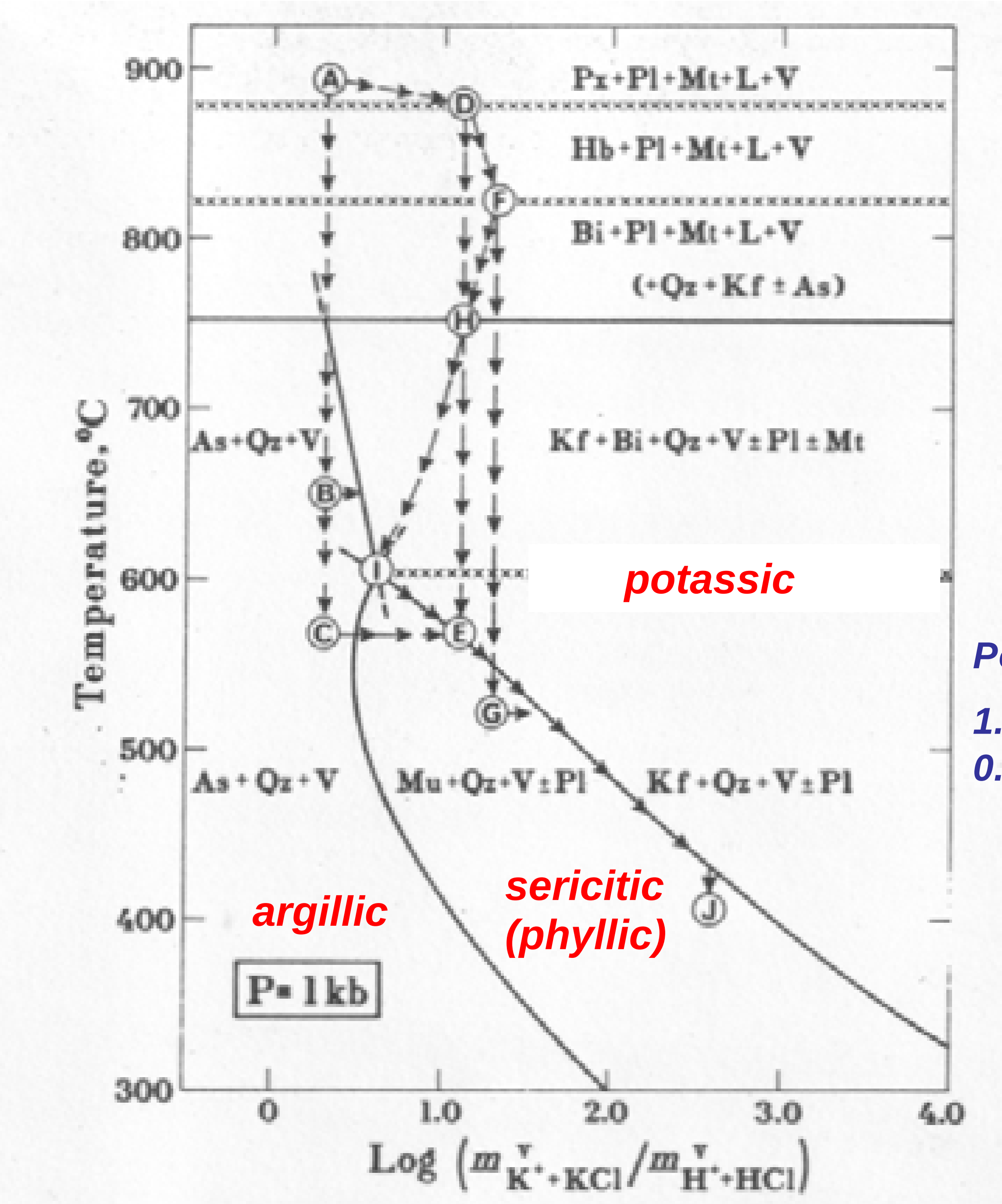

Potassic to phyllic:

$1.5\ KAlSi_3O_8 + H^+ = 0.5\ KAl_2AlSi_3O_{10}(OH)_2 + 3\ SiO_2 + K^+$

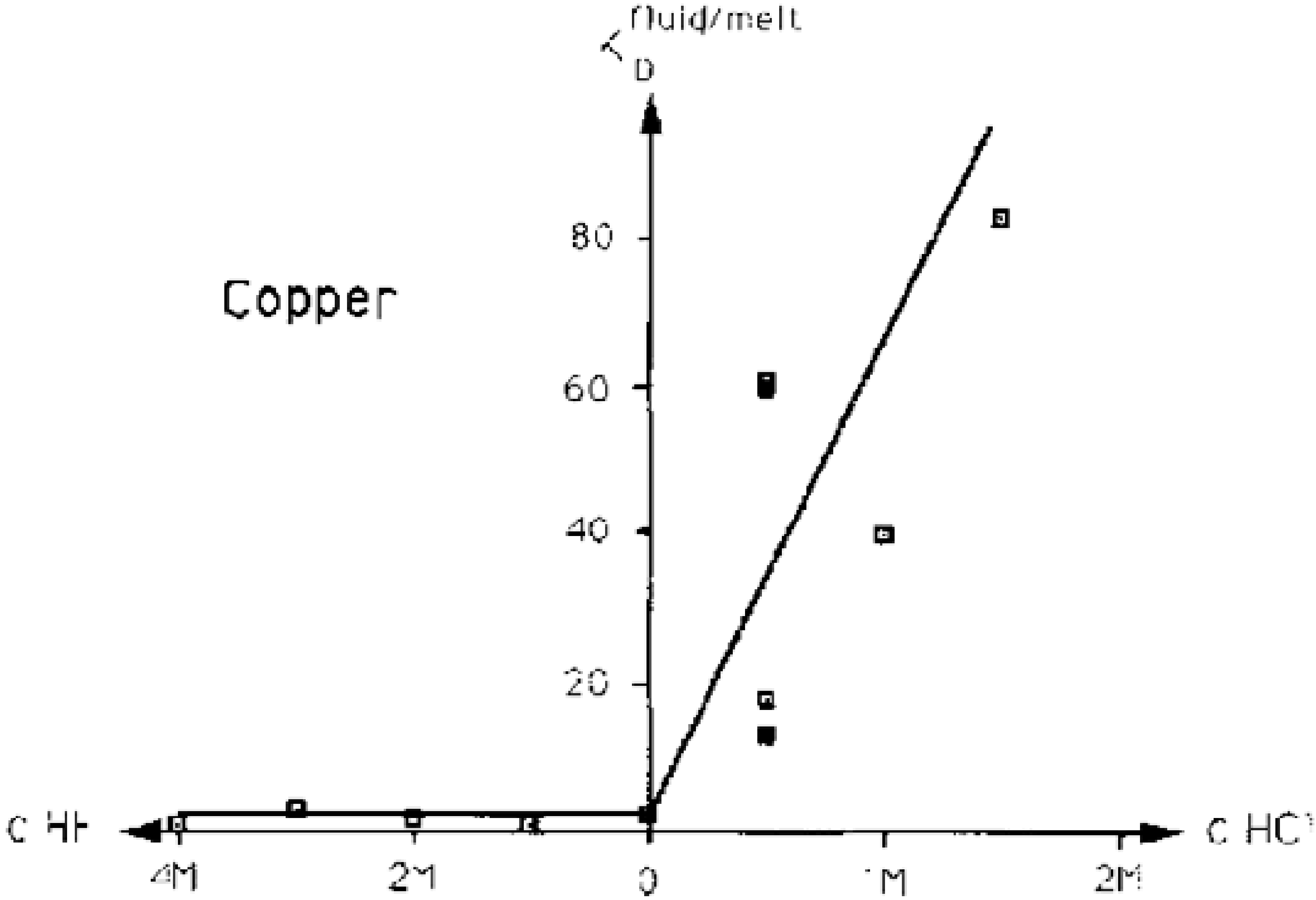

Partitioning of copper between melt and aqueous fluid in the system haplogranite-H_2O-HCl-HF at 2 kb, 750°C, Ni-NiO buffer. Keppler and Wyllie (1991) CMP 109: 141

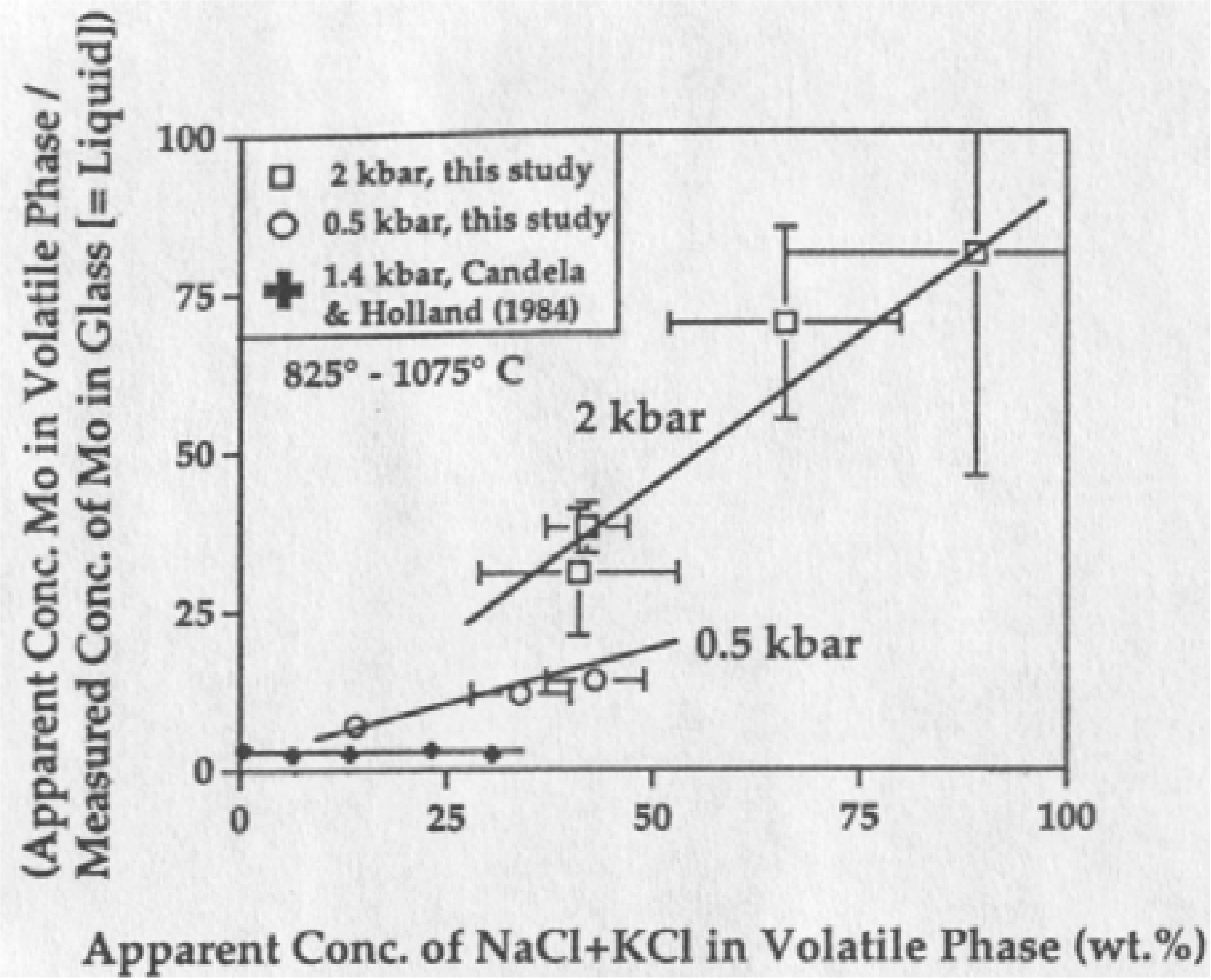

Molybdenum in saline aqueous fluid coxisting with granitic melt (glass)

Webster (1997) GCA 61: 1024

Melt-fluid partitioning of sulfur

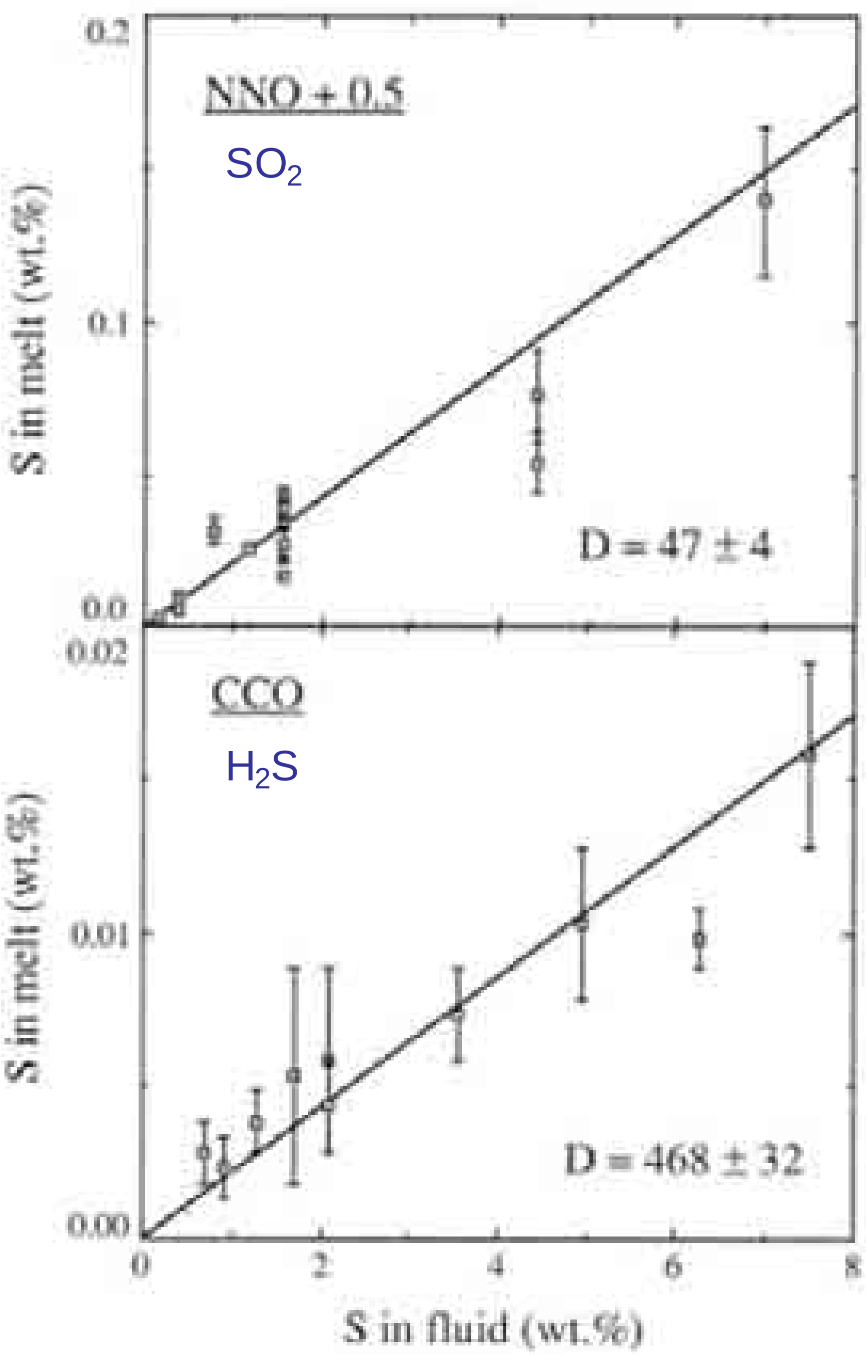

Fig. 1. Distribution of sulfur between haplogranitic melt and hydrous fluid at 2 kbar and 850°C. Oxygen fugacity in the experiments was 0.5 log units above the Ni-NiO buffer (NNO + 0.5) or equivalent to the Co-CoO buffer (CCO). Fluid/melt partition coefficients *D* were determined by linear regression.

Keppler (1999) Science 284: 1653

Heat and mass transport in pluton environments

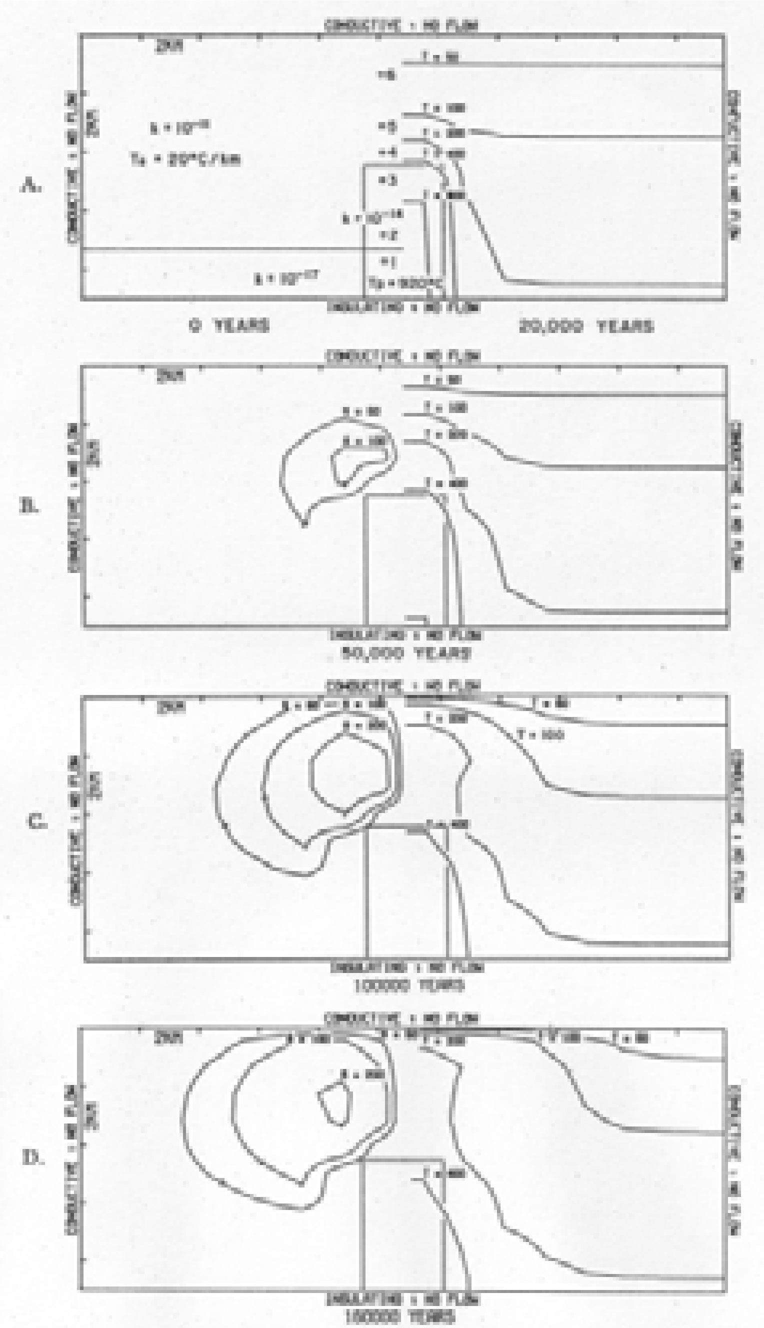

Cross section of model of convective fluid flow around a cooling pluton from 0 to 160,000 years: Temperature distribution (right) and steady-state dimensionless stream function (left).

Norton D, Knight J (1977) Am J Sci 277: 937-981

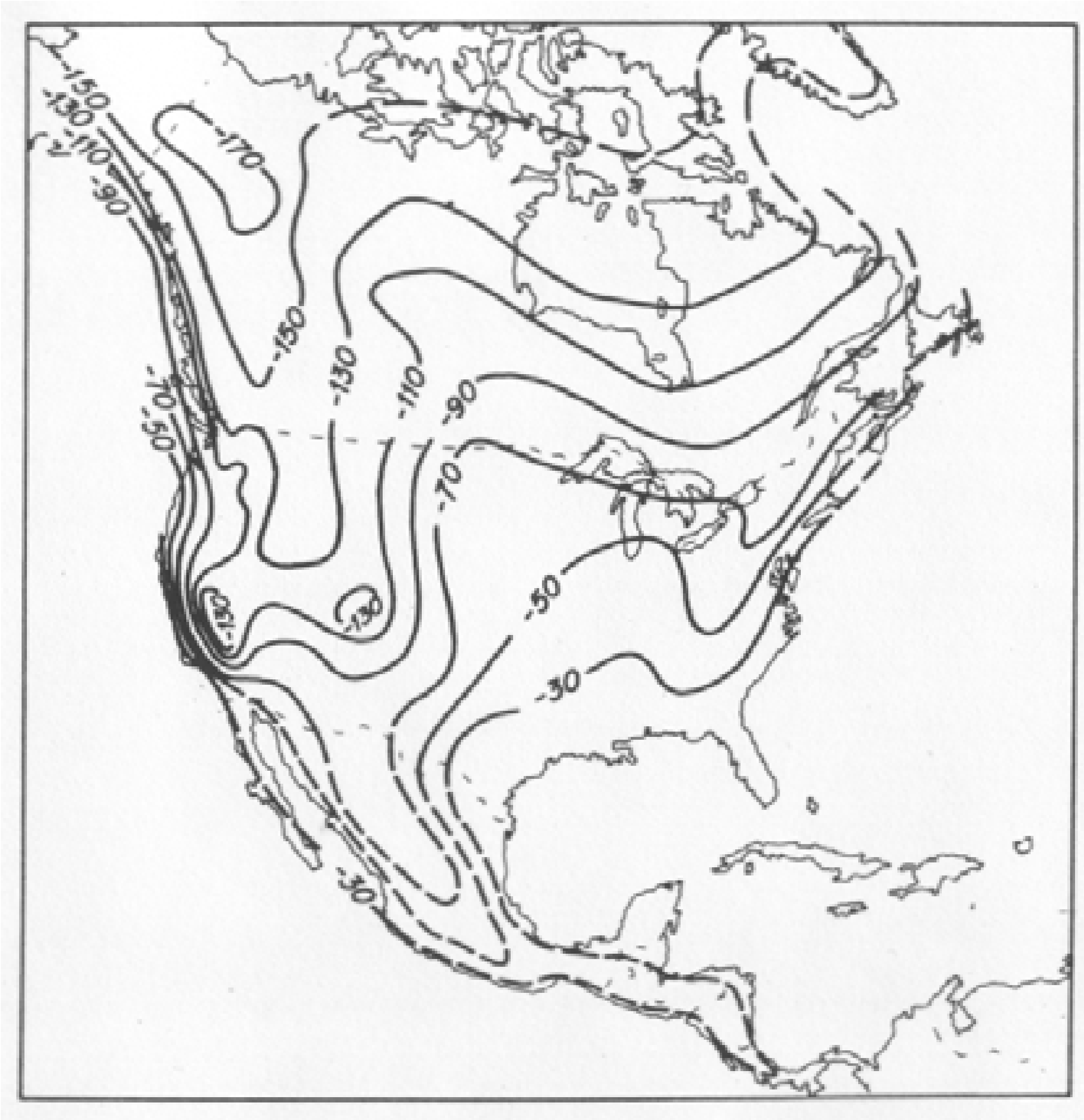

Stable isotope fractionation

Meteoric surface water: Map of δD values for North America

„Meteoric water line“:
$\delta D = 8\ \delta^{18}O + 10$ (per mil)

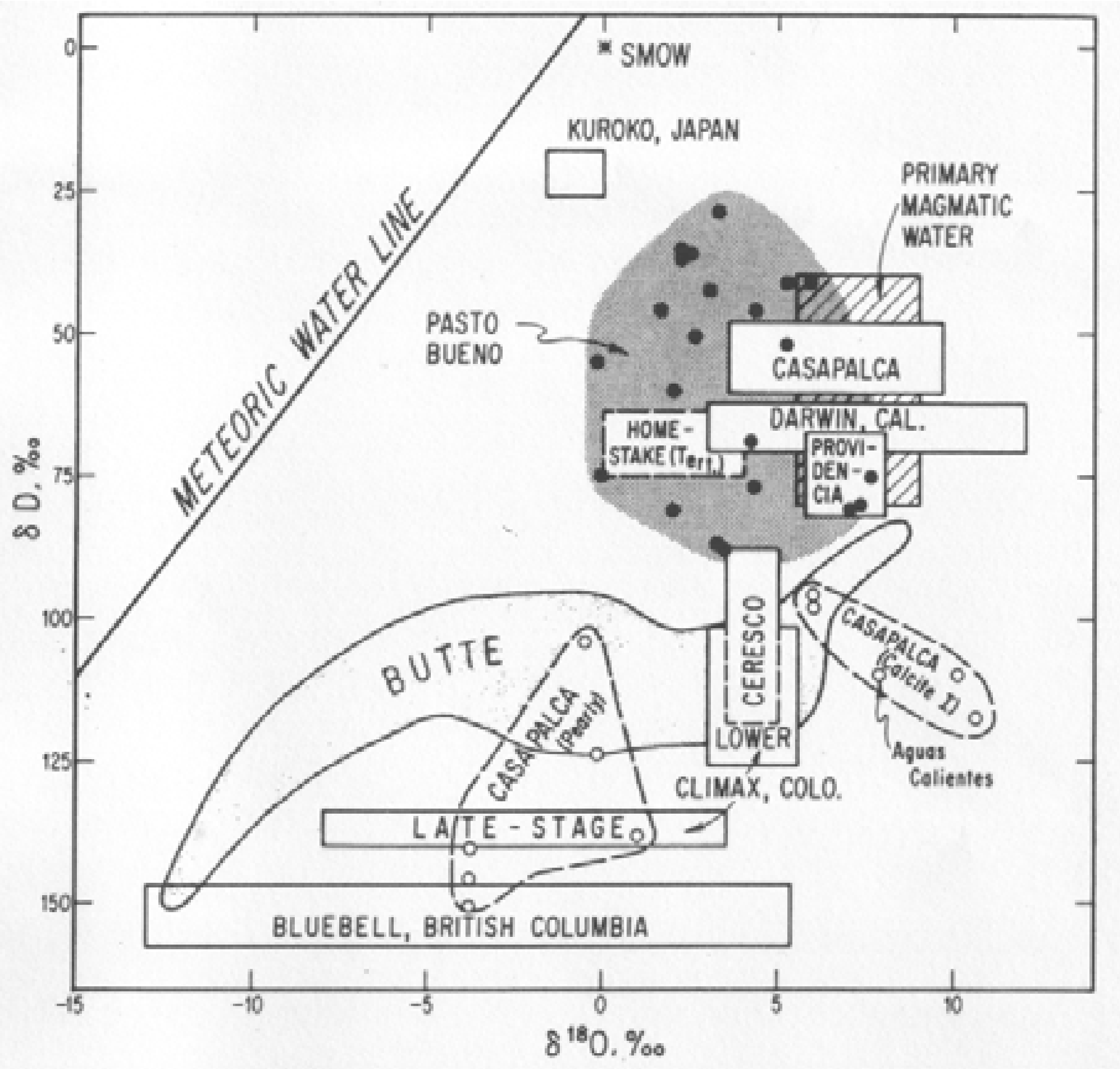

δD of fluid inclusions vs calculated $\delta^{18}O$ values of hydrothermal fluids in a variety of ore deposits

Taylor HP Jr (1979)

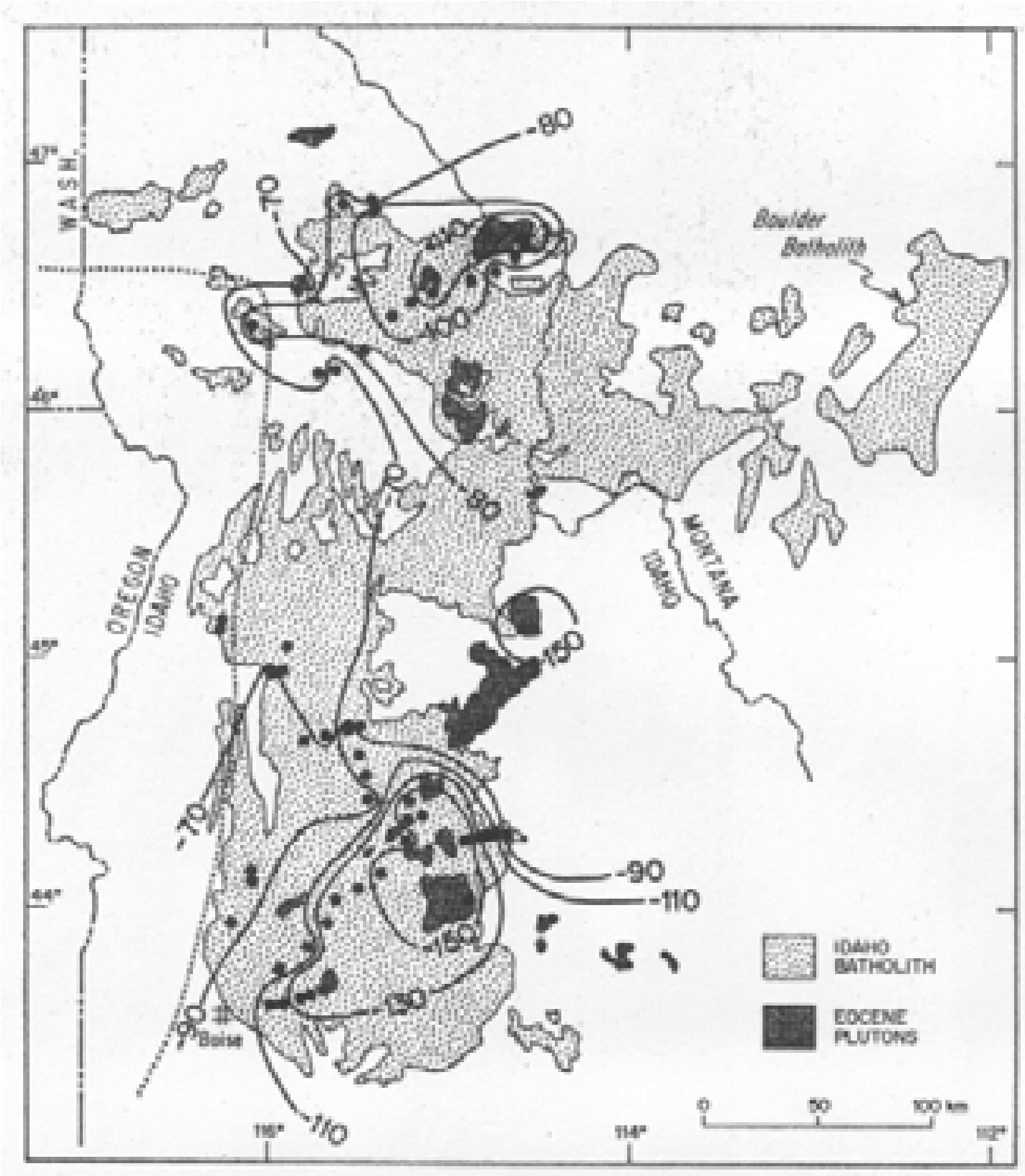

Idaho batholith with sampling localities (black dots) and δD contours for biotite and hornblende

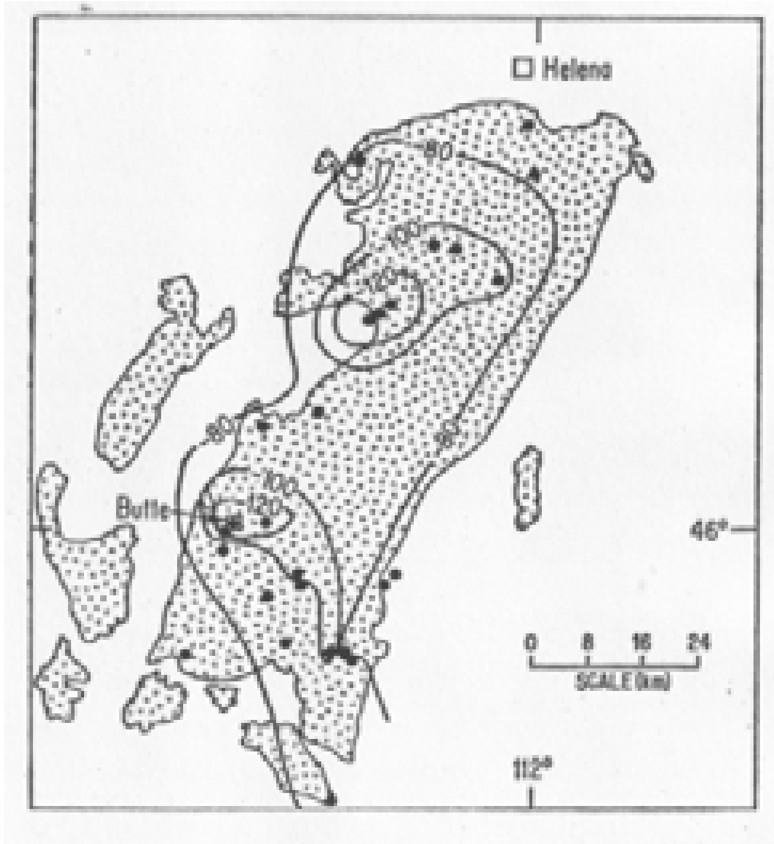

Boulder batholith
with sampling
localities (black dots)
and δD contours for
biotite and hornblende

Taylor HP Jr (1977) J geol Soc London
133: 509-558


Chuquicamata

Panguna (Papua New Guinea)

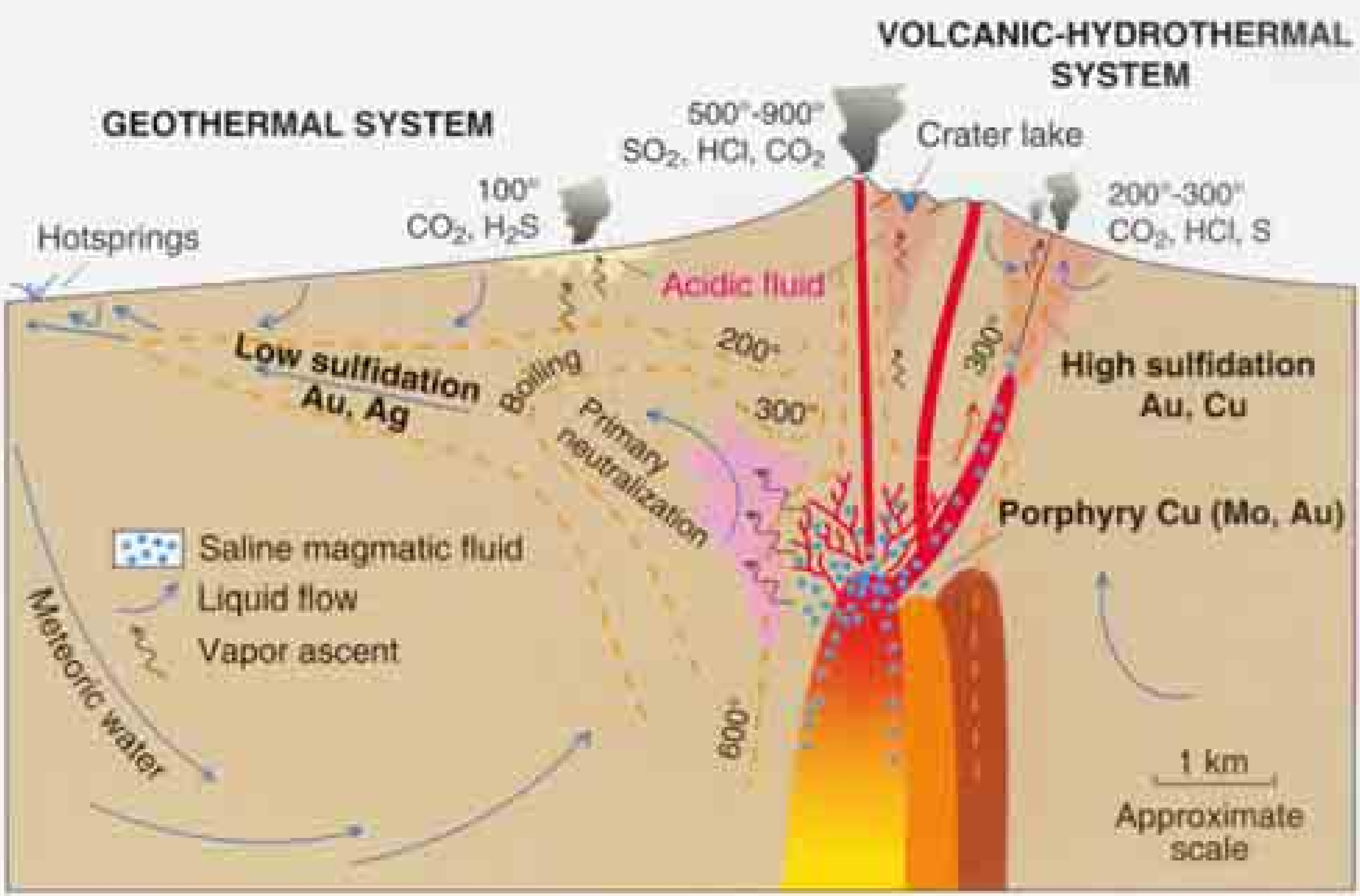

Fig. 1.1 Schematic cross-section showing shallow sub-volcanic intrusions and associated stratovolcano, and environments deduced for formation of porphyry Cu, and high- and low-sulfidation epithermal ore deposits [20,25]. Active volcanic-hydrothermal systems extend from degassing magma to fumaroles and acidic springs, and incorporate porphyry and/or high-sulfidation ore environments, whereas low-sulfidation ore deposits form from geothermal systems characterized by neutral-pH waters that may discharge as hot springs.

Hedenquist et al. (1996) Soc Res Geol Japan

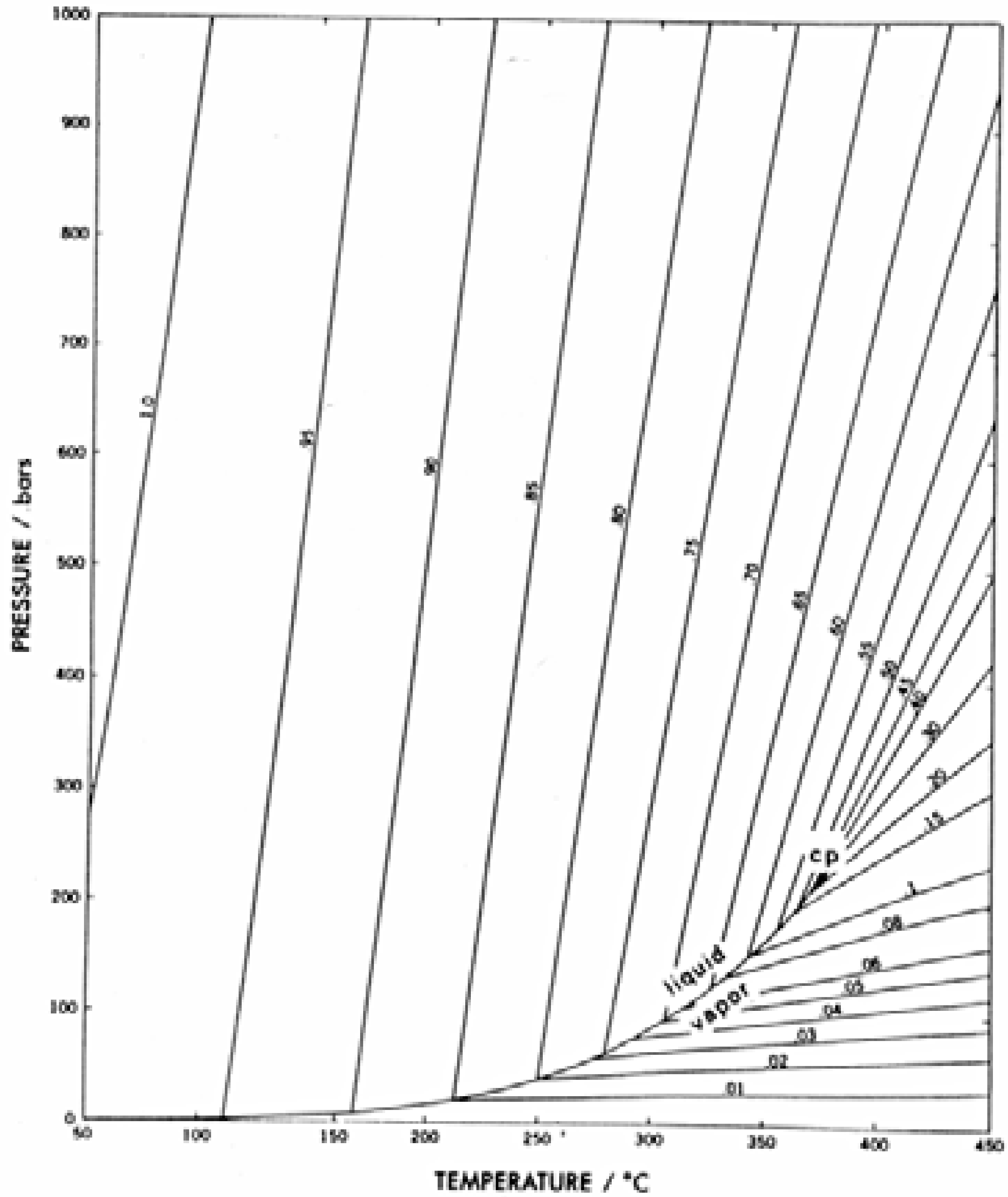
PRESSURE / bars
TEMPERATURE / °C
liquid
vapor
cp
1.0
.95
.90
.85
.80
.75
.70
.65
.60
.55
.50
.45
.40
.30
.20
.15
.1
.08
.06
.05
.04
.03
.02
.01

Water

Solubility of quartz in water

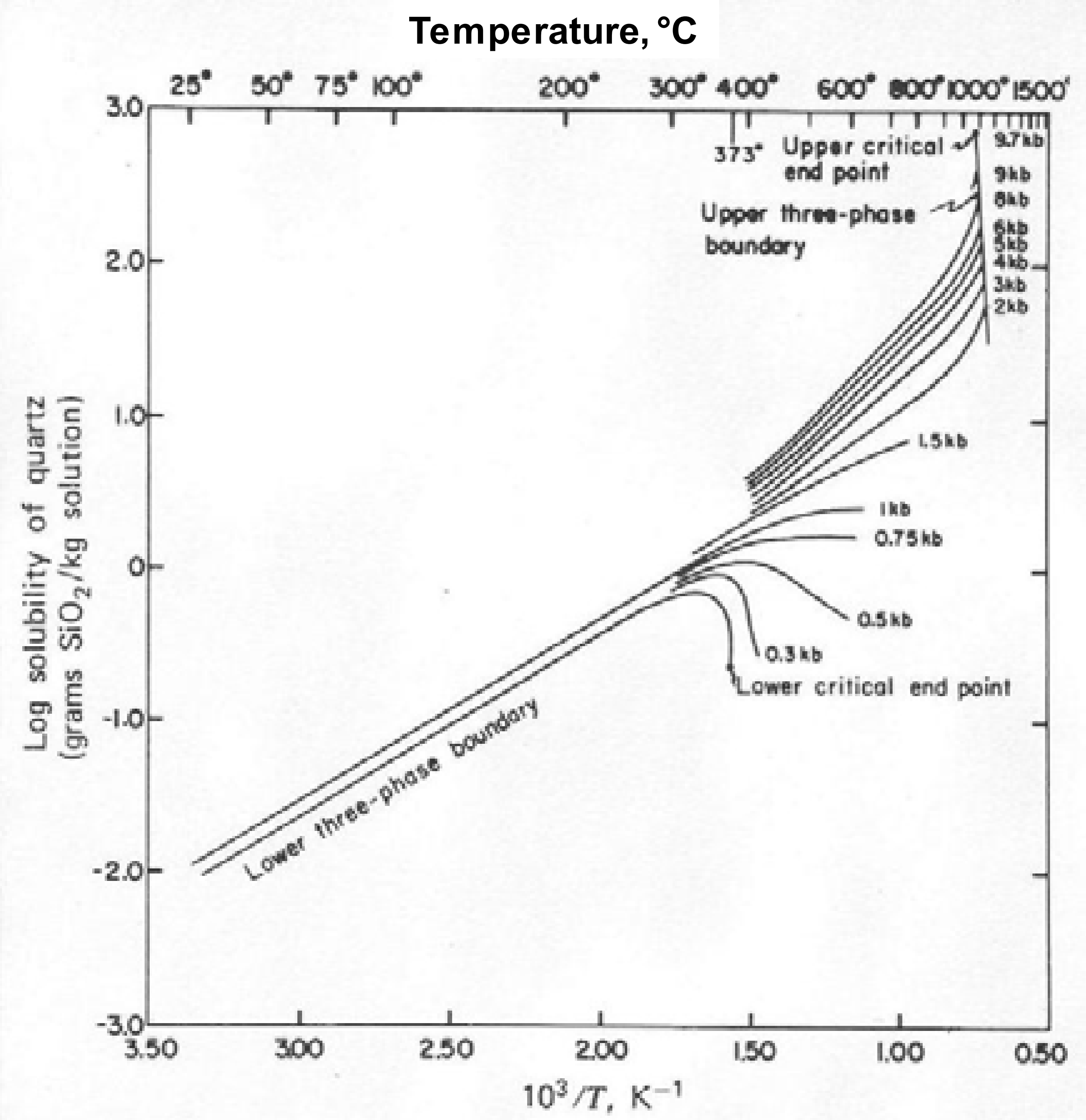

COPPER WORLD MINE PRODUCTION 2008 (15.7 Mt)

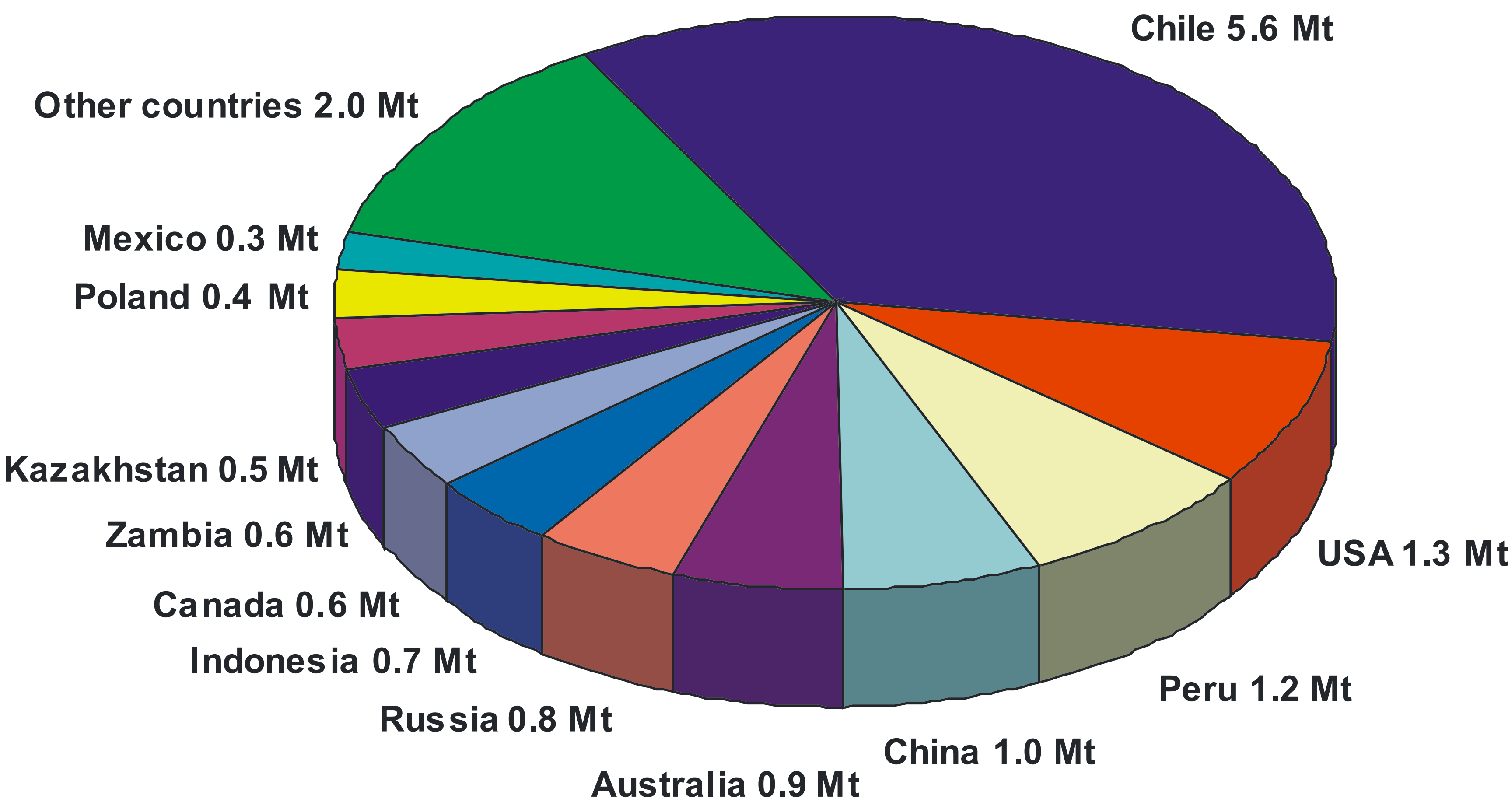

Seafloor spreading in the Pacific

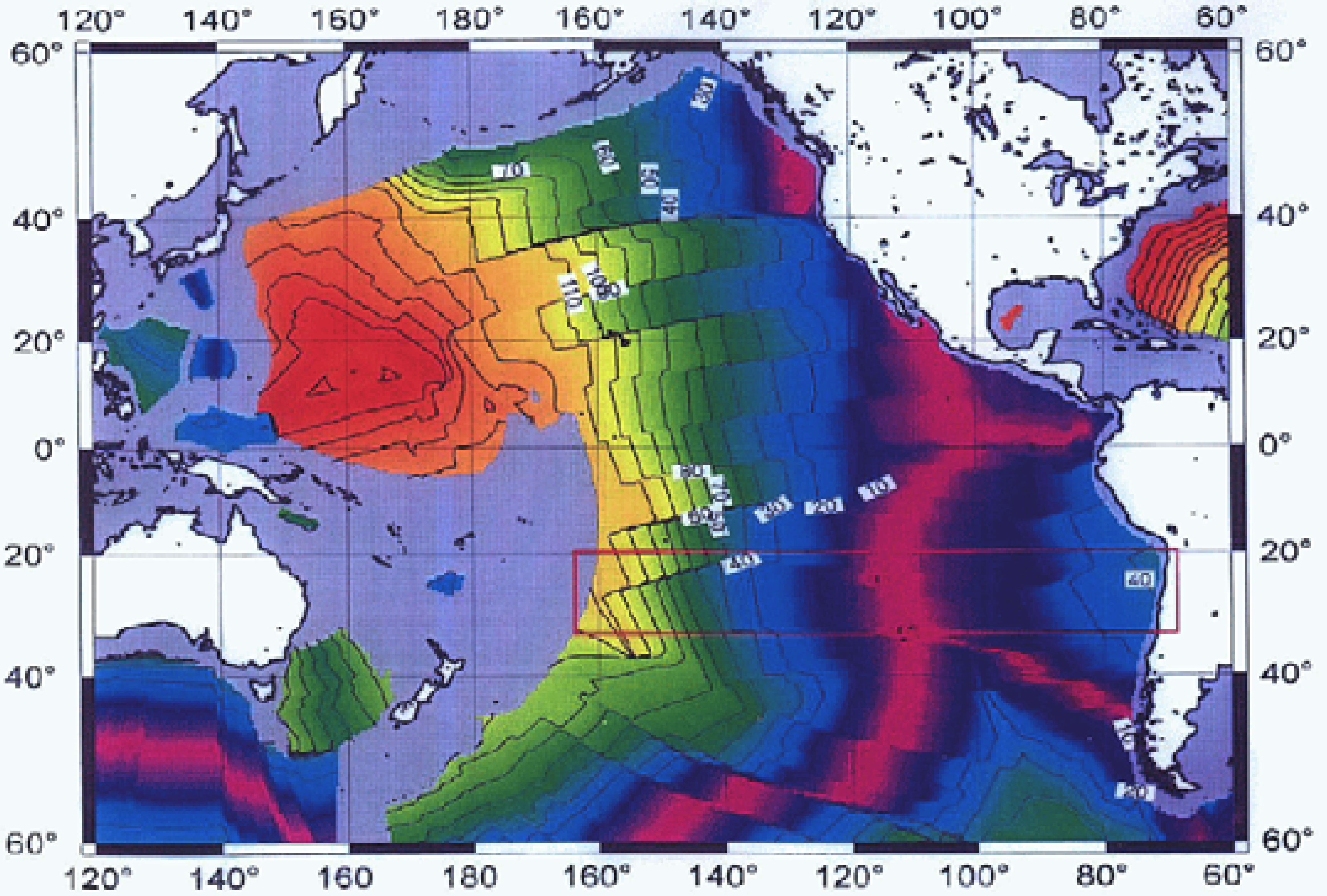

Mueller et al 1997

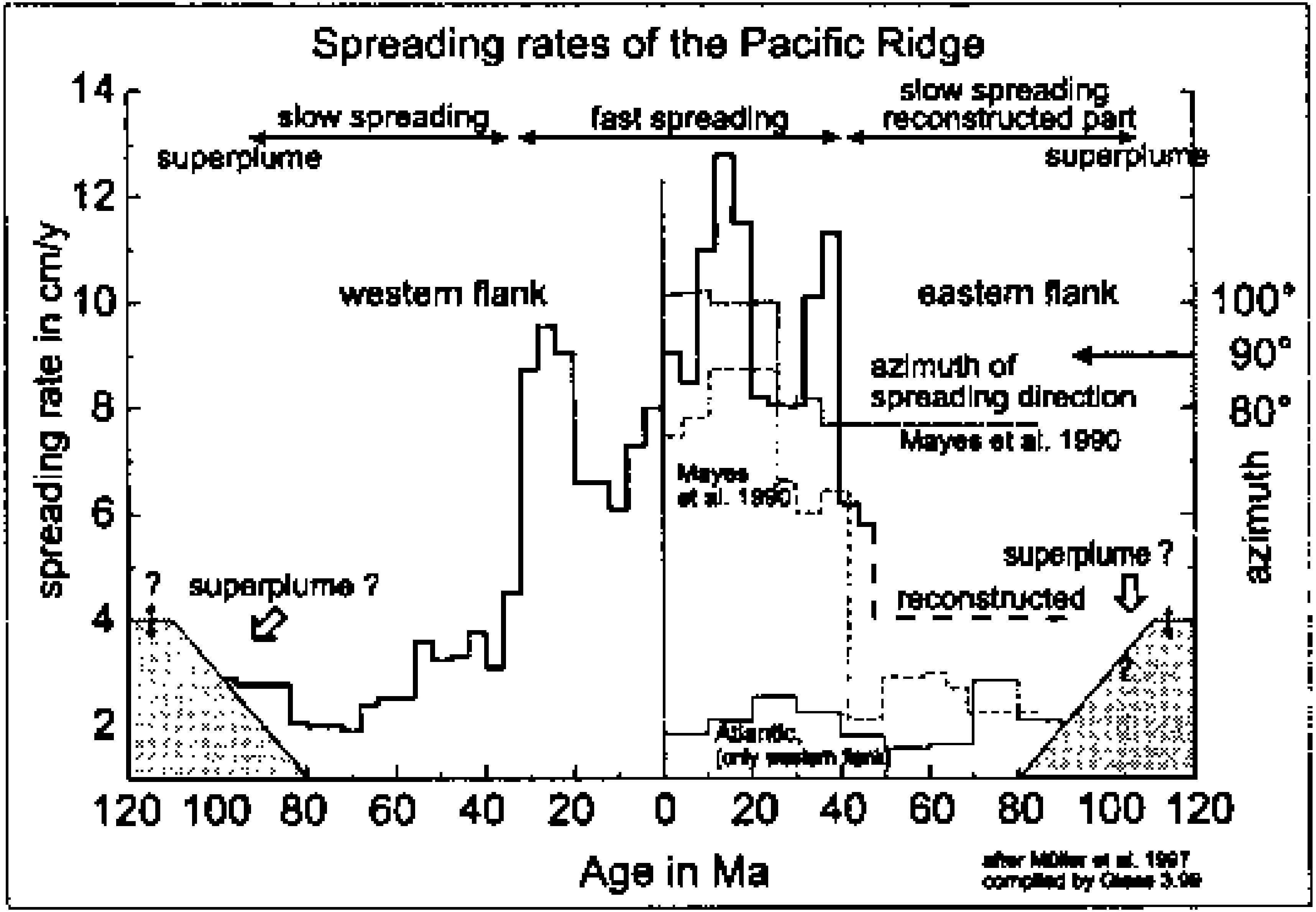

Giese et al. (1999) Ext Abstr 4th ISAG, p. 274

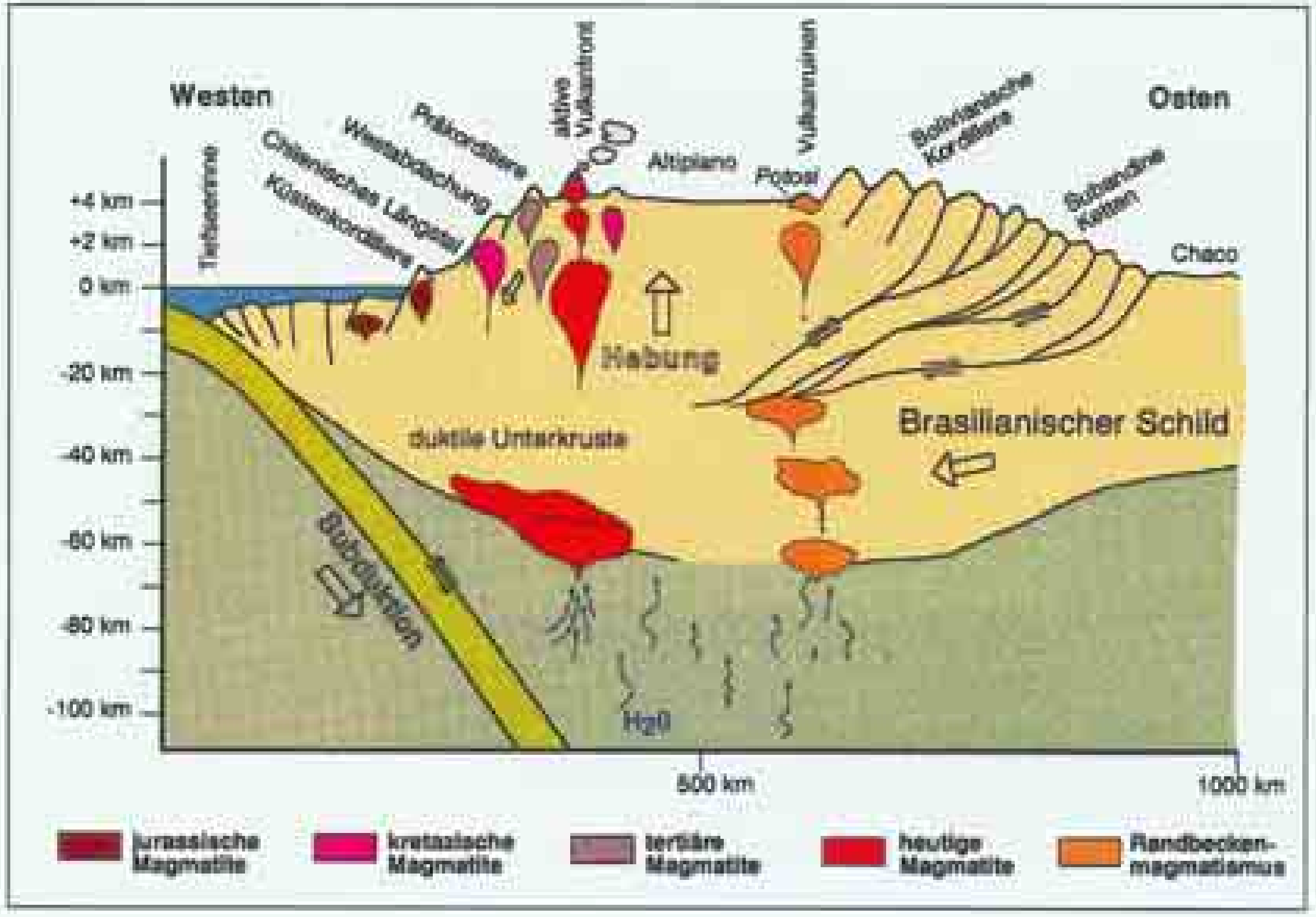

Abb. 2: Ein Querschnitt durch die zentralen Anden auf der Höhe von Arica veranschaulicht die wahrscheinliche Ursache der Gebirgsbildung. Durch das stetige Hineinpumpen von Magma in den Rand des Kontinents wurde die Unterkruste duktil, so daß sich von Osten her der kalte (und damit steifere) Brasilianische Schild in diese hineinschieben konnte und dabei die Oberkruste des Kontinentalrandes nach oben drückte. Als Folge dieser Hebung kam es im Westen zu gewaltigen Abschiebungen und im Osten zum Ausfließen eines verschuppten Deckenstapels auf das Vorland des Gebirges. Die Abbildung ist nicht maßstäblich und nichtlinear überhöht.

Seyfried et al (1994) Jb Univ Stuttgart: 60-71

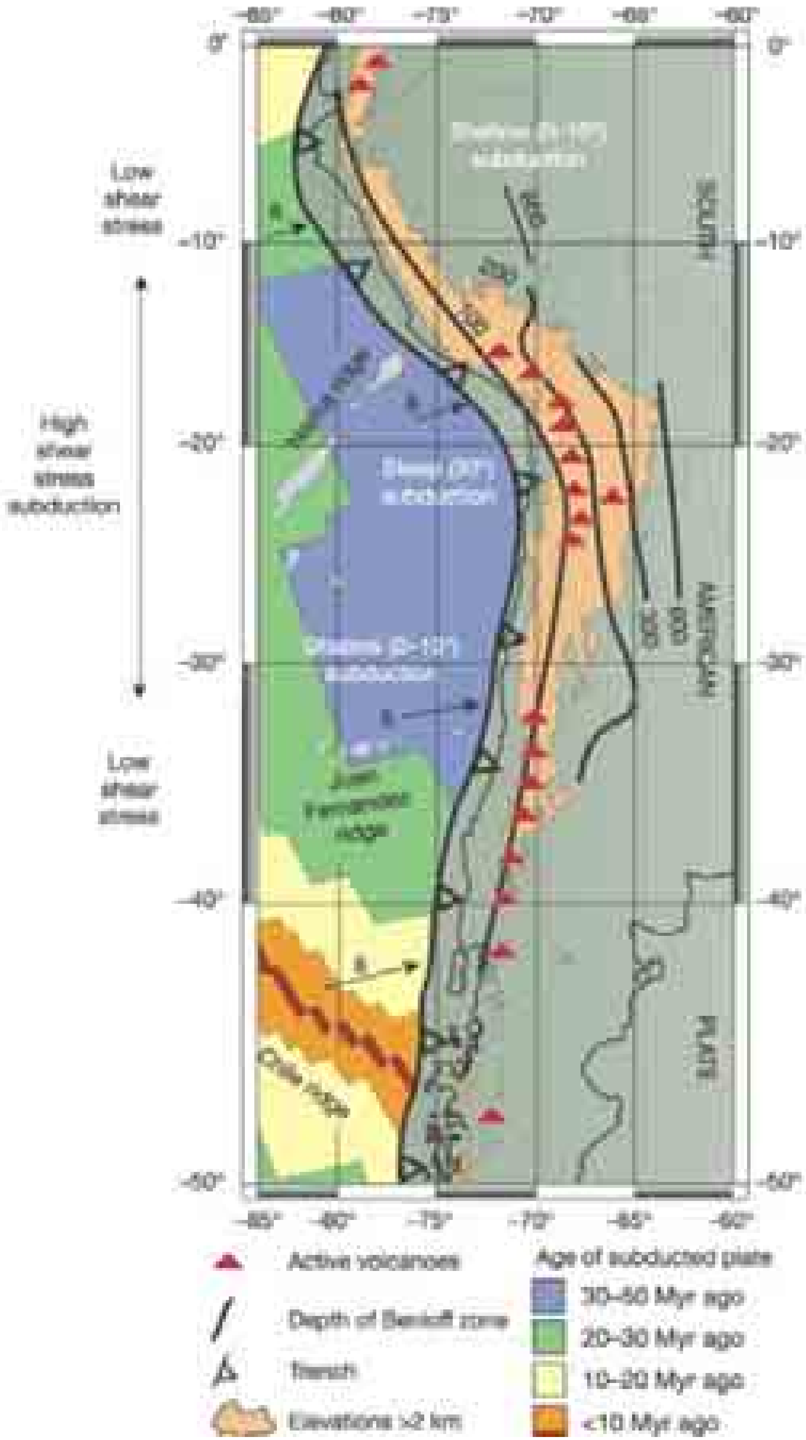

At 24°S:
13 km elevation contrast
from trench to high Andes

Lamb and Davis (2003)
Nature 425: 792-797

Peru–Chile current system and oceanic upwelling: sea surface temperatures July 2002, National Oceanographic Data Center

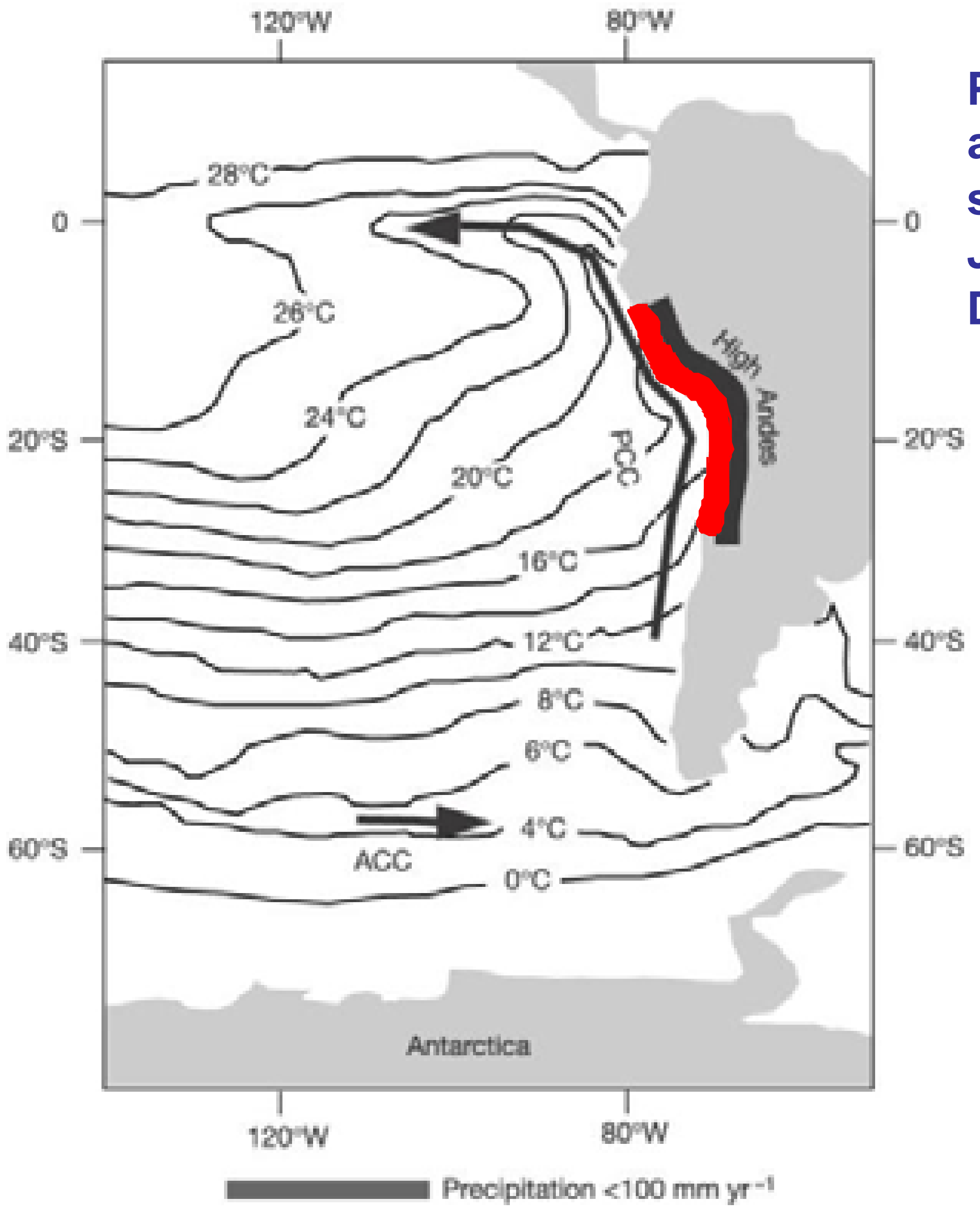

Lamb and Davis (2003)
Nature 425: 792-797

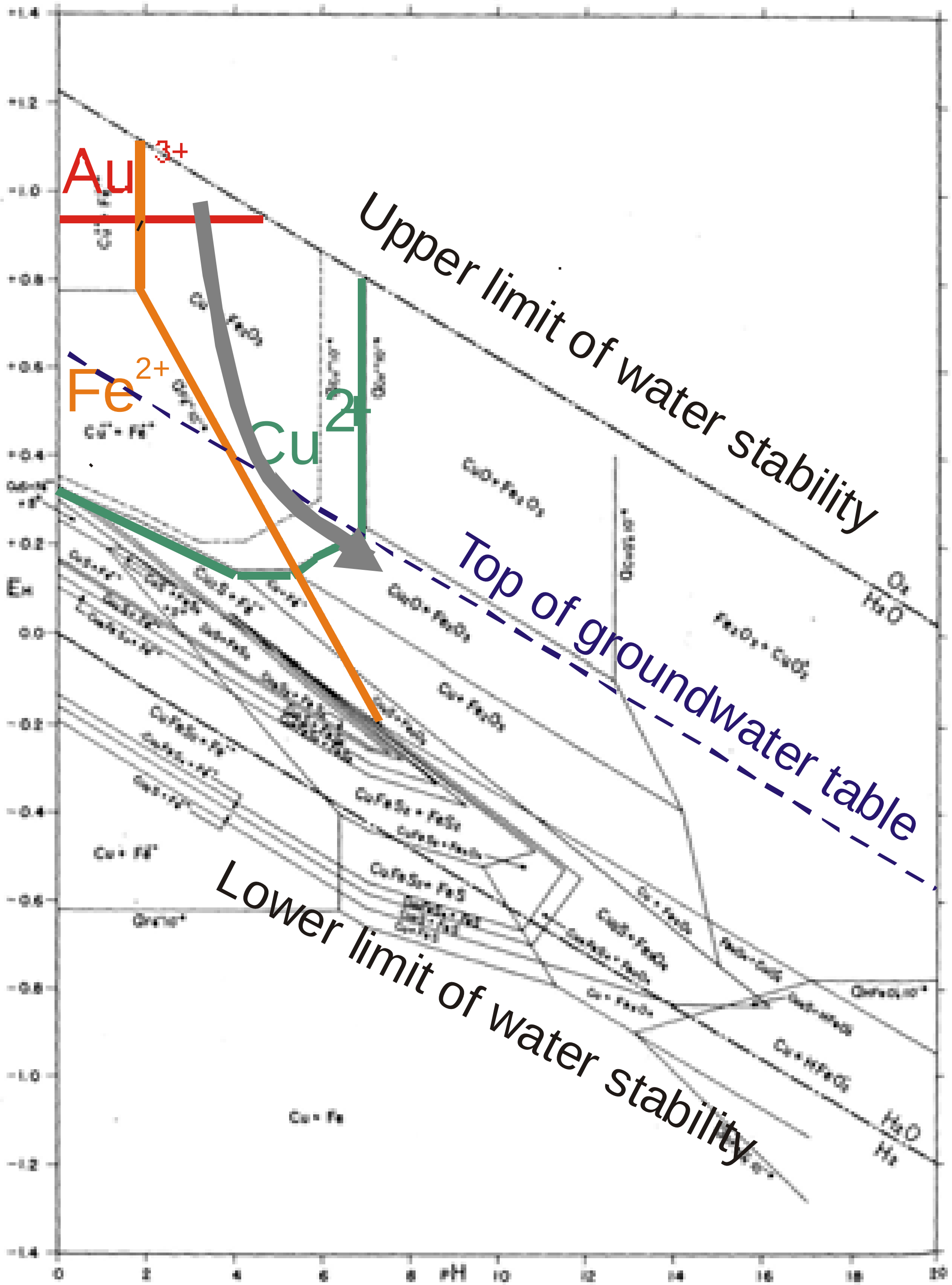

Supergene enrichment

Dissolution of Cu by rain water and precipitation at the groundwater table

The system Cu-Fe-S-O-H at 25°C and 1 bar.
Total dissolved sulfur = 10^{-4} m
From Garrels and Christ (1965: 231)

The colored solubility limits of Au^{3+}, Fe^{2+} and Cu^{2+} are drawn at 10^{-6} m Fe (56 ppb Fe), 10^{-6} m Cu (64 ppb Cu) and 10^{-8} m Au (2 ppb Au).

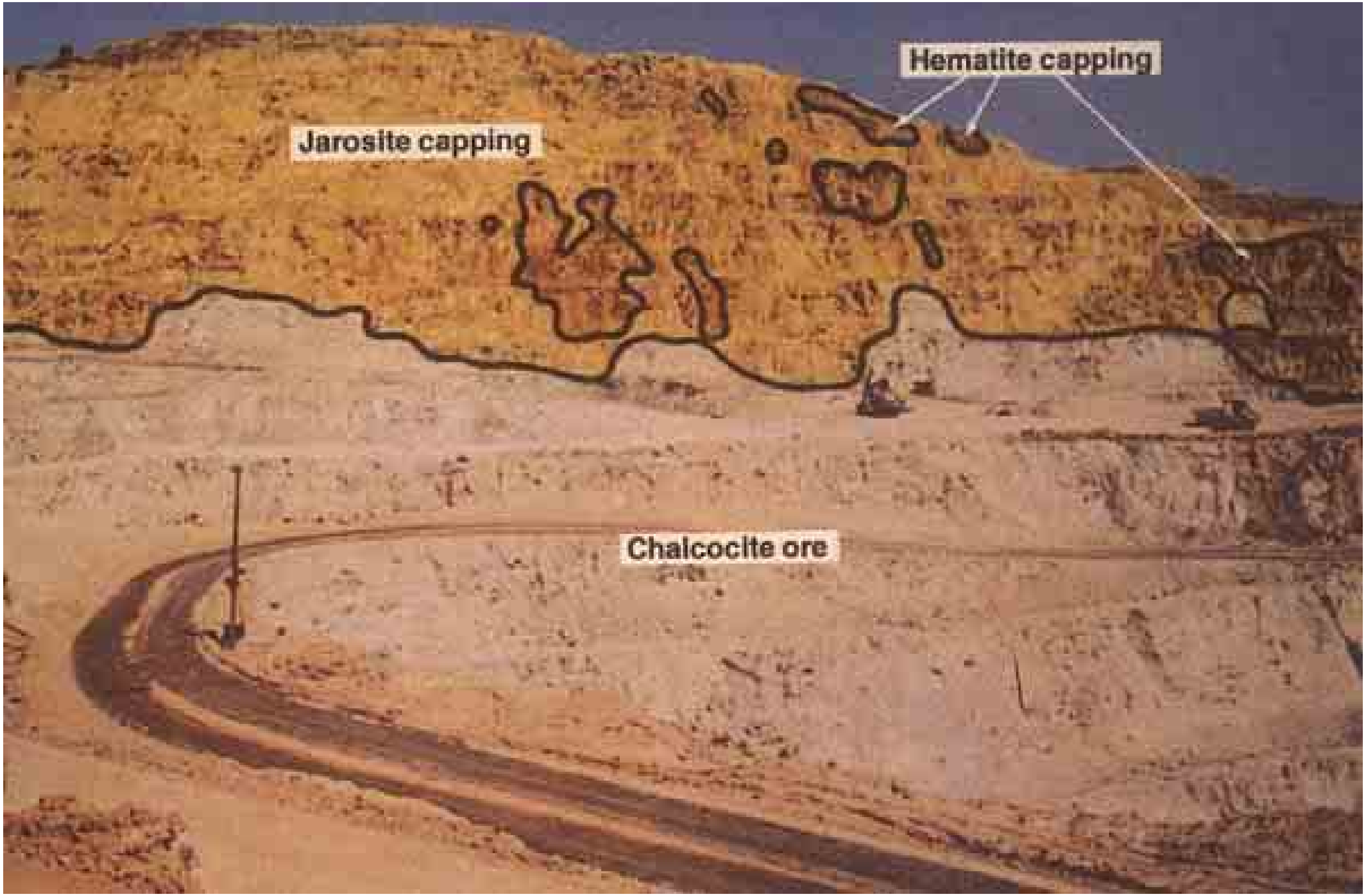

Leached capping at Butte, Montana
Anderson, in: Titley, ed., 1982

Leached capping at Chino (Santa Rita), New Mexico, USA
Anderson, in: Titley, ed., 1982

Radomiro
Tomic

Chuqui

MM

Calama

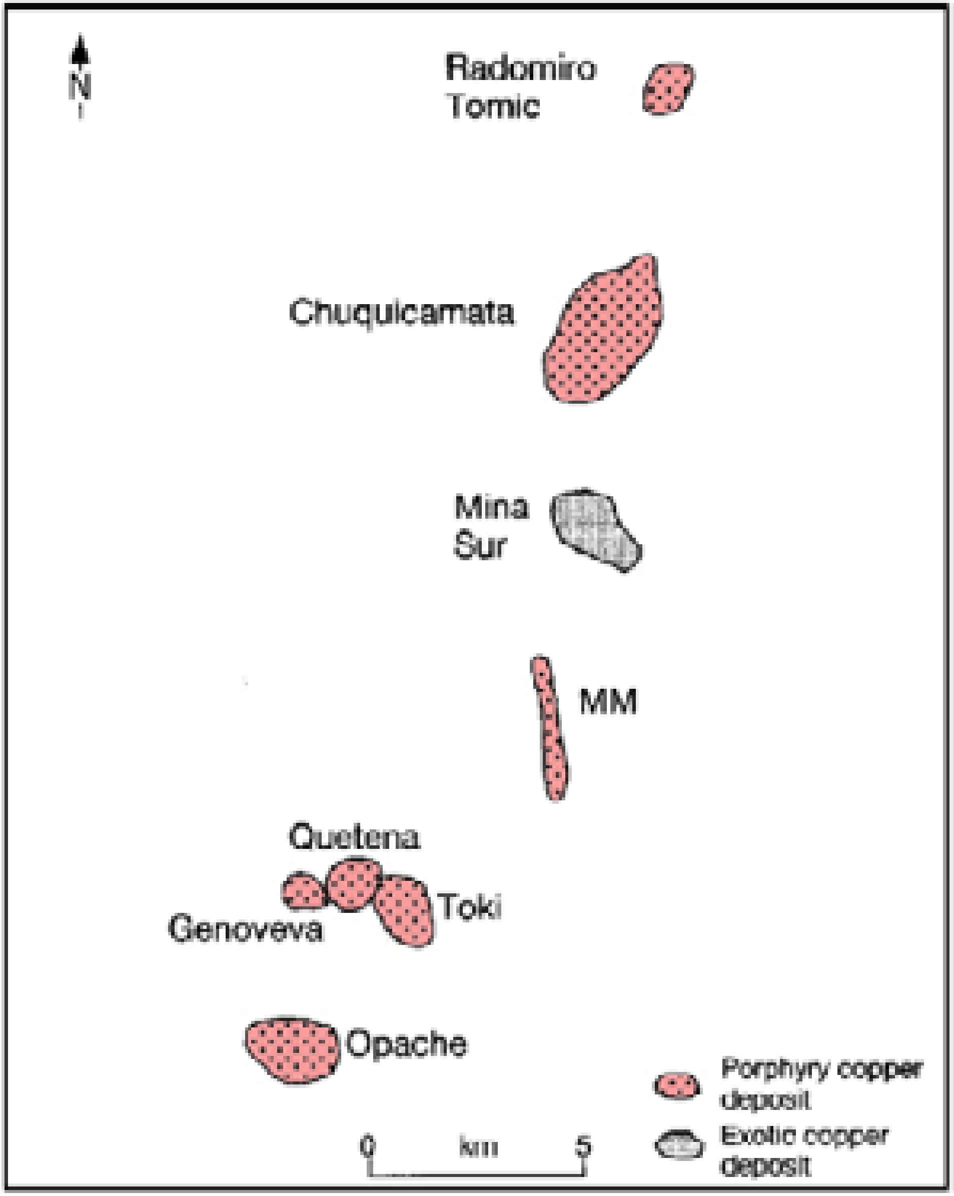

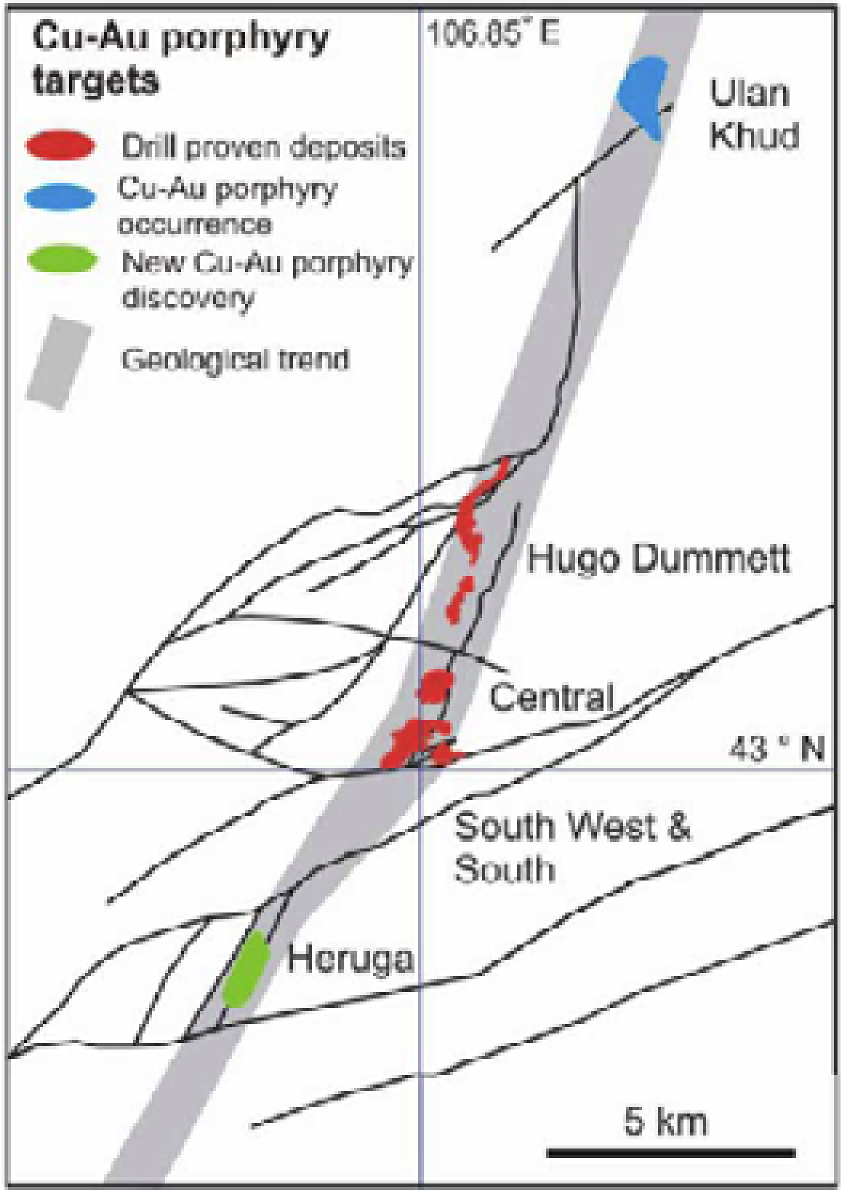

Chuquicamata ore cluster, Chile

Oyu Tolgoi ore cluster, Mongolia

**Chuqui-
camata,
Chile**

350.000 t
ore with
1 % Cu=
~3.500 t
Cu/day

+
350,000 t
waster


Chuquicamata
smelter: SO_2↑

Chuquicamata open pit in 2003: 2 x 3 km wide, 810 m deep. Total metal value: 45 billion USD
Historic mining: 1.5 Gt @ 1.5 % Cu + 0.07 % Mo. Reserves: 1.3 Gt @ 0.6-0.7 % Cu.
Current production/day: 350,000 t ore (1.0-1.1 % Cu + 200 g/t Mo+Re) plus 350,000 t waste.


Collahuasi, Chile


Quebrada Blanca, Chile

141°E
THE FLY RIVER CATCHMENT
PAPUA NEW GUINEA
IRIAN JAYA
INDONESIA
Ok Tedi (460 Mt @ 0.72 % Cu, 0.7 ppm Au
Grasberg
1.2 Gt @
1.4 % Cu,
1.5 ppm Au
TABUBIL
PORT
MORESBY
5°S
10°S
DARWIN
N
0 100 200 300 400 500
SCALE IN KILOMETRES

OK Tedi pit 1994

OK Tedi pit 1994

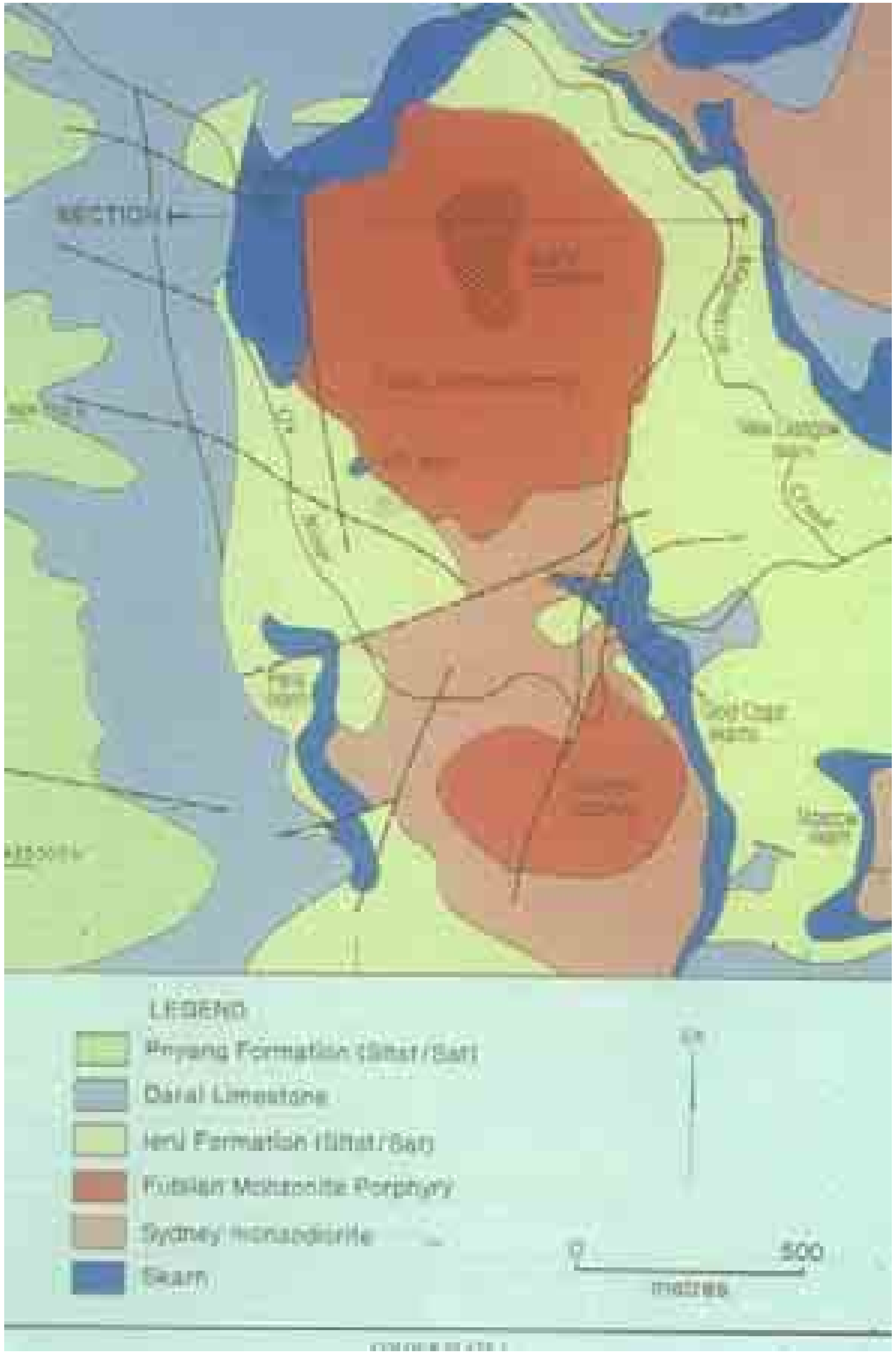
SECTION
LEGEND
Pnyang Formation (Sltst / Sst)
Darai Limestone
Ieru Formation (Sltst / Sst)
Fubilan Monzonite Porphyry
Sydney Monzodiorite
Skarn
0
500
metres

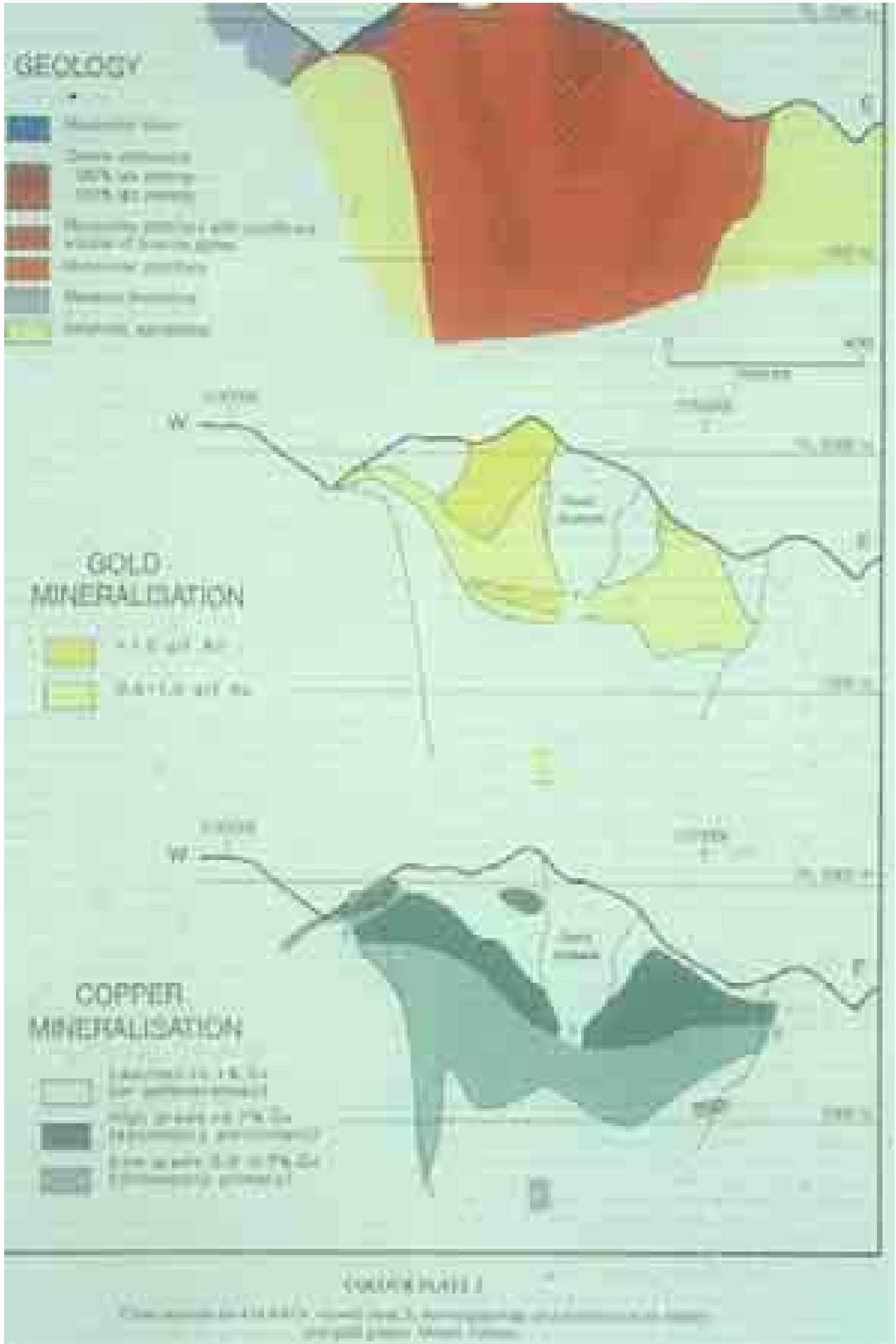

Ok Tedi/
Papua New Guinea

460 Mt @ 0.72 % Cu,
0.7 g/t Au

Gossan ore:
30 Mt x 3 g/t Au =
90 t Au
~ 2.5 billion USD

Secondary enrich-
ment zone:
265 Mt x 0.82 % Cu =
2 Mt Cu
~ 14 billion USD

265 Mt x 0.65 g/t Au =
170 t Au

Protore:
0.2-0.4 % Cu
0.3-0.5 g/t Au

Davies et al. (1978)
Econ Geol 73: 796-
809

OK Tedi „Erodible dump“ main site (1994)

OK Tedi „Erodible dump“ (1994)

OK Tedi „Erodible dump“

OK Tedi river near Tabubil

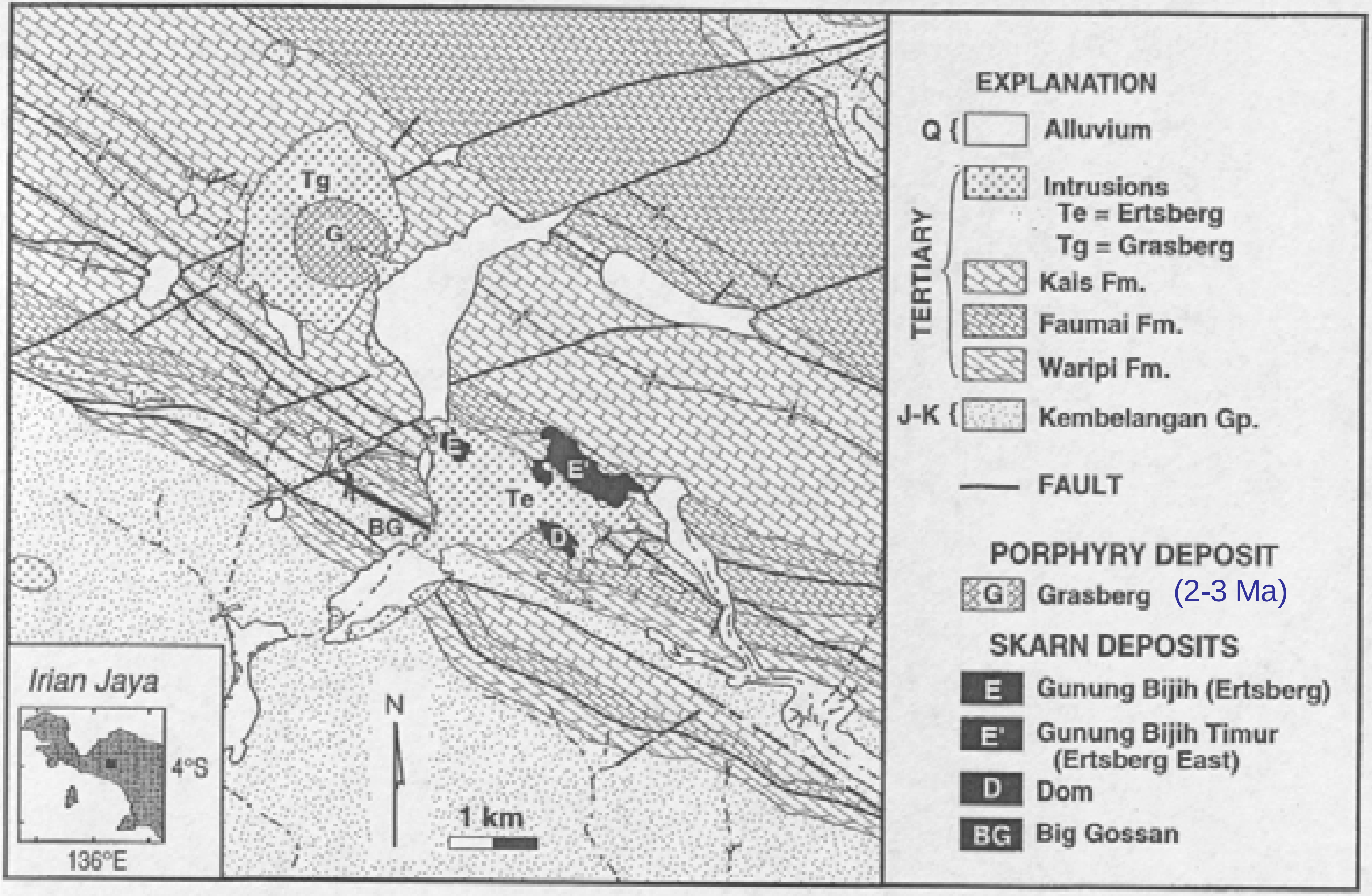

FIG. 2. Geologic map of the Ertsberg district showing locations of ore deposits. Generalized from 1:10,000 mapping of Freeport Indonesia geologists from 1970–1996. Limited areas of glacial ice are omitted from the northeastern part of the area.

Grasberg road (Aug 99)

Grasberg road (Aug 99)

Grasberg (Aug 99)

Grasberg (Aug 99)

Grasberg, Irian Jaya, Indonesia (Aug 1999): 3.5 Gt @~1 % Cu, ~1 g/t Au

Grasberg Open Pit

View Looking South

October 9, 2003

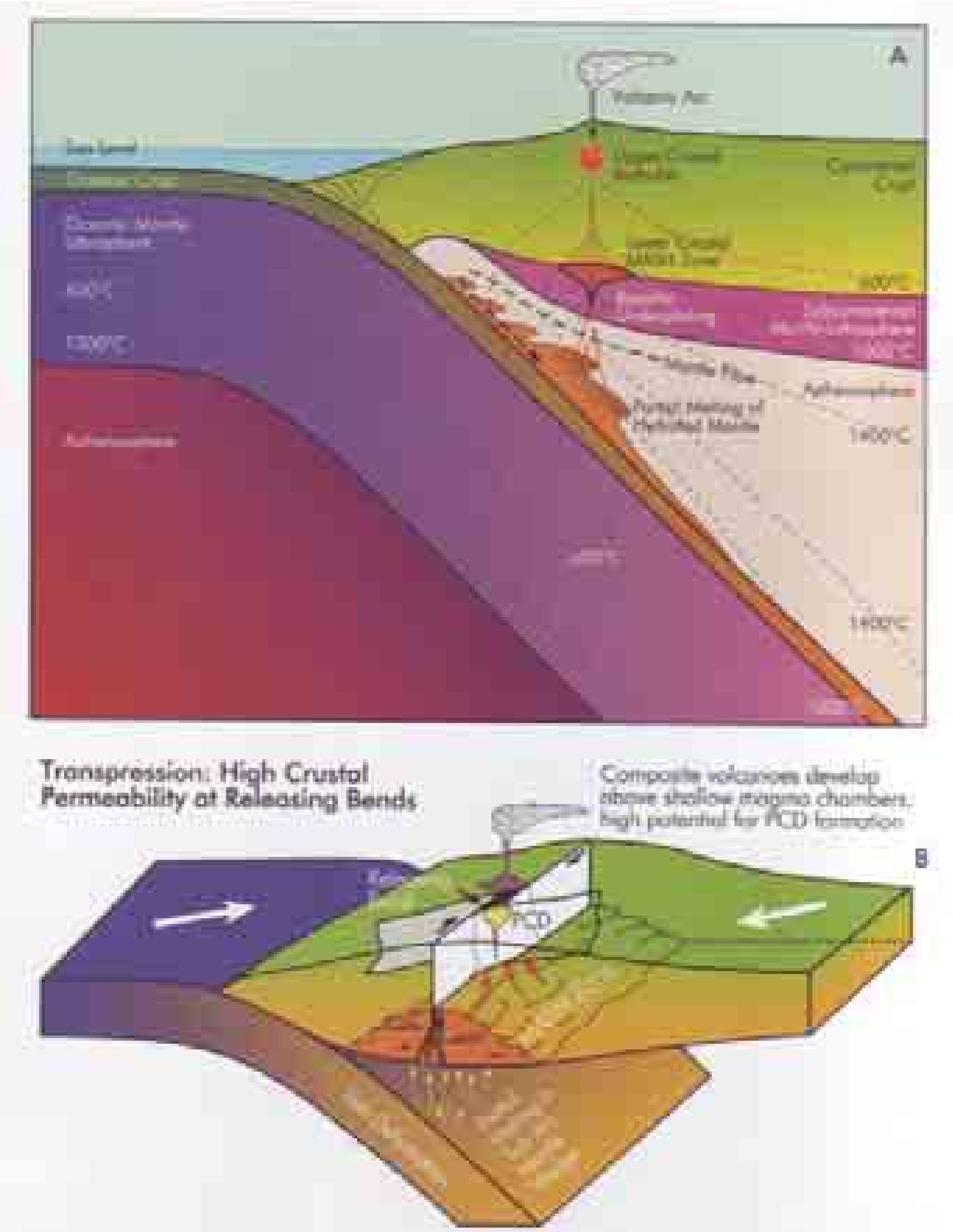

Copper porphyries:

Normal subduction beneath a continental arc: Slab dehydration, partial melting of asthenospheric mantle wedge, basaltic underplating, MASH processes in continental crust (melting-assimilation-storage-homogenization)

Large copper porphyry systems are in a setting of oblique con-vergence of oceanic and continental plate which produces extensional domains in strike-slip systems, favoring large-scale melt emplace-ment in the upper crust

Kerrich et al. (2005) EG Anniv Vol: 1112

GOLD WORLD MINE PRODUCTION 2008 (2,330 t)

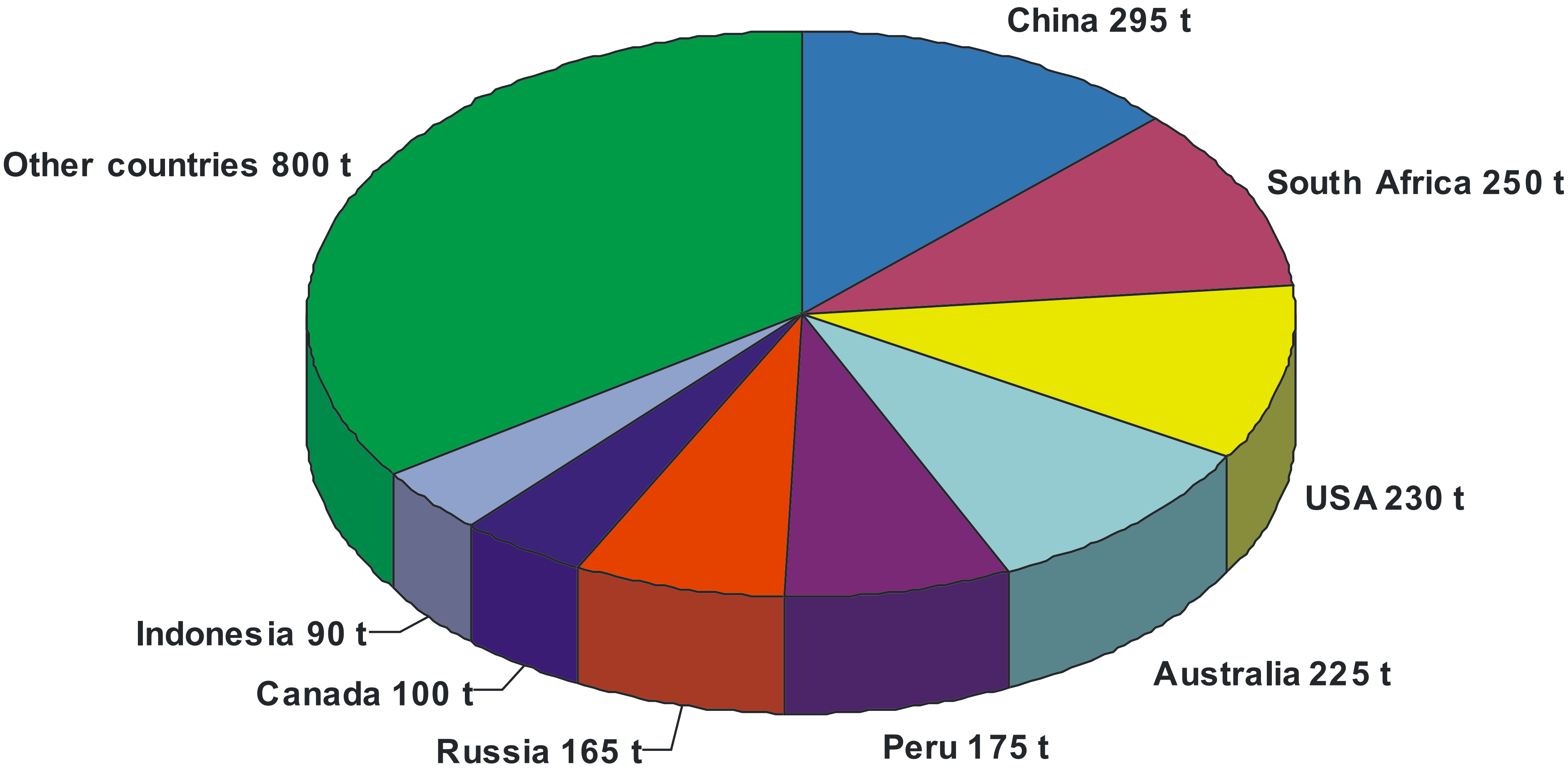

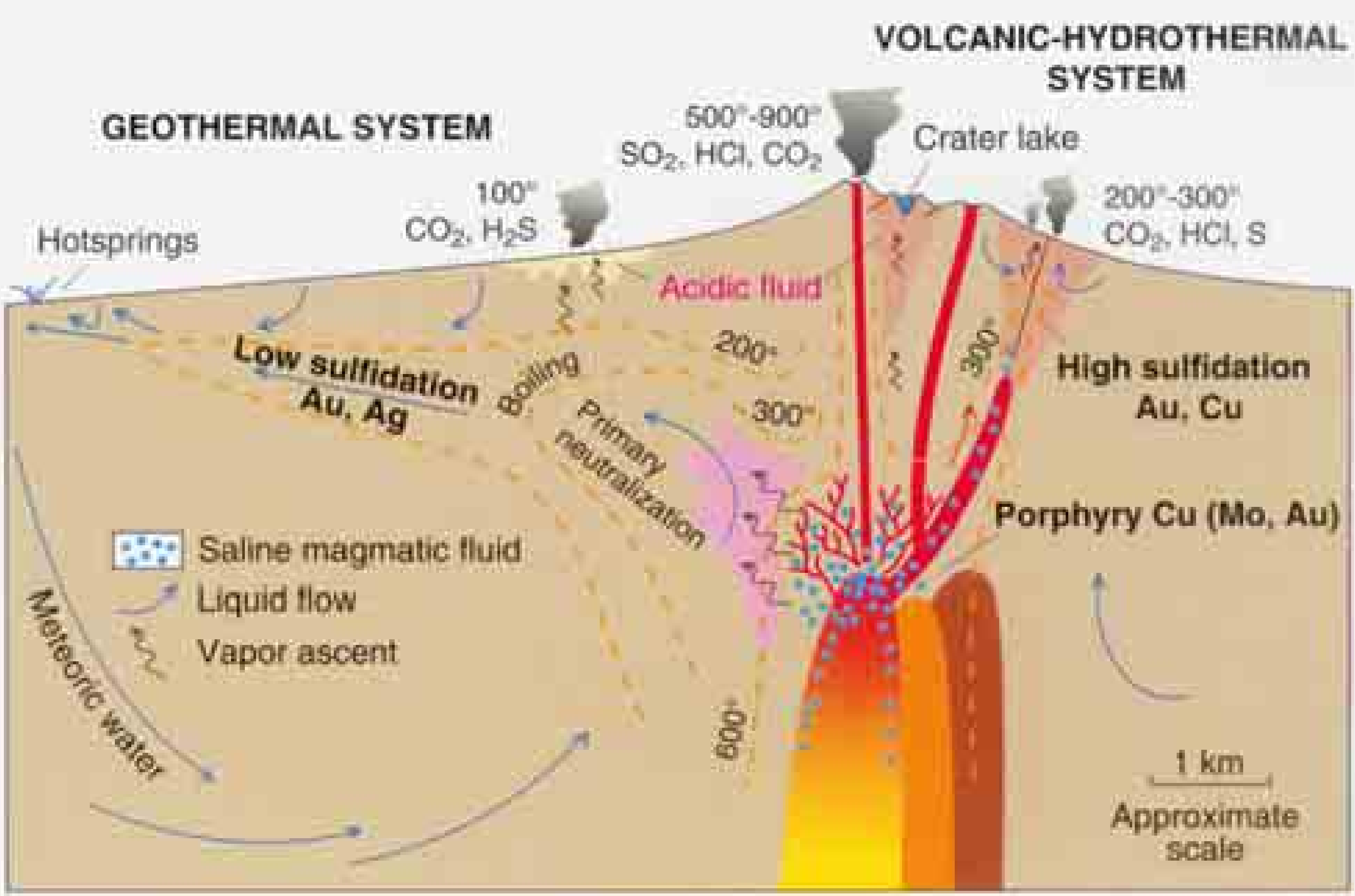

Fig. 1.1 Schematic cross-section showing shallow sub-volcanic intrusions and associated stratovolcano, and environments deduced for formation of porphyry Cu, and high- and low-sulfidation epithermal ore deposits [20,25]. Active volcanic-hydrothermal systems extend from degassing magma to fumaroles and acidic springs, and incorporate porphyry and/or high-sulfidation ore environments, whereas low-sulfidation ore deposits form from geothermal systems characterized by neutral-pH waters that may discharge as hot springs.

Hedenquist et al. (1996) Soc Res Geol Japan

Orogenic gold deposits: metamorphic dehydration and focussed fluid flow in shear zones

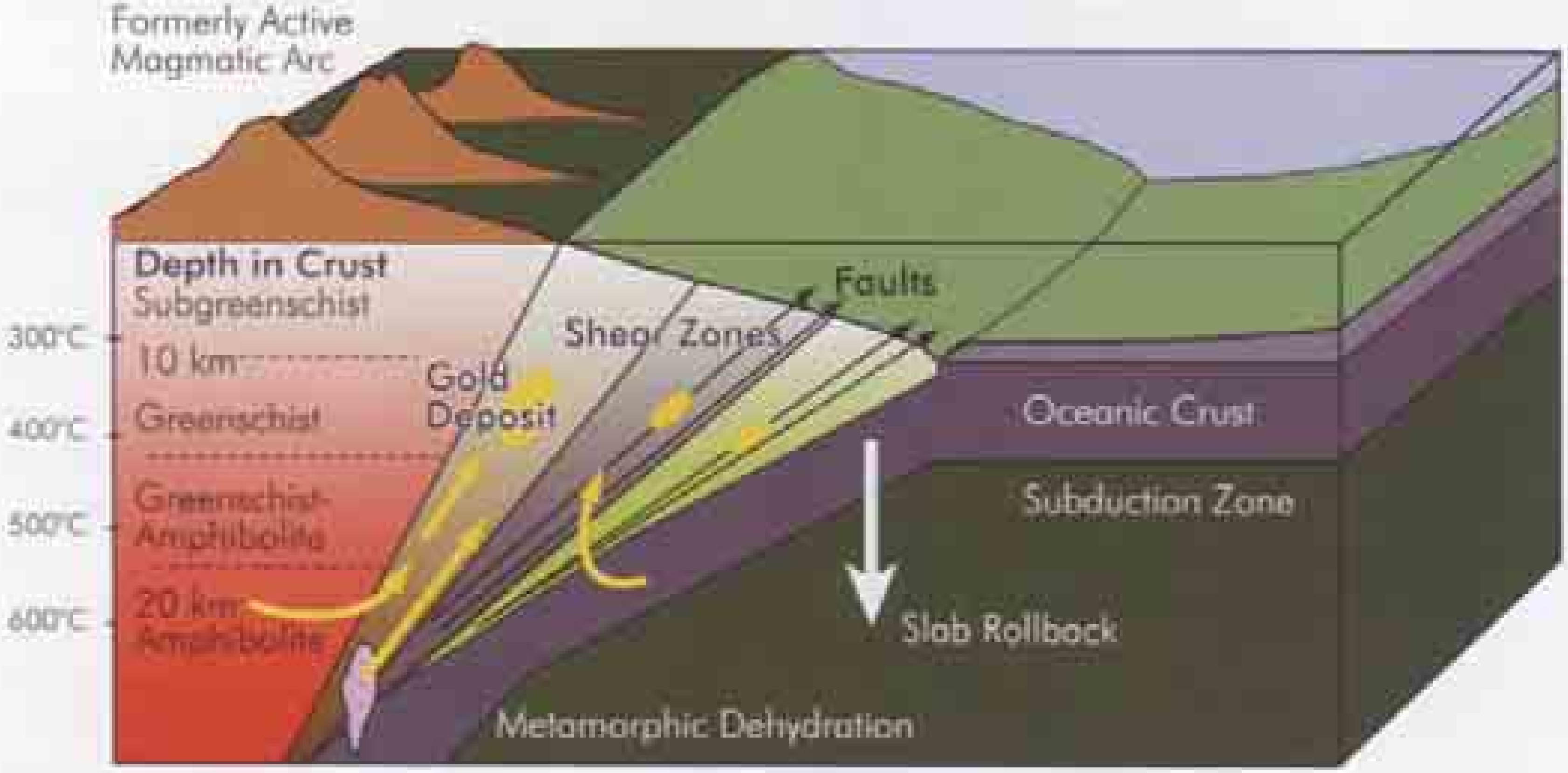

FIG. 7. Cordilleran-type orogens are recognized for the widespread distribution of orogenic gold deposits in metamorphosed juvenile rocks on either side of the magmatic arc. Ore-forming fluids in the fore arc may be derived from prograde metamorphism of accreted material above a subducting slab and from the slab itself; where slab fluids are released into the mantle wedge, mantle-derived melts may carry some of the fluid into the accreted oceanic rocks. The metalliferous fluids are focused along major crustal shear zones in the fore arc, which previously may have been sites of terrane suturing.

Kerrich et al. (2005) EG Anniv Vol: 1114

$Au + 4H_2S + \frac{1}{2}O_2 = AuHS(H_2S)_3 + \frac{1}{2}H_2O$

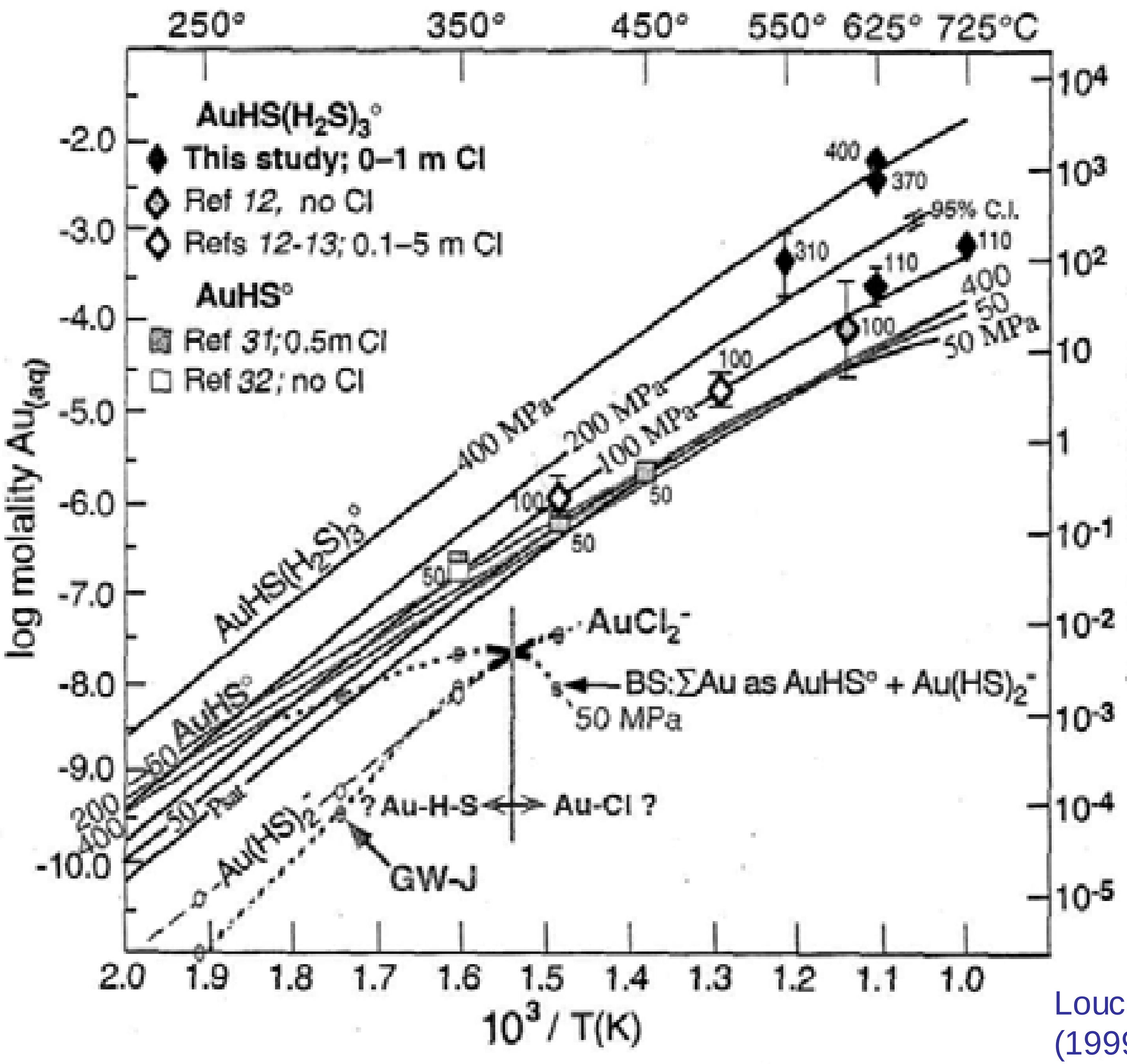

Gold solubilty oxygen-buffered (pyrrhotite-pyrite-magnetite) and pH-buffered (orthoclase-muscovite-quartz) as typical of orogenic gold deposits

Loucks and Mavrogenes (1999) Nature 284: 2162

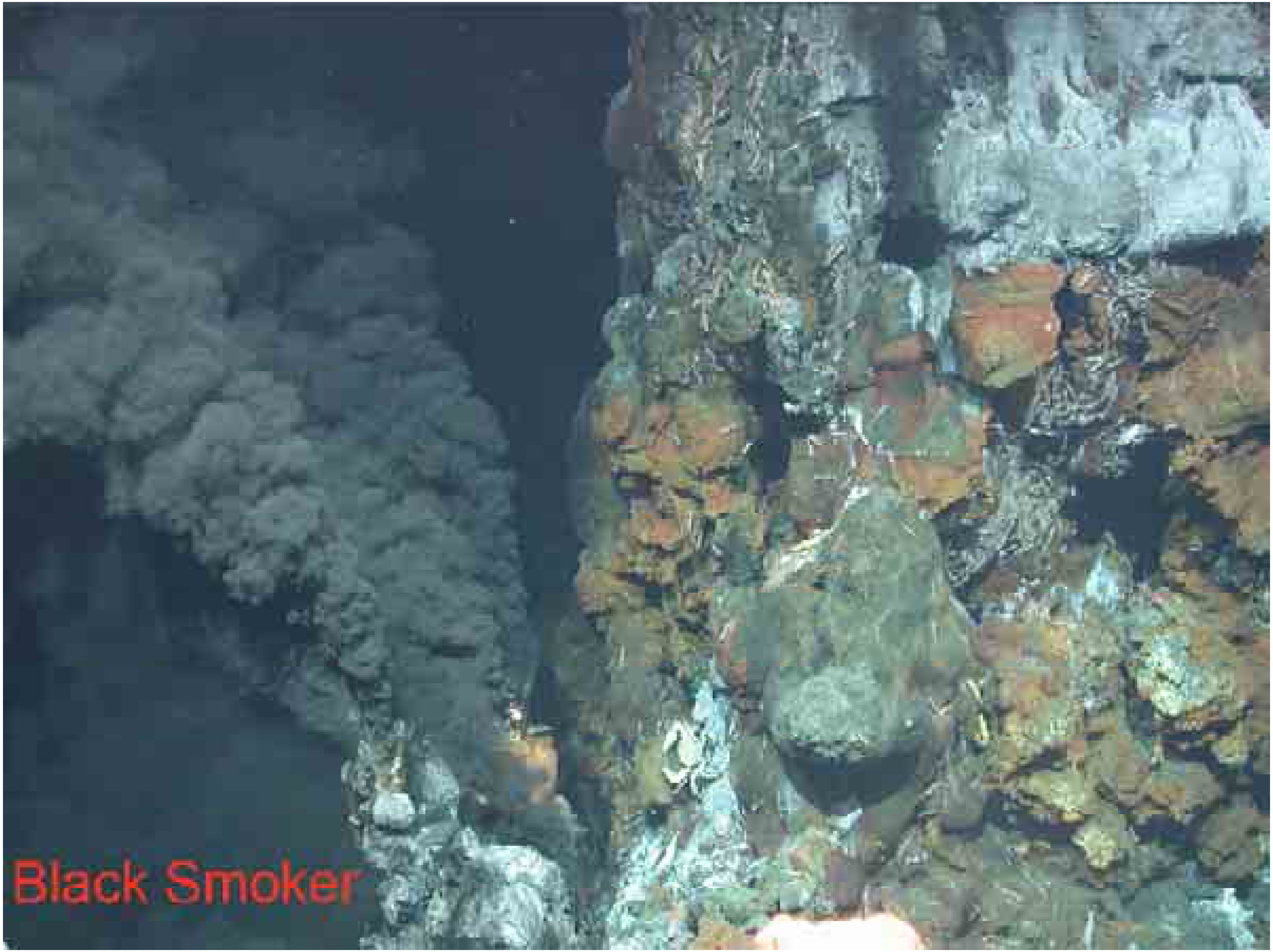
Black Smoker

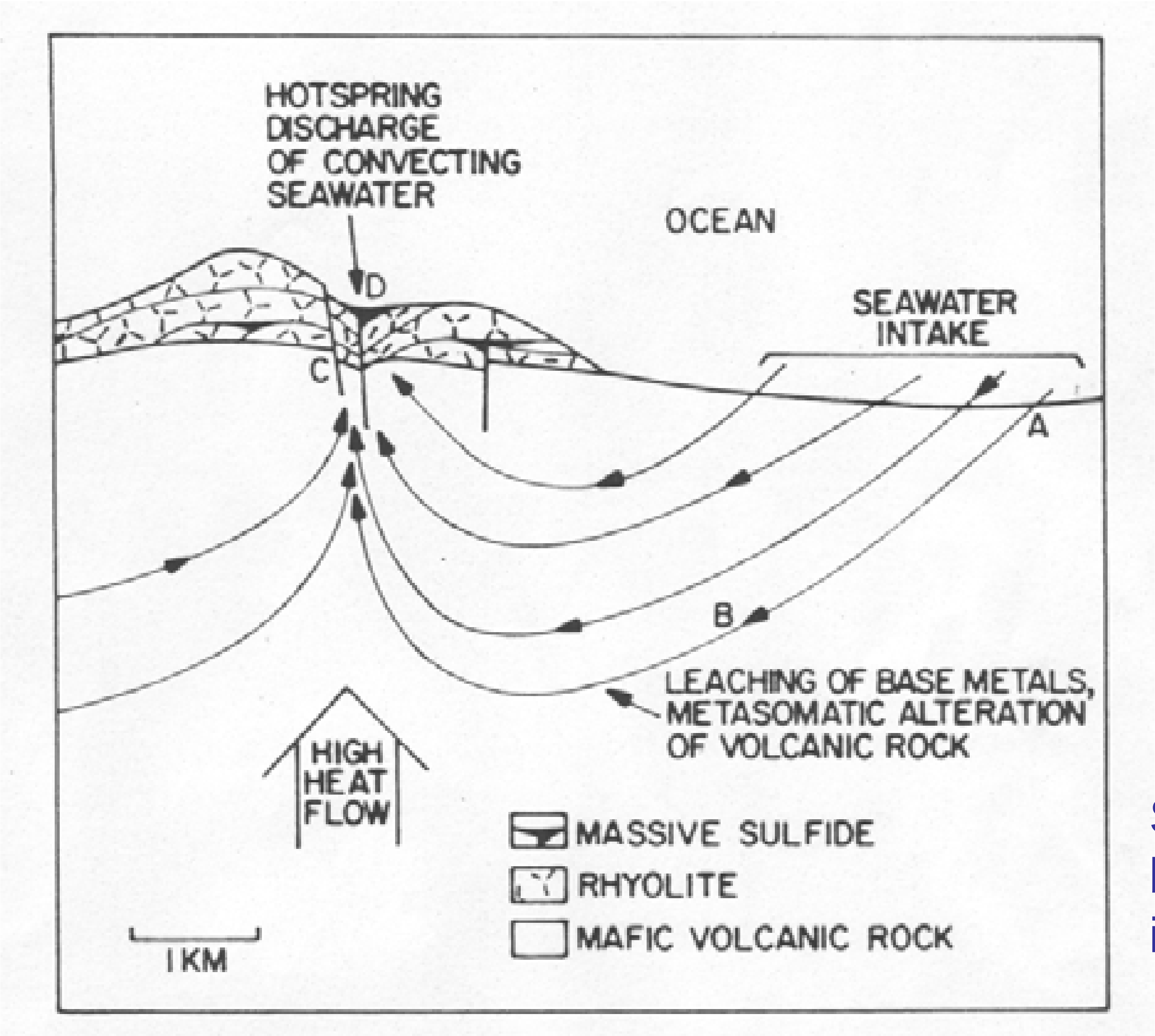

Reed (1983) EG 78: 466-485

Seawater-basalt interaction

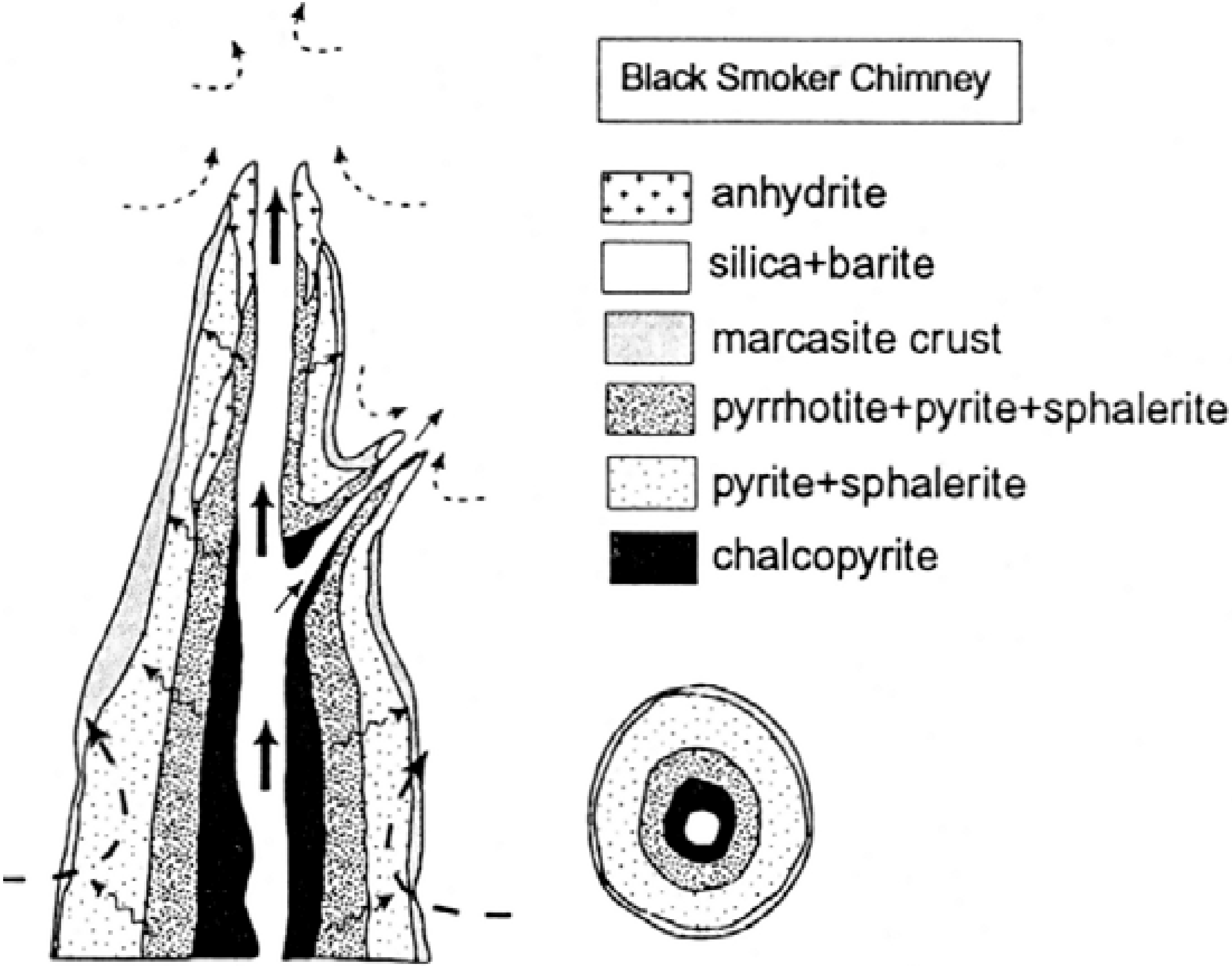
Black Smoker Chimney
anhydrite
silica+barite
marcasite crust
pyrrhotite+pyrite+sphalerite
pyrite+sphalerite
chalcopyrite

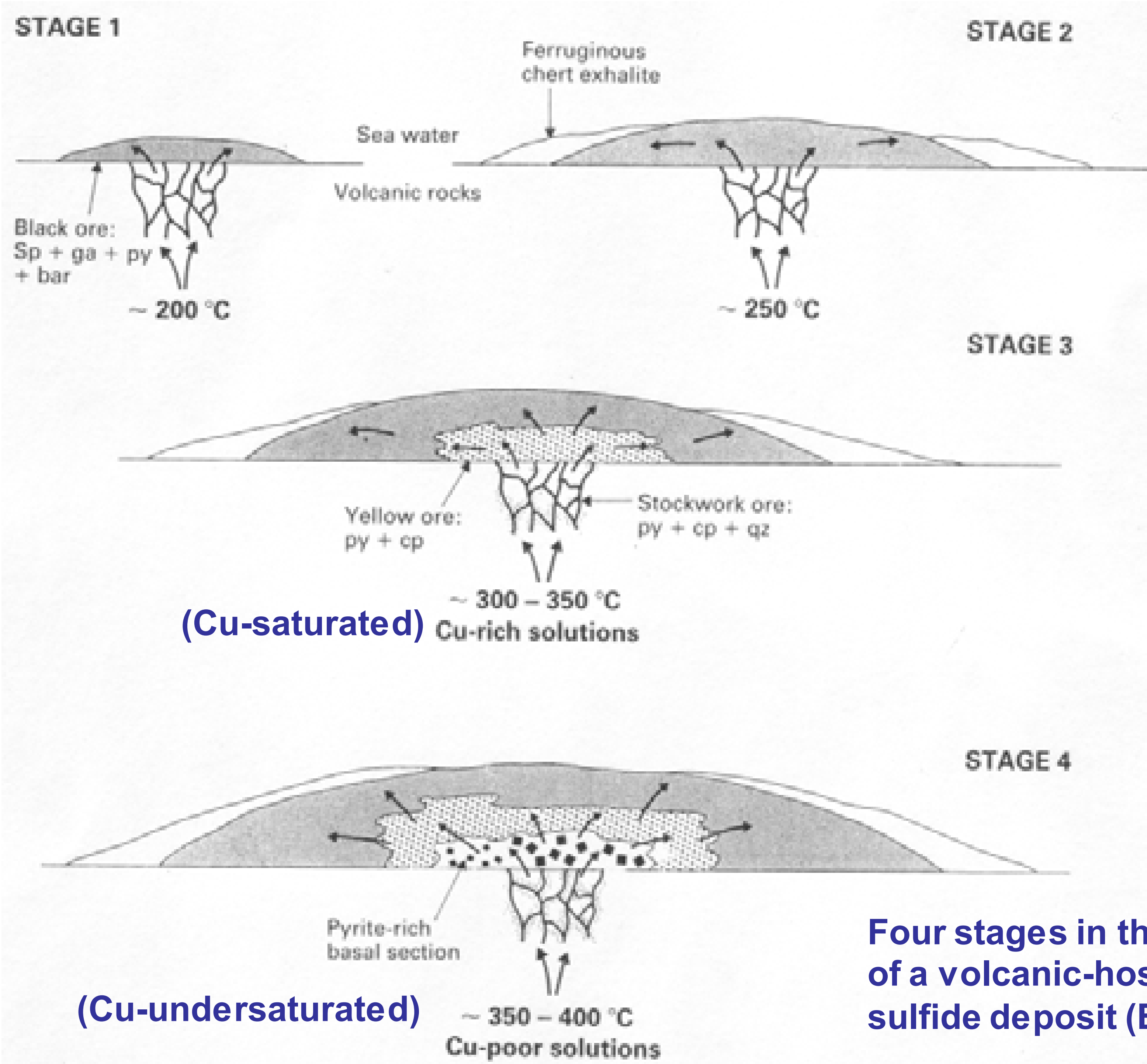

Four stages in the evolution of a volcanic-hosted massive sulfide deposit (Evans 1992: 74)

Hydrogeologic and tectonic regimes for large-scale groundwater flow in sedimentary basins: Formation of Pb-Zn, Cu and U deposits

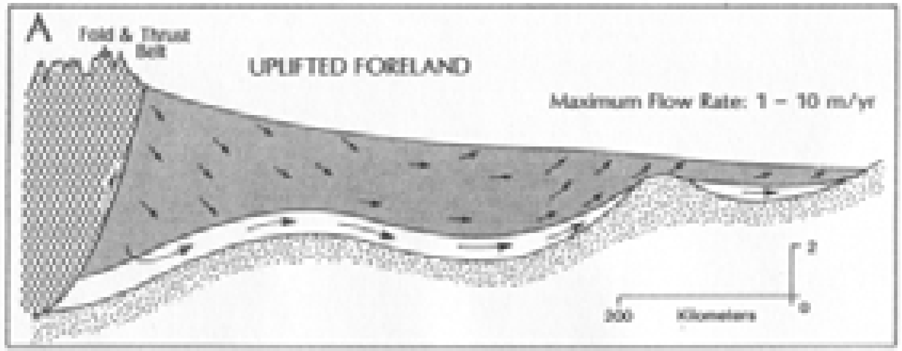

Gravity- or topography-driven flow

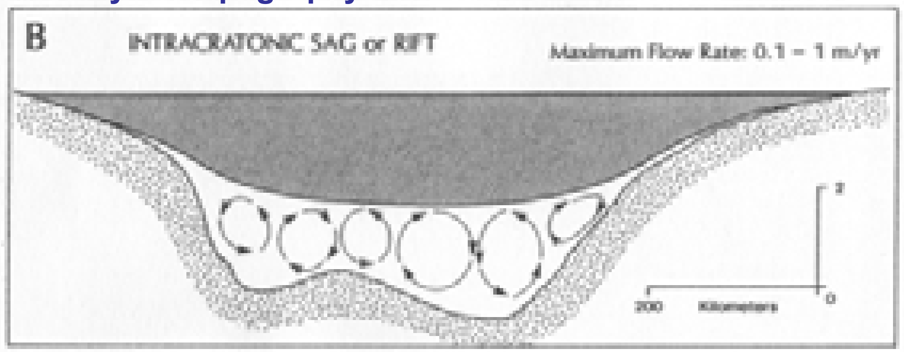

Thermally-driven convection

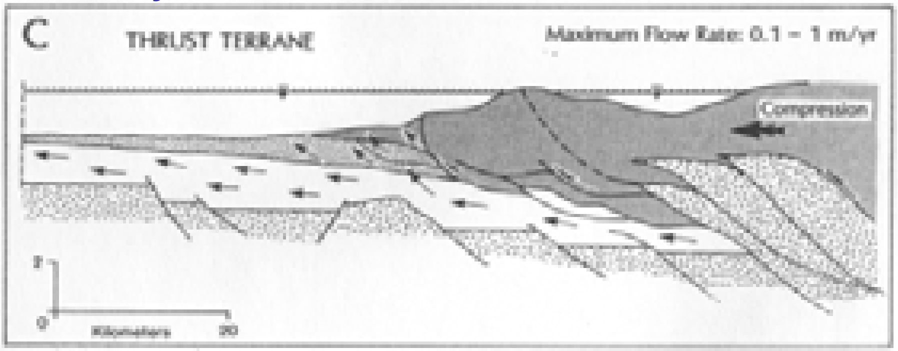

Tectonically-driven (fold- and thrust belt)

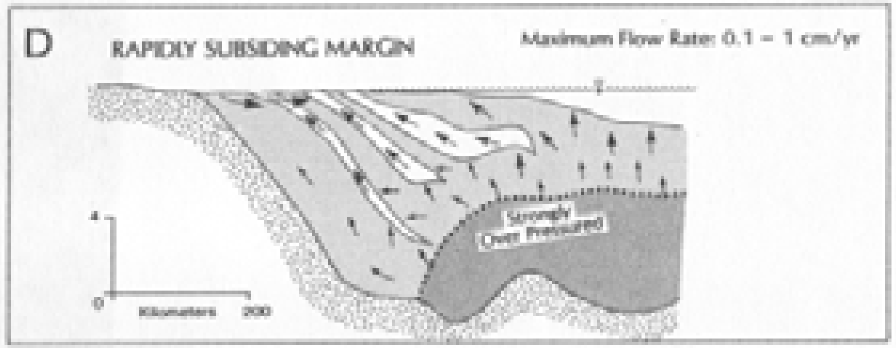

Overpressuring on a continental margin

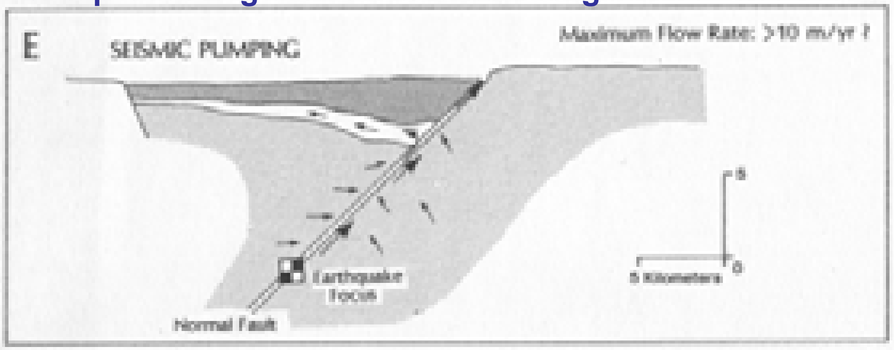

Seismic pumping

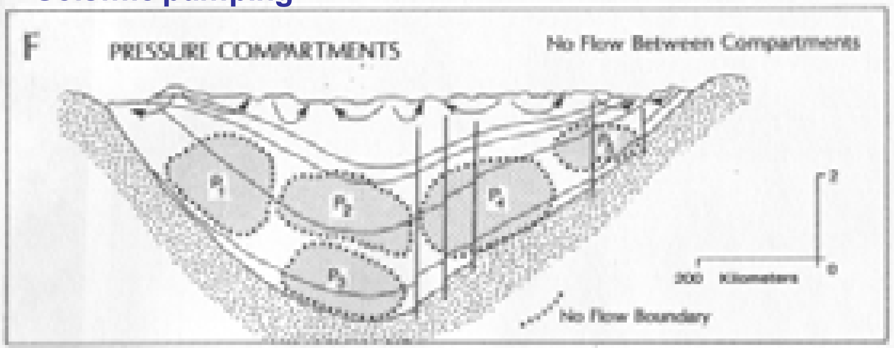

Pressure compartments

Garven and Raffensperger (1997)

The Great Oxidation Event (GOE): 2.4-2.0 Ga

Oxygen from photosynthesis is essentially fixed in Fe-oxides and gypsum. Free oxygen in the atmosphere (>10^{-5} PAL) only after the GOE.

(1) Oxygen from oxygenic photosynthesis is fixed in BIF

$$2Fe^{2+} + 2H_2O + \frac{1}{2}O_2 = Fe_2O_3\,(s) + 4H^+$$

(2) Anoxygenic photosynthesis by reduction of CO_2

$$4Fe^{2+} + CO_2 + 11H_2O = 4Fe(OH)_3\,(s) + 8H^+ + [CH_2O]$$

The two mechanisms for formation of iron ore deposits of the „Banded Iron Formation“ (BIF) family

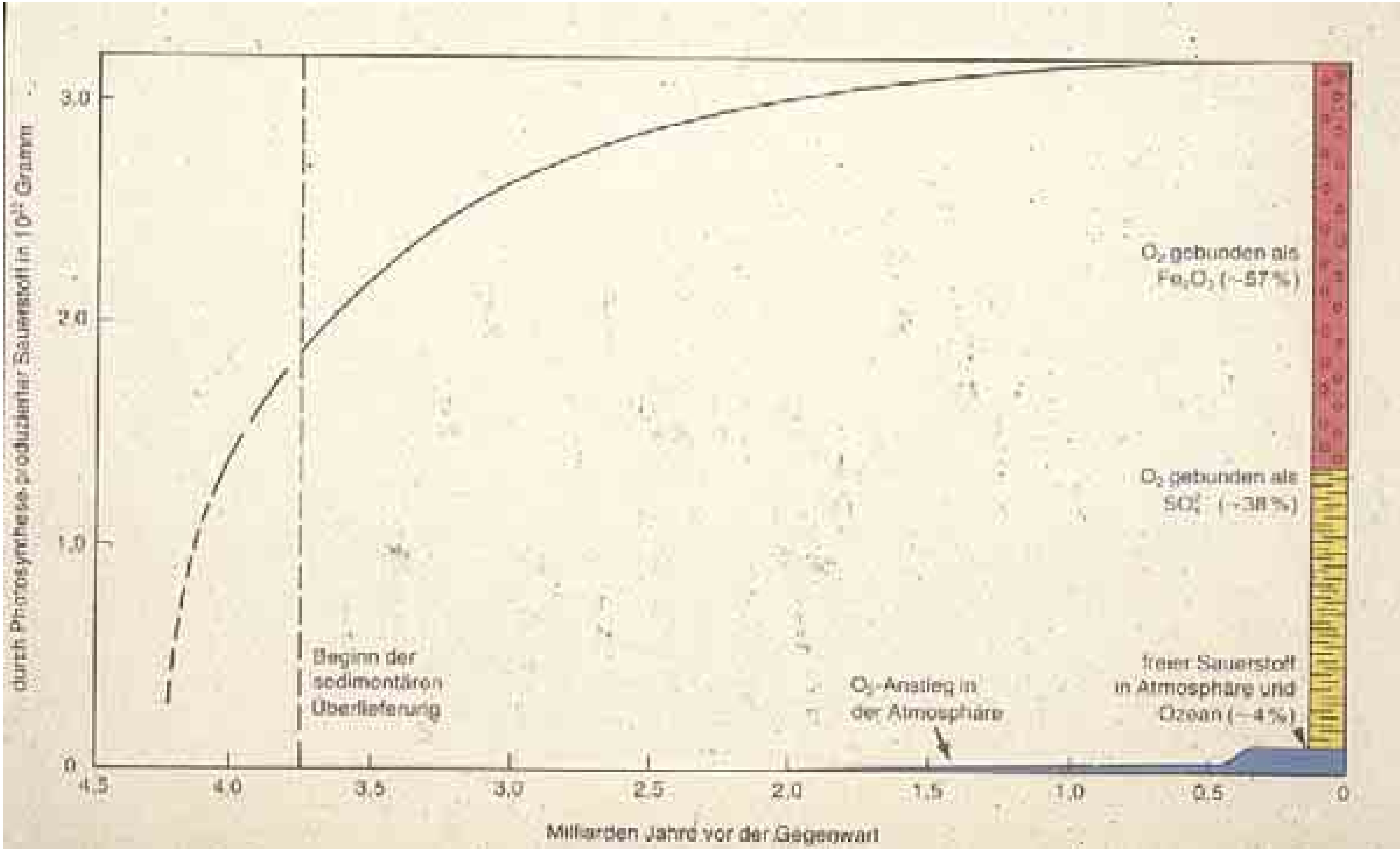

durch Photosynthese produzierter Sauerstoff in 10²¹ Gramm
3,0
2,0
1,0
0
Beginn der
sedimentären
Überlieferung
O₂-Anstieg in
der Atmosphäre
O₂ gebunden als
Fe₂O₃ (~57 %)
O₂ gebunden als
SO₄²⁻ (~38 %)
freier Sauerstoff
in Atmosphäre und
Ozean (~4 %)
4,5
4,0
3,5
3,0
2,5
2,0
1,5
1,0
0,5
0
Milliarden Jahre vor der Gegenwart

Cumulative oxygen evolution from photosynthesis with geological time

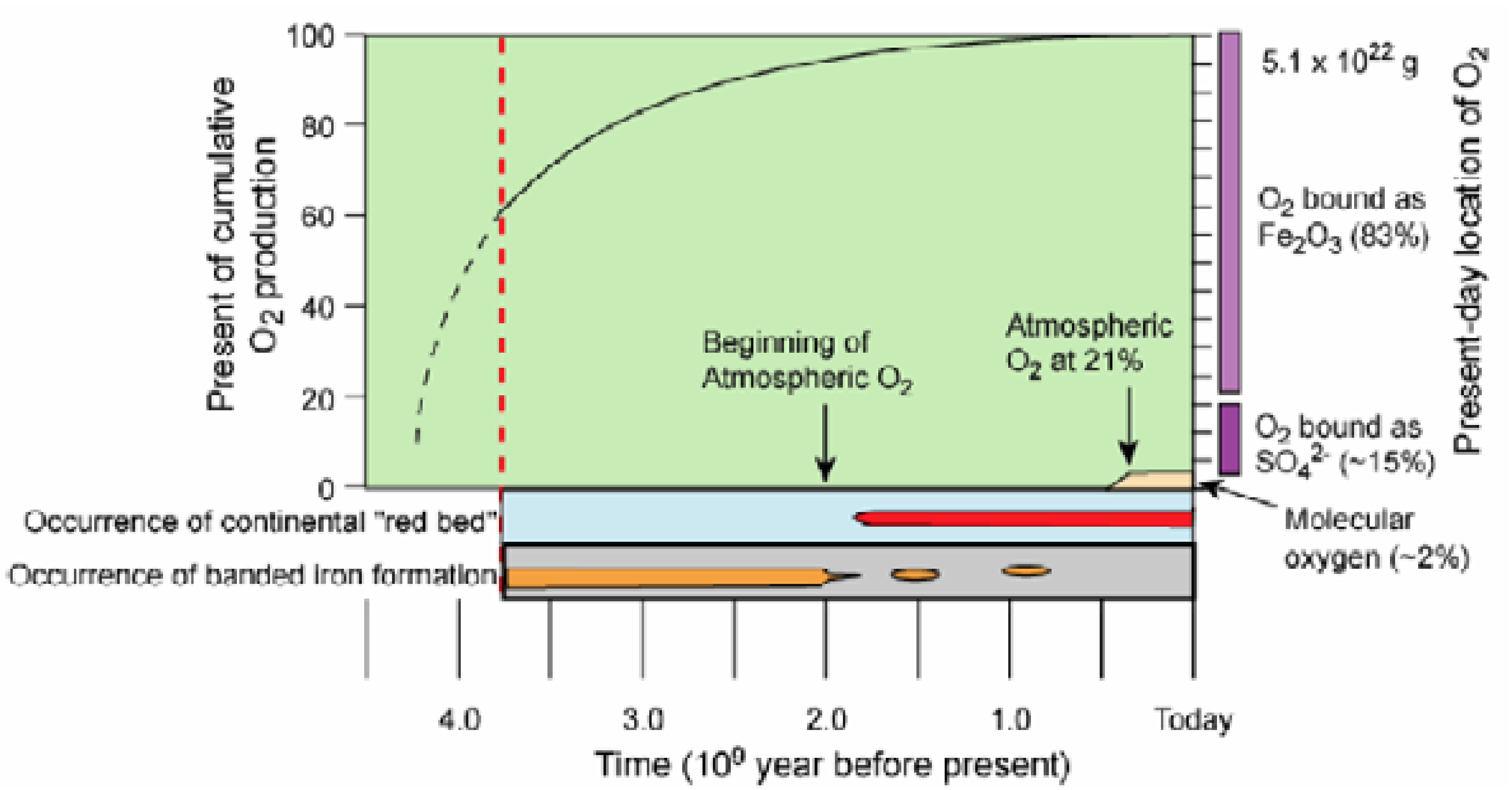

Model by Schidlowski (1978) Pure Appl Geophysics 116: 234-238

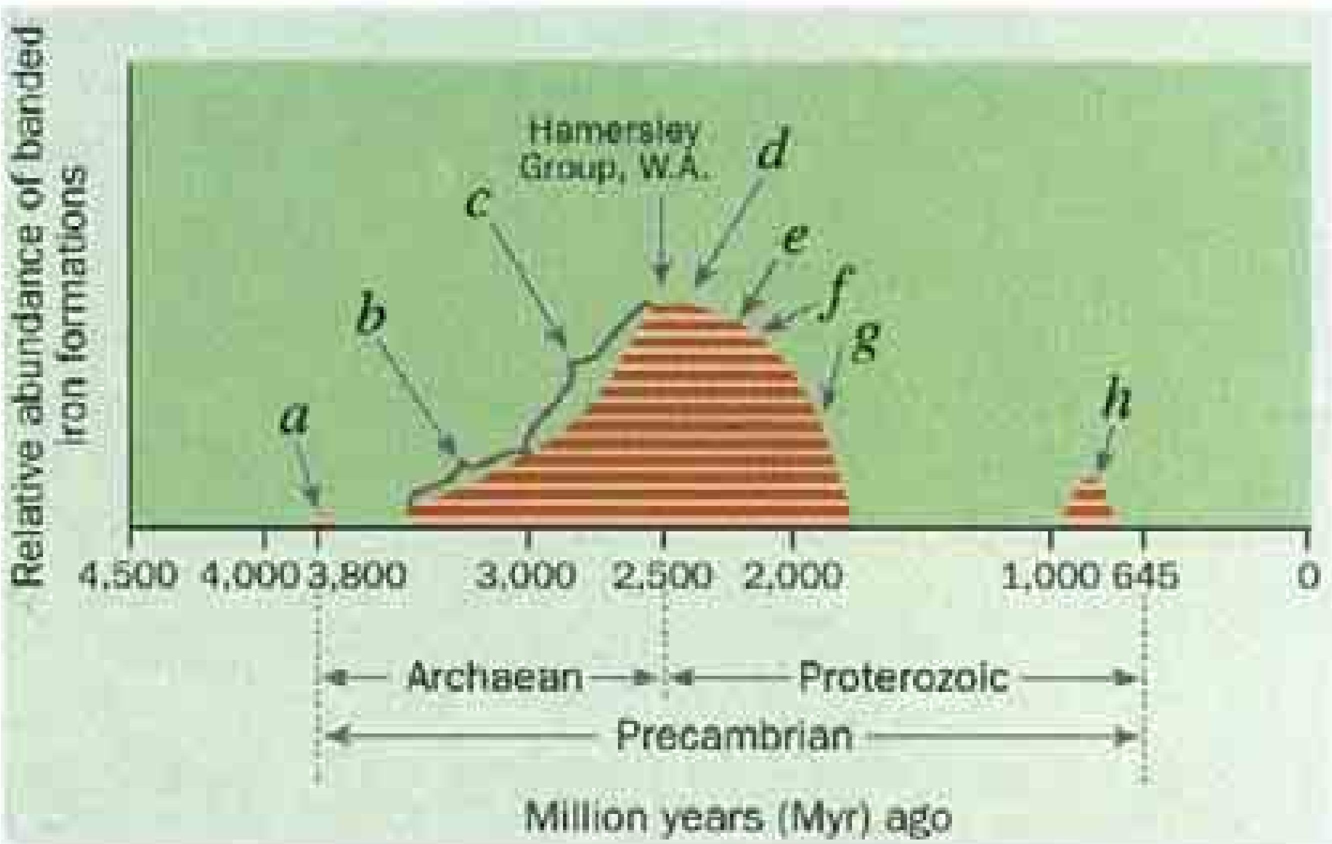

FIG. 1 The relative abundance of banded iron formations in the Precambrian. Estimated values are relative to those of the Hamersley Province, which is the largest BIF province in the world[2,3]. *a*, Isua (West Greenland); *b*, Zimbabwe, South Africa, Ukraine, Venezuela, Western Australia; *c*, Canadian greenstone belts, Yilgarn block (Western Australia); *d*, Transvaal Supergroup (South Africa); *e*, Lake Superior region (USA); *f*, Krivoy Rog series (Russia); *g*, Labrador Trough (Canada); *h*, Rapitan Group (Canada), Urucum region (Brazil), Damara Supergroup (Namibia).

Klein (1997) Nature 385: 25

Banded Iron Formation (BIF)

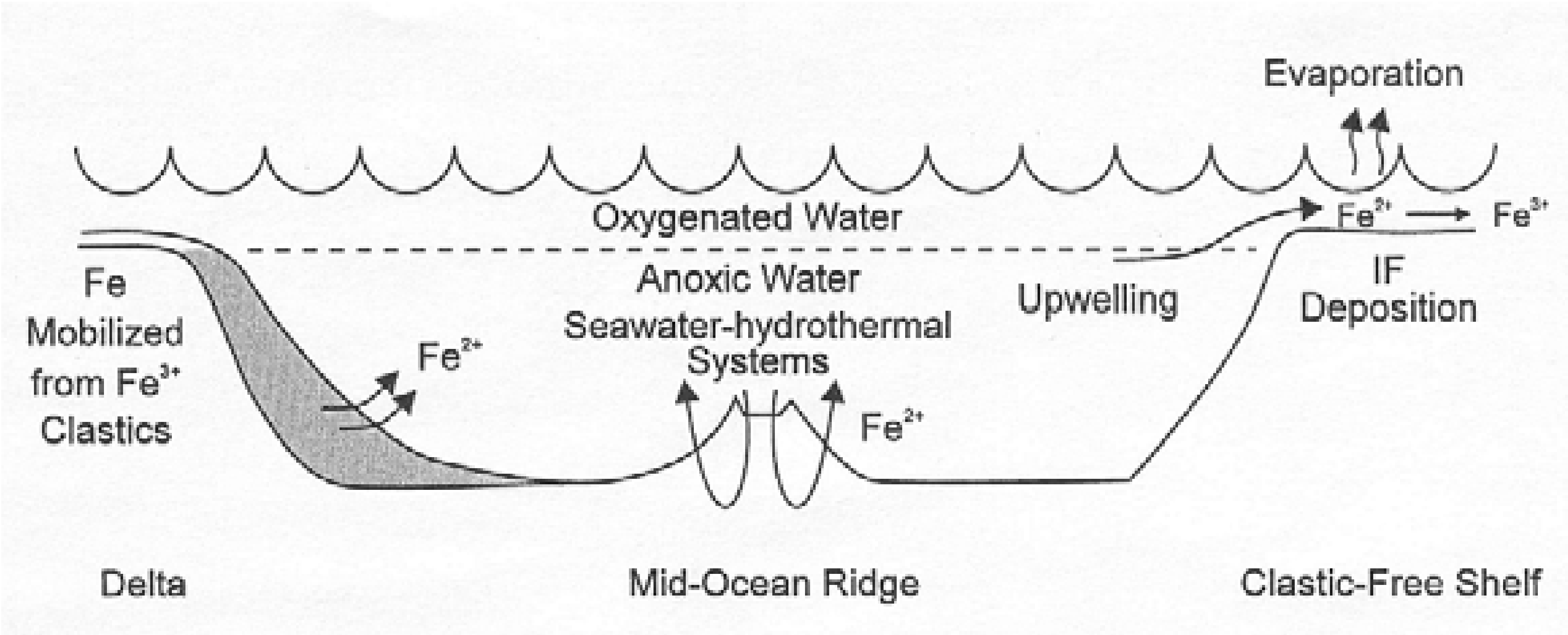

Model for the deposition of Lake Superior-type iron formations (Holland 1995:181): Deeper water, enriched in Fe^{2+} from either volcanic or diagenetic sources, moves up onto a shallow shelf, where iron minerals and SiO_2 are precipitated as a result of oxidation, mixing, and possibly evaporation.

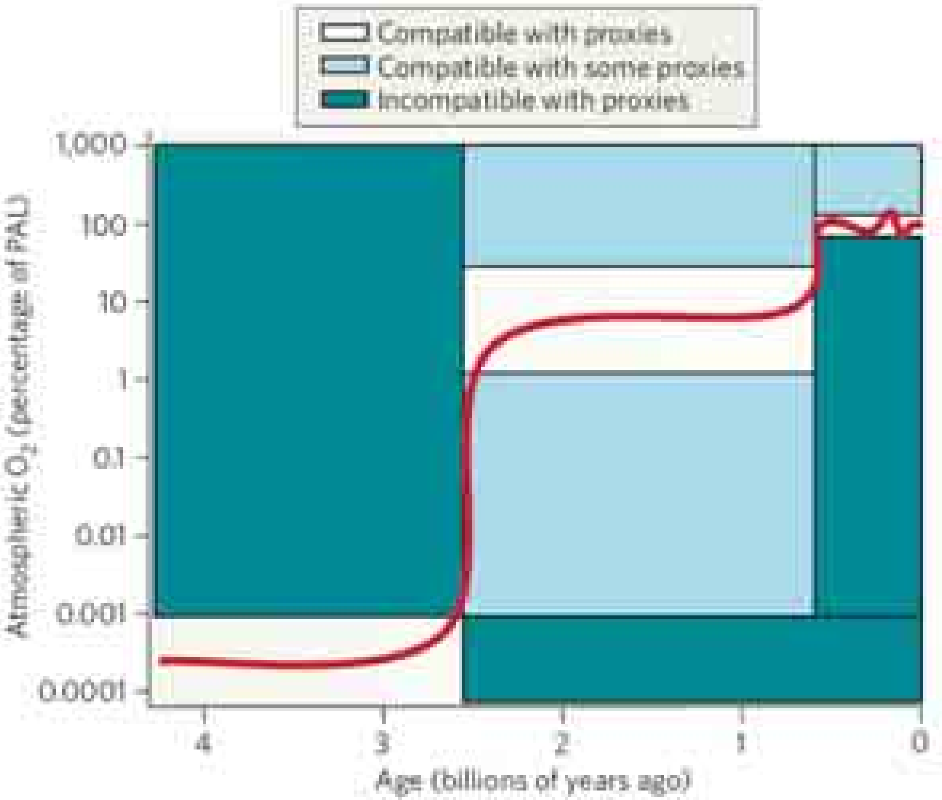

Figure 2 | Prevailing view of atmospheric oxygen evolution over time. The red line shows the inferred level of atmospheric oxygen bounded by the constraints imposed by the proxy record of atmospheric oxygen variation over Earth's history[2,20]. The signature of mass-independent sulphur-isotope behaviour sets an upper limit for oxygen levels before 2.45 billion years ago and a lower limit after that time. The record of oxidative weathering after 2.45 billion years ago sets a lower limit for oxygen levels at 1% of PAL, whereas an upper limit of 40% of PAL is inferred from the evidence for anoxic oceans during the Proterozoic. The tighter bounds on atmospheric oxygen from 420 million years ago to the present is set by the fairly continuous record of charcoal accumulation[19]: flames cannot be sustained below an oxygen level of 60% of PAL, and above about 160% of PAL the persistence of forest ecosystems would be unlikely because of the frequency and vigour of wildfires[21].

Kump (2008)
Nature 451: 278

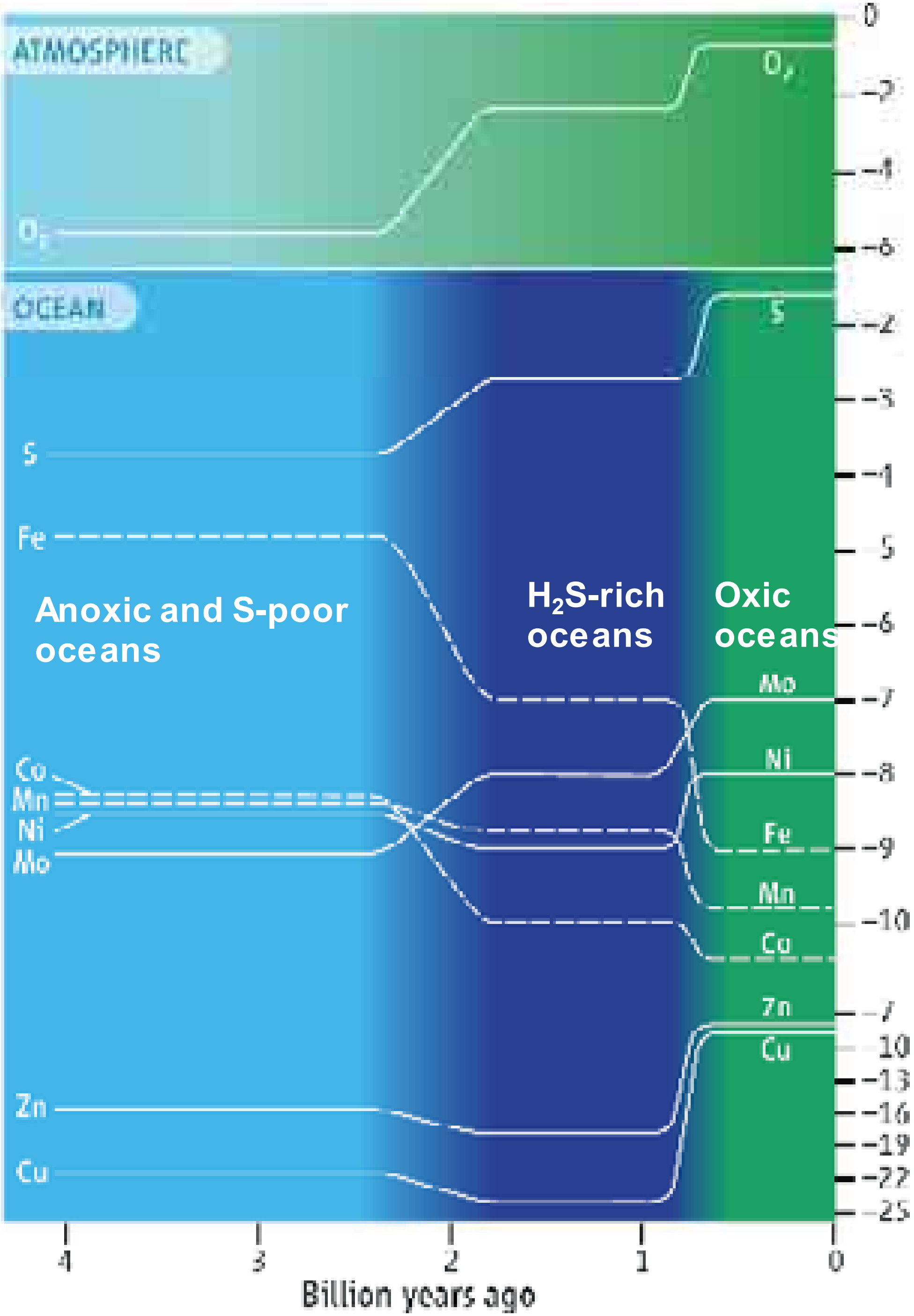

Changes in element abundances through time. These histories are approximate, based on simple geochemical models and inferences from ancient sediments. An expansion in H_2S-rich ocean regions after 2.4 billion years ago is assumed (2, 5). Color gradations indicate a transition from anoxic, S-poor oceans before 2.4 billion years ago (light blue) to H_2S-rich oceans between 1.8 billion and 800 million years ago (dark blue), subsequently giving way to complete ocean oxygenation (green). Different line styles are for clarity only: dashed lines are for elements with falling concentrations. [Adapted from (26), based on data from (2, 5, 9, 10)].

Anbar (2008) Science 322: 1482

IRON ORE WORLD MINE PRODUCTION 2008 (2.19 Gt)

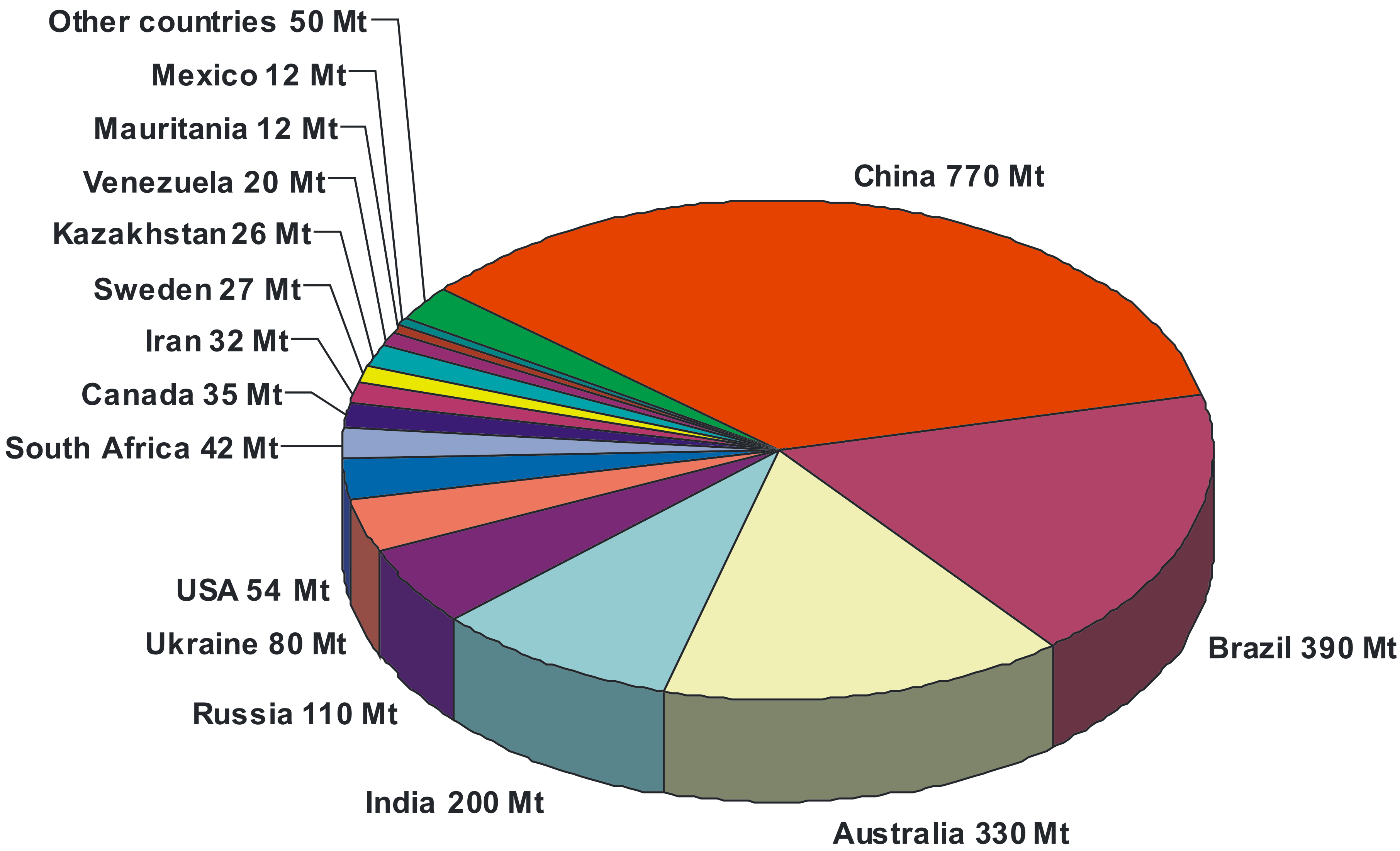

Feb 2009, Fines (64.5 % Fe), fob Europe: 86 USD/t

Pico de Itabirito, Minas Gerais, Brazil: Hard hematite ore (subvertical) with soft hematite ore at the Pico mine to the left, and Sapecado mine to the right

Conceicao
pit

Mount Tom Price, Hamersley Basin, Western Australia


Carajas mineral province, Amazonas basin, Brazil

Central part of the Carajas mineral province

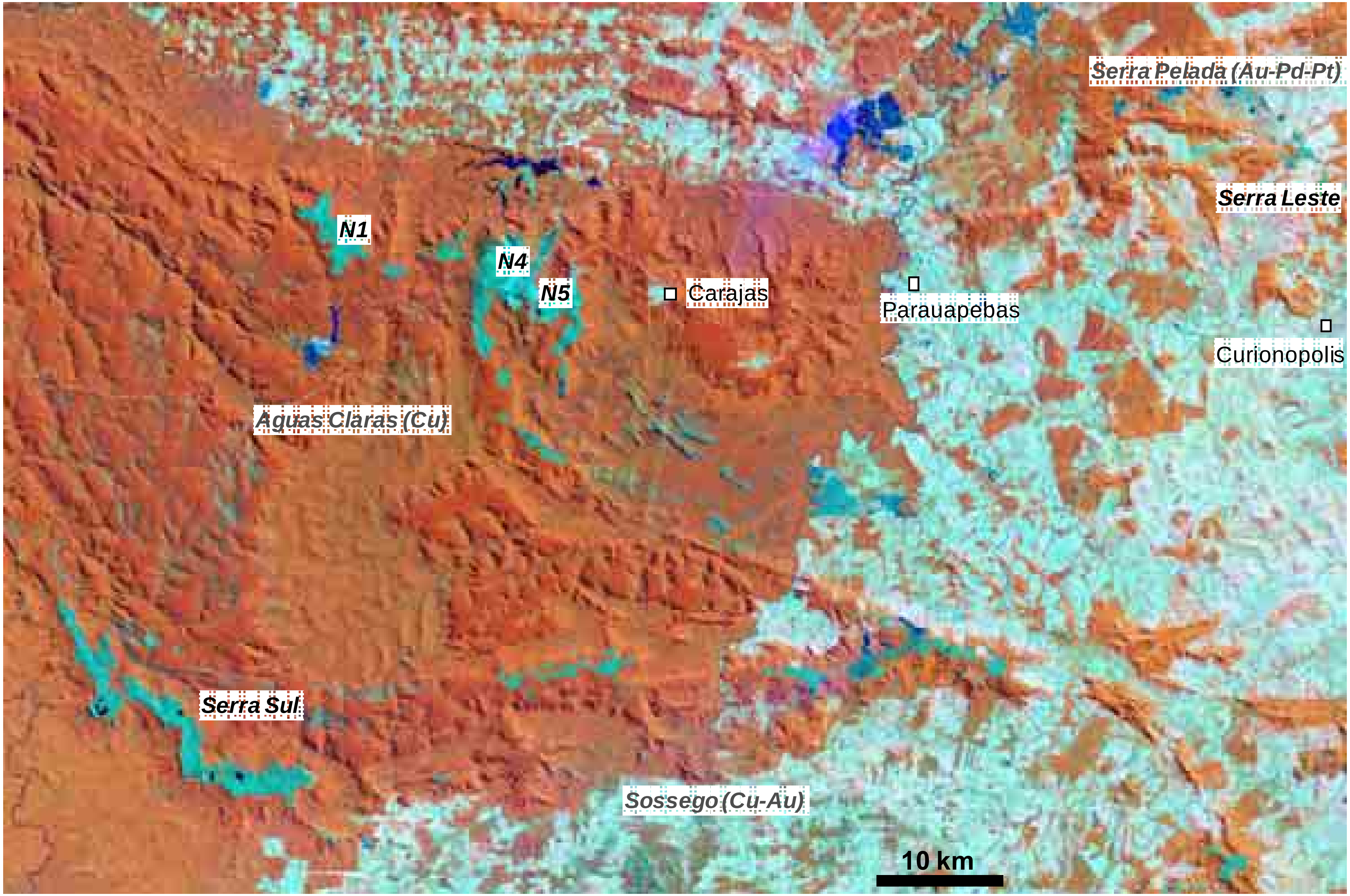

Landsat ETM7+ (August 1999)

Aeromagnetic map

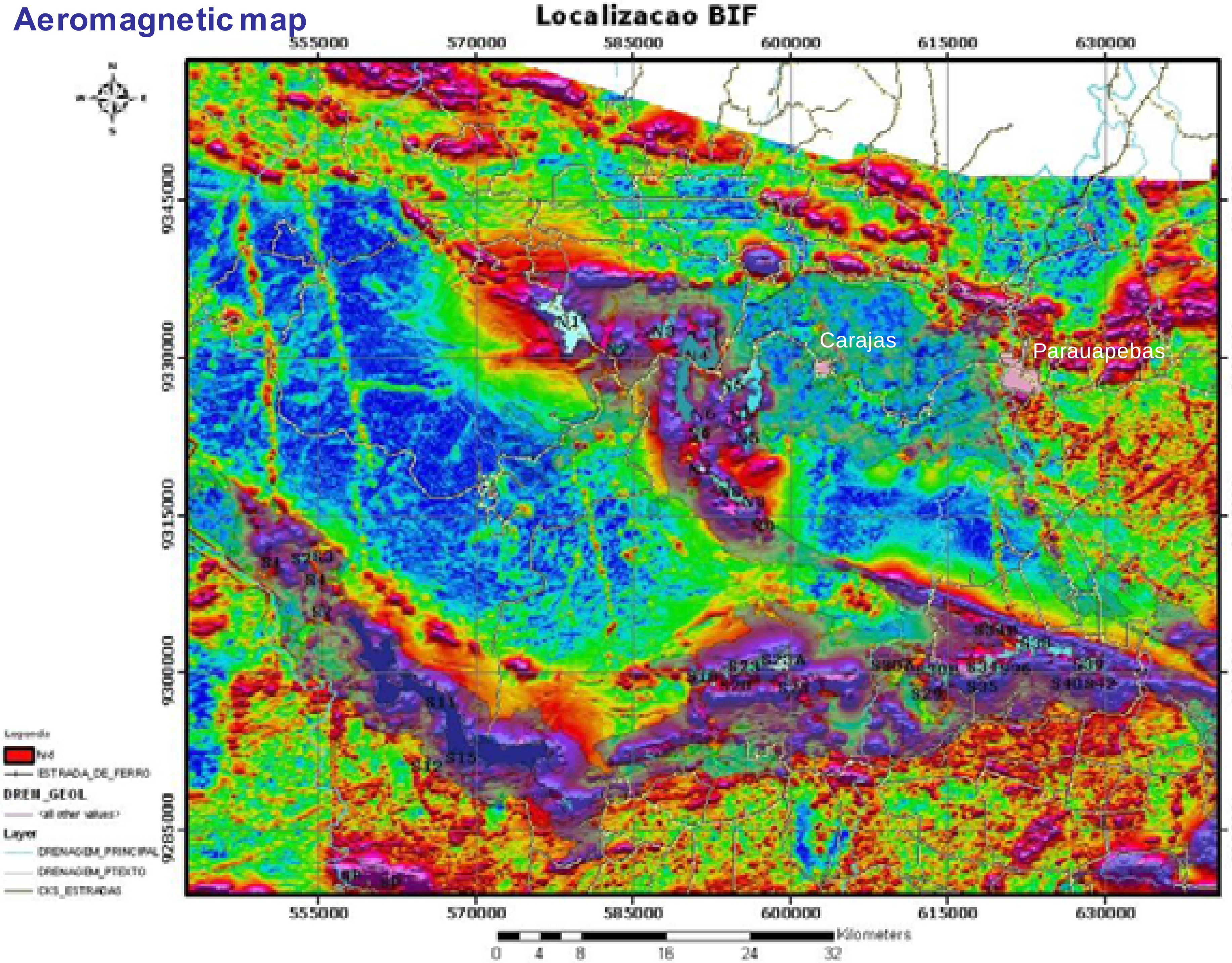

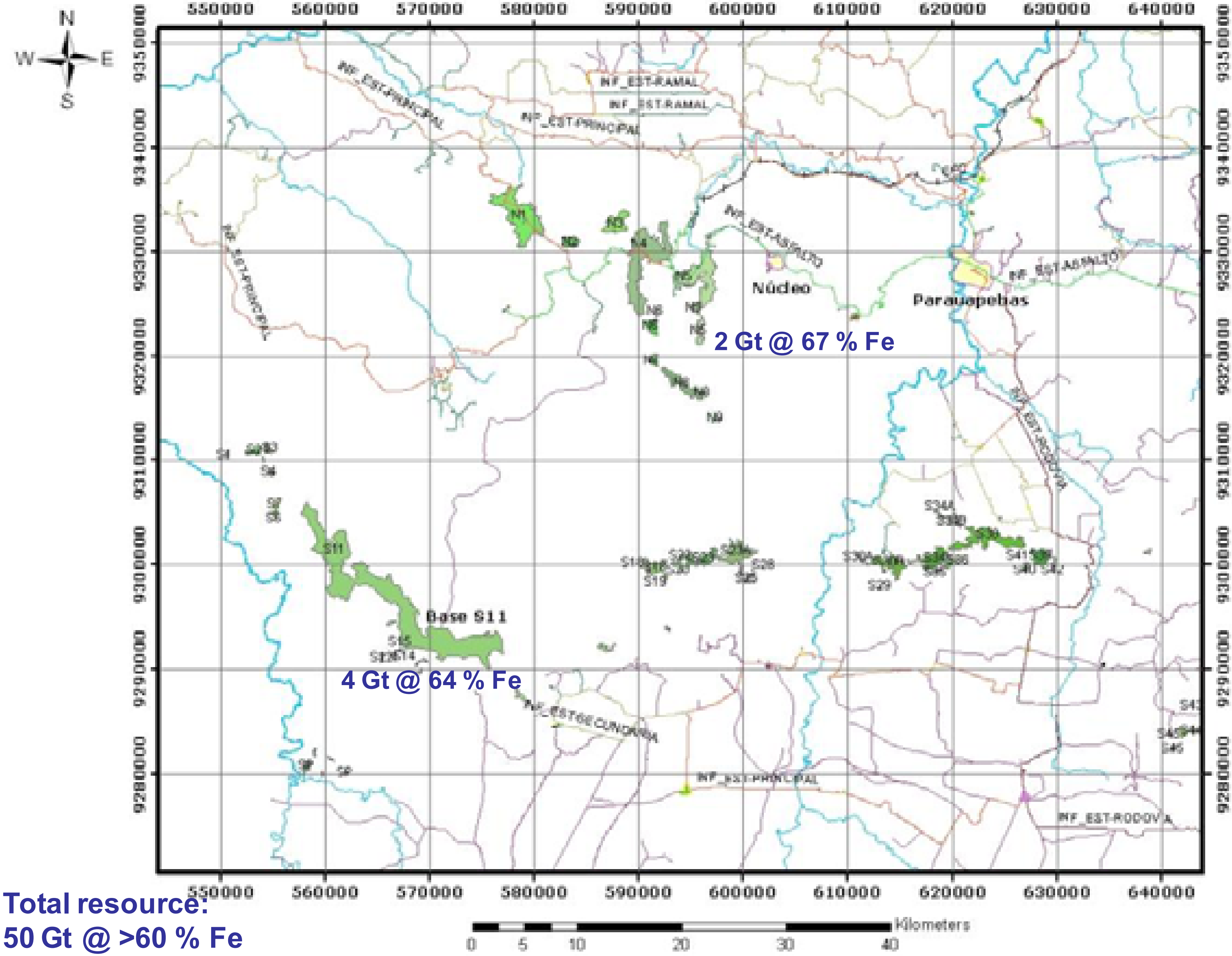

Total resource:
50 Gt @ >60 % Fe


Mina N4E

N5E pit


Banded iron formation (waste)


Greenstone
Serra Sul, Orebody A

A B C D **4 Gt @ 64 % Fe measured**

D orebody: 25,000 m drilled (200 x 200 m)

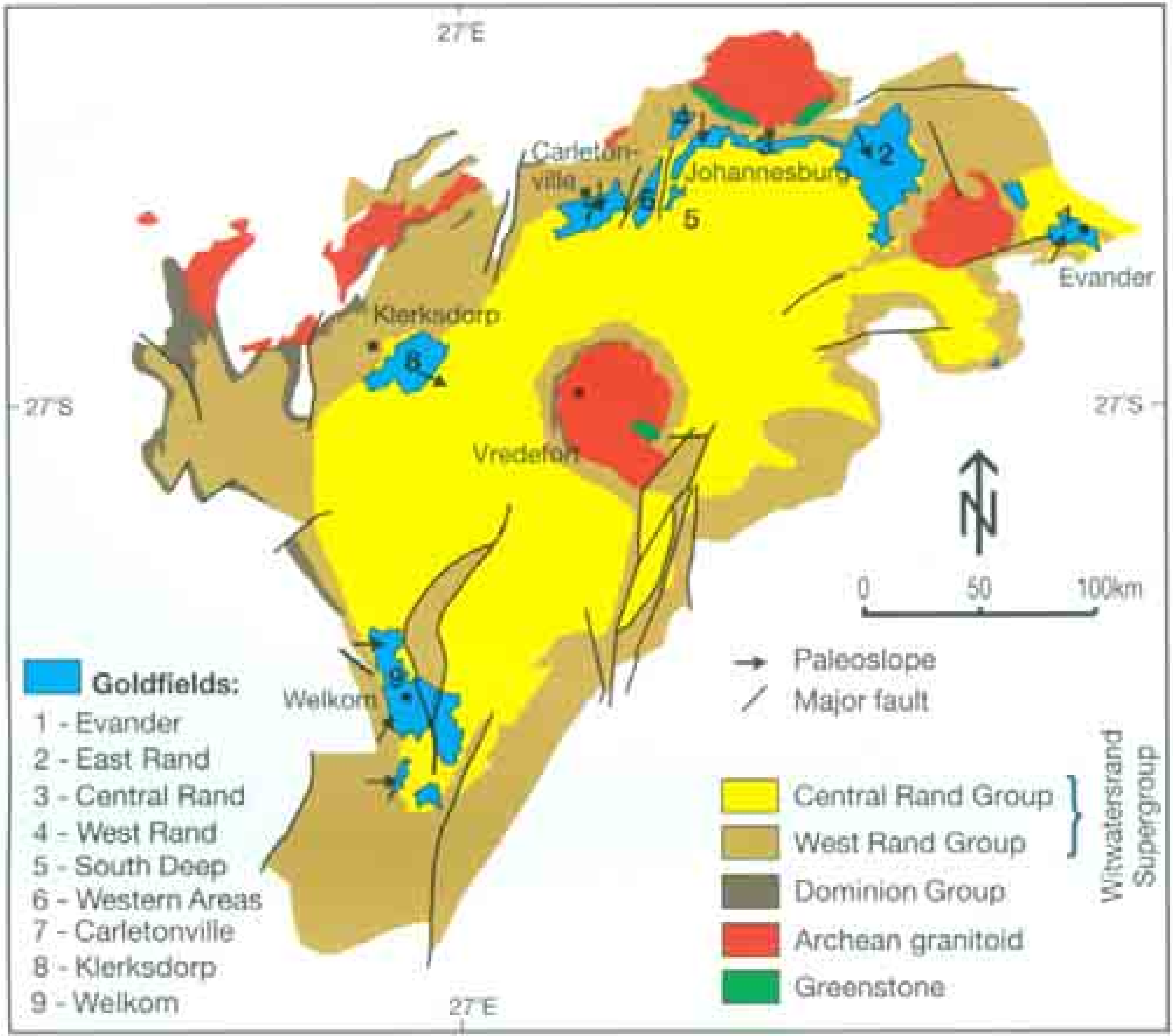
27°E
Carleton-ville
Johannesburg
Evander
Klerksdorp
Vredefort
Welkom
27°S
27°S
0
50
100km
N
Goldfields:
1 - Evander
2 - East Rand
3 - Central Rand
4 - West Rand
5 - South Deep
6 - Western Areas
7 - Carletonville
8 - Klerksdorp
9 - Welkom
Paleoslope
Major fault
Central Rand Group
West Rand Group
Dominion Group
Archean granitoid
Greenstone
Witwatersrand Supergroup
27°E

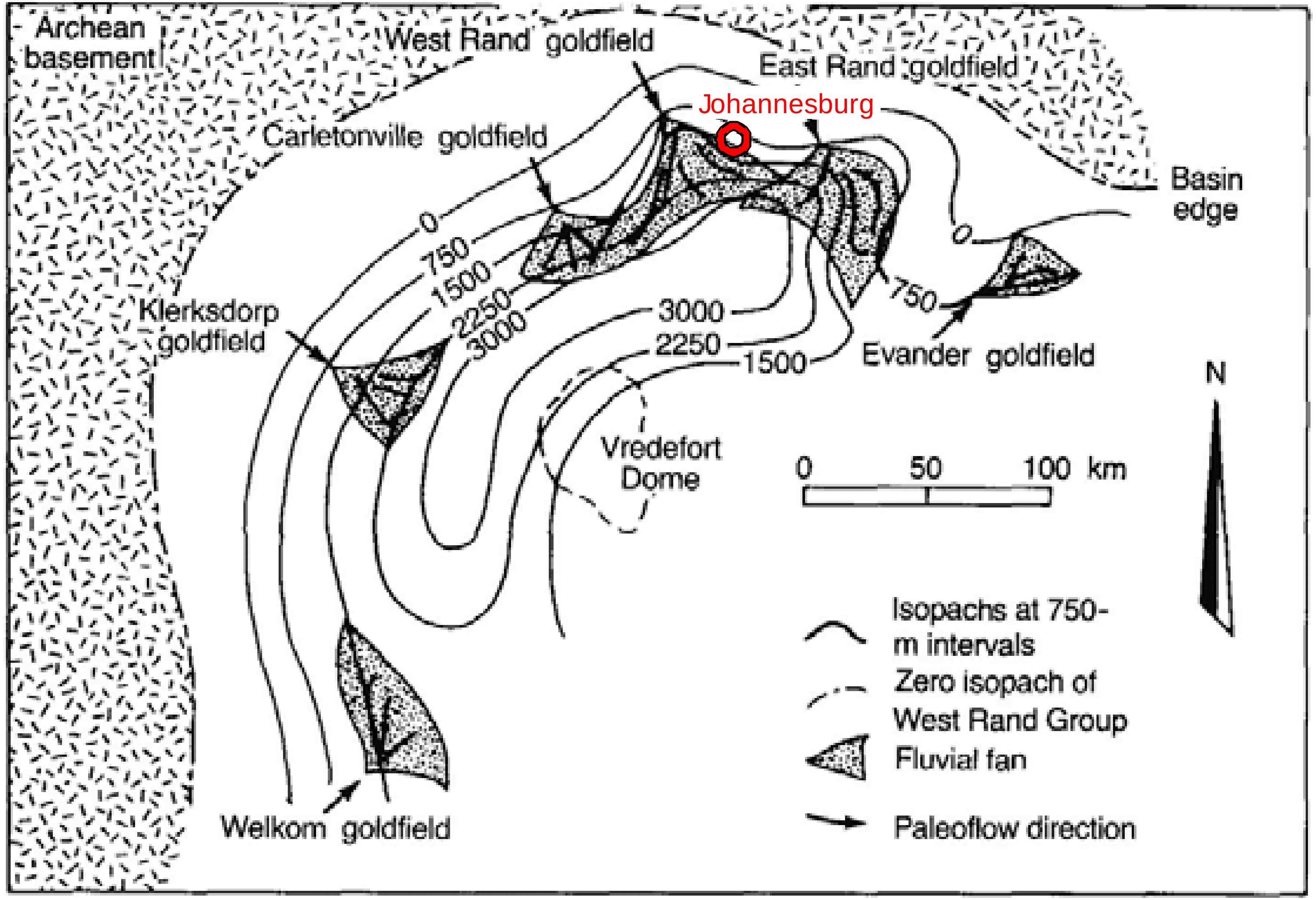

Archean basement
West Rand goldfield
East Rand goldfield
Johannesburg
Carletonville goldfield
Basin edge
0
750
1500
2250
3000
Klerksdorp goldfield
3000
2250
1500
750
0
Evander goldfield
N
Vredefort Dome
0 50 100 km
Isopachs at 750-m intervals
Zero isopach of West Rand Group
Fluvial fan
Paleoflow direction
Welkom goldfield

Quartz-pebble meta-conglomerate, Ventersdorp, 2.8 Ga, Witwatersrand, S-Africa

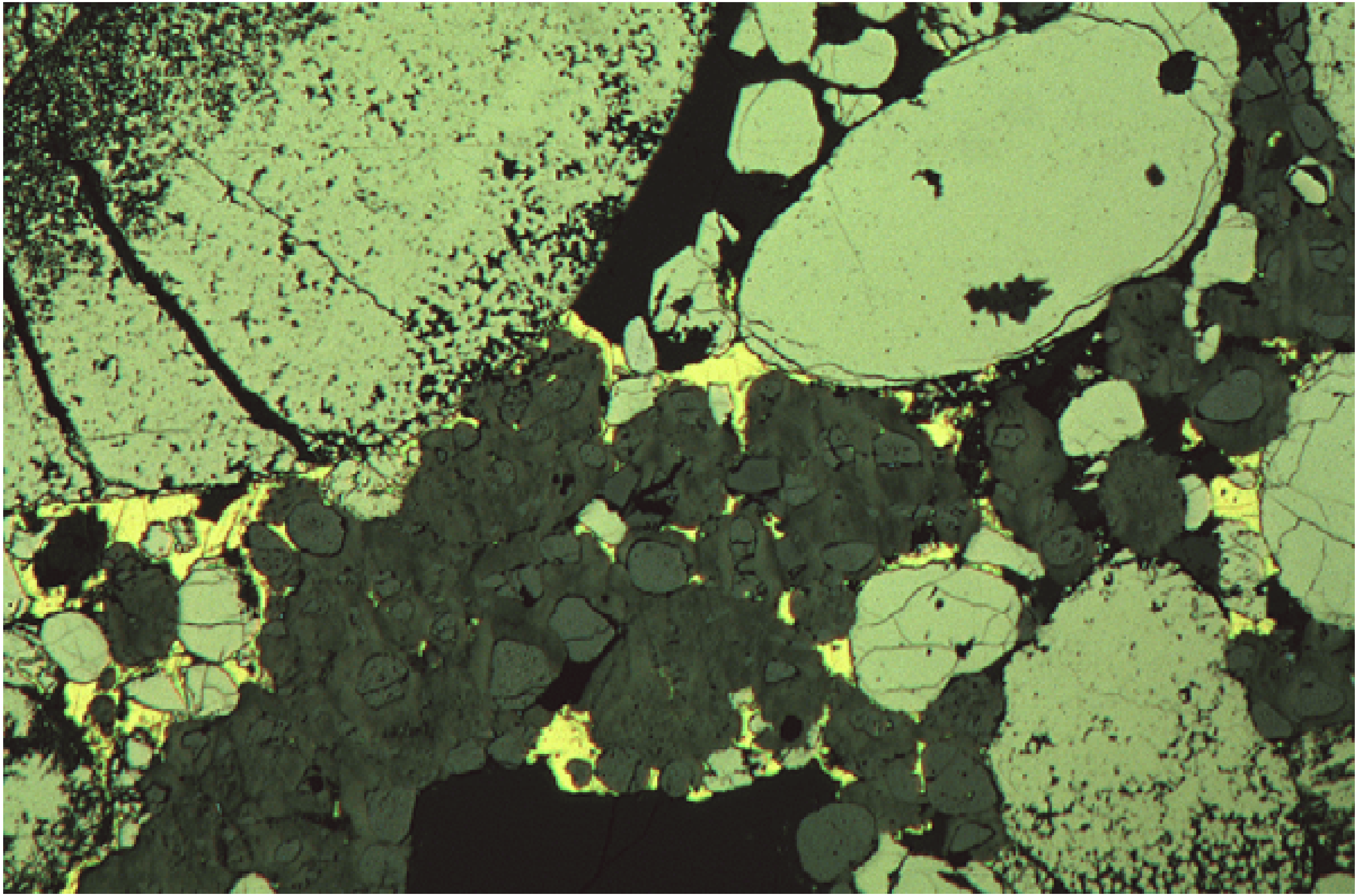

Polished section (3 mm length):
Elsburg mine, pyrite pebbles, uraninite-thucholite, gold

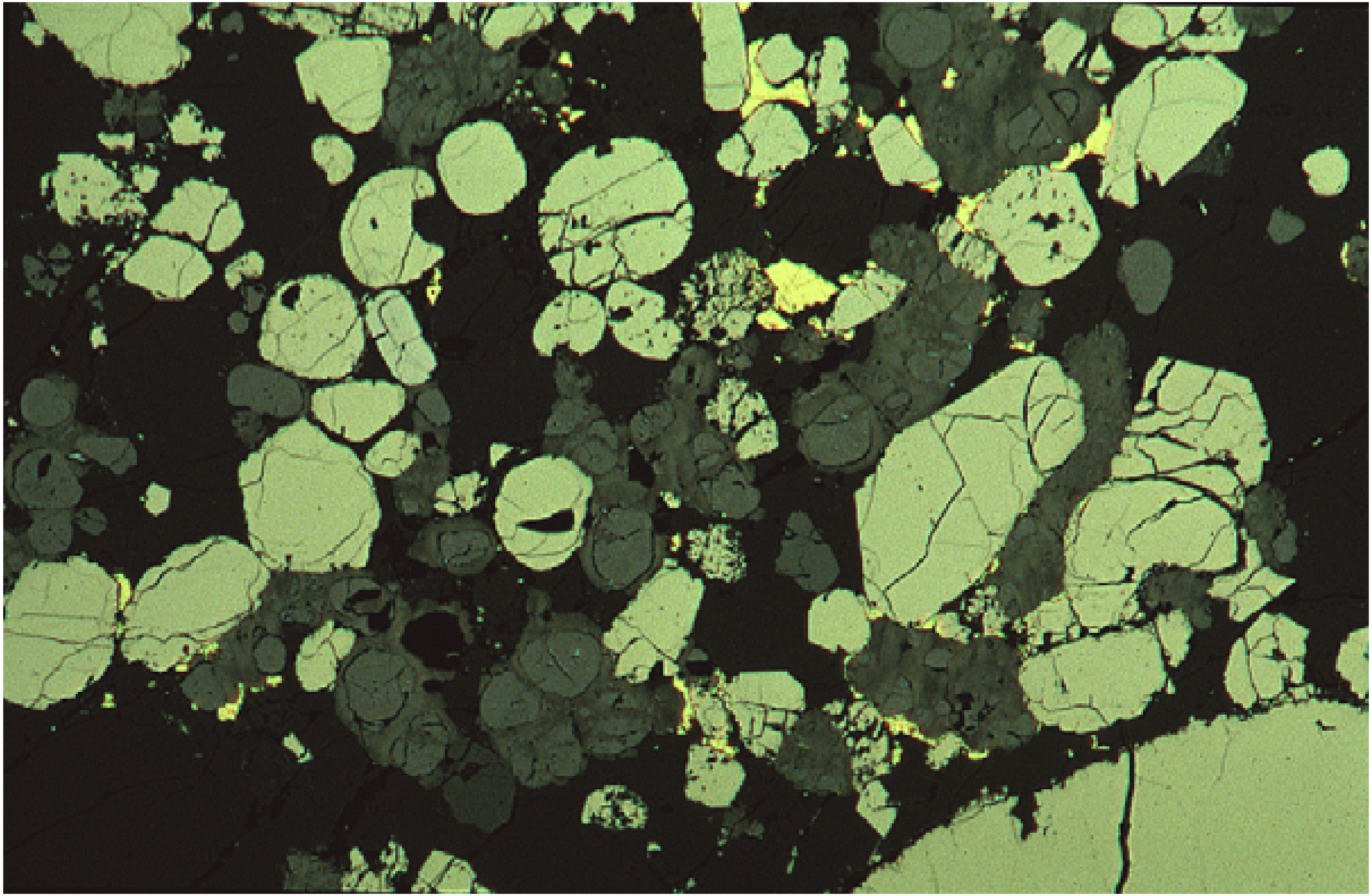

Polished section (3 mm length):
Elsburg mine, pyrite pebbles, uraninite-thucholite, gold

Uranium Isotopic Abundances

Solar system uranium today

^{238}U	99.2745 %
^{235}U	0.7202 ± 0.0006 %

OKLO ^{235}U

First measurement : 0.7171 % (a diff of 0.42 %)

Typical value in Oklo fossil reactors: 0.65 %

Lowest measurement : 0.29 %

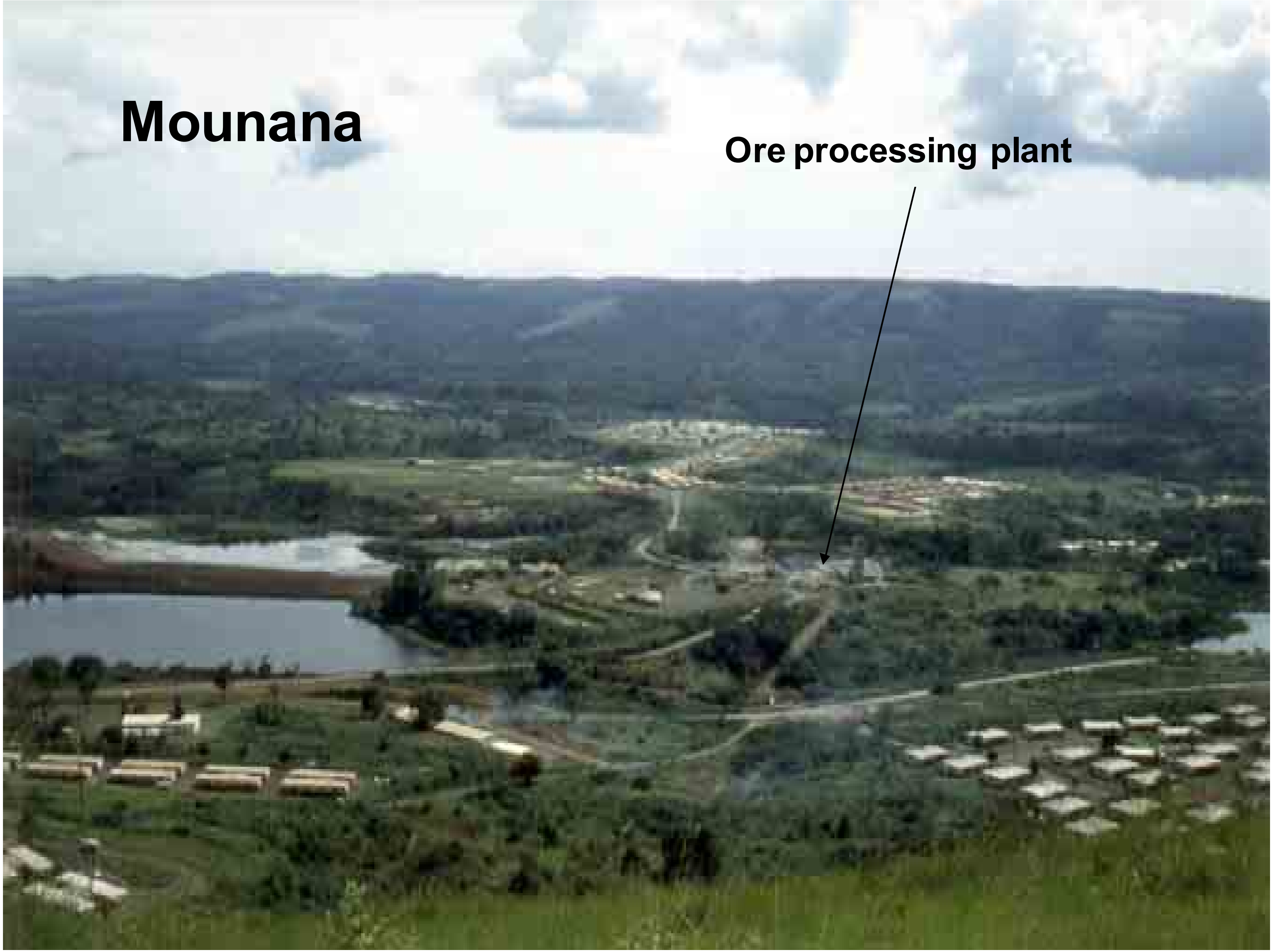
Mounana
Ore processing plant

Oklo Today

Mining ceased in 1979

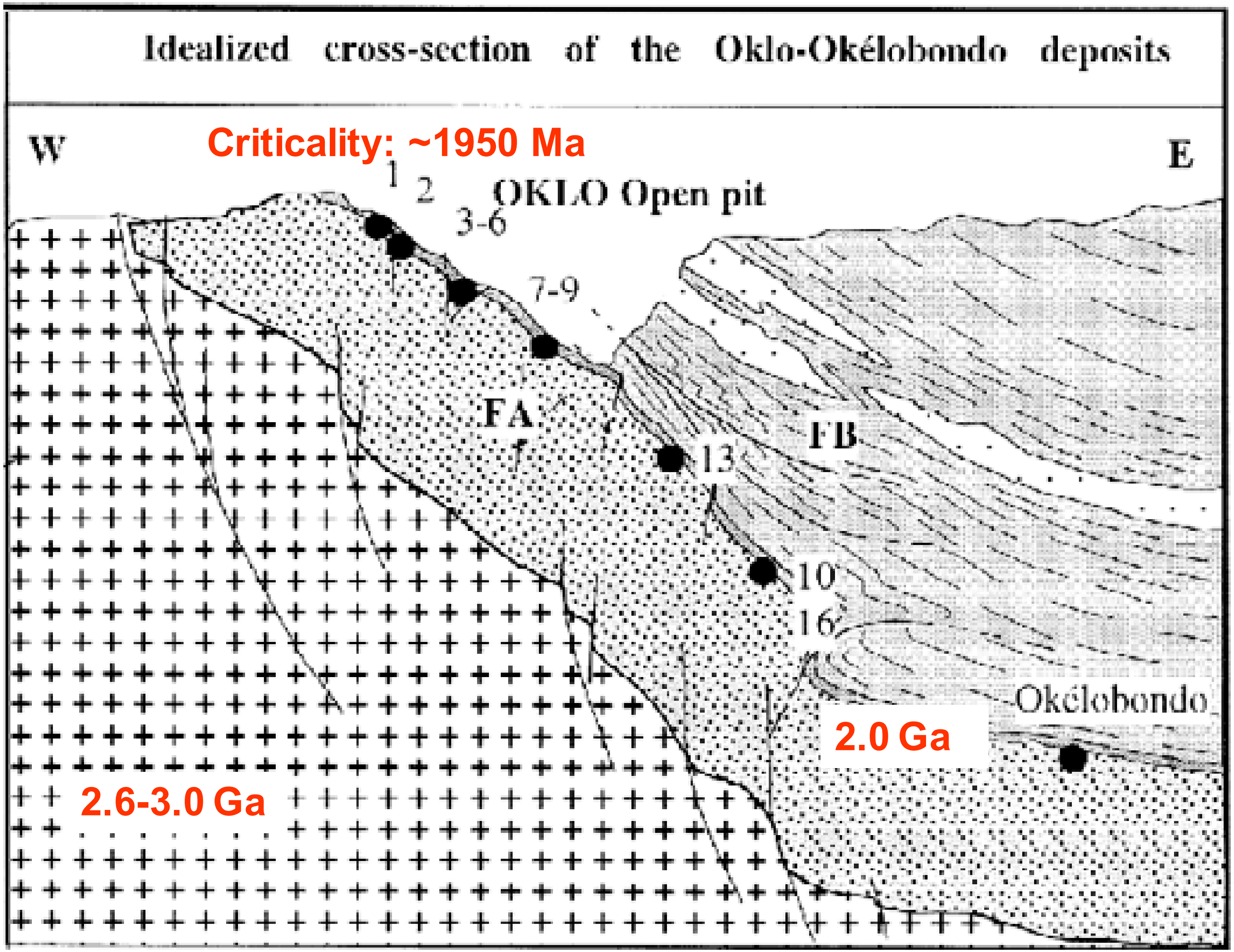

Pourcelot and Gauthier-Lafaye (1999) Chem Geol 157: 156

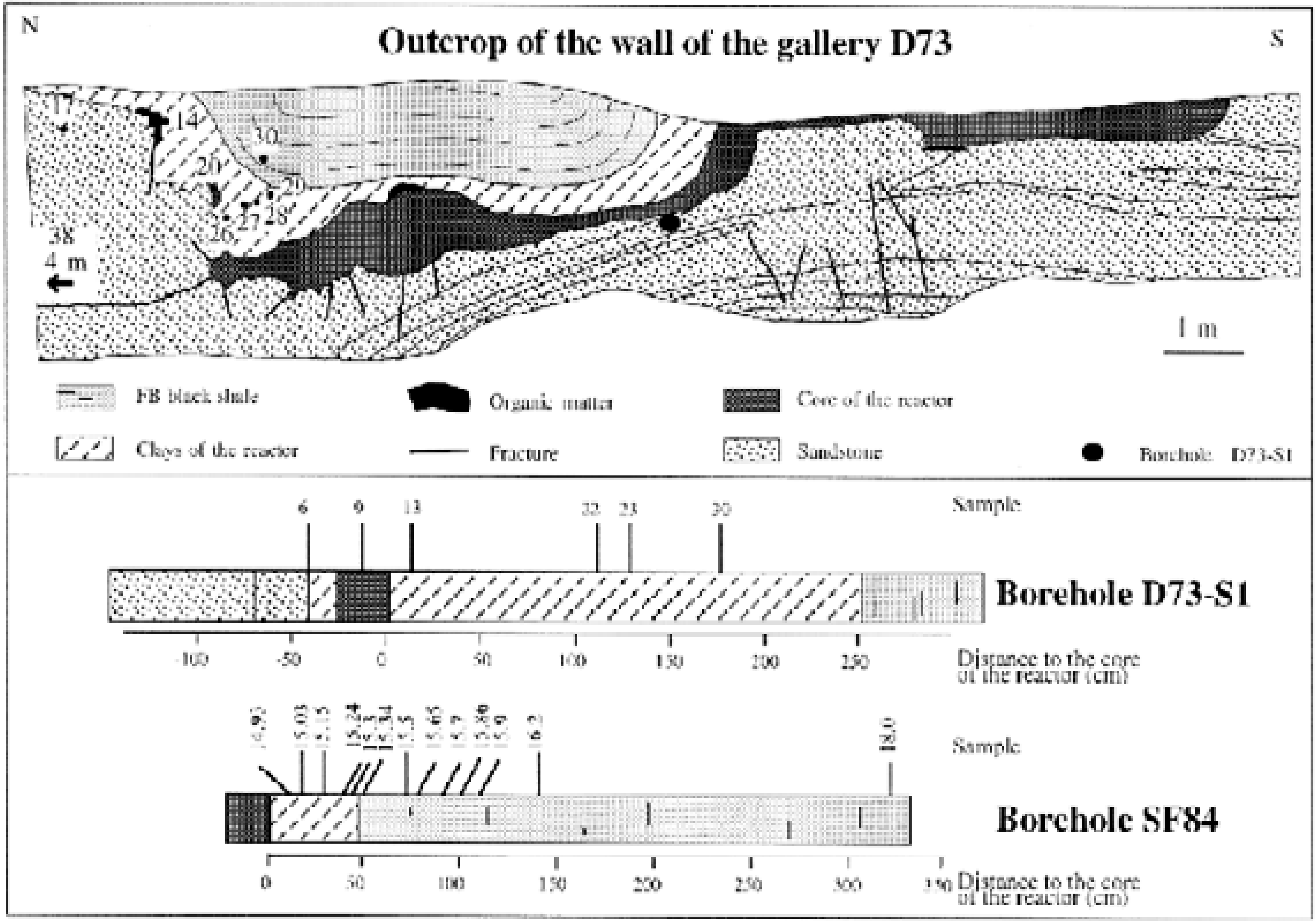

Pourcelot and Gauthier-Lafaye (1999) Chem Geol 157: 157


10
13
14
12
9
2
1


Zone 10
Doleritic
Dyke
Zone 13
Zone 14


Zone 2
Entrance to Zone 15


F_B Pelites
F_A Sandstones
Zone 15

Reactor Requirements

Uranium
Reactor: ^{235}U 1-10 %
Natural ^{235}U 0.72%

U Fuel Quality
Free of neutron
poisons (Cd, REE)

FISSION REACTOR

Moderator
Thermalised neutrons
H_2O or C

Reactor Size
Able to utilise neutrons
Fuel assemblage vol of
cubic metres

Reactor Requirements

Uranium
Reactor: ^{235}U 1-10 %
Natural ^{235}U 0.72%
Oklo ~3%

U Fuel Quality
Free of neutron poisons (Cd, REE) √

FISSION REACTOR

Moderator
Thermalised neutrons
H_2O or C

Reactor Size
Able to utilise neutrons
Fuel assemblage vol of cubic metres √

Oklo: a "Breeder" reactor

~50 % of the total energy released at Oklo (~15 GWa) is from breeding of ^{239}Pu and decay to ^{235}U

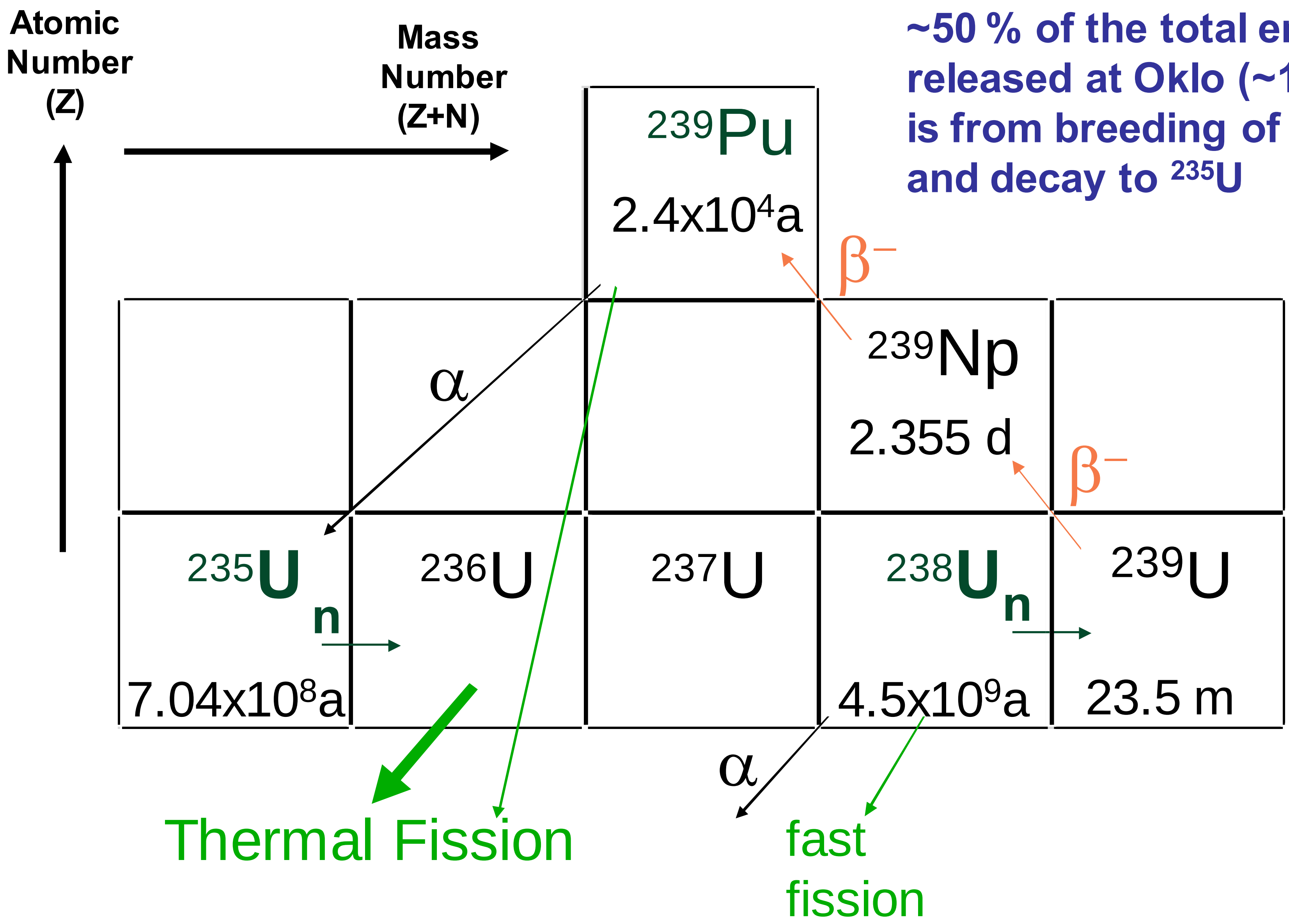

Retention of Fission Products at OKLO

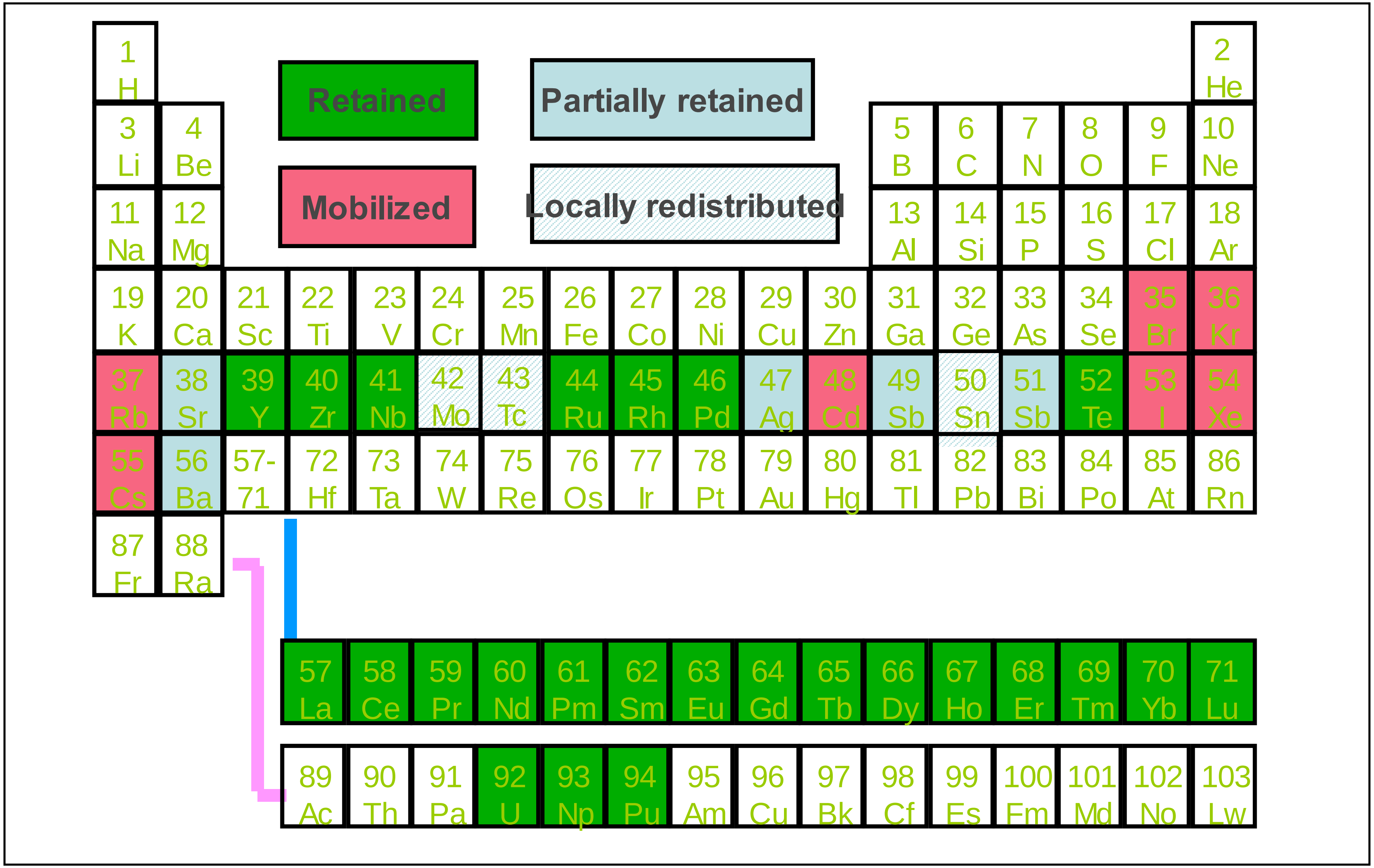

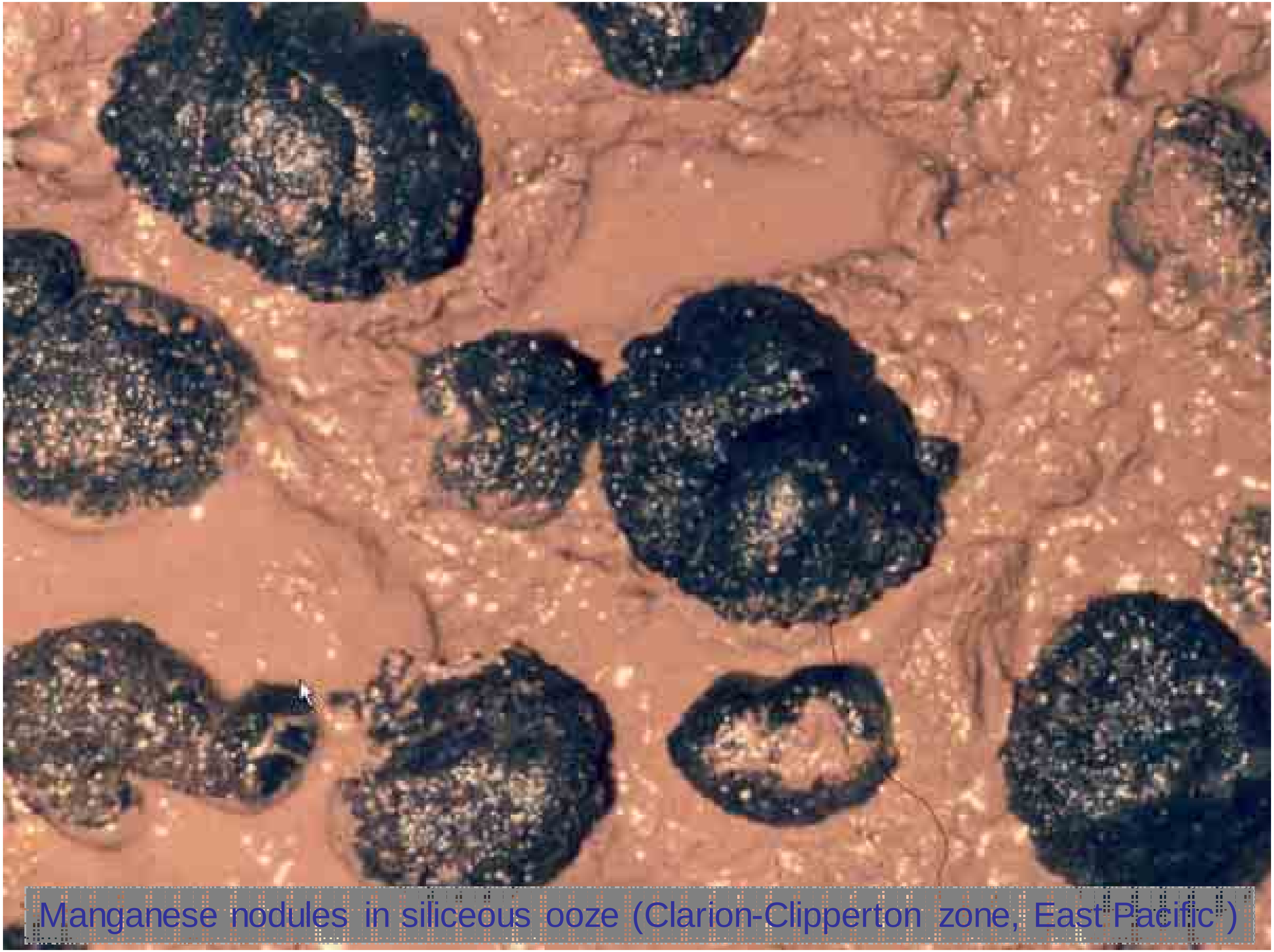

Manganese nodules in siliceous ooze (Clarion-Clipperton zone, East Pacific)

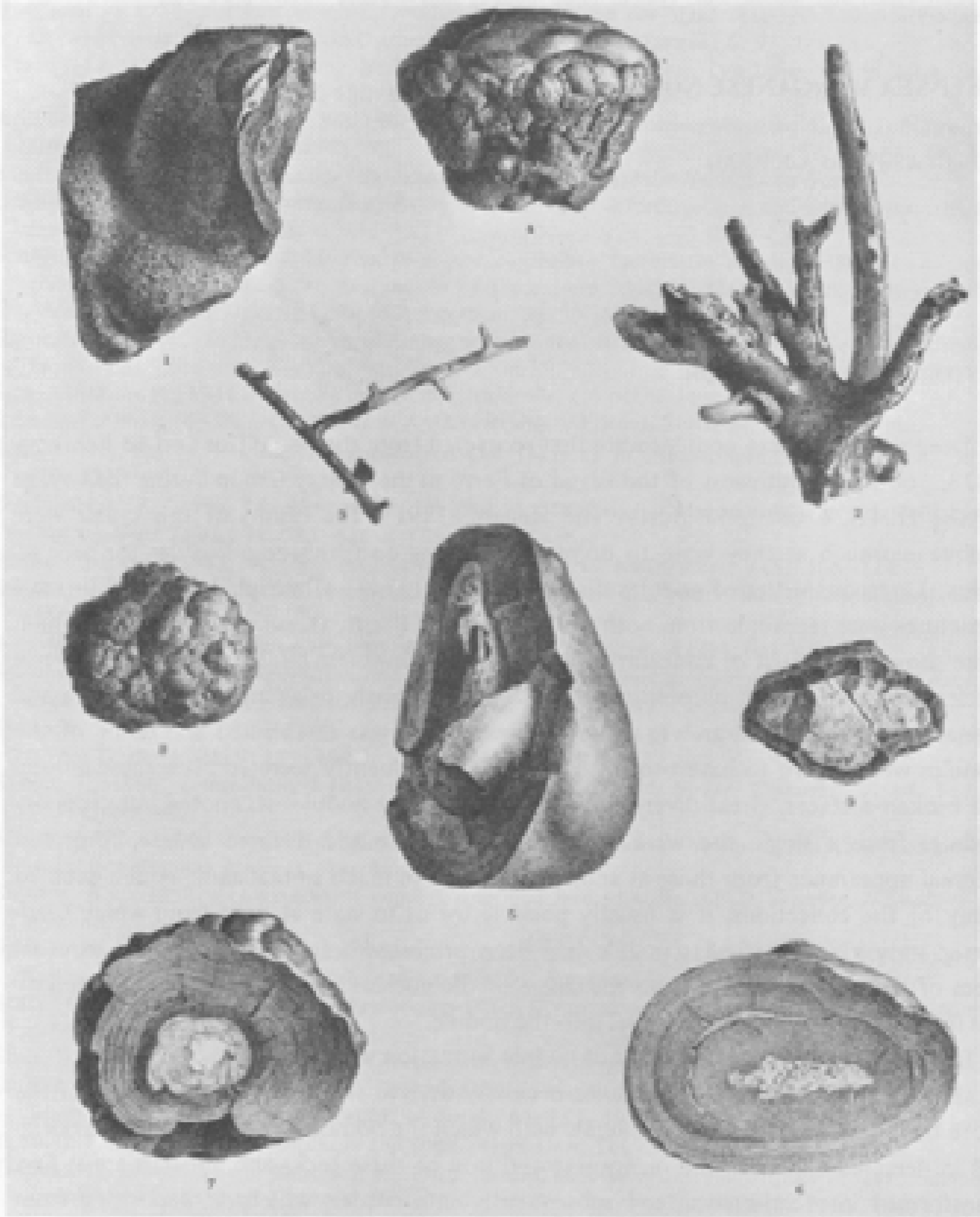

Fig. 1. Line drawing of manganese-iron nodules collected during the H.M.S. *Challenger* Expedition (1872–1876). (Murray and Renard, 1891, plate III).

Manganese nodules and crusts: Hydrogenetic formation in the deep sea with extremely low clastic deposition.

Growth rate of a few mm/Ma allows concentration of a wide range of elements from seawater (Mn, Fe, Ni, Co, Cu, Pb, Ba, Mo, V, Ti, Pt, Au) by adsorptive and redox processes.

Ore deposits form in any aqueous environment: the lower the temperature, the more water is needed to transport the amount of metals for enrichment to ore level (up to 100 million times in Mn nodules with respect to sea water)

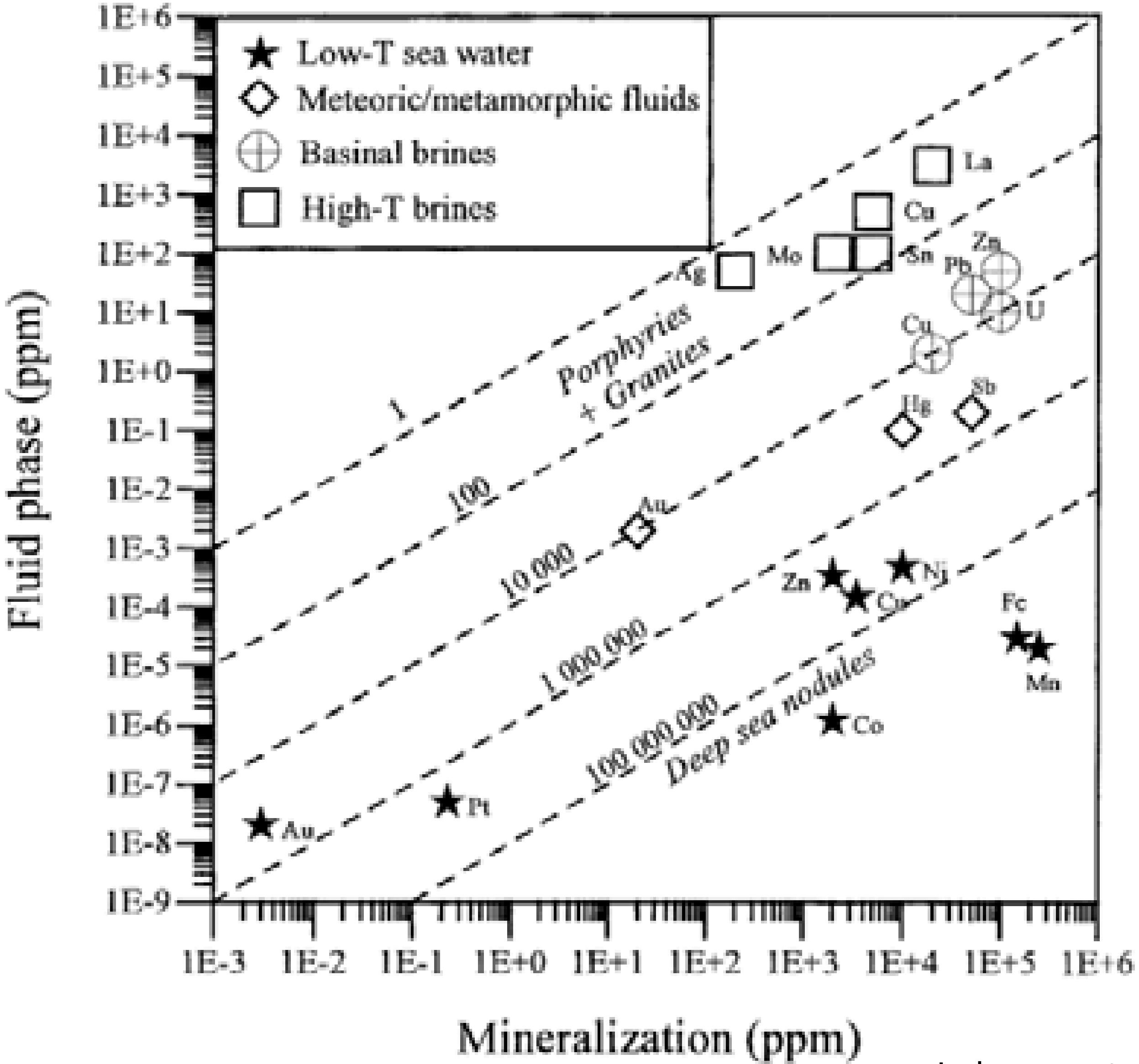

Lehmann et al. (2000) Int J Earth Sci 89: 286

Ice on Mars,
Phoenic Mission;
Smith et al. (2009)
Science 325: 60